Vol. 17 • No. 1 • April 2023

JOURNAL OF GEOMATICS

ISSN: 0976 - 1330

An official publication of Indian Society of Geomatics

Journal of Geomatics

(A publication of the Indian Society of Geomatics)

Editorial Board

Chief Editor: Dr. R.P. Singh
(Address for Correspondence: Director, Indian Institute of Remote Sensing, ISRO, Dehradun - 248001, India)
Phone: +91-135-2744583, 2524101 (O), Email: rpsingh@iirs.gov.in, editorjogisg@gmail.com

Associate Editors:

Harish Chandra Karnatak	Dehradun, Email: harish.karnatak@gmail.com
Bijoy K. Handique	Shillong, Email: bkhandique@gmail.com
D. Giri Babu	Jodhpur, Email: giribabu.d@nrsc.gov.in
R. Ratheesh	Ahmedabad, Email: ratheeshr@sac.isro.gov.in
S.V.V. Arun Kumar	Ahmedabad, Email: arunkumar@sac.isro.gov.in
R. Agrawal	Ahmedabad, Email: ritesh_agrawal@sac.isro.gov.in

Guest Editors:

C. P. Singh	Ahmedabad, Email: cpsingh@sac.isro.gov.in
Shard Chander	Ahmedabad, Email: schander@sac.isro.gov.in

Members:

A.R. Dasgupta	Ahmedabad, Email: arup@ieee.org
P.K. Garg	Dehradun, Email: gargpfce@iitr.ernet.in
P.K. Verma	Bhopal, Email: drpkverma@rediffmail.com
Ashok Kaushal	Pune, Email: akaushal1960@yahoo.co.in
T.T. Medhavy	Australia, Email: medhavy.thankappan@ga.gov.in
I.V. Murali Krishna	Hyderabad, Email: ivm@ieee.org
S.M. Ramasamy	Tiruchirapalli, Email: grucc@ruraluniv.ac.in
P.S. Roy	Hyderabad, Email: psroy1952@yahoo.in
Milap Chand Sharma	New Delhi, Email: milap@mail.jnu.ac.in
Tara Sharma	Canada, Email: sharmatara@yahoo.com
P. Venkatachalam	Mumbai, Email: pvenk@csre.iitb.ac.in
Claudio Zucca	Morocco Email: c.zucca@cgiar.org

Advisory Board

Paul J. Curran	Vice-Chancellor, Bournemouth University, Poole, **UK**
V. Jayaraman	Bengaluru, **India**
R. Krishnan	Thiruvananthpuram, **India**
P. Nag	Varanasi, **India**
M.P. Narayanan	President, CSDMS, NOIDA, U.P., **India**
R.R. Navalgund	Bengaluru, **India**
Y.S. Rajan	Bengaluru, **India**
Josef Strobl	Interfaculty Dept. of Geoinformatics, University of Salzburg, **Austria**

Indian Society of Geomatics
Executive Council 2020-2023

Secretary: (address for correspondence)
6202, Space Applications Centre, ISRO, Bopal Campus, Ahmedabad-380058, India
Email: secretary@isgindia.org; sasharma@sac.isro.gov.in

Journal of Geomatics

(A Publication of the Indian Society of Geomatics)
Vol. 17. No. 1 Research articles April 2023

Journal of Geomatics Vol. 17, No. 1, April 2023

Monitoring of monthly scale chlorophyll concentration variability in the Bay of Bengal and Arabian Sea using MODIS Aqua Satellite Data

*K. Nanthini Devi[1,2] and R.K. Sarangi[1]
Marine Ecosystem Division
[1]BPSG/EPSA, Space Applications Centre (ISRO), Ahmedabad-380 015, Gujarat
[2]Marine Planktonology & Aquaculture Lab., Department of Marine Science
School of Marine Sciences, Bharathidasan University, Tiruchirappalli-620 024, Tamil Nadu
*Email: nanthinidevi74@gmail.com

(Received: 25 Feb 2022, Accepted in final form: 13 April 2023)

DOI: *https://doi.org/10.58825/jog.2023.17.1.77*

Abstract: Study has been carried out to monitor the phytoplankton biomass in Bay of Bengal (BoB) and Arabian Sea (AS) using Moderate Resolution Imaging Spectroradiometer (MODIS) Aqua satellite data. Cloud masking, geometric corrections and subsets generations were performed to retrieve chlorophyll images from MODIS-Aqua data during the periods January - December for the years 2007 and 2008. The two regions (BoB & AS) have been divided into four subsets; subset-1 (Northern Bay of Bengal), subset-2 (Southern Bay of Bengal), subset-3 (Northern Arabian Sea) and subset-4 (Southern Arabian Sea). The results were analyzed and confirmed that chlorophyll concentration mean range was high (0.97-1.89 mg m^{-3}) in northern Arabian Sea during the months of July for both years 2007 and 2008 and low concentration range (0.12-0.35 mg m^{-3}) was obtained during April month for both years in southern Bay of Bengal. This study found to be important as information about the chlorophyll concentration in the Northern Indian Ocean.

Keywords: Phytoplankton, Bay of Bengal, Arabian Sea, MODIS-Aqua, chlorophyll

1. Introduction

Oceans occupy almost 70% of the Earth's surface, which play an important role in climatic conditions of the adjacent land regions. In ocean, the physical, chemical and biological processes are linked in intimate manner (Tang et al., 2002). Oceanic features such as currents boundaries, sea surface temperature, ocean fronts and eddies, suspended particulate matter and dissolved organic matter influence the ocean dynamics and its interaction with the atmosphere. Long-term ocean colour satellite monitoring provides an important tool for better understanding of the marine processes, ecology and coastal environmental changes (Yoder et al. 1993; Tang et al. 1998 & 1999; Tang & Kawamura, 2001; Tang et al. 2002). Remote sensing of ocean colour yields information on the constituents of seawater such as concentration of phytoplankton pigments, suspended sediments and yellow substance. The methods of detecting and mapping seawater constituents from aircraft and from space-borne platform have been successfully developed during past three decades. Routine monitoring of regional and temporal variability of ocean chlorophyll provides information on primary production and subsequent assessment of secondary and higher order production processes such as zooplanktons and marine fisheries (Chauhan et al. 2001). The phytoplanktons are critical to all life on earth because of their great contribution to food webs and their generation of large amounts of atmospheric oxygen through photosynthesis (Sarangi et al. 2005).

Ocean colour is determined by the interactions of incident light with constituents present in the water. Accurate measurements of light radiance at visible wavelengths produce ocean color data, which are related to constituents present in the water. Such measurements are used to monitor the level of biological activity and presence of materials in ocean water. Ocean colour information on a global scale is also important in studying the bio-geochemical cycles of carbon-nitrogen and sulfur (Chauhan et al. 2002). Efforts have been made to study the chlorophyll distributions in Arabian Sea (Nakamoto et al. 2000; Madhupratap et al. 1996 & Tang et al. 2002) and its influence on the sea surface temperature (Sathyendranath et al. 1991), whereas limited efforts on the detailed study with high-resolution data have been made in coastal regions of Arabian Sea and Bay of Bengal. The northeastern part of the Arabian Sea is one of high productive zones and southern part of the Bay of Bengal is not much productive compared to northern Bay of Bengal (Chauhan et al. 2001).
The continental shelf in this part of Arabian Sea is much shallower compared to shelf in Bay of Bengal. Arabian Sea (AS) and Bay of Bengal (BoB) are two basins in Northern Indian Ocean. Though AS and BOB are landlocked to the north, they show large contrast in salinity, SST and even productivity pattern. Both the basins are influenced by south westerly wind in summer and north easterly wind in winter season. Rather than monsoonal wind very high intense but short duration cyclonic winds are frequent in both the basins. There are increases in occurrences of intense cyclones in AS as well as in the entire world basin and change of oceanic property was observed after cyclone

travel (Madhumita et al. 2012). Cyclonic disturbances caused an enhanced phytoplankton biomass in Open Ocean of upper stratified water column in Bay of Bengal (BoB) and Arabian Sea (AS). Higher cyclonic wind speed caused high phytoplankton biomass in Indian Ocean. The earlier studies have reported that chlorophyll biomass was increased more than five times after cyclone passage in Indian Ocean compared with before occurrence of cyclone. The objective of the present study is to study the variability of chlorophyll concentrations in these regions, Arabian Sea and Bay of Bengal for the years, 2007 and 2008 since more number of cyclones has been documented.

2. Data and Methodology

The retrieval of ocean color parameter such as phytoplankton pigment (Chlorophyll-a) in oceanic waters, involves two major steps, the atmospheric correction of visible channels to obtain normalized water leaving radiances in shorter wavelengths and application of the bio-optical algorithm for retrieval of phytoplankton pigment concentrations.

2.1 Study area

Phytoplankton productivity was determined based on chlorophyll concentrations from two regions, Bay of Bengal and Arabian Sea (68° - 91°E Longitude; 5°- 23.8° N Latitude) from January - December during the years, 2007 and 2008. The Bay of Bengal region is divided into two subsets, subset 1 is Northern Bay of Bengal (Longitude: 77.5° - 91° E, Latitude: 14° - 23.8° N) and subset 2 is Southern Bay of Bengal (77.5° - 91° E, 5° - 14° N), correspondingly Arabian sea region is also divided in to two subsets, subset 3 is Northern Arabian sea (68° - 77.5° E; 14° - 23.8° N) and subset 4 is Southern Arabian sea (68° - 77.5° E; 5° - 14° N).

2.2 Satellite Chl- a data

MODIS datasets were processed in order to analyze the monthly changes in chlorophyll pattern from Bay of Bengal and Arabian Sea. The MODIS sensor onboard Terra and Aqua satellites has been boon to scientific community and involved in analysis and characterization of global dynamics and processes occurring on land, in oceans, and in lower atmosphere. It also played vital role in development of validated, global, interactive earth system models able to predict global change accurately enough to assist policy makers in making sound decisions concerning the protection of environment. MODIS sensor has 36 spectral bands between 0.405 - 14.385 µm and acquires data at three spatial resolutions 250m, 500m and 1000m and viewing swath width of 2,330 km and revisit cycle of 2 days.

2.3 Data Processing

Two years monthly cloud free and less cloud cover Level-3 MODIS Aqua data were averaged from January-December during the years, 2007 and 2008 and has been analyzed. Processing and analysis of the MODIS data derived chlorophyll-a images has been done using ENVI- 4.4 software. The chlorophyll concentration of Bay of Bengal and Arabian Sea ranged 0 - 2 mg m^{-3}.

3. Results

3.1 Chlorophyll concentration in Bay of Bengal and Arabian Sea during 2007

The results revealed that chlorophyll concentration was determined from two regions, Bay of Bengal and Arabian Sea. MODIS derived chlorophyll-a images of Bay of Bengal and Arabian Sea during 2007 & 2008 are given in Figure 1 & 2 and different four subsets (subsets 1, 2, 3 & 4) during 2007 & 2008 are shown in Figure 3 & 4. Chlorophyll concentration mean values for four subsets (subsets 1, 2, 3 & 4) were calculated for the year, 2007 at different months. The results are discussed that, subset-1 (Northern Bay of Bengal - NBoB) showed chlorophyll concentration ranged between 0.19 - 0.56 mg m^{-3}, the maximum chlorophyll concentration was found in August and minimum was found in June. Correspondingly, subset-2 (Southern Bay of Bengal - SBoB) showed the chlorophyll concentration ranged from 0.14 - 0.50 mg m^{-3}, chlorophyll level was high in July and low in April. Subset-3 (Northern Arabian Sea - NAS) illustrated that chlorophyll concentration range was 0.35 - 0.97 mg m^{-3}, highest level was present in July and lowest level was in May. Subset-4 (Southern Arabian Sea - SAS) displayed that chlorophyll concentration range from 0.12 - 0.38 mg m^{-3}, more value was obtained from the month of September and less value was in April. Among four subsets, NAS exhibited high concentration of chlorophyll (0.97 mg m^{-3}), moderate level was observed from NBoB (0.56 mg m^{-3}) and SBoB (0.50 mg m^{-3}) and low concentration was recorded from SAS (0.38 mg m^{-3}).

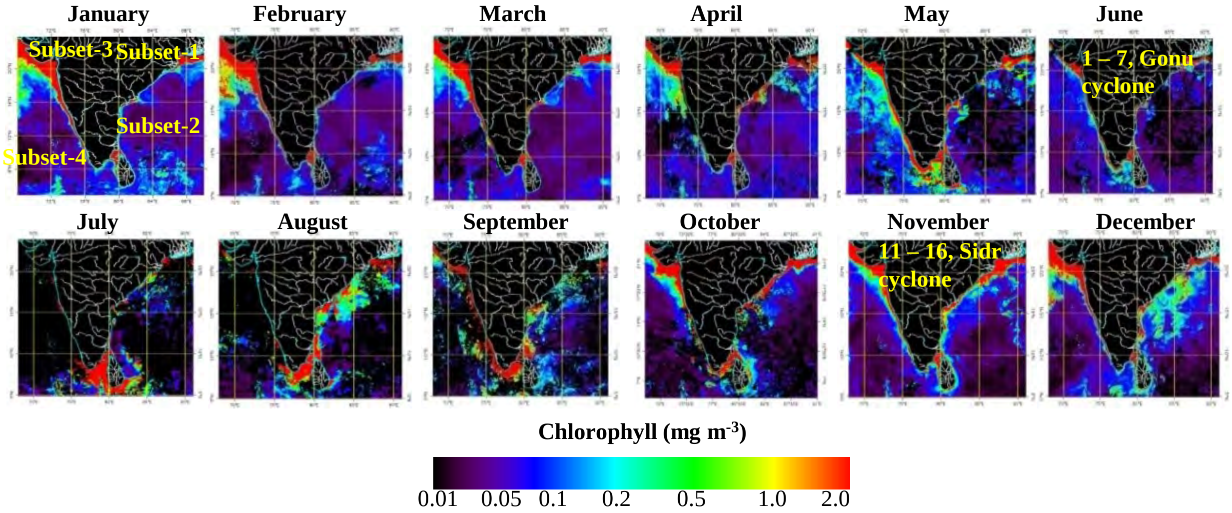

Figure 1. January-December monthly chlorophyll image during 2007 displaying subset 1-4

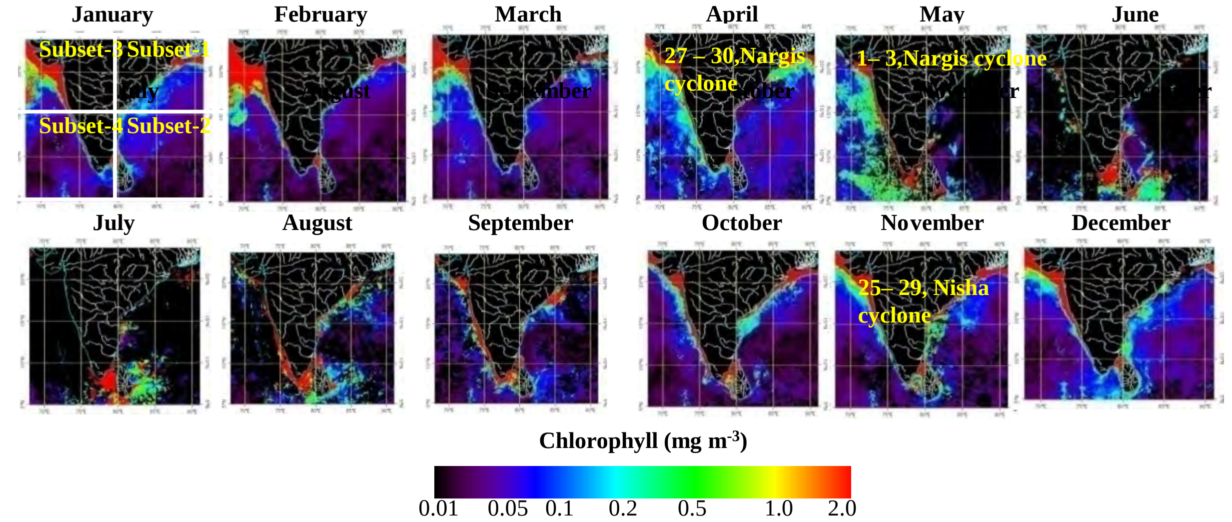

Figure 2. January-December monthly chlorophyll image during 2008 displaying subset 1-4

Chlorophyll concentration standard deviation (SD) values of four subsets during the year, 2007 at different months (January - December) are determined. The results concluded that NBoB showed the SD values from 0.28 - 0.57 mg m^{-3}, maximum variation of chlorophyll concentration (CC) in October and minimum was in June, subsequently SBoB (0.21 - 0.61 mg m^{-3}), more variation was found in July and less in February & March. In NAS (0.50 - 0.75 mg m^{-3}), highest level of variations between CC was noticed from July and lowest level was in May. Similarly, SAS (0.11 - 0.47 mg m^{-3}), CC variation was high in September and low in April. Compared with four subsets, NAS exhibited more (0.75 mg m^{-}3) variations of chlorophyll concentration followed by SBoB, NBoB and SAS.

3.2 Chlorophyll concentration in Bay of Bengal and Arabian Sea during 2008

The chlorophyll concentrations (CC) for four subsets at different months for the year, 2008. The results showed that NBoB shows the mean value from 0.22 - 0.57 mg m^{-3}, maximum value was observed in July and minimum value was observed in April followed by SBoB is 0.14 - 0.51 mg m^{-3}, highest level was obtained from month of July and lowest level was found in April; NAS is 0.33 - 1.89 mg m^{-3}, maximum value was documented from July and minimum value was from May and SAS is 0.15 - 0.47 mg m^{-3}, mean value was high in August and low in April & November. Between four subsets, NAS exhibited the maximum mean (1.89 mg m^{-3}) value of chlorophyll compared with other subsets. The SD values of chlorophyll for four subsets during the year, 2008 at different months. From these results, NBoB showed the maximum and minimum SD values from 0.34 - 0.57 mg m^{-3}, maximum variation of chlorophyll concentration (CC) in September and minimum was in April, subsequently SBoB (0.19 - 0.56 mg m^{-3}), more variation was found in July and less in April. Equally, NAS (0.35 - 0.75 mg m^{-3}), highest level of variations between CC was noticed from February and lowest level was in July and SAS (0.13 - 0.62 mg m^{-3}), CC variation was high in August and low in April. Compared with four subsets, NAS showed highest (0.75 mg m^{-3}) variation of chlorophyll concentration consequently, SAS, NBoB and SBoB.

3.3 Correlation between Chlorophyll concentrations in Bay of Bengal and Arabian Sea during 2007 and 2008

Interrelations of chlorophyll mean four subsets (ss-1, ss-2, ss-3 & ss-4) of BoB and AS for the year, 2007 are given in Table 1.

Table 1. Interrelations of chlorophyll mean for Bay of Bengal & Arabian Sea during 2007 & 2008.

Iterations	Interrelations of Chlorophyll mean of subsets (ss-1 to ss-4)	R^2 value (Year 2007)	R^2 value (Year 2008)
1	ss-1 vs ss-2	0.27	0.52
2	ss-1 vs ss-3	0.17	0.37
3	ss-1 vs ss-4	0.10	0.47
4	ss-2 vs ss-3	0.64	0.27
5	ss-2 vs ss-4	0.62	0.70
6	ss-3 vs ss-4	0.33	0.17
7	ss-1 & 2 vs ss-3 & 4	0.31	0.43

Correlation between chlorophyll concentrations of subsets-1&2, subsets-1&3, subsets-1&4, subsets-2&3, subsets-2&4 and subsets-3&4 during Jan - Dec, 2007 are shown in Table 1. Since these results confirmed that NBoB observed chlorophyll concentration (CC) was less (R^2 value = 0.27) correlated with SBoB (a), subsequently, NBoB was lowest level (R^2 = 0.17) correlated with NAS and SAS (R^2 = 0.10). Also, SBoB of CC was maximum (R^2 = 0.64) correlated with NAS and SAS (R^2 = 0.62), followed, NAS of CC was minimum (R^2 = 0.33) correlated with SAS respectively. Correlation between chlorophyll concentrations of subsets-1&2, subsets-1&3, subsets-1& 4, subsets-2&3, subsets-2&4 and subsets-3&4 during Jan - Dec, 2008 are shown in Table 1. The results shows that NBoB observed chlorophyll concentration was higher (R^2 value = 0.52) correlated with SBoB, followed shows minimum correlation (R^2 = 0.37) with NAS and maximum correlated with SAS (R^2 = 0.47). SBoB was incredibly less (R^2 = 0.27) correlated with NAS and highest correlated with SAS (R^2 = 0.70), subsequently, NAS was lowest (R^2 = 0.17) correlated with SAS.

Subset 1 (2007)

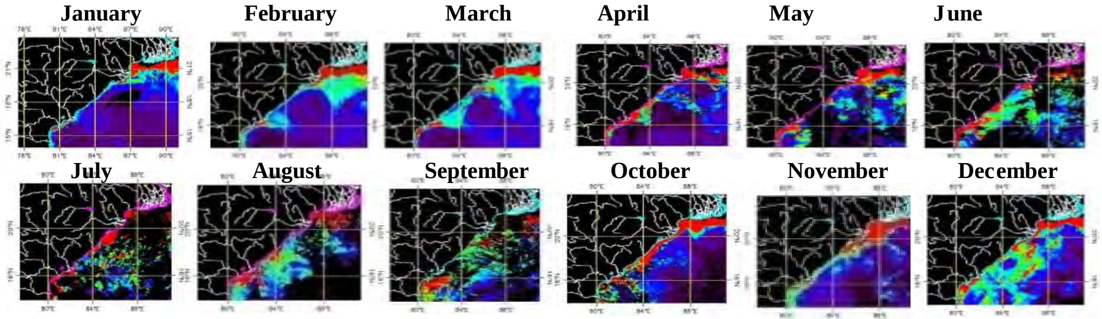
January February March April May June
July August September October November December

Subset 2 (2007)

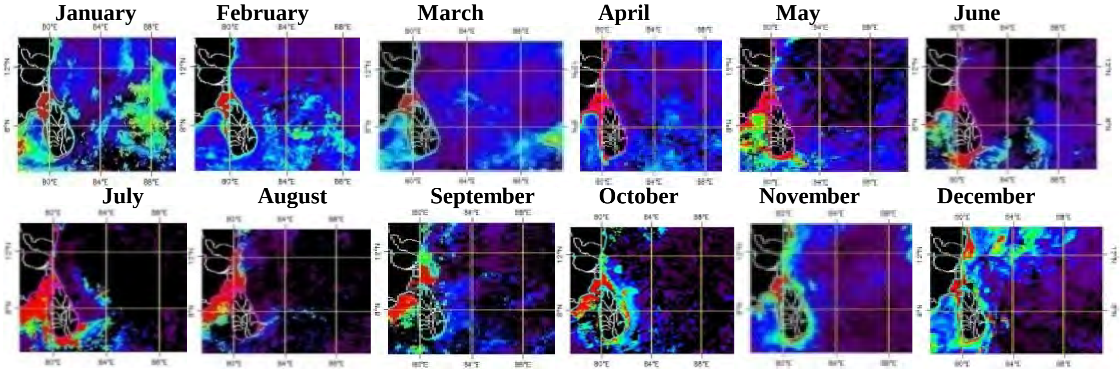
January February March April May June
July August September October November December

Subset 3 (2007)

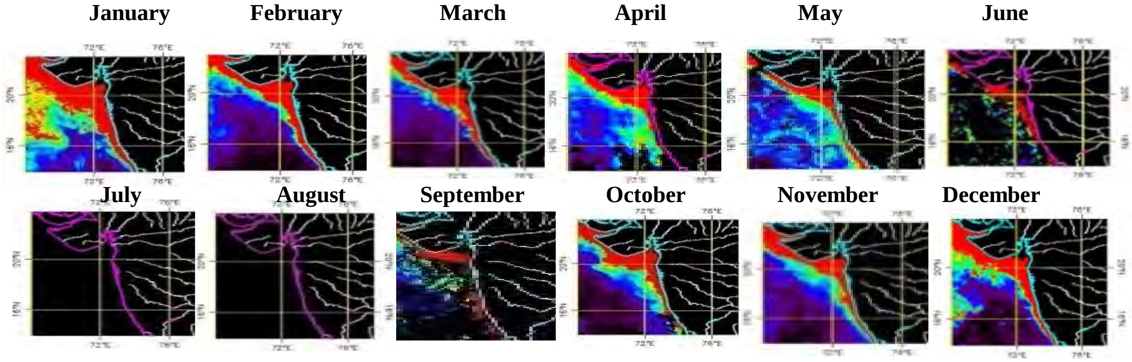
January February March April May June
July August September October November December

Subset 4 (2007)

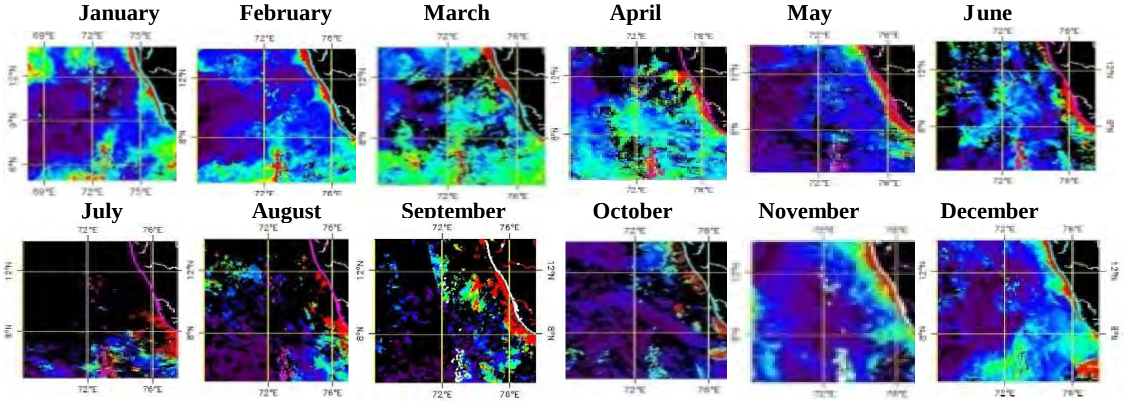
January February March April May June
July August September October November December

Figure 3. Chlorophyll image for four subset during January-December , 2007

Table 2. Interrelations of chlorophyll mean for Bay of Bengal & Arabian Sea during Jan - Dec, 2007 & 2008

Iterations	Chlorophyll mean of subsets	R^2 value (Years 2007 & 2008)
1	Subset-1	0.06
2	Subset-2	0.72
3	Subset-3	0.56
4	Subset-4	0.49
5	ss-1 & 2 vs ss-1 & 2	0.39
6	ss-3 & 4 vs ss-3 & 4	0.69
7	Four subsets	0.65

Association between chlorophyll concentrations of subset-1, subset-2, subset-3 & subset-4 during Jan - Dec, 2007 & 2008 are displayed in Table 2. The results are demonstrated that, chlorophyll concentration of NBoB during the year, 2007 was extremely less ($R^2 = 0.06$) correlated with NBoB for the year, 2008, equally, SBoB during the year, 2007 was exhibited highest ($R^2 = 0.72$) correlated with SBoB for the year, 2008 (b), followed NAS (2007) was maximum ($R^2 = 0.56$) correlated with NAS (2008) and SAS (2007) was minimum correlated ($R^2 = 0.49$) with SAS during 2008. Chlorophyll concentrations of subsets-1&2, 3&4 and subsets-1&2, 3&4 during January - December, 2007 and 2008 are shown in Table 1. The results are concluded, chlorophyll concentrations of NBoB & SBoB was less ($R^2 = 0.31$) correlated with NAS & SAS during the year 2007 and chlorophyll concentrations of NBoB & SBoB was more ($R^2 = 0.43$) correlated with NAS & SAS during the year 2008.

Comparison of Chlorophyll mean concentrations of Bay of Bengal subsets-1&2 (2007&2008) and Arabian sea subsets-3& 4 (2007&2008) during Jan - Dec, 2007 and 2008 are illustrated in Table 2. From these results, NBoB & SBoB (2007) was showed minimum ($R^2 = 0.39$) correlation with NBoB & SBoB for the year, 2008, followed, NAS & SAS (2007) was expressed maximum ($R^2 = 0.69$) correlation with NAS & SAS for the year, 2008. Differences between chlorophyll mean concentrations of Bay of Bengal & Arabian Sea four subsets (Subsets 1-4) during January - December, 2007 and 2008 are mentioned in Table 2. From these results, chlorophyll concentrations of four subsets (NBoB, SBoB, NAS & SAS) for the year, 2007 was moderately ($R^2 = 0.65$) correlated with four subsets during the year, 2008.

4. Discussion

Cyclonic events are characterized by a low-pressure center and numerous thunderstorms. The response of the chlorophyll concentration to propagating cyclones should be associated with phase of seasonal cycle of the concentration, as well as translation speed of the cyclone. Cyclones, eddies and circulation pattern have significant influence on distribution of chlorophyll pattern in Ocean. The present study, spatial and temporal distributions of the chlorophyll concentrations in parts of the Bay of Bengal and Arabian Sea have been observed during these years, 2007 and 2008. The present study results show higher chlorophyll concentration (CC) in northern Arabian Sea and more variations of CC also high in that region during July month compared with other months of NBoB, SBoB and SAS regions for the year, 2007. Correspondingly, NAS has highest value of CC variations were recorded from the month of July compared with other months of NBoB, SBoB and SAS regions during 2008. In addition, chlorophyll concentration was also high in NBoB during August month and variations of CC were high in October month compared with SBoB & SAS for the year, 2007. In 2008, maximum CC value was recorded from July month in NBoB followed by SBoB and SAS and variations between CC was found maximum in NBoB during September compared with other months.

Similar earlier studies have reported, seasonal variation has very prominent in Arabian Sea. The northern Arabian Sea is characterized by offshore and onshore chlorophyll blooms during the northeast monsoon period (Tang and Kawamura, 2001), where the southern Bay of Bengal is found to produce no such bloom. Yoder (2000) has found anomalous pattern of chlorophyll concentration caused by monsoon wind-induced upwelling in North Indian Ocean compared to other oceans. In Arabian Sea, similar trend has been found reported by previous studies (Chauhan et al., 2001;2002; Dey & Singh, 2003; Sarangi et al., 2001; 2005; Singh & Chaturvedi, 2010; Maneesha et al., 2011; Patissier et al., 2014), from this study findings are proved that chlorophyll biomass high in Arabian Sea compared with Bay of Bengal region (Dey & Singh, 2003; Chauhan et al., 2001; Chaturvedi et al., 2013) confirmed with high resolution data.

The present study findings are concluded that Arabian Sea has high chlorophyll biomass compared with Bay of Bengal (BoB) during the year, 2008 than 2007 for the reason that more cyclonic events were documented from October – December 2007 in Arabian Sea, accordingly end of cyclones passages leads to enhanced nutrients level in waters is responsible for more chlorophyll concentration in that region was found during the year 2008. In addition, BoB has lower nutrient concentrations and less cyclonic events were documented than AS.

Subset 1 (2008)

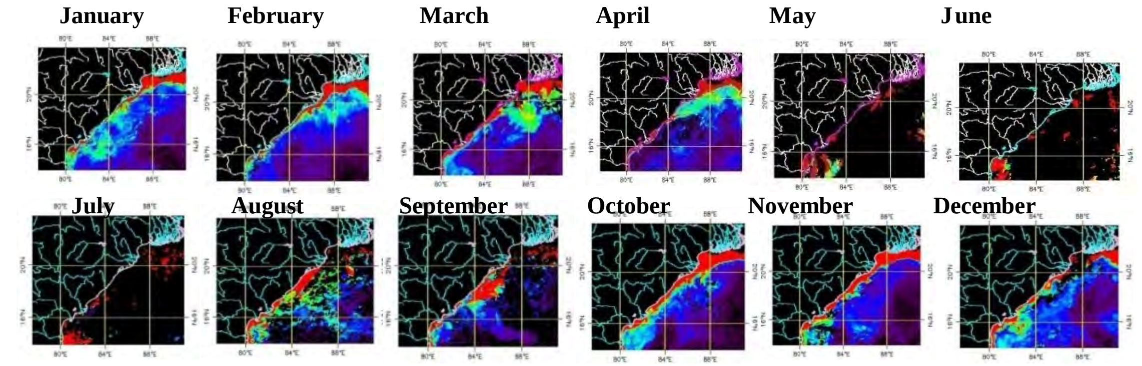

Subset 2 (2008)

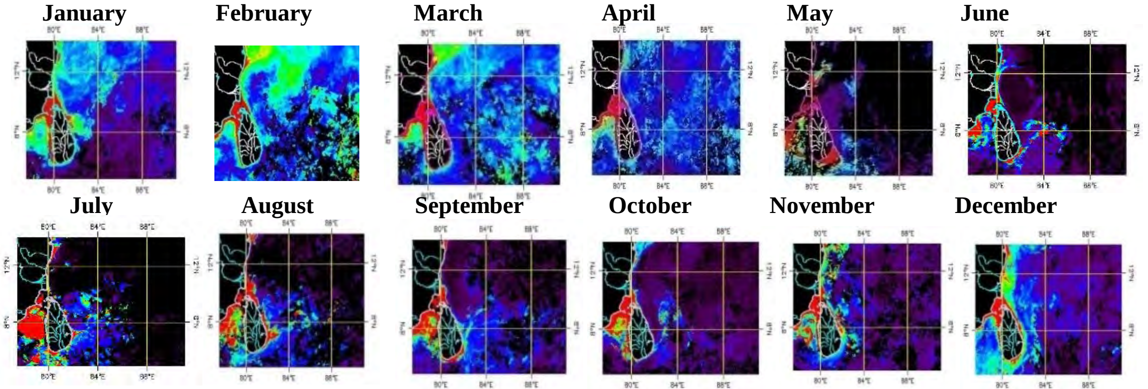

Subset 3 (2008)

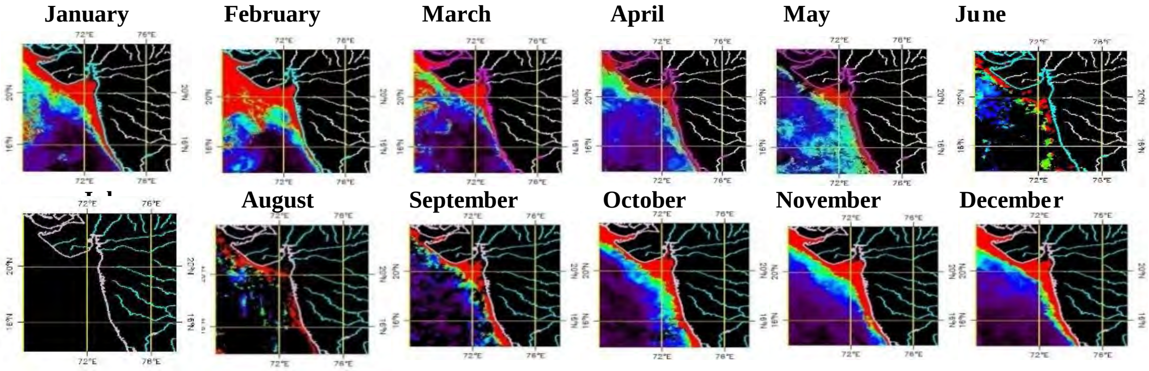

Subset 4 (2008)

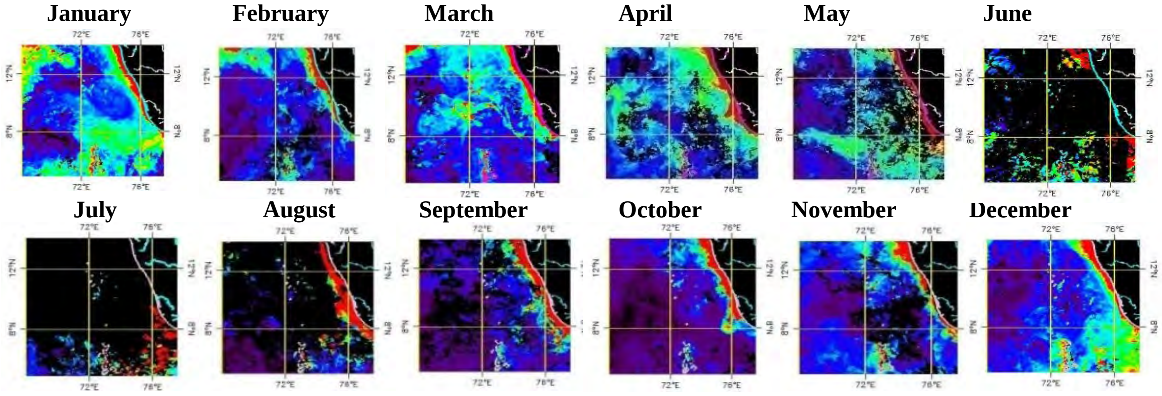

Figure 4. Chlorophyll image for four subset during January-December , 2008

The low nutrients content in BoB waters are prime cause of low chlorophyll concentration. In addition, vertical mixing and upwelling of the nutrients are not strong enough to support high primary production in BoB compared to AS. Various similar studies are supported observed that nutrients supplied by super cyclone enhanced Chl-*a* concentrations (5–10 times) also noted enhanced nutrient concentrations and the consequent increase in primary production in Indian Ocean by super cyclone. Satellite Chl-*a* imageries revealed the occurrence of phytoplankton bloom in southwestern Bay during monsoon due to upwelling caused by cyclones. Maneesha et al. (2011) examined the influence of extreme atmospheric events, such as heavy rainfall and cyclone Sidr, on phytoplankton biomass in western Bay of Bengal using both *in situ* time-series observations and satellite derived Chlorophyll *a* and sea surface temperature (SST). From this study findings, similar increase in Chl *a* by 3 to 10 times was observed in central Bay of Bengal after the cyclone Sidr which also enhanced 40% of fishery production during October–December 2007 compared to same period in 2006.

The present study, two years (2007&2008) assessment of CC and correlation between CC are documented, from these results proved; higher chlorophyll concentration in Northern Arabian Sea during July month for both years 2007 & 2008. Tang et al. (2002) have also found similar chlorophyll concentrations in northern Arabian Sea using OCTS images. In Bay of Bengal, though higher chlorophyll concentrations are found during the months of August for 2007 & July for 2008 due to more numbers of cyclonic events and rivers fluxes of Krishna and Godavari delta in NBoB is basis for high chlorophyll biomass compared with SBoB and SAS. In contrast, compared with SAS, NAS is characterized by cooling and densification phenomenon and cyclonic disturbances. This leads to high salinity of the Arabian Sea water, which initiates convective mixing and injection of nutrients into sea surface from thermocline regions. The nutrient injection is responsible for higher chlorophyll concentrations in NAS. The NBoB & SBoB, though experiences the onset and retreat of monsoon compared to Arabian Sea, the low nutrient concentration of water, and the lack of upwelling of nutrients due to its typical ocean dynamics, caused low chlorophyll biomass compared to those in the AS and supplementary basis for variations of chlorophyll concentration occurred due to river fluxes. The higher CC values in NAS due to cyclones passages and also mixing of major rivers fluxes of Narmada, Tapi, Mahi, sabarmathi and Indus on the west coast, On the east coast of India, large-scale river fluxes (Krishna, Godavari, Brahmaputra, Ganges, Mahanadi and Kaveri rivers) extending deep in to the open ocean has been detected, although, BoB region has less numbers of rivers fluxes compared to AS, its reasons for high phytoplankton biomass in AS (Sarangi, 2016; Shanthi et al., 2015.

However, in evaluation with previous reported studies the chlorophyll concentration ranges from 0.4 - 1.0 mg m^{-3} was observed in Arabian Sea using satellite data reported by Chauhan et al., 2001; 2002; Dey & Singh, 2003; Sarangi et al., 2001; 2005; Singh & Chaturvedi, 2010 and recently Madhumita et al. (2012) reported increased chlorophyll was observed by super cyclones roughly from 0.25 - 0.4 mg m^{-3} in Arabian Sea in May 2007. Chaturvedi et al. (2013) studied the SeaWiFS derived eight-day average chlorophyll images for 10 years (1997 – 2008) reported chlorophyll concentration was increased (0.3 - 0.8 mg m^{-3}) every year in northwest Arabian Sea compared to previous report (0.05 - 0.3 mg m^{-3}) in 1980's from OCTS images. The present study was recorded the maximum chlorophyll biomass values (1.89 mg m^{-3}) in NAS for the year, 2008 compared with 2007 (0.97 mg m^{-}3) because more number of cyclonic events were documented during April – December, 2008 in North Indian Ocean however end of cyclones passages leads to enhanced more nutrients level in that region is answerable for highest chlorophyll concentration was obtained for the year 2008 compared with 2007 and previous studies also.

5. Conclusion

The present study summarizes that chlorophyll concentration observed higher in northern Arabian Sea compared to southern Arabian Sea, northern and southern Bay of Bengal. Higher chlorophyll values in the northern Arabian Sea are associated with cyclones passages and winter cooling phenomenon. During this period, atmospheric forcing that leads to observed changes in upper layer of the ocean (reduction in sea surface temperature) this leads to formation of Arabian Sea has high salinity waters, which further leads to sinking and convective mixing of nutrients to upper layers of water column triggers the higher primary production and river fluxes also played a major role for high chlorophyll biomass in that region and moreover southern Arabian Sea has minimum chlorophyll biomass observed, but northern and southern Bay of Bengal has reflected moderate chlorophyll biomass. In addition, northern Bay of Bengal being evaluated with southern Bay of Bengal, shows high chlorophyll biomass due to more number of cyclonic events and river fluxes from Krishna and Godavari and its leads to vertical mixing of nutrients in that region caused maximum biomass than southern Bay of Bengal. There is no mixing of river fluxes found from southern Bay of Bengal, hence low chlorophyll biomass was obtained. To conclude, the present study will useful for studying the changes of primary production and new production in Arabian Sea and Bay of Bengal regions and moreover, to find out oceanic and coastal processes, cyclonic effects, phytoplankton diversity and their growth and distribution prior and end of cyclones passages in Indian Ocean for future evaluation.

Acknowledgements

The authors are thankful to Head, MED; Group Director, BPSG; Deputy Director, EPSA and Director, Space

Applications Centre (ISRO) for providing necessary guidance and facilities for carrying out the work.

References

Chaturvedi N, M. Shah, Ajai and Y. Jasrai (2013). Is there impact of climate change on biological productivity in the Indian Ocean. Indian Journal of Marine Sciences, 42(1), 50-57.

Chauhan P, M. Mohan, RK Sarangi, B. Kumari, S. Nayak and SGP Natondkar (2002). Surface chlorophyll estimation in the Arabian Sea using IRS-P4 OCM Ocean Color Monitor (OCM) satellite data. International Journal of Remote Sensing, 23(8), 1663-1676.

Chauhan P, CRC Nagur, M. Mohan, S. Nayak and RR Navalgund (2001). Surface chlorophyll-α distribution in Arabian Sea and Bay of Bengal using IRS-P4 Ocean Colour Monitor satellite data. Current Science, 80(2), 127-129.

Dey S and RP Singh (2003). Comparison of chlorophyll distributions in the northeastern Arabian Sea and southern Bay of Bengal using IRS-P4 Ocean Color Monitor data. Remote Sensing of Environment, 85, 424–428.

Madhumita T, M. Raman, D. Rashmin and Ajay (2012). Frequency of Cyclonic Disturbances and Changing Productivity Patterns in the North Indian Ocean Region: A Study Using Sea Surface Temperature and Ocean Colour Data. International Journal of Geosciences, 3, 490-506.

Madhupratap M, S. Prasanna Kumar, PMA Bhattathiri, MK Dileep, S raghukumar, KKC Nair and N Ramaiah (1996). Mechanism of the biological response to winter cooling in the Northeastern Arabian Sea. Nature, 384, 549-552.

Maneesha K, VVSS Sarma, NPC Reddy Y Sadhuram, TVR Murty, VV Sarma and MK Dileep (2011). Meso-scale atmospheric events promote phytoplankton blooms in the coastal Bay of Bengal. Journal of Earth System Science, 120(4), 773–782.

Nakamoto S, SK Prasanna, JM Oberhuber, K Muneyama and R Froulin (2000). Chlorophyll modulation of sea surface temperature in the Arabian Sea in a mixed-layer isopycnal general circulation model. Geophysical Research Letters, 27(6), 747-750.

Patissier DP, JFR Gower, AG Dekker, RP Stuart and VE Brando (2014). A review of ocean color remote sensing methods and statistical techniques for the detection, mapping and analysis of phytoplankton blooms in coastal and open oceans. Journal of Progress in Oceanography, 123–144.

Sarangi RK, P Chauhan and SR Nayak (2001). Phytoplankton bloom monitoring in the offshore water of Northern Arabian Sea using IRS-P4 OCM Satellite data. Indian Journal of Marine Sciences, 30, 214 - 221.

Sarangi RK, P Chauhan, SR Nayak (2005). Inter-annual variability of phytoplankton blooms in the northern Arabian Sea during winter monsoon period (February-March) using IRS-P4 OCM data. Indian Journal of Marine Sciences, 34(2), 163 - 173.

Sarangi, R. K. (2016). Remote sensing observations of ocean surface chlorophyll and temperature with the impact of cyclones and depressions over the Bay of Bengal water. Marine Geodesy, 39(1), 53-76.

Sathyendranath S, AD Gouveia, SR Shetye, P Ravindran and P. Trevor (1991). Biological controls of surface temperature in the Arabian Sea. Nature, 349, 54–56.

Shanthi, R., D. Poornima, K. Raja, RK Sarangi, A. Saravanakumar and T. Thangaradjou (2015). Inter-annual and seasonal variations in hydrological parameters and its implications on chlorophyll a distribution along the southwest coast of Bay of Bengal. Acta Oceanologica Sinica, 34(6), 94-100.

Singh RP and P. Chaturvedi (2010). Comparison of chlorophyll concentration in the Bay of Bengal and the Arabian Sea using IRS-P4 OCM and MODIS Aqua. Indian Journal of Marine Science, 39(3), 334–340.

Tang DL, H. Kawamura and AJ Luis. (2002). Short-term variability of Phytoplankton blooms associated with a cold eddy in the northeastern Arabian Sea. Remote Sensing of Environment, 81, 82–89.

Tang DL and H. Kawamura (2001). Long-term time series satellite ocean color products on the Asian waters. Proceedings of the 11th PAMS/JECSS workshop (pp. 49–52). Seoul, South Korea: Hanrimwon Publishing (CD-ROM: O112-P03).

Tang DL, IH Ni, DR Kester and FE Muller-Karger (1999). Remote sensing observation of winter Phytoplankton blooms southwest of the Luzon Strait in the South China Sea. Marine Ecology Progress Series, 191, 43-51.

Tang DL, IH Ni, FE Muller-Karger and ZJ Liu (1998). Analysis of annual and spatial patterns of CZCS - derived pigment concentrations on the continental shelf of China. Continental Shelf Research, 18, 1493 - 1515.

Yoder JA, CR McClain, GF Feldman and WE Esalas (1993). Annual cycles of phytoplankton chlorophyll concentrations in the global ocean: a satellite view. Global Biogeochemical Cycles, 7, 181 - 193.

Yoder JA (2000). An overview of temporal and spatial patterns in satellite-derived chlorophyll imagery and their relation to ocean processes. In D. Halpern (Ed.), Satellites, Oceanography and Society (pp. 225– 238). Elsevier Science BV, Netherlands.

Journal of Geomatics Vol. 17, No. 1, April 2023

Temporal status and change detection of stone quarrying and crushing activities using multi-temporal google earth images

R. S. Chaurasia* and S. N. Mohapatra
School of Studies in Earth Science, Jiwaji University, Gwalior, India
*Email: sharan25.jhs@gmail.com

(Received: 21 July 2022, Accepted in final form: 19 April 2023)

DOI: *https://doi.org/10.58825/jog.2023.18.1.71*

Abstract: Stone quarrying and crushing (SQC) activities under mining operations normally produce a destructive landscaping impression during the period from start to end. Spatio-temporal data, downloaded from Google Earth Pro s/w, coupled with remote sensing, GIS, and GPS has been used to evaluate time series (2003, 2008, 2015 and 2021) analysis of stone quarrying and crushing activities in a part of Jhansi Tehsil. Results show that the variability and pressure on land resources due to stone quarry and crushing activities were found in linear increments during the time. There was annual heavy exploitation record during 2003-2008 (30.83%) of stone from quarry sites and total increments of SQC activities were found to be 277.64% in the last 18 years. This study exhibited the prospective advantage of annual monitoring over the period and support to make the possible preparations/ management for destructive mining operations.

Keywords: Change detection, geographical information system (GIS), google earth images, mining activities, remote sensing, stone quarrying

1. Introduction

Stone quarrying is the removal process of valuable geological materials from the Earth. These materials are a form of mineral package that have economic interest to the mineworker. In a broader sense, mining refers to the extraction of any non-renewable resource such as rock, petroleum, natural gas etc. Stone mining has been a human activity since pre-historic time. The activities associated with mining frequently have a detrimental influence on the environment, both during and after the mining activity. Mining operations are related to the opening of large pits on the Earth's surface to extract land resources. The degree to which these processes are involved is largely determined by the value of the mineral resources and the quality and quantity of the output. These activities cause a notable impression on the surroundings (Valdiya 1987).

Stone quarrying and crushing activities lead to a massive change in biodiversity, this degrades the ecology and landscape. (Al-Joulani 2008; Bhadra et al. 2007; Odell et al. 2018; Zia-Khan et al. 2015). Stone dust is a by-product of stone crushing and shipping process which produces various respiratory issues as well as it directly threatens the health of mine workers and nearby people (Ahmad 2014; Chopra et al. 2012; Solanki et al. 2014; Yarahmadi et al. 2013). Soil quality and agricultural productivity are directely affect by deposition of stone dust in the surrounding region (Prajapati 2012; Zia-Khan et al. 2015). The improper handling of the massive daily amounts of stone and slurry waste produced by quarrying activities is another significant issue (Forestner 1999).
The ability to differentiate between natural changes and those imposed by human activities is essential for an effective monitoring strategy for assessing surface mining operations and their dynamics on a regional scale. Accurate and current information is required to overcome these problems. Since 1970, spatial changes in mining areas have been mapped by using analogue aerial images (Anderson et al. 1977).

This data may now be obtained by remote sensing, It has the potential to create calibrated observations with an appropriate geographic resolution with decadal time scale. The dynamics of quarries have been the subject of several local and regional studies utilising a range of remotely sensed datasets with different spatial and temporal resolutions (Bonifazi et al. 2003; Karuppasamy et al. 2016; Koruyan et al. 2012; Latifovic et al. 2005; C. C. Liu et al. 2005; Nikolakopoulos et al. 2010; Nikolakopoulos and Raptis 2014; Saroglu et al. 2005; Uça et al. 2011).

Remote sensing is an aerospace technology that uses electromagnetic energy to capture data from the Earth's surface and its surrounding atmosphere by remote sensing systems. The ERDAS Imagine, ArcGIS s/w can be used to develop the land use/ land cover changes using multi-temporal google earth images. A group of modest tools/ software such as Google Maps, Bing Maps, and Google Earth Pro can be used successfully for geo-environmental studies because of synoptic coverage and high spatial resolution satellite images. Google Earth may be utilised in a variety of fields, including transportation, urban planning, time series analysis, real-time research analysis using the Global Positioning System (GPS), environmental and climatic studies, and more, due to its simple operations and online accessibility (Singhal and Goel 2019).

The application of remote sensing and GIS in the field of comprehensive environmental issues which could be distinguishable in aerial photographs and satellite imagery (Kumar et al. 2013). Remote Sensing and GIS has developed as a major contrivance for collecting information about all features present on the Earth's surface. In recent years, very high resolution (both spatial and spectral) satellite data are available and the application has increased with respect to numerous purposes. Remote sensing and GIS have been subsidised meaningfully towards progressive activities for decades in India (Kumar et al. 2013).

The change in land cover as a result of anthropogenic activities has played a major role in global environmental change and has become a hot spot for researchers (Liu et al. 2002). Changes in land use pattern by means of remotely sensed global data is based on the evaluation of temporal data. The change in land resources over time can be determined and evaluated using digital techniques (SAC-ISRO 1990). Remote sensing techniques have been successfully applied to monitor the land use changes due to opencast strip mining, evolution of dumping of mine wastes, deforestation and erosion due to mining activities (Gupta 2005).

Remote sensing and GIS play a pivotal role in monitoring the temporal changes on the Earth's surface due to stone quarrying and crushing activities. The objective of the study is mainly focused on evaluating the temporal status of stone quarrying and crushing activities and change assessment from 2003 to 2021. This may be useful to assess the impact on land resources and control hazardous effects on the health of local workers/ villagers with proper planning.

2. Materials and Methods

This study is precisely devoted to assessing the temporal changes in stone quarrying and crushing activities using geospatial tools. The quantitative/ numerical method for identifying the temporal changes was used. To evaluate the change, stone quarrying and crushing activities were identified and stored using multi-temporal google earth images. The resulting classified area under stone quarrying and crushing activities were obtained and compared accordingly. The adopted procedure are as follows:

2.1. Software used for the study

Google Earth Pro, ERDAS Imagine and ArcGIS s/w were used to identify stone quarrying and crushing activities, data processing, thematic mapping and creation of geodatabase for temporal change assessment.

2.2. Study Area

There are 5 Tehsil under the Jhansi District of Uttar Pradesh, India *viz.*, Jhansi, Mauranipur, Moth, Garautha and Tehrauli. The north eastern part of tehsil Jhansi is primarily underlain by high rank igneous rocks of Bundelkhand cratons generally trending, these rocks consist of gneiss and granites etc. hence are quite suitable for quarry business. In this study, the cluster group of mining sites were identified for the assessment of temporal changes, that occur due to stone quarrying and crushing activities in the north eastern part of Jhansi Tehsil were determined. The study area is lies between 25° 26' 27.2616" to 25° 28' 17.5080" N and 78° 39' 5.1840" to 78° 41' 49.3008" E.

2.3. Data collection

Various data were used to assess the temporal status/ changes and the creation of thematic layers. The data included ground control points (stored from GPS), required photographs (captured from Sony camera) and high quality google earth images for the validation of the work. Total four temporal Google Earth images (Imagery Date: 31/12/2003, 29/05/2008, 14/03/2015 and 15/01/2021) with high spatial resolution have been downloaded from Google Earth Pro s/w for accurate temporal assessment.

2.4. Raster processing: Google Earth Images

Raster processing is the process that treats directly to the pixels of the image. With the help of geoprocessing tools, every pixel present on the raster image was globally positioned. The transformed coordinates are stored in georeferenced file formats like GeoTIFF and *.img. Georeferencing of temporal google earth images has been done using ERDAS imagine with the help of collected ground control points, and projected to the Geographic - WGS 1984 and re-projected into UTM44N (Universal Transverse Mercator) WGS 1984 (USGS 2018). The area of interest with reference to the study area were masked/ cliped by using the masking tool in Arc GIS.

2.5. Record the precise locations and current status of stone quarrying and crushing sites

Current field photographs and precise locations of stone quarrying and crushing sites have been recorded with the help of Sony Digital Camera and Garmin GPS for the validation of the study.

2.6.Multi-date google earth images of the study area

After the completion of the raster processing of raw data using ERDAS Imagine, the final clipped temporal google earth images for 2003, 2008, 2015 and 2021 were stored for the study (Figure 1).

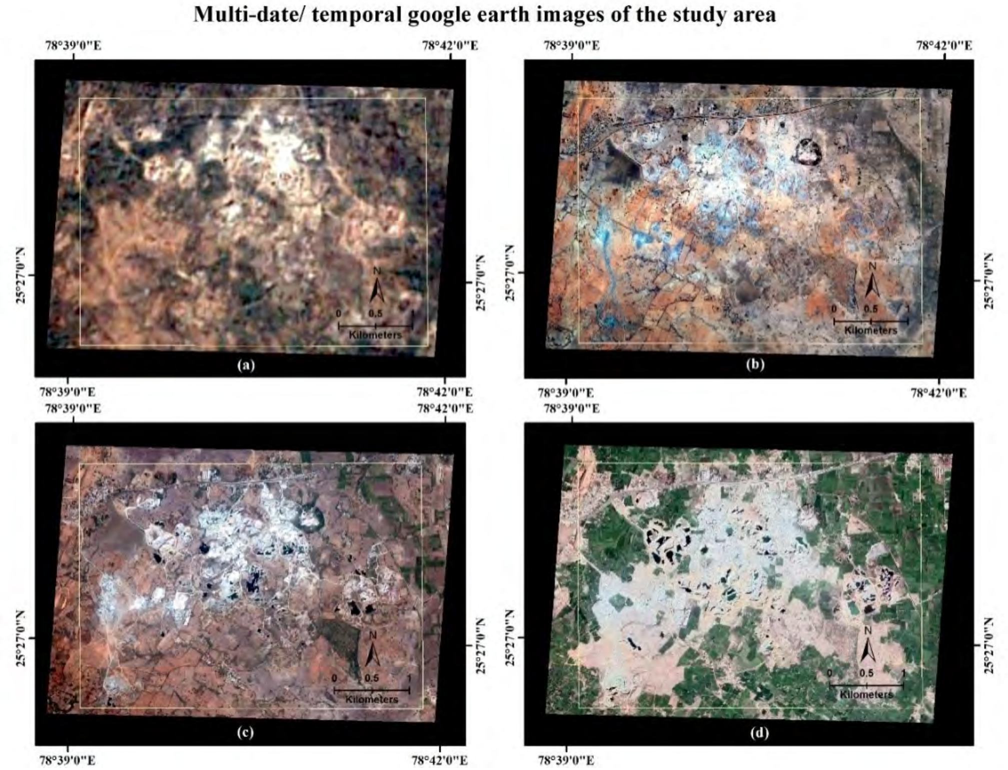

Figure 1. Multi-date google earth images of the study area: (a) acquisition date: 31/12/2003; (b) acquisition date: 29/05/2008; (c) acquisition date: 14/03/2015; (d) acquisition date: 15/01/2021

2.7. Identification of the stone quarrying and crushing activities

For the drive of identification of the stone quarrying and crushing activities, georeferenced multi-temporal google earth images were used using ArcMap. A temporal study based on the stone quarrying and crushing activities for 2003, 2008, 2015 and 2021 was done by using the manual digitization method.

2.8. Change Assessment

Temporal google earth images have been of substantial advantage in monitoring the temporal changing pattern over the year. Change detection analyses were estimated through equation 1, 2, 3 and 4 (Kashaigili and Majaliwa 2010; Kleemann et al. 2017). The magnitude of change is a degree of expansion or reduction in the LULC size. A negative value will present a decrease in LULC size while a positive value will indicate an increase in the size of LULC class (Mahmud and Achide 2012).

$$Area\ change = Area_{i\ year\ x+1} - Area_{i\ year\ x} \tag{1}$$

$$Area\ change\ (\%) = \frac{Area_{i\ year\ x+1} - Area_{i\ year\ x}}{\sum_{i=1}^{n} Area_{i\ year\ x}} X\ 100 \tag{2}$$

$$Annual\ rate\ of\ change = \frac{Area_{i\ year\ x+1} - Area_{i\ year\ x}}{t_{years}} \tag{3}$$

$$Annual\ rate\ of\ change\ (\%) = \frac{Area_{i\ year\ x+1} - Area_{i\ year\ x}}{\sum_{i=1}^{n} Area_{i\ year\ x}\ X\ t_{years}} X\ 100 \tag{4}$$

Where: $Area_{iyearx+1}$ = Area of land use/ land cover for the following year

$Area_{iyearx}$= Area of land use/ land cover of the current year

$\sum_{i=1}^{n} Area_{i\ year\ x}$= The total area of land use/ land cover of the current year

t_{years}= the years' difference between the first and second period

3. Results and Discussion

The total geographical area of the study area was calculated as 1532.18 ha. Assessment of temporal changes was calculated between six time series *i.e.*, 2003-08, 2003-15, 2003-21, 2008-15, 2008-21 and 2015-21. During ground trothing, the current status was categorised as active, abandoned and partially abandoned which was formed due to rigorous/ unplanned mining under the selected cluster group (Figure 2).

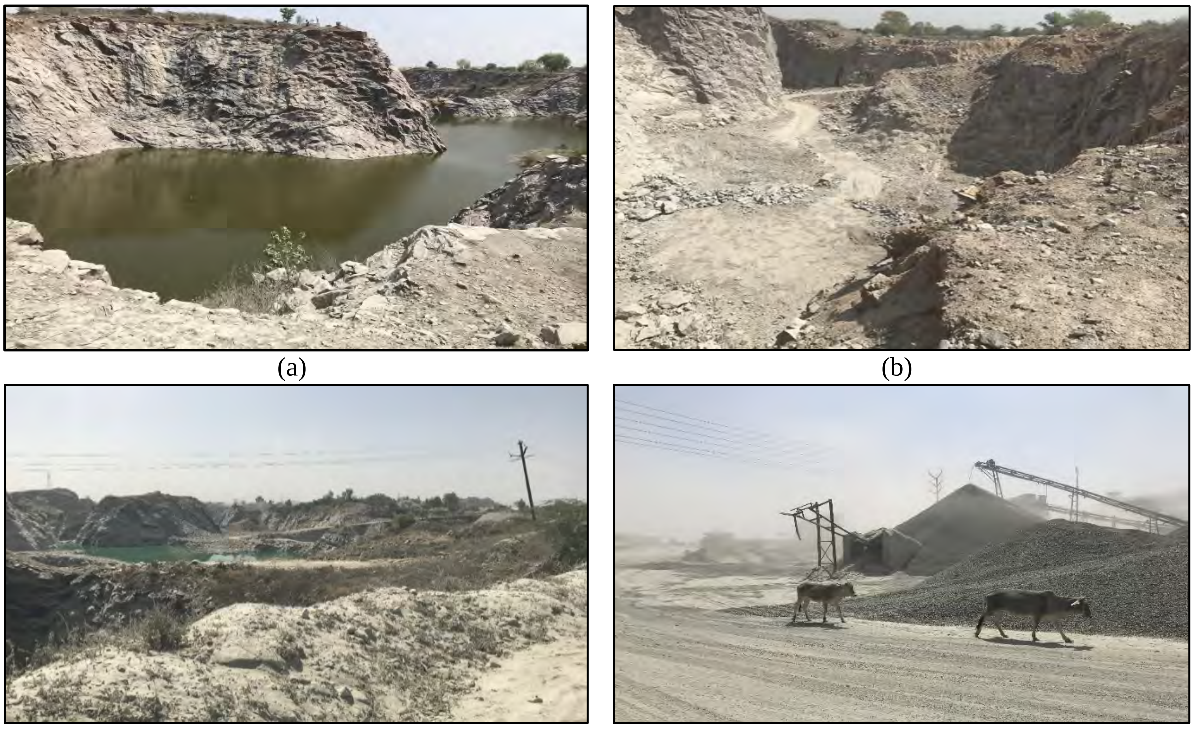

(a) (b)

(c) (d)

Figure 2. Current status: (a) abandoned (25.463743°, 78.660621°); (b) active (25.455811°, 78.692110°); (c) partially abandoned (25.466625°, 78.671545°); (d) active crushing unit (25.455303°, 78.656038°).

3.1. Temporal status of stone quarry and crushing activities (SQCA)

Area (%) was calculated out of total geographical area (1532.18 ha) of the study area

Out of the total geographical area (1532.18 ha), stone quarry and crushing activities account 8.23% (126.14 ha) in 2003, 20.92% (320.58 ha) in 2008, 24.75% (379.25 ha) in 2015 and 31.09% (476.35 ha) in 2021 (Table 1). Figure 3 shows that there are linear increments occurring from 2003 to 2021, but the area of SQC activities was found to be maximum during 2003-2008 and found minimum between 2008-2015. The spatial distribution and temporal status of SQC activities are shown in Figure 4.

Table 1. Temporal status of stone quarry and crushing activities

	2003		2008		2015		2021	
	Hectare	%	Hectare	%	Hectare	%	Hectare	%
Area of SQCA	126.14	8.23%	320.58	20.92%	379.25	24.75%	476.35	31.09%

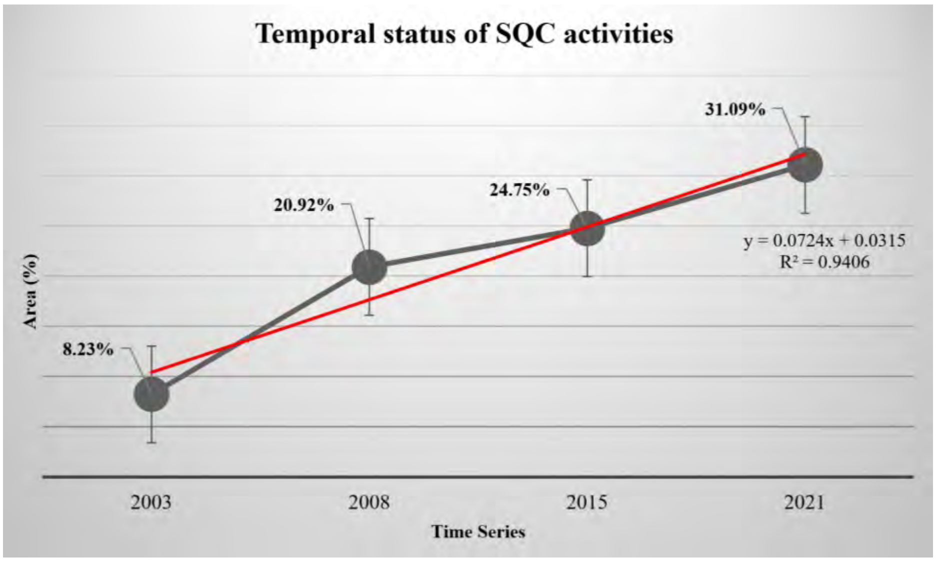

Figure 3. Temporal status of SQC activities; Red line shows a linear trend line.

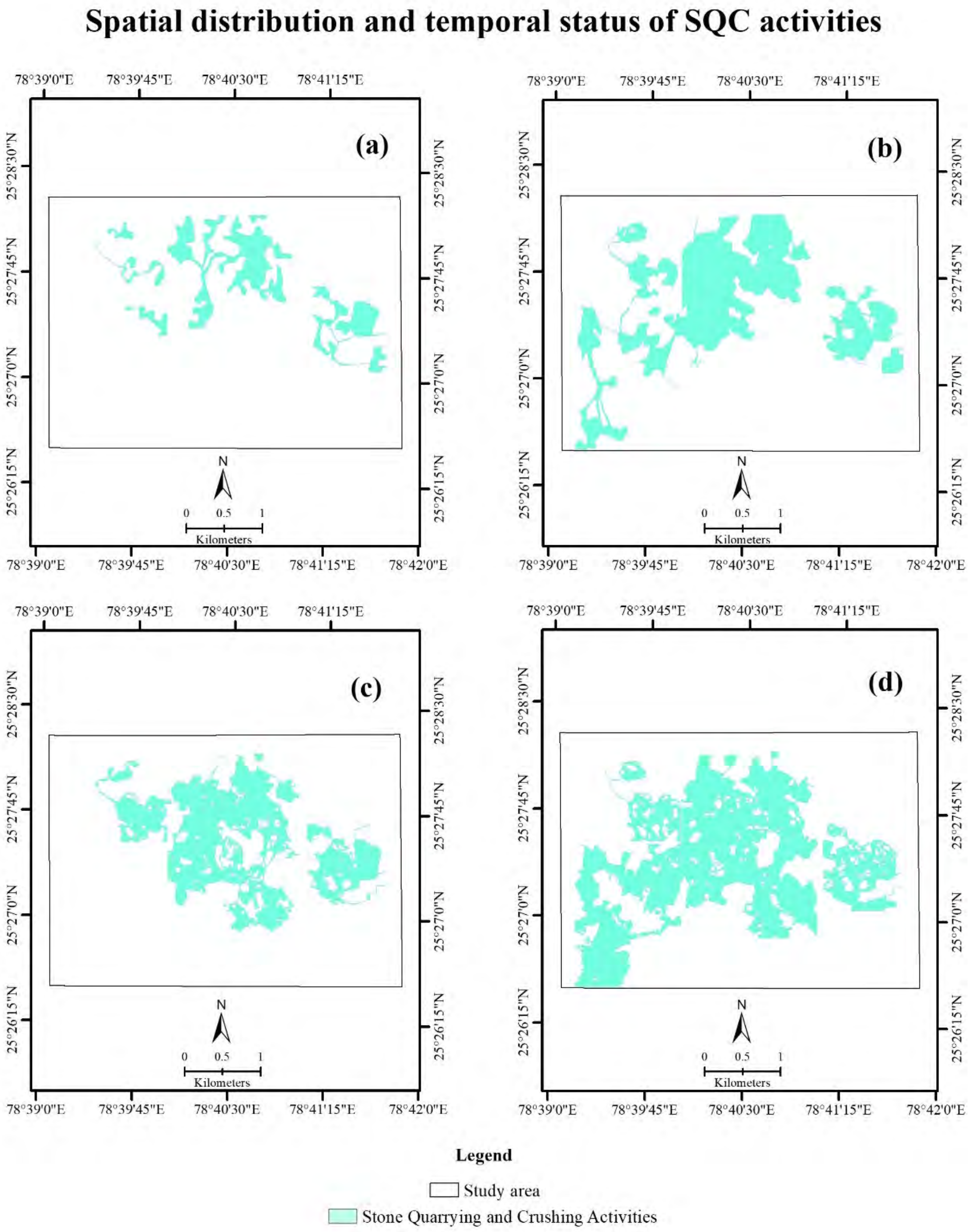

Figure 4. Spatial distribution and temporal status of SQC activities: (a) 2003; (b) 2008; (c) 2015; (d) 2021.

3.2. Temporal change assessment of stone quarry and crushing activities (SQCA)

The area change in six time series, 2003-08 (194.44 ha); 2003-15 (253.11 ha); 2003-21 (350.21 ha); 2008-15 (58.67 ha); 2008-21 (155.77 ha) and 2015-21 (97.1 ha), shows increased in every time interval due to ongoing mining activities (Table 2). The temporal change in percent was found 154.15%, 200.66%, 277.64%, 18.3%, 48.59% and 25.6% in 2003-08, 2003-15, 2003-21, 2008-15, 2008-21 and 2015-21 respectively (Figure 5). The annual rate of changes was calculated as 38.89 ha (30.83%), 21.09 ha (16.72%), 19.46 ha (15.42%), 8.38 ha (2.61%), 11.98 ha (3.74%) and 16.18 ha (4.27%) in 2003-08, 2003-15, 2003-21, 2008-15, 2008-21 and 2015-21 respectively. The annual rate of change in percent was found to be highest (38.83%) during 2003-2008 and found low (2.61%) between 2008-2015 (Figure 6). The total increments of SQC activities were found to be 277.64% in the last 18 years.

Table 2. Temporal change assessment of SQC activities

Change assessment	2003-08	2003-15	2003-21	2008-15	2008-21	2015-21
Area Change (ha)	194.44	253.11	350.21	58.67	155.77	97.1
Area Change (%)	154.15%	200.66%	277.64%	18.30%	48.59%	25.60%
Annual Rate of Change (ha)	38.89	21.09	19.46	8.38	11.98	16.18
Annual Rate of Change (%)	30.83%	16.72%	15.42%	2.61%	3.74%	4.27%

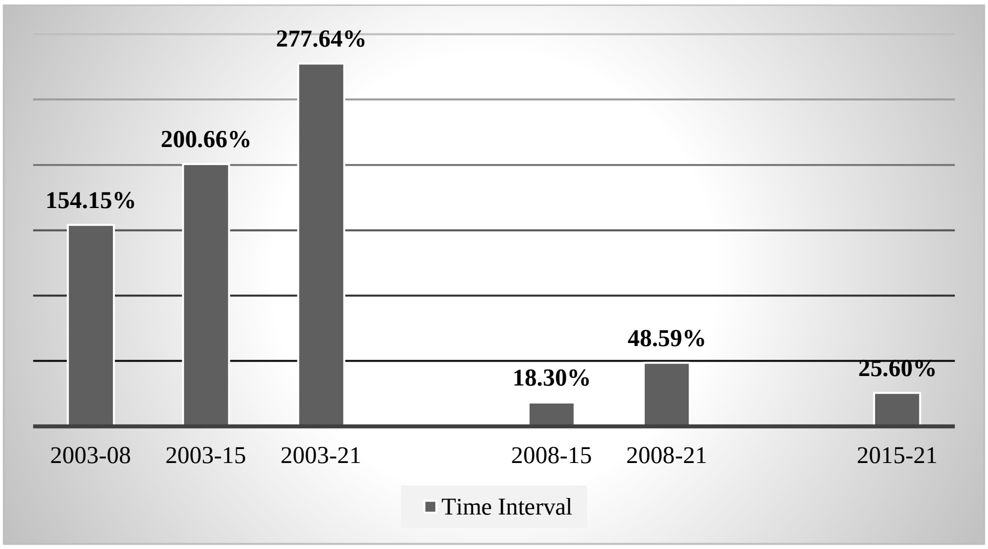

Figure 5. Temporal change in area (%) of SQC activities

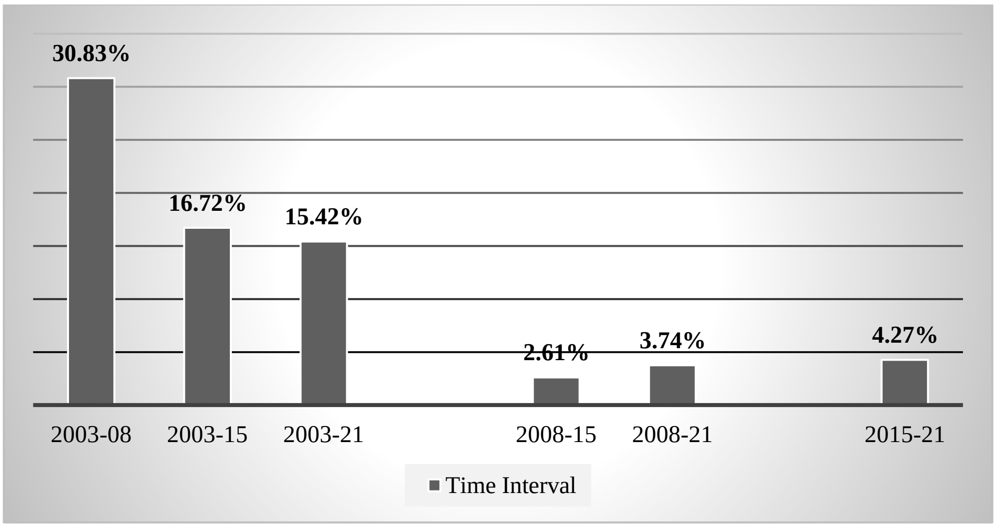

Figure 6. Annual rate of change in area (%) of SQC activities

The results show that the analysis of temporal status in and around the SQC sites after 18 years contributes to dynamic changes caused by crushing activities. In the current study, there are linear increments occur from 2003 to 2021 but in some belongings and dynamic changes occurred in the area of SQC activities was fall down due to mining pits, caused by small and large scale quarrying activities, this is because mining is predominantly undertaken in waterlogged areas (Obodai et al. 2019; Pei et al. 2017; Xiao et al. 2017). This increments has remunerated by the loss or decrease of different land use features. In 18 years time span, the overall annual rate of change in SQC activities caused the loss of important land resources. In conformity with the findings, destructive mining activities have been increased. Stone quarrying and crushing activity include the removal of earth surface features to dig out stones for building materials purpose. Therefore, the dynamic changes of the SQCA provide an excellent explanation of mining operations. In fact, the topographic changes produced by mining operations are also a result of the development of the local economy. Thus, annual monitoring of the mining area can provide information about the strategies of the economy and geo-environmental fortification (Zhao et al. 2018). Careful planning with suitable mitigation measures can be converted the local landscape of mining sites into a vegetation cover, water and wildlife century etc.

4. Conclusions

Space-born built methodology for calculating the changes in SQCA is presented and beneficial for the assessment in an area.With the help of Google Earth images, the change was found to be about 277.64% for the last 18 years (2003-2021). SQCA activities would be dangerous without proper planning/ management. The variability and pressure on land resources due to stone quarry and crushing activities has been recorded and found in linear increments during the period of time. The study showed that there was heavy exploitation of stone from quarry sites during 2003-2008. The derelict ponds form appearance as a result of rigorous quarrying and are resulting in environmental degradation which are dangerous to both human and surroundings.The prospective advantage of annual monitoring over the period and support to make the possible preparations/ management for destructive mining operations.

References

Ahmad A. (2014). A study of miners, Demographics and health status in Jodhpur district of Rajasthan,India. *International Journal of Development Studies and Research*, *3*(1), 113–121.

Al-Joulani N. (2008). Soil contamination in Hebron district due to stone gutting industry. *Jordan Journal of Applied Sciences - Natural Sciences*, *10*(1).

Anderson AT, D Schultz, N Buchman and HM Nock (1977). LANDSAT IMAGERY FOR SURFACE-MINE INVENTORY. *Photogrammetric Engineering and Remote Sensing*, *43*(8).

Bhadra BK, AK Gupta, JR Sharma and BR Choudhary (2007). Mining activity and its impact on the environment: Study from Makrana marble and Jodhpur sandstone mining areas of Rajasthan. *Journal of the Geological Society of India*, *70*(4).

Bonifazi G, L Cutaia, P Massacci and I Roselli (2003). Monitoring of abandoned quarries by remote sensing and in situ surveying. In *Ecological Modelling* (Vol. 170). https://doi.org/10.1016/S0304-3800(03)00228-X

Chopra K, P Prakash, S Bhansali, A Mathur and PK Gupta (2012). Incidence and prevalence of silicotuberculosis in western Rajasthan: A retrospective study of three years. *National Journal of Community Medicine*, *3*(1), 161–163.

Forestner U (1999). Introduction to environmental impacts of mining activities. In J. M. Azcue (Ed.), *Environmental impacts of mining activities* (pp. 1–3). Springer.

Gupta RP (2005). *Remote Sensing Geology* (Second Edi.). Springer Publications.

Karuppasamy S, S Kaliappan, R Karthiga and C Divya (2016). Surface Area Estimation, Volume Change Detection in Lime Stone Quarry, Tirunelveli District Using Cartosat-1 Generated Digital Elevation Model (DEM). *Circuits and Systems*, *07*(06). https://doi.org/10.4236/cs.2016.76073

Kashaigili JJ and AM Majaliwa (2010). Integrated assessment of land use and cover changes in the Malagarasi river catchment in Tanzania. *Physics and Chemistry of the Earth*, *35*(13–14), 730–741. https://doi.org/10.1016/j.pce.2010.07.030

Kleemann J, G Baysal, HNN Bulley and C Fürst (2017). Assessing driving forces of land use and land cover change by a mixed-method approach in north-eastern Ghana, West Africa. *Journal of Environmental Management*, *196*, 411–442. https://doi.org/10.1016/j.jenvman.2017.01.053

Koruyan K, AH Deliormanli, Z Karaca, M Momayez, H Lu and E Yalçin (2012). Remote sensing in management of mining land and proximate habitat. *Journal of the Southern African Institute of Mining and Metallurgy*, *112*(7), 667–672.

Kumar S S, S Arivazhagan and N Rengarajan (2013). Remote Sensing and GIS Applications in Environmental Sciences - A Review. *Journal of Environmental Nanotechnology*, *2*(2), 92–101. https://doi.org/10.13074/jent.2013.06.132025

Latifovic R, K Fytas, J Chen and J Paraszczak (2005). Assessing land cover change resulting from large surface mining development. *International Journal of Applied Earth Observation and Geoinformation*, *7*(1). https://doi.org/10.1016/j.jag.2004.11.003

Liu CC, CA Wu, ML Shieh, JG Liu, CW Lin and CL Shieh (2005). Monitoring the illegal quarry mining of gravel on the riverbed using daily revisit formosat-2 imagery. In *Proceedings of the IGARSS'05 IEEE International Geoscience and Remote Sensing Symposium, 29–29 July 2005* (pp. 1777–1780). Seoul, Korea.

Liu XH, AK Skidmore and VH Oosten (2002). Integration of Classification Methods for Improvement of Land-cover Map Accuracy. *Journal of Photogrammetry and Remote Sensing*, *56*, 257–268.

Mahmud A and AS Achide (2012). Analysis of Land Use/Land Cover Changes to Monitor Urban Sprawl in Keffi-Nigeria. *Environmental Research Journal*, *6*(2), 129–134.

Nikolakopoulos KG and I Raptis (2014). Open quarry monitoring using gap-filled LANDSAT 7 ETM SLC-OFF imagery. In *Earth Resources and Environmental Remote Sensing/GIS Applications V* (Vol. 9245). https://doi.org/10.1117/12.2066799

Nikolakopoulos KG, PI Tsombos and AD Vaiopoulos (2010). Monitoring a quarry using high resolution data and GIS techniques. In *Earth Resources and Environmental Remote Sensing/GIS Applications* (Vol. 7831). https://doi.org/10.1117/12.864527

Obodai J, KA Adjei, SN Odai and M Lumor (2019). Land use/land cover dynamics using landsat data in a gold mining basin, Ankobra, Ghana. *Remote Sensing Application* , *13*, 247–256.

Odell SD, A Bebbington and KE Frey (2018). Mining and climate change: A review and framework for analysis. *The*

Extractive Industries and Society, *5*(1), 201–214.

Pei W, S Yao, JF Knight, S Dong, K Pelletier, L P Rampi (2017). Mapping and detection of land use change in a coal mining area using object-based image analysis. *Environmental Earth Sciences*, *76*(3). https://doi.org/10.1007/s12665-017-6444-9

Prajapati SK (2012). Ecological effect of airborne particulate matter on plants. *Environmental Skeptics and Critics*, *1*(1), 12–22.

SAC-ISRO. (1990). *Impact of Mining Activities and Super thermal Power Stations on Environment*.

Saroglu E, F Bektas, AO Dogru, C Ormeci and N Musaoglu (2005). Environmental Impact Analyses of Quarries Located on the Asian Side of Istanbul Using Remotely Sensed Data. *XXII International Cartographic Conference (ICC), Corunna, Spania*, (July), 11–16.

Singhal A and S Goel (2019). Environmental Impacts of Sandstone Quarrying and Its Waste: A Case Study of Jodhpur, India Designing Integrated Waste Management System for Guawahati City View project Ganga Environment Management Plan View project Environmental Impacts of Sandstone Quarrying and Its Waste: A Case Study of Jodhpur, India. *Springer, Cham.* 159–183. https://www.researchgate.net/publication/344876280

Solanki J, S Gupta and S Chand (2014). Oral health of stone mine workers of Jodhpur City, Rajasthan, India. *Safety and health at work*, *5*(3), 136–139.

Uça AZD, M Karaman and E Özelkan (2011). Use of remote sensing in determining the environmental effects of open pit mining and monitoring the recultivation process. In *IMCET 2011 - Proceedings of the 22nd International Mining Congress of Turkey*. Turkey.

USGS. (2018). What does Georeferenced mean. https://www.usgs.gov/faqs/what-does-georeferenced-mean?qt-news_science_ products =0#qt-news_science_products. Accessed 19 October 2018

Valdiya KS (1987). *Environmental Geology, Indian Context*. New Delhi: Tata McGraw-Hill Publishing Company Ltd., New Delhi.

Xiao W, Z Wang, R Zhang and S Li (2017). The “golden ten years”: Underground coal mining and its impacts on land use and subsequent social problems: A case study on the Jining city region, China. *International Journal of Mining and Mineral Engineering*, *8*(1), 19–34. https://doi.org/10.1504/IJMME.2017.082681

Yarahmadi A, MM Zahmatkesh, M Ghaffari, S Mohammadi, Y Labbafinejad, SM Seyedmehdi (2013). Correlation between silica exposure and risk of tuberculosis in Lorestan Province of Iran. *Tanaffos*, *12*(2), 34–40.

Zhao H, Y Ma, F Chen, J Liu, L Jiang, W Yao and J Yang (2018). Monitoring quarry area with Landsat long time-series for socioeconomic study. *Remote Sensing*, *10*(4). https://doi.org/10.3390/rs10040517

Zia-Khan S, W Spreer, Y Pengnian, X Zhao, H Othmanli, X He and J Müller (2015). Effect of dust deposition on stomatal conductance and leaf temperature of cotton in Northwest China. *Water (Switzerland)*, *7*(1), 116–131. https://doi.org/10.3390/w7010116

Journal of Geomatics Vol. 17, No. 1, April 2023

Identification of suitable ecotourism sites in Himalayan mountainous setting using Analytical Hierarchy Process (AHP) and GIS: A case study of Chamoli district, Uttrakhand.

Rahul Das*, Mohit Singh, Vipul Malhotra, Soumyadeep Roy, Kamal Pandey, Harish Karnatak
Indian Institute of Remote Sensing, ISRO, Dehradun, India
*Email: rdas52571@gmail.com

(Received: 23 January 2023, Accepted in final form: 23 April 2023)

DOI: *https://doi.org/10.58825/jog.2023.17.1.35*

Abstract: With the ever-increasing need to manage and conserve the ecosystem, as well as the growing business potential for tourism, it's becoming increasingly important to address and align these two domains. Ecotourism enters the scene to provide a solution for anthropogenic interruptions at ecological tourist sites, with its potential to provide sustainable maintenance and development of both the environment and the local communities closely related to natural ecosystems. Tourism is one of the most valuable industries in India and the world, accounting for a considerable portion of most countries' economies. Chamoli is one of the tourist hotspot districts in India. Along with being an ecologically rich zone residing in the Himalayas, it possesses some of the highest peaks and national parks like Nanda Devi and Valley of flowers. The study area is also prone to various natural disasters like floods, earthquakes, landslides, and the recent one being the Rishiganga landslide of February 2021. The use of GIS tools in conjunction with AHP allows for a more streamlined and holistic approach to making scientifically calculated conclusions. We attempted to establish the prospective zones of ecotourism sites in our study region by considering a variety of factors that influence those sites of sustainable zones, such as slope, topographic roughness, elevation, road closeness, river proximity, and proximity to a protected area. The study area's data and information were geospatially analyzed to build an ecotourism potential map that can be used as a guide for planning sustainable resource management and development operations in the Chamoli district.

Keywords: - Ecotourism (ET), Analytical Hierarchy Process (AHP), Site-Suitability, Chamoli.

1. Introduction

With the emergence of sustainable development which was defined as development and careful utilisation of resources without making the future generation compromise for the resources, many other concepts of sustainability came into existence. Ecotourism is also a part of sustainable development which comes under sustainable tourism. According to the International Ecotourism Society, ecotourism is about uniting conservation, communities and sustainable travel (ecotourism.org). This means that practising ecotourism and promoting it should experience the richness and pureness of a scenic place along with trying to engage with the local community of the place in a positive manner, supporting them towards financial and cultural growth and also building conservational facilities towards the ecosystem. Ecotourism is a type of tourism that, along with giving the tourist the beautiful experience of travel, also generates growth for the local communities by giving them opportunities to grow financially by creating a link between the communities and the small industries and also holds the integrity and respect of the culture and most importantly providing conservational benefits to the environment (Scheyvens, 1999). Such type of tourism has become a need of the hour where the growing demand for both touristic activities as well as concerns related to environmental degradation are increasing hand in hand. Also, countries, especially India have seen great growth in the tourism industry. According to WTTC's Economic Impact and Trend 2021 report, India's Travel & Tourism GDP contribution grew by 4.9%, which was the third highest after China and Philippines. Thus, ecotourism is a linkage between solving economic problems for a community and also in aiding environmental issues (Goodwin, 1996). The consequences of unorganised tourism are felt equally by the environment and both the residents and the people sojourning at the tourist place, in the form of noise-air pollution, congesting traffic in peak hours, water scarcity, improper infrastructure (Sundriyal et al., 2018). This becomes even worse when touristic activities promote the disordered increment of built-up areas and road networks without bringing in the focus of environmental and geological factors, which in turn triggers the natural hazards like landslides (Cohen, 1978), (Khanduri,2017). In addition to that, issues of climate change uncontrolled construction activities in the seismic vulnerability zones are making it more prone to natural hazards, especially in the Himalayan region (Ramya et al. 2023), which has been inducted in the seismic zone IV and V (Rautela et al., 2015). Ecotourism, as discussed above which seeks to alleviate the pressure on the ecosystem as well as promote the livelihood of the local population still seems to be in its juvenile stage, where the limelight still focuses on tourism (Weaver & Lawton, 2007). In order to make ecotourism a successful concept and not merely a word in the literature, proper connecting link between local agricultural practices and tourism, promotion of tourist sites, community involvement as well as education can significantly enhance the future of ecotourism (Sharpley, 2006; Batta, 2006).

This report attempts to consider all the influencing parameters in order to setting up an ecotourism zone to analyse the suitability region within the Chamoli district of

Uttarakhand. The method adopted for this purpose is the Analytical Hierarchy Process given by (Saaty, 1980) which is one of the most sought out in the Multicriteria Decision Analysis technique (Fung & Wong, 2007) with the help of GIS. GIS based multi criteria analysis has been extensively used in different fields of the world, such as forestry, geohazard risk mapping, agriculture etc. The utilization of GIS and AHP technique is a valuable, cost-efficient, and time-saving tool to identify potential locations that are appropriate for the development of ecotourism (Ghorbanzadeh et al. 2019a), (Mahdavi et al. 2015). Various fields employ GIS-based MCDA as a decision-making support tool, using data structure, weighting, and integration techniques for a wide range of optimization applications (Debesa et al. 2020), (Sahani 2020), (Ghorbanzadeh, Pourmoradian, et al. 2019). Integrating GIS and MCDA is crucial for evaluating potential nature-based tourism sites (Ghorbanzadeh et al. 2019b). A combination of GIS and AHP techniques can effectively organize data for spatial planning and minimize negative environmental impacts while maximizing economic value in the selection of potential ecotourism sites(Al-Awadhi et al. 2019). The ability of GIS to store, display, manipulate, and retrieve spatial data has proved to be very beneficial in all types of mapping and other developmental works. One of the most important characteristics of the GIS is that it can support different formats of geospatial as sell attribute data that makes its application very broad in all divisions of life. The integration of remote sensing with GIS has greatly benefitted the users in analysing and maintaining the earth repository and also in Earth observations. In order to consider a site suitable for ecotourism, it has to be quantitatively and qualitatively assessed for by considering some important factors that require the utilization of earth observation geospatial data and also for the fact that not all the areas of the earth are easily accessible. These considerations make GIS and remote sensing an integral part of research and development in the present scenario and thus GIS has been taken as the base in order to come up with some meaningful result in this study in a stipulated time. The AHP is a multicriteria decision making algorithm which involves recognising criteria that has an influencing factor on the decision-making process (Saaty& Vargas, 2012). Many of the scientific analysis which has to deal with multiple criteria influencing the occurring phenomena or setting up a potential zone utilize the process, (Yuwono et al., 2020) based on 8 thematic maps generated 8 criteria for ecotourism potential size investigation. (Ullah& Hafiz, 2014) adopted 15 thematic layers based on 5 criteria landscape, wildlife, topography characteristics, cultural heritage and community characteristics.

2. Study Area

Chamoli district hosts variety of people each year due to its famous pilgrimage sites and for its tourist interests. This district is mountainous and is bounded by the Tibet region and the district of Pithoragarh, Bageshwar, Almora, Pauri Garhwal, Rudraprayag and Uttarkashi. It extends between 29°55’34’’ N- 31°4’29’’ N latitude and 79°4’47’’E - 80°6’17’’ longitude and covers 7837.330 km^2 area. The study area is shown in Figure 1. Looking into physiographical characteristics, this region is a part of the north-west Himalayas and the elevation ranges from 702 meters to 7739 meters from the mean sea level. Famous pilgrimage sites like Badrinath, Hemkund Sahib, Bansinarayan, Kalpeshwar, Rudranath, Urgam, Joshimath and tourist attractions like Auli, Valley of flowers are situated in this district and make it an important tourist place. Auli is one of the most famous skiing spots in the world is situated in this district. Presence of Nanda Devi Peak which is the third highest peak of India, makes this an important destination for mountaineers as well. Also, the Rudranath is a famous trekking site that attracts the attention of adventurers over the world. The tourist statistics of this district is shown in Table 1. This district falls under the Himalayan biodiversity hotspot zone and the existence of Nanda Devi National Park (a world heritage site declared by UNESCO helps to protect the natural resources of this area) is gifted with rich flora which also has medicinal prospects and covered with alpine meadows, which serves as habitat for some exclusive faunas (Bosak, 2008), which were prone to hunting and smuggling activities prior to the government's declaration of it as a National Park and subsequently a Biosphere Reserve (Singh & Singh, 2004). The increasing tourist activities and related environmental degradation can be a matter of concern. The study area has been subjected to several disastrous geohazards, the recent one was from the Rishiganga region (a debris flow avalanche) and left severe causalities of lives and infrastructures (Pandey et al., 2021;Shugar et al., 2021).

Table 1. Tourism State of Chamoli of the year 2020

No. of tourist places	No. of Accommodation	No. of Indian Tourists (excluding bio-reserve)	No. of Foreign Tourists (excluding bio-reserve)	No. of Indian Tourists (only bio-reserve)	No. of Foreign Tourists (only bio-reserve)
20	497	2745413	2927	16904	520

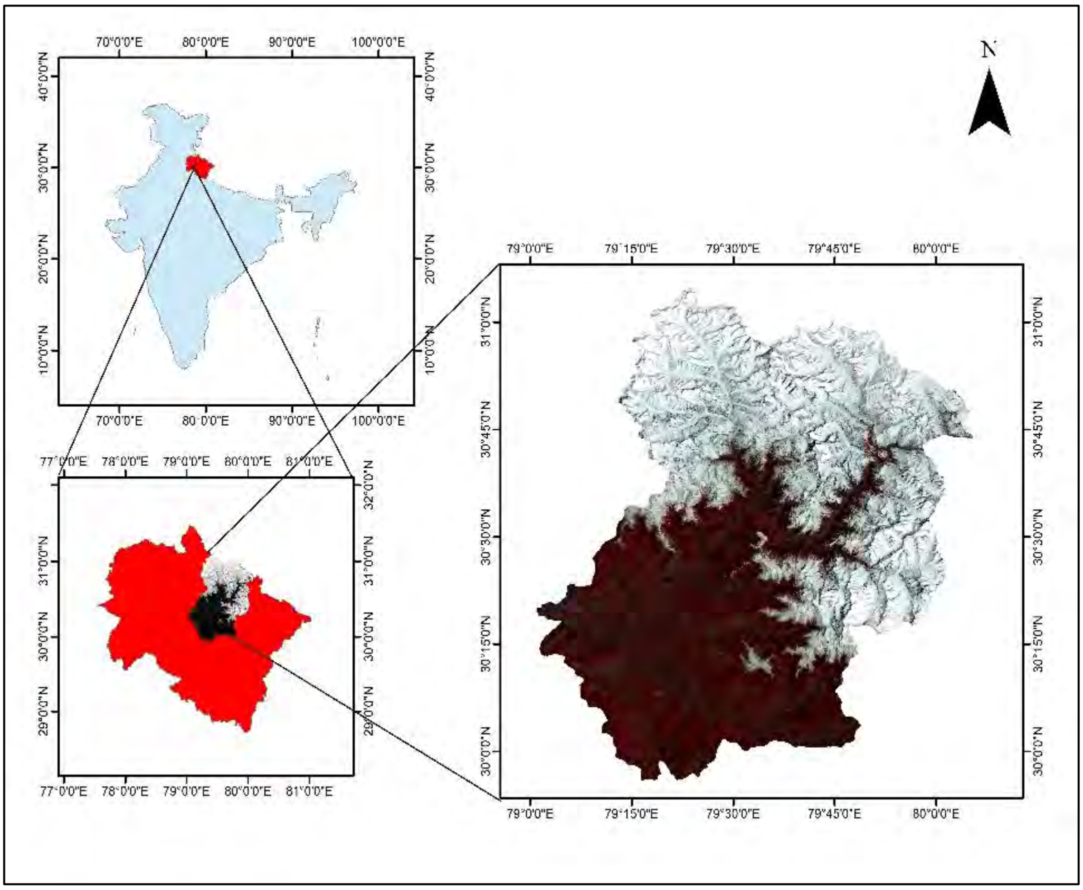

Figure 1. Map of the study area Chamoli district

The data used in this study has been taken from two major sources; satellite remote sensing imagery and available map. To obtain slope and elevation CARTOSAT-1: DEM version 3 R1 having 30 meters spatial resolution from Bhuvan Geo-portal of ISRO (https://bhuvan.nrsc.gov.in/) has been used. It is a Digital Elevation Model (DEM) generated by Cartosat-1 PAN (2.5m) Stereo data. The other information about the maps of roads, villages, surface water and protected area, we have used Open Street Map portal (https://www.openstreetmap.org/). It is an open-source platform having digitized maps of all over the world. The tourist hotspot locations are digitized using high-resolution satellite imageries like Airbus and Maxar technologies through the Google Earth Pro platform. The details of data sources are written in Table:2.

Table 2. Data Sources and Resolution.

Elements	Data Source	Scale/resolution
Slope	CARTOSAT 1: DEM	30m spatial resolution
Touristic Hotspots	High Resolution Imagery (Airbus, Maxar Technologies), through Google Earth Pro	Digitized Vector data
Elevation	CARTOSAT 1: DEM	30m spatial resolution
River Proximity	Open Street Map portal (https://www.openstreetmap.org/).	Digitized Vector Data
Road Proximity	Open Street Map portal (https://www.openstreetmap.org/).	Digitized Vector Data
Village Proximity	Open Street Map portal (https://www.openstreetmap.org/).	Digitized Vector Data
Protected Area Proximity	Open Street Map portal (https://www.openstreetmap.org/).	Digitized Vector Data

3. Methodology

From a detailed literature review, it is observed that the ET is a function of seven parameters as defined as per Equation 1

$$\boldsymbol{E = F(S, TH, E, RP, R_dP, VP, PAP)} \qquad (\mathbf{1})$$

where, S = Slope, TH = Touristic Hotspots, E = Elevation, R_dP= River Proximity, RP = Road Proximity, VP = Village Proximity, PAP = Protected Area Proximity

The algorithm for deriving the suitability of an area for ecotourism development while considering the above parameters using AHP- MCE approach is described in the following 7 steps by (Ullah& Hafiz, 2014), are represented in the flowchart of Figure 2.

Step 1. Making pairwise comparison through AHP.

Step 2. Preparation of comparison matrices.

Step 3. Normalization of the matrices

Step 4. Checking consistency ratios and finalizing th weight values.

Step 5. Transferring the weights to the geospatial database.

Step 6. Overlaying operation in the thematic layers and making a composite map.

Step 7. Classifying the final suitability map into different suitable zones.

Step 1: Selection of Thematic Layer: The first step in every site suitability analysis is choosing the thematic layer of the study area and selecting the attributes we are taking into consideration. For selecting the study area as a potential ecotourism spot, we have taken the following thematic layers such as slope, touristic hotspots, elevation, river proximity, road proximity, village proximity and protected area proximity. The elements responsible for ecotourism in this study area were selected according to the literature (Kumari et al., 2010).

Step 2: Geospatial Database Generation: One of the major important factors of ecotourism is slope (Kumari et al., 2010). The slope map has been generated using CARTOSAT 1 DEM version 3R, and the degree method was used to calculate the slope map. The slope layer is further reclassified into five subclasses naming Very High, High, Moderate, Low, Very Low, respectively. The preference was set as the area with a higher slope will have the lesser potential of developing into an ecotourism zone.

Now while analyzing elevation, we can infer that the area with higher elevation has lower suitability for ecotourism and the weight has been set accordingly. Elevation is an important index for ecotourism (Ahmadi et al., 2015). Higher elevation will have less concentration of oxygen means a higher possibility of humans to face hypoxia in those places, resulting in lesser suitability of tourism. Also, as the Chamoli district has a wide range of elevation values (lowest point 651 m and highest point 7816 m) so it is essential to see the influence of elevation over this area.

The primary data extracted from OSM using QGIS like River Proximity (RP) is a great potential for tourism, as it facilitates the development of attractive spots, in addition to its protection and respectful use. Protected area, as the name suggests, areas that are oriented to protect biodiversity relatively undisturbed natural environments, place a tremendous role in developing ecological friendly society and ecotourism. Roadway and its proximity (R_dP) allowing the travellers for inter-city travel giving services in rural areas also, influence other branches of the tourism industry. Villages and its proximity (VP) help in customizing trips and promoting culture and heritage, however, conversely helps them to enhance their infrastructure and income are rasterized, converting vector files into raster files as it aids the process.

The secondary data, proximity analyzed data which is attained by analyzing the location of features by measuring the distance between them and other features by area. It is done to get approximate interval between attributes. Followed by reclassifying the layers where one or more values are reassigned to a raster data set to new output values, this is to find out that the value of a cell which changes with respect to time like land use, weather, etc.

The data of touristic hotspot locations were digitized through high resolution satellite imageries with reference to Chamoli district and Uttarakhand state tourism department, these locations are popular for the pilgrimage reasons or mountain sports like trekking, hiking, camping, bonfire, skiing, mountaineering etc. The treks through deep valley, green meadows with snow laden mountains peak's view, makes them a strong attraction among tourists. Euclidian distance algorithm (equation 2) was applied to the touristic hotspot locations to generate the touristic hotspot map, where the smallest distance between pair of points of two locations was calculated. The proximity maps with suitable values are given in Figure 3 to Figure 9.

$$\boldsymbol{d(p, q) = \sqrt{(p_1 - q_1)^2 + (p_2 - q_2)^2 + \cdots + (p_n - q_n)^2}} \qquad \mathbf{(2)}$$

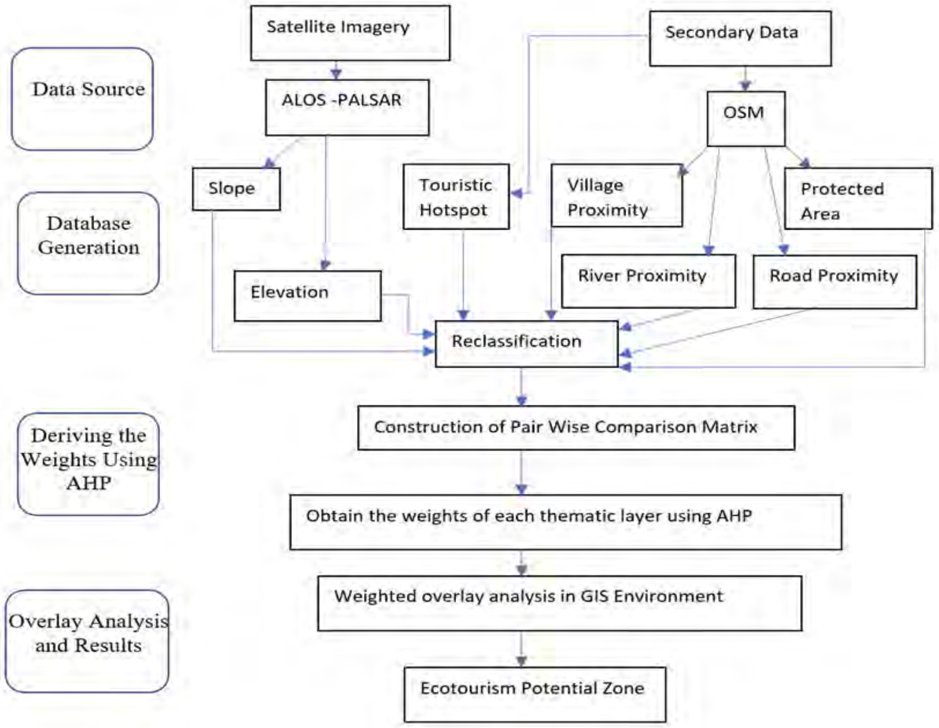

Figure 2. Flowchart of Methodology

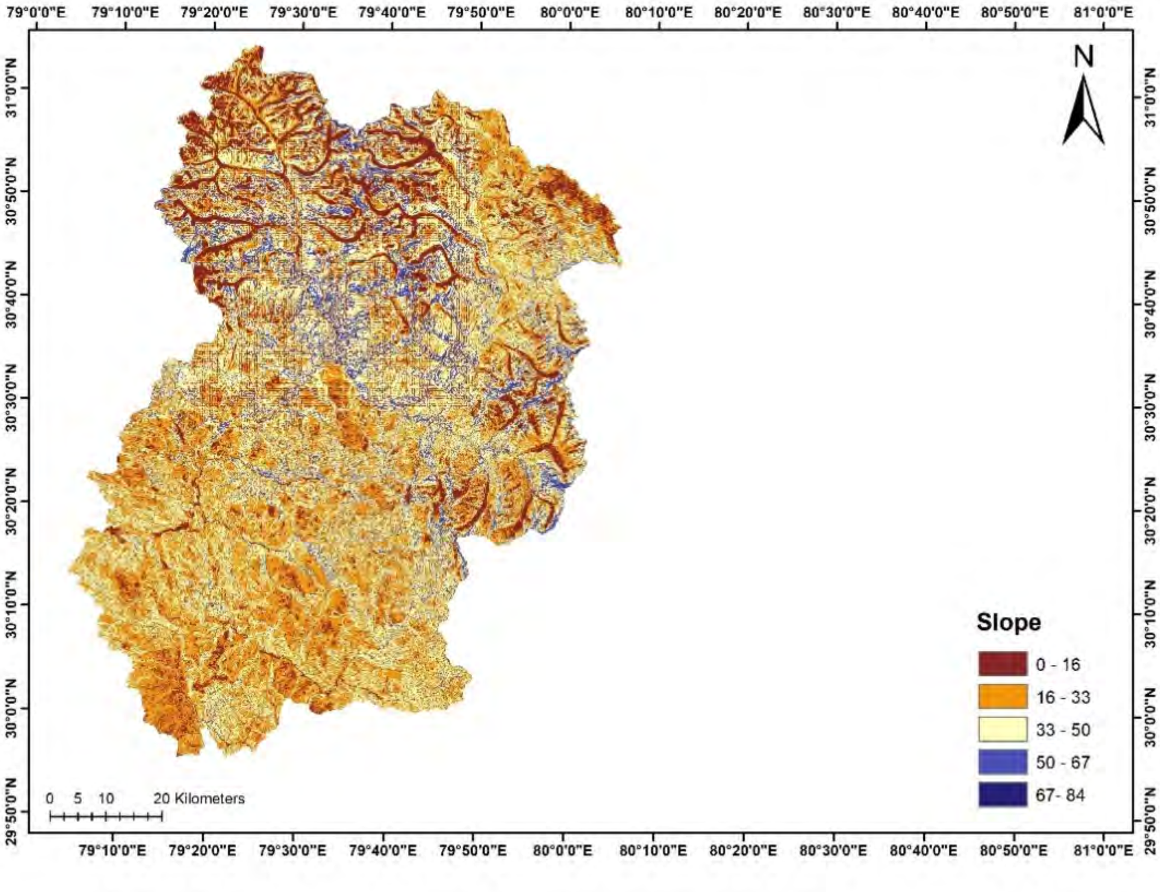

Figure 3. Slope map of Chamoli District

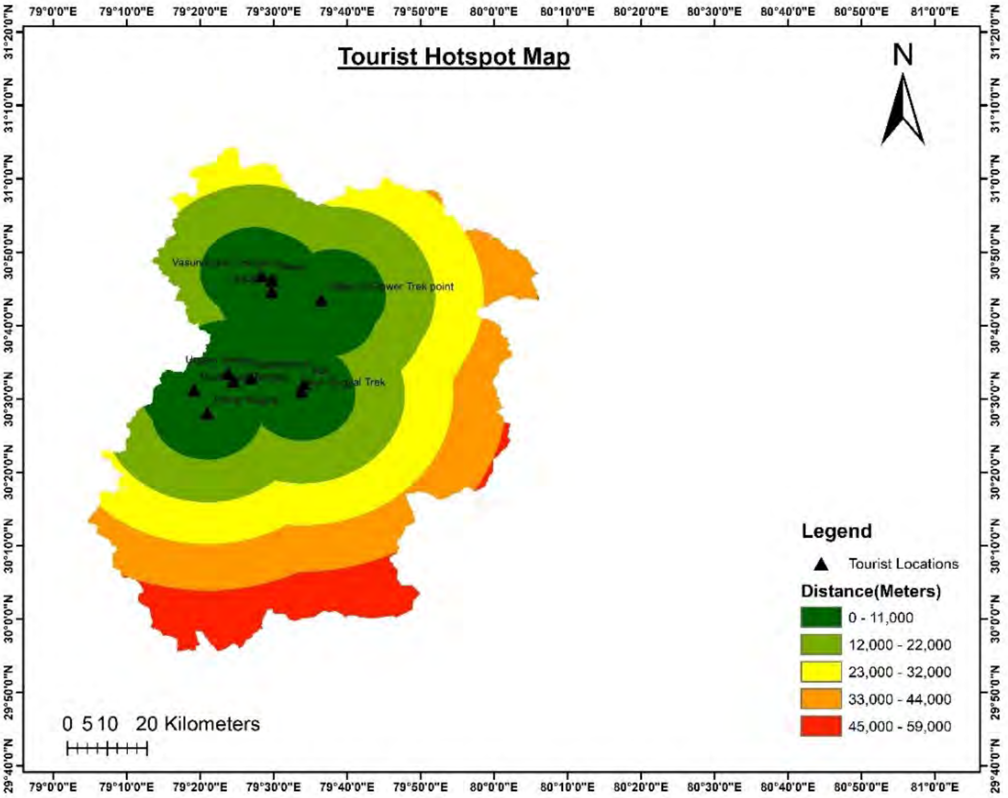

Figure 4. Touristic Hotspot map of Chamoli District

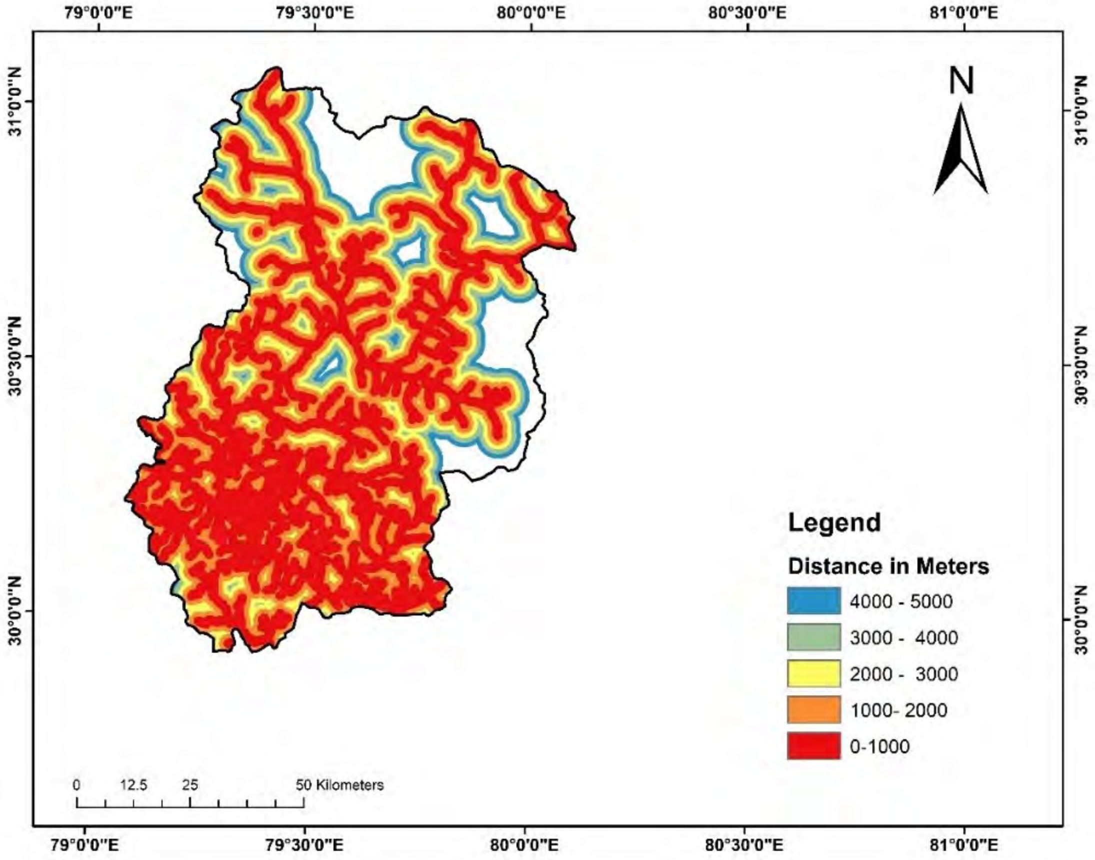

Figure 5. River Proximity Map of Chamoli District

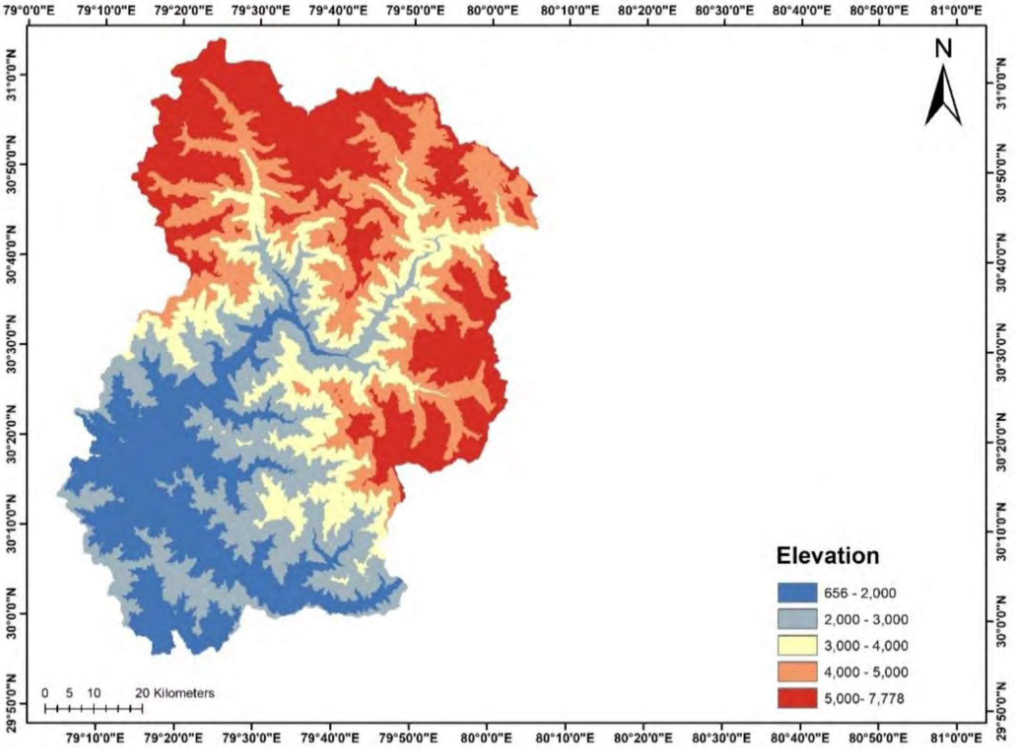

Figure 6. Elevation map of Chamoli District

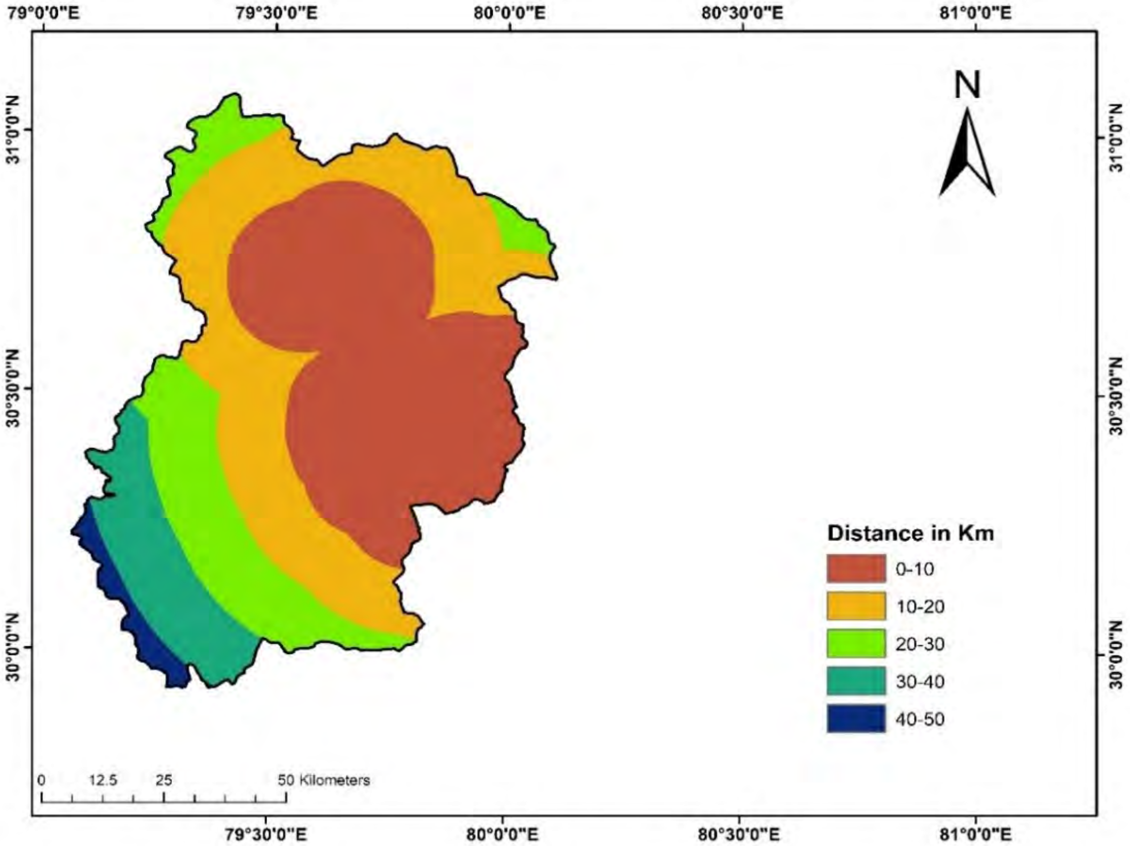

Figure 7. Protected Area Proximity Map of Chamoli District

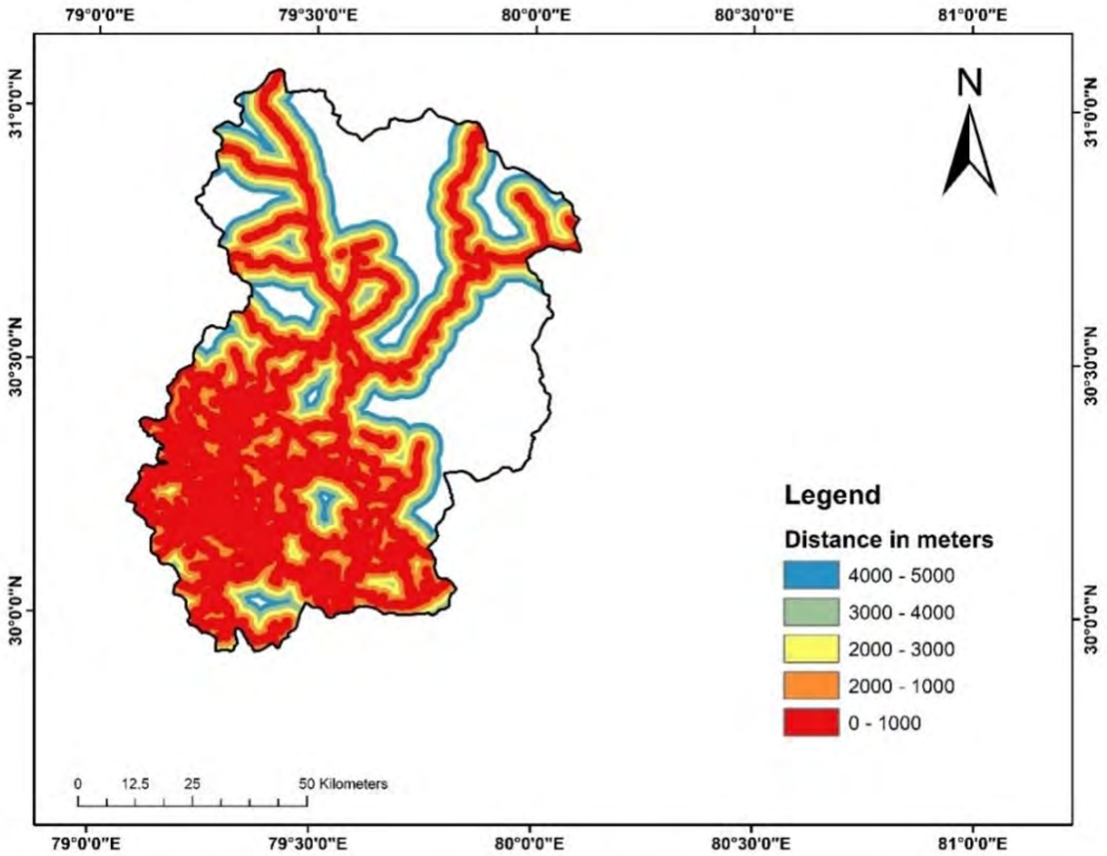

Figure 8. Road Proximity map of Chamoli District

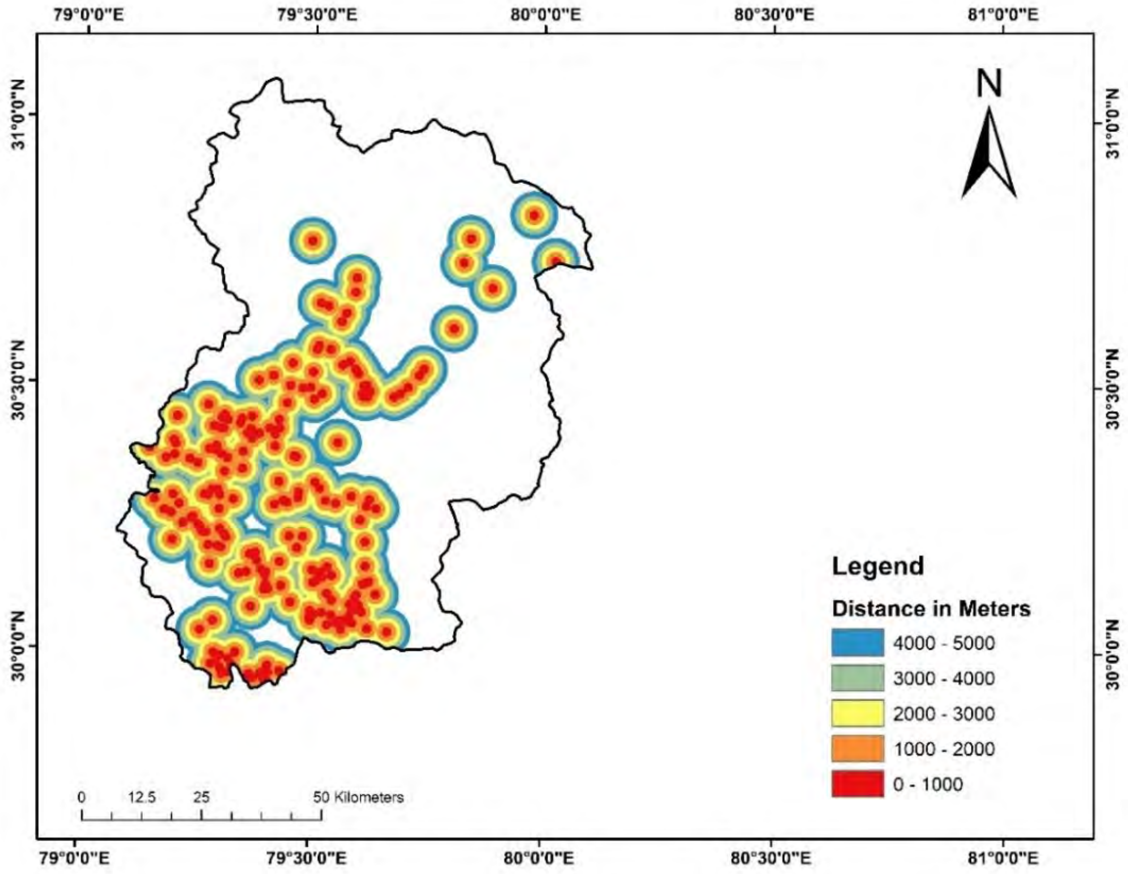

Figure 9. Village Proximity map of Chamoli District

Step 3: Normalized weights for different thematic layers.

The Analytical Hierarchy Process which is one of the multi criteria decision analyses was utilized for the purpose of the ecotourism suitability potential generation. This process is widely used in natural resources management and in mapping geohazard potential zones such as floods, landslide zonation etc. In this process, the criteria which have been considered as an influencing parameter are arranged in a hierarchical structure and matrices are being created by assigning scale factors to the criteria (Saaty, 1980), are represented in Table 3. A comparison between all the criteria is done taking two at a time and realising one criteria's importance over another. The scale factors are assigned to each of them, giving more weightage to the one having more importance over another and thus a matrix is generated in this way which is called as the pairwise comparison matrix as shown in Table 4. In the next step the matrix is normalized by dividing each of the weights by the column sums thus generating a normalised pairwise matrix.

In the present study where the number of criteria that has been taken is 7 which are Slope, Touristic hotspots, Elevation, Road Proximity, Village Proximity, River Proximity and Protected area. The criteria which have been considered, therefore make a 7x7 matrix which is a pairwise comparison matrix has been made by assigning weights based on the scale provided by (Saaty, 1980) in which weights have been assigned based on the relative importance between two criteria.

Table 3. Saaty's scale factor for comparison

Scale	Importance
1	Equal Importance
2	Intermediate
3	Weak importance
4	Intermediate
5	Moderate Importance
6	Intermediate
7	Strong Importance
8	Intermediate
9	Extremely Important

After normalization of the matrix and estimation of the weights for each of the criteria, the matrix is checked for consistency. This is primarily done in order to check whether the assigned weights are consistent with being transferred to the geospatial database. This requires the estimation of two important parameters which are consistency index (C.I) and consistency ratio (C.R). The consistency ratio which is the ratio between the consistency index and the random index (as shown in Table 5) should be less than 0.1 to be considered as consistent and if not, the weights should be modified again in order to maintain the consistency. The C.I is calculated using the λ value which is the largest eigen value of the matrix. In our study, the CI came to be around 0.096. Now the CI value should be divided by the random index value based on the number of criteria (Saaty, 1980) The random matrix is as follows

Table 4. Pairwise Comparison Matrix

	Tourist Hotspot	Protected Area	Village Proximity	Surface water	Road Proximity	Slope	Elevation
Tourist Hotspot	1	3	3	5	5	7	9
Protected Area	1/3	1	3	5	5	7	9
Village Proximity	1/3	1/3	1	1	3	5	7
Surface Water	1/5	1/5	1	1	3	5	7
Road Proximity	1/5	1/5	1/3	1/3	1	3	5
Slope	1/7	1/7	1/5	1/5	1/3	1	3
Elevation	1/9	1/9	1/7	1/7	1/5	1/3	1

Table 5. Random Index (Saaty, 1980)

Number of Criteria	Random index (R.I)
3	0.52
4	0.89
5	1.11
6	1.25
7	1.35
8	1.40
9	1.45

The comparison matrix generated from all the criteria is as follows :

The Consistency Ratio (CR) is calculated using equation 3

$$\mathbf{CR} = \frac{\textit{Consistency Index}}{\textit{Randon Index}\ (n=7)} = \mathbf{0.096/1.35 = 0.07} \qquad \mathbf{(eq3)}$$

The CR value which came to be around 0.07 is less than 0.1 which makes the weight consistent to be used for assigning weights to the thematic layers.

Step 4: Overlay operation by assigning weights in GIS. The weights generated in the AHP process were implemented in overlay analysis by weighted linear combination using equation 4. Here all 7 thematic layers are multiplied with the assigned weights and summed together to get the overlay map. Each of the classes of the thematic layers are also given weights according to the suitability in the overlay analysis only, as shown in Table 6 and Figure 10. The result of the overlay analysis in the GIS results in the final suitability maps shown in Figure 11. The final suitability map generated by the overlay analysis is then reclassified according to the suitability regions into 5 classes as very low suitability, low suitability, medium suitability, high suitability and very high suitability. This generates the final suitability of potential zones.

$$\boldsymbol{E = w_1SL + w_2TH + w_3RP + w_4E + w_5PA + w_6R_dP + w_7VP} \qquad (\boldsymbol{eq4})$$

where, E= Ecotourism Potential, SL = Slope, TH = Touristic Hotspots, RP= River Proximity, E= Elevation, PA= Protected Area Proximity, R_dP= Road Proximity, VP= Village Proximity, w_1 to w_7 are individual weights of the criteria.

4. Results and Discussion

Seven criteria were taken into consideration in this study. Using these criteria, an ecotourism potential zone map was developed to visualise the potential sites. The potential zones were categorised in to 5 divisions according to suitability, namely as Very Low, Low, Moderate, High, Very High. Very Low suitability zone covers 4.15% area, Low suitability zone covers 28.42% area, Moderate suitability zone covers 32.02% area, High suitability zone covers 25.75% area, and Very High suitability zone covers an area of 9.66%. The Very High suitable areas are more concentrated around the Nanda Devi range consisting the peaks like Hathi Parvat, Trishul Parvat, and Dronagiri Parvat. High suitable area is more or less around the Alaknanda and Dhauliganga Rivers are also scattered in the area of Nanda Devi National Park. Moderately suitable area is almost scattered all over the study area ranging from the northern higher Himalayas to the southern middle Himalayas, Very Low, Low suitable areas are distributed mostly in the inaccessible higher Himalayas (near Indo-China border) and also southern part of the study area. The majority of valley regions are devoid of ecotourism potential areas because of seasonal fluctuations in the stream flow like flash floods. A general observation could be drawn from the map that high to very high suitable regions are in an around the areas of tourist hotspot zones like Badrinath, Joshimath, Auli, and Nanda devi national park which is enriched in biodiversity.

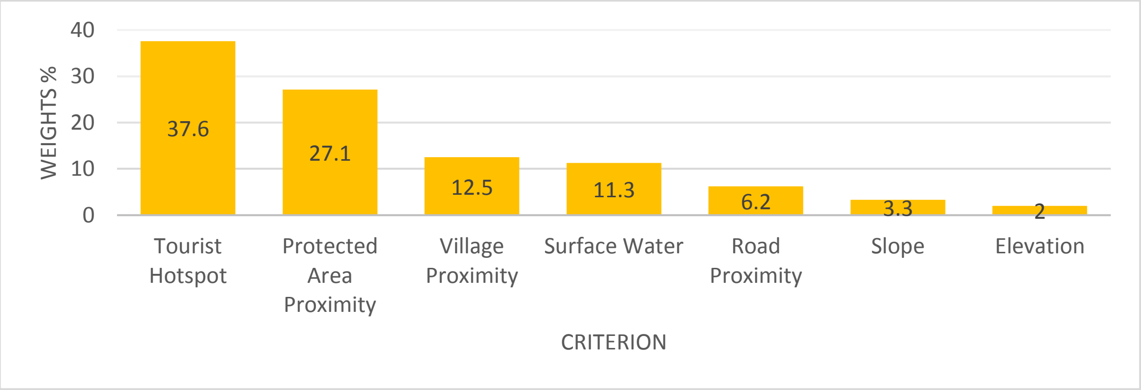

Figure 10. Bar graph of criteria and weight percentage.

Table 6. Overlay weightage table

Factors	*Category Class*	*Assigned Weight*	*Normalised Weight*
Village Proximity	*0 – 1000*	*5*	*0.124*
	1000-2000	*4*	
	2000-3000	*3*	
	3000-4000	*2*	
	4000-5000	*1*	
Protected Area Proximity	*0 – 1000*	*3*	*0.271*
	1000-2000	*5*	
	2000-3000	*4*	
	3000-4000	*2*	
	4000-5000	*1*	
River Proximity	*0 – 1000*	*5*	*0.113*
	1000-2000	*4*	
	2000-3000	*3*	
	3000-4000	*2*	
	4000-5000	*1*	
Road Proximity	*0 – 1000*	*5*	*0.061*
	1000-2000	*4*	
	2000-3000	*3*	
	3000-4000	*2*	
	4000-5000	*1*	
Slope	*Very Low*	*5*	*0.033*
	Low	*4*	
	Medium	*3*	
	High	*2*	
	Very High	*1*	
Tourist Hotspot	*Very Low*	*5*	*0.376*
	Low	*4*	
	Medium	*3*	
	High	*2*	
	Very High	*1*	
Elevation	*Very Low*	*2*	*0.019*
	Low	*3*	
	Medium	*5*	
	High	*4*	
	Very High	*1*	

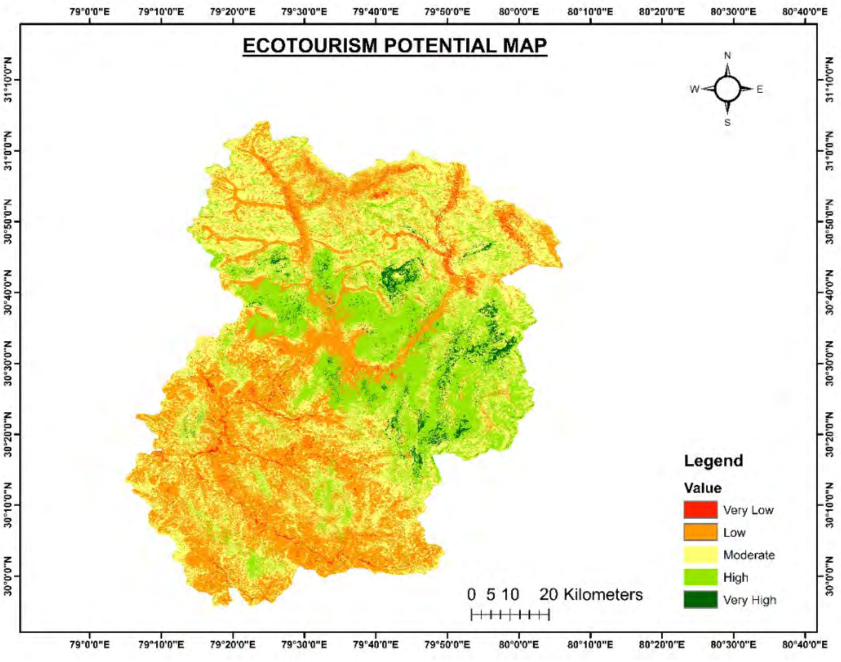

Figure 11. Ecotourism Potential Map for Chamoli District

5. Conclusion

This study draws the unified approach of Geographic Information System and Analytical Hierarchical Process to mark the zonation of potential ecotourism zones. This is performed by matching the features of an area with related criteria. This study recognizes and categorises the potential ecotourism zones in the Chamoli district of Uttarakhand state. This study is performed by implementing seven criteria in the form of GIS layers viz. Road Proximity, River Proximity, Village Proximity, Protected Area Proximity, Slope, Elevation, Touristic Hotspots. The potential to be developed as tourist sites needs a few basic facilities like proper connectivity of roads, availability of hotels, homestays and amenities of health centres and hospitals. Apart from that, even areas devoid of sufficient facilities have the potential to be developed as tourist sites because of the possibility to have mountain adventures. So, there is a huge requirement for infrastructure and emergency facilities in hard terrain as well. Overcrowdedness due to improper tourist management could lead to unplanned infrastructure development which could lead to serious situations like Joshimath subsidence. There should be proper daily control over the influx of tourists and ideal distribution of facilities to facilitate the uniform distribution of tourists. This study suggests about the zones that can be developed as an ecotourism site which will facilitate the development of the local community and enrichment of the local economy along with environmental awareness among the tourists in a sustainable manner.

References

Ahmadi M., S Asgari and E Ghanavati (2015). Land capability evaluation for ecotourism development in Ilam province, A GIS APPROACH. Boletim de CiênciasGeodésicas, 21, 107–125. https://doi.org/10.1590/S1982-21702015000100008

Al-Awadhi T, SM Al-Hatrushi, S Mansour, T Al-Awhadi and S Al-Hatrushi (2019). “Geospatial Based Multi-Criteria Analysis for Ecotourism Land Suitability Using GIS & AHP: A Case Study of Masirah Island, Oman.” Taylor & Francis. doi: 10.1080/14724049.2019.1663202.

Batta R. N. (2006). Evaluating Ecotourism in Mountain Areas: A Study of Three Himalayan Destinations. 6(1), 21.

Bosak K. (2008). Nature, Conflict and Biodiversity Conservation in the Nanda Devi Biosphere Reserve. Conservation and Society, 6(3), 211–224.

Cohen E. (1978). The impact of tourism on the physical environment. Annals of Tourism Research, 5(2), 215–237. https://doi.org/10.1016/0160-7383(78)90221-9

Debesa G, SL Gebre, A Melese, A Regassa and S Teka. (2020). “GIS and Remote Sensing-Based Physical Land Suitability Analysis for Major Cereal Crops in Dabo Hana District, South-West Ethiopia.” Cogent Food and Agriculture 6(1). doi: 10.1080/23311932.2020.1780100.

Fung, T. and FKK Wong (2007). Ecotourism planning using multiple criteria evaluation with GIS. Geocarto International, 22(2), 87–105. https://doi.org/10.1080/10106040701207332

Ghorbanzadeh, O. and S. Pourmoradian (2019) “Mapping Potential Nature-Based Tourism Areas by Applying GIS-Decision Making Systems in East Azerbaijan Province, Iran.” Taylor & Francis.

Ghorbanzadeh O, B Thomas, G Khalil G, SR Meena, T Dirk and J Aryal (2019a). “Evaluation of Different Machine Learning Methods and Deep-Learning Convolutional Neural Networks for Landslide Detection.” Remote Sensing 2019, Vol. 11, Page 196 11(2):196. doi: 10.3390/RS11020196.

Ghorbanzadeh O, S Pourmoradian, B Thomas and F Bakhtiar (2019b). “Mapping Potential Nature-Based Tourism Areas by Applying GIS-Decision Making Systems in East Azerbaijan Province, Iran.” Journal of Ecotourism 18(3):261–83. doi: 10.1080/14724049.2019.1597876.

Goodwin H. (1996). In pursuit of ecotourism. Biodiversity & Conservation, 5(3), 277–291. https://doi.org/10.1007/BF00051774

Khanduri S (2017). “Landslide Hazard around Mussoorie: The Lesser Himalayan Tourist Destination of Uttarakhand, India.” Pdfs.Semanticscholar.Org.

Kumari S., MD Behera and HR Tewari (2010). Identification of potential ecotourism sites in West District, Sikkim using geospatial tools. Tropical Ecology, 51(1), 75–85.

Mahdavi A., M Niknejad, O Karami-Caspian (2015) “A Fuzzy Multi-Criteria Decision Method for Ecotourism Development Locating.” Cjes.Guilan.Ac.Ir.

Pandey P., P Chauhan, CM Bhatt, PK Thakur, S Kannaujia, PR Dhote, A Roy, S Kumar, S Chopra, A Bhardwaj and SP Aggrawal (2021). Cause and Process Mechanism of Rockslide Triggered Flood Event in Rishiganga and Dhauliganga River Valleys, Chamoli, Uttarakhand, India Using Satellite Remote Sensing and in situ Observations. Journal of the Indian Society of Remote Sensing, 49(5), 1011–1024. https://doi.org/10.1007/s12524-021-01360-3

Ramya A, R Poornima, G Karthikeyan, S Priyatharshini, GK Thanuja and P Dhevagi (2023). “Climate-Induced and Geophysical Disasters and Risk Reduction Management in Mountains Regions.” Climate Change Adaptation, Risk Management and Sustainable Practices in the Himalaya 361–405. doi: 10.1007/978-3-031-24659-3_16.

Rautela P, GC Joshi, B Bhaisora, C Dhyani, S Ghildiyal and A Rawat (2015). Seismic vulnerability of Nainital and Mussoorie, two major Lesser Himalayan tourist destinations of India. International Journal of Disaster Risk Reduction, 13, 400–408. https://doi.org/10.1016/j.ijdrr.2015.08.008

Saaty T. L. (1980). The Analytic Hierarchy Process: Planning, Priority Setting, Resource Allocation. McGraw-Hill International Book Company.

Saaty T. L. and LG Vargas (2012). How to Make a Decision. In T. L. Saaty& L. G. Vargas (Eds.), Models, Methods, Concepts & Applications of the Analytic Hierarchy Process (pp. 1–21). Springer US. https://doi.org/10.1007/978-

Sahani N (2020). “Application of Analytical Hierarchy Process and GIS for Ecotourism Potentiality Mapping in Kullu District, Himachal Pradesh, India.” Environment, Development and Sustainability 22(7):6187–6211. doi: 10.1007/S10668-019-00470-W.1-4614-3597-6_1

Scheyvens R. (1999). Ecotourism and the empowerment of local communities. Tourism Management, 20(2), 245–249. https://doi.org/10.1016/S0261-5177(98)00069-7

Sharpley R. (2006). Ecotourism: A Consumption Perspective. Journal of Ecotourism, 5(1–2), 7–22. https://doi.org/10.1080/14724040608668444

Shugar D. H., M Jacquemart, D Shean, S Bhushan, K Upadhyay, A Sattar, W Schwanghart, S McBride, MVW de Vries, M Mergili, A Emmer, C Deschamps-Berger, M McDonnell, R Bhambri, S Allen, E Berthier, JL Carrivick, JJ Clague, M Dokukin and MJ Westoby (2021). A massive rock and ice avalanche caused the 2021 disaster at Chamoli, Indian Himalaya. Science, 373(6552), 300–306. https://doi.org/10.1126/science.abh4455

Singh T. V. and S Singh (2004). On bringing people and park together through ecotourism: The Nanda Devi National Park, India. Asia Pacific Journal of Tourism Research, 9(1), 43–55. https://doi.org/10.1080/1094166042000199602

Sundriyal S., V Shridhar, S Madhwal, K Pandey and V Sharma (2018). Impacts of tourism development on the physical environment of Mussoorie, a hill station in the lower Himalayan range of India. Journal of Mountain Science, 15(10), 2276–2291. https://doi.org/10.1007/s11629-017-4786-0

Ullah K. M. and R Hafiz (2014). Finding suitable locations for ecotourism development in Cox’s Bazar using Geographical Information System and Analytical Hierarchy Process. Geocarto International, 29(3), 256–267. https://doi.org/10.1080/10106049.2012.760005

Weaver D. B. and LJ Lawton (2007). Twenty years on: The state of contemporary ecotourism research. Tourism Management, 28(5), 1168–1179. https://doi.org/10.1016/j.tourman.2007.03.004

Yuwono E., RI Maulany and RA Barkey (2020). Site suitability evaluation for ecotourism development: a case study in Bulue village, Soppeng district, Indonesia. Journal of Sustainability Science and Management, 16(1), 129–140. https://doi.org/10.46754/jssm.2021.01.012

Journal of Geomatics Vol. 17, No. 1, April 2023

Study the effect of MRF Model based NC classifier with different distance measures and parameters

Shilpa Suman[1*], Anil Kumar[2], Dheeraj Kumar[1]
[1]Remote sensing and GIS laboratory, Department of Mining Engineering, Indian Institute of Technology (Indian School of Mines), Dhanbad 826004, India (dheeraj@iit.ism.ac.in)
[2]Indian Institute of Remote Sensing (IIRS), Dehradun 248001, India (anil@iirs.gov.in)
*Email: shilpa.suman011@gmail.com

(Received: 26 August 2022, Accepted in final form: 11 November 2022)

DOI- *https://doi.org/10.58825/jog.2023.17.1.79*

Abstract: The accuracy of satellite image classification and the computational complexity is reduced due to the image's noisy pixels. Therefore, spatial contextual information-based classifiers are required to handle the noisy pixels and obtain the neighborhood information. This paper represents Noise clustering (NC) based Markov Random Field (MRF) models (SP, DA (H1, H2, H3, and H4)) that handle the noisy pixels and provide the information. The Smoothing Prior (SP) and Discontinuity Adaptive (DA) models are useful for reducing noise by smoothing the images and showing the boundary of classes, respectively. This study has carried out a comparative study among MRF model-based NC classifiers SP and DA for different distance measures and parameters. MRF models based on NC classifiers were tested for classifying Eucalyptus, Water, Riverine sand, Grassland, Dense Forest, and Wheat classes using the Formosat-2 and Landsat-8 multispectral images of the Haridwar area. The DA (H1) model provides the best overall accuracy (85.09%) for m=1.3, λ=0.2, $\delta=10^4$,γ=0.8, and Mean Absolute Difference.

Keywords: NC, MRF, DA, SP, Distance Measures

1. Introduction

A hard/conventional classification technique does not look after the neighborhood pixel and noisy pixel information of land cover classes. The neighborhood, noisy and mixed pixels are essential in the gradual boundary change problem. To incorporate this problem, many researchers implemented the “Soft Classification” approach; these techniques follow fuzzy logic theory and the fuzzy set applied to handle the problem of noisy and mixed pixels (Fisher 1997). The occurrence of noisy pixels degrades the accuracy of image classification (Singh and Garg 2017). The fuzzy based-approach allocates individual pixels to one or more classes. Fuzzy classification is also known as the soft classification technique (Binaghi and Rampini 1993). Fuzzy classification is illustrated by Possibilistic c-means (PCM) (Krishnapuram and Keller 1993), Fuzzy c-means (FCM) (Bezdek et.al, 1984), and Noise Clustering (NC) (Dave and Krishnapuram 1997). This paper concentrates on NC classifiers proposed by Dave R. N. (1991) to handle the sensitivity of the FCM algorithm from noisy and outlier pixels. The NC classifier introduced the additional cluster that is supposed to contain all outliers. This classifier minimizes the noise and outliers but does not give spatial contextual information. This information provides the neighboring pixel relationship, which helps handle mixed and noisy pixels and offers good accuracy results. The spatial context represents the relation between the adjacent pixels.

In order to extract the neighborhood pixel information and handle the noisy pixel, MRF models were introduced in the NC classifier, which is a visionary approach to considering spatial contextual information (Geman and Geman 1984). MRF models were initially introduced for computer vision, image processing, and statistical physics; recently, this model has been applied to classify and interpret remote sensing images (Zhang et al. 2011). MRF model considers the spatial attraction among pixels in the images. The property of contextual information is implemented using Smoothness Priors (SP). It smooths the images to reduce the noise, but it does not take about the edges or boundaries of classes in the smoothing process (Li 1995). DA model overcomes the problem of over-smoothing and is used for edge enhancement (Li 1995). Various applications need of MRF model to distinctly extract the information. Solberg et al. (1996) used the MRF model to classify the satellite images, and it was observed that the MRF model obtained 2% higher classification accuracy. Tso and Olsen (2005) analyzed that the MRF method increased classification accuracy as well as visual interpretation. Zhang et al. (2011) reported that MRF based model improved the classification accuracy. To increase the overall accuracy and reduce the noisy data and outliers, this paper studies the outcome of the MRF model-based NC classifier concerning various distance measures and different parameters. This optimized algorithm may be used to create a land use land cover map that can be used in integration with hazard maps to prepare a risk map for the desired area, agricultural mapping, and other fields that require a highly accurate LULC map (Rawat et al. 2022a; Saha et. al, 2022; Rawat et al. 2022b; Suman et.al, 2022)

The aims of this study show how different parameters (fuzziness factor (m), beta (β), lambda (λ), and gamma (γ)) and distance measures affect the MRF model with NC as the basic classifier. This study gives the optimized algorithm concerning different distance measures and parameters that handle the noisy data and enhance accuracy. A fuzzy Error Matrix (FERM) (Binaghi et al. 1999) has been implemented in this paper to obtain the overall accuracy of the classified output.

2. Mathematical details of NC and MRF Model

2.1 Noise Clustering

Noise clustering classifiers introduced a new cluster to contain all outliers to increase the accuracy (Davé and Krishnapuram 1997). Noise distance (δ) has an essential role in selecting which membership values lie on the new clusters. The NC algorithm objective function was given in eq. (1):

$$J_m = \sum_{i=1}^{N}\sum_{k=1}^{C} u_{ki}^{m}\|x_i - v_k\|^2 + \sum_{i=1}^{N}\delta^2\left(1 - \sum_{k=1}^{C} u_{ki}\right)^{m} \quad (1)$$

The membership value, mean value, and noise distance were obtained from eq. (2), eq. (3), and eq. (4) respectively, and updated this equation in equation 1 to get the objective function of the NC classifier.

$$u_{ki} = \frac{1}{\sum_{j=1}^{C}\left[\frac{\|x_i-v_k\|^2}{\|x_i-v_j\|^2}\right]^{\frac{1}{m-1}} + \left[\frac{\|x_i-v_k\|^2}{\delta^2}\right]^{\frac{1}{m-1}}} \quad (2)$$

$$v_k = \frac{\sum_{k=1}^{N}(u_{ki})^m x_i}{\sum_{k=1}^{N}(u_{ki})^m} \quad (3)$$

$$\delta^2 = \lambda\left[\frac{\sum_{k=1}^{C-1}\sum_{i=1}^{N}\|x_i-v_k\|^2}{n(c-1)}\right] \quad (4)$$

Here, u_{ki}= Degree of membership represents of ith pixel for cluster k,x_i= ith d-dimensional measured data,v_k= mean value (cluster center) of the kth class, m = Fuzziness factor (with a real value greater than one), N = total no of a pixel in the image, v_j= mean value (cluster center) of the jth class, C =Number of classes, δ= Noise Distance,$\|x_i - v_k\|$= distance betweenx_i and $v_k$and $\|x_i - v_j\|$= distance between x_i and v_j .

1.1. Discontinuity Adaptive (DA)

Discontinuity Adaptive (DA) is an important technique in the MRF model. This model conserves the edges and boundaries of classes. The required condition for a regulizer to be DA is defined in eq. (5) (Smits and Dellepiane 1997).

$$\lim_{n\to\infty}|g'(\eta)| = \lim_{n\to\infty}|2\eta h(\eta)| = c \quad (5)$$

c = constant (cε[0,∞])

The DA model (H1, H2, H3, and H4) is shown in eqs. (6-9).

$$g_{1\gamma}(\eta) = -\gamma e^{\frac{\eta^2}{\gamma}} \quad (6)$$

$$g_{2\gamma}(\eta) = \frac{-\gamma}{1+\frac{\eta^2}{\gamma}} \quad (7)$$

$$g_{3\gamma}(\eta) = \gamma \ln\left(1 + \frac{\eta^2}{\gamma}\right) \quad (8)$$

$$g_{4\gamma}(\eta) = \gamma|\eta| - \gamma^2 \ln\left(1 + \frac{|\eta|}{\gamma}\right) \quad (9)$$

1.2. Smoothing Prior (SP)

The MRF Smoothing Prior (SP) gives context information. It provides the concerned pixel as well as neighboring pixel information. A prior probability mathematically gave the smoothness assumption in the form of energy (Li 1995). For representing the prior energy, an analytical regulizer is implied. The basic structure of the regulizer is given in eqs. (10).

$$U(F) = \sum_{n=1}^{N} U_n(f) = \sum_{n=1}^{N} \lambda_n \int_n^b g(f^n(x))dx \quad (10)$$

U(f) = prior energy, represents the n^{th} order regularizer, λ_n=weighting factor, where(λ_n>=0) and$g(f^n(x))$ =potential function.

$$g(f^n(x)) = g(n) = \eta^2 \quad (11)$$

3. Study Area and Dataset Used

The study area (Figure 1.) for this research was the Haridwar district in the Indian state of Uttarakhand. This study lies between latitudes 29°49'14" and 29°52'21” and longitudes 78°9'17” and 78°13'4”. The coverage area is 5.92×5.95 km^2, north to south and east to west. This study area mainly contains Eucalyptus, Riverine sand, Water, Grassland, Dense Forest, and Wheat to examine the different fuzzy classifier methods. Table 1. shows the specification of Landsat-8 and Formosat-2 sensors used in this study

.

Table 1. Specification of Landsat-8 and Formosat2 sensors

Specification	Landsat-8	Formosat-2
Spatial Resolution (m)	30 m	8 m
Spectral Resolution (µm)	B1: 0.450-0.515 µm (Blue) B2: 0.525-0.600 µm (Green) B3: 0.630-0.680 µm (Red) B4: 0.845-0.885 µm (Near Infrared)	B1: 0.45-0.52 µm (Blue) B2: 0.52-0.60 µm (Green) B3: 0.63-0.69 µm (Red) B4: 0.76-0.90 µm (Near Infrared)
Revisit Period	Repeat every 16 days	Daily

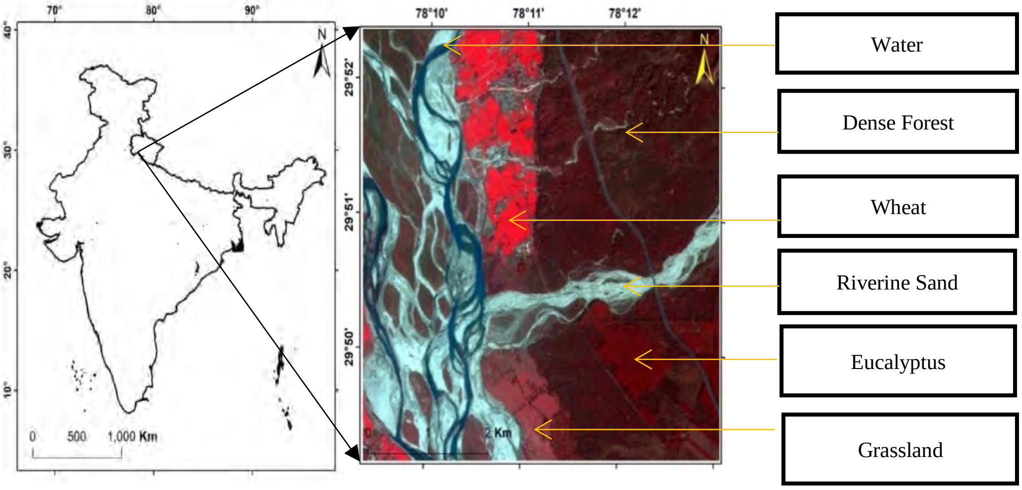

Figure 1. Study Area

4. Methodology Adopted

Figure 2 shows the methodology used for this study. This research focused on studying the effect of various parameters and distance measures by applying the NC as base classifiers for the MRF model. NC was used as the base classifier for MRF models, including contextual and spatial information (SP and DA (H1, H2, H3, and H4). The fraction output images from Landsat-8 and Formosat-2 were classified, and reference datasets were created. Various parameters were employed in this study, including λ (0.2-0.9) and γ (0.1-9) with a period of 0.1, m (1.1-3), and β (1-9) with intervals of 0.2 and 1, respectively. In the SP algorithm, the γ and m parameters were used, whereas, in the DA algorithm, β and m parameters were used. Mean Absolute Difference (Vassiliadis et al. 1998), Median Absolute Difference (Scollar et al, 1984), Normalized Square Euclidean (Hasnat et al. 2013), Canberra(Agarwal et.al, 2009), Manhattan (Hasnat et al. 2013), Chessboard (Baccour and John 2014) and Braycurtis (Bray and Curtis 1957), Cosine (Senoussaoui et al. 2014), Correlation (Székely et. al, 2007), and Euclidean (Baccour and John 2014) are different distance measures.

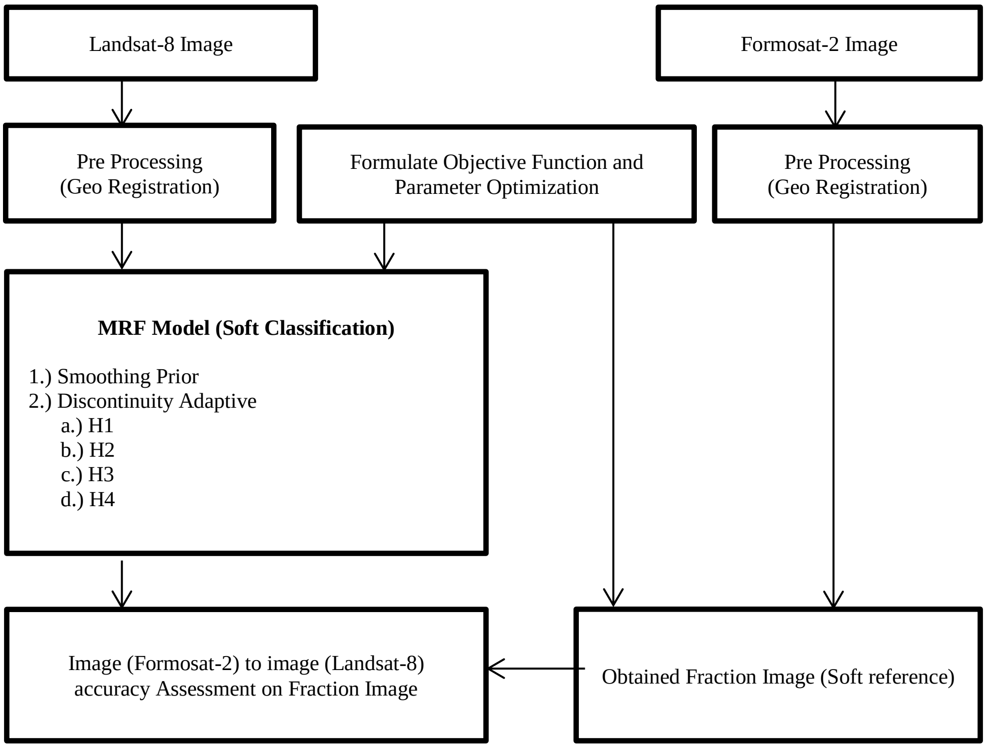

Figure 2. Methodology Adopted

The following steps show the adopted methodology.

Step 1: The satellite images were classified using the MRF model, which used NC as the base classifier for various parameters and distance measures, with m=1.1 and $\delta=10^4$.
Step 2: The optimized parameters have been obtained for the classified images' overall accuracy (OA).
Step 3: Obtained optimum parameters and different m values between 1.1 and 3 with a period of 0.2 were applied to classify the MRF model with NC as the base classifier.
Step 4: Finally, the Accuracy Assessment optimized the approach for various distance measures and parameters.

5. Results and Discussion

In this research, results were divided mainly into two parts. In the first part, the optimized parameter was obtained for SP and DA. The second part used optimized parameters to obtain the optimized MRF model technique, where NC was applied as the base classifier. The graph was built between parameters (λ, γ, β) and Overall Accuracy (OA) for various distance measures.

Figure 3 shows the DA (H1) (Figure 3(a-h)) and DA (H2) (Figure 3 (i–p)) algorithm applying NC as base classifier overall accuracy concerning γ and distance measures for the various value of λ (0.2-0.9) with an interval of 0.1

Table 2 represents the interpretation of Figure 3. It shows maximum overall accuracy for H1 and H2 using NC as the base classifier for the combination of distance measures and γ for different values of λ where m=1.1.

Figure 4 depicts the DA (H3) (Figure 4 (a-h)) and DA (H4) (Figure 4 (i–p)) algorithms for overall accuracy with regard to γ and distance measures for various values of (0.2-0.9) with an interval of 0.1 applying NC as a base classifier.

Table 3 obtains the analysis of Figure 4. It represents maximum overall accuracy for H3 and H4 using NC as the base algorithm for the combination of distance measures and γ for the various value of λ where m=1.1

Figure 5 represents the SP algorithm using NC as a base classifier for overall accuracy concerning γ and distance measures for the various value of λ (0.2-0.9) with an interval of 0.1

Table 4 represents the interpretation of Figure 5. It shows maximum overall accuracy for SP using NC as the base classifier for the combination of distance measures and γ for different values of λ where m=1.1.

Table 5 shows the highest overall accuracy of SP and DA (H1, H2, H3, H4) for various parameters (λ, γand β) and distance measurements where 'm'=1.1 using the basic classifier NC. Figure 6 was created using several distance measures between m and overall accuracy (OA), applying optimized parameters obtained from Table 5. Figure 6 depicts the NC, DA, and SP algorithms, with NC acting as the basic classifier for determining the optimal approach for different distance measures and m values.

Table 6 represents the inference of Figure 6. It shows the highest OA occurred for NC and NC based MRF model for different m value and distance measures.

Table 7 represents the maximum overall accuracy obtained from the various algorithms (DA (H1, H2, H3, and H4), SP, and NC) for m value and distance measures.

Table 2. Maximum overall accuracy for H1 and H2 using NC as a base classifier for the combination of distance measures and γ for different values of λ where m=1.1

	DA(H1)			DA(H2)		
λ	γ	Overall Accuracy (OA)	Distance Measures	γ	Overall Accuracy (OA)	Distance Measures
0.2	0.8	84.93	Mean Absolute Difference	0.8	1.79	Canberra
0.3	0.7	83.88	Canberra	0.9	1.86	Bray-Curtis
0.4	0.7	83.22	Bray-Curtis	0.9	16.92	Chessboard
0.5	0.7	82.51	Mean Absolute Difference	0.9	24.66	Chessboard
0.6	0.8	83.12	Mean Absolute Difference	0.9	49.26	Canberra
0.7	0.7	82.52	Canberra	0.9	63.98	Chessboard
0.8	0.8	83.58	Mean Absolute Difference	0.8	69.94	Mean Absolute Difference
0.9	0.7	84.32	Mean Absolute Difference	0.8	79.58	Bray-Curtis

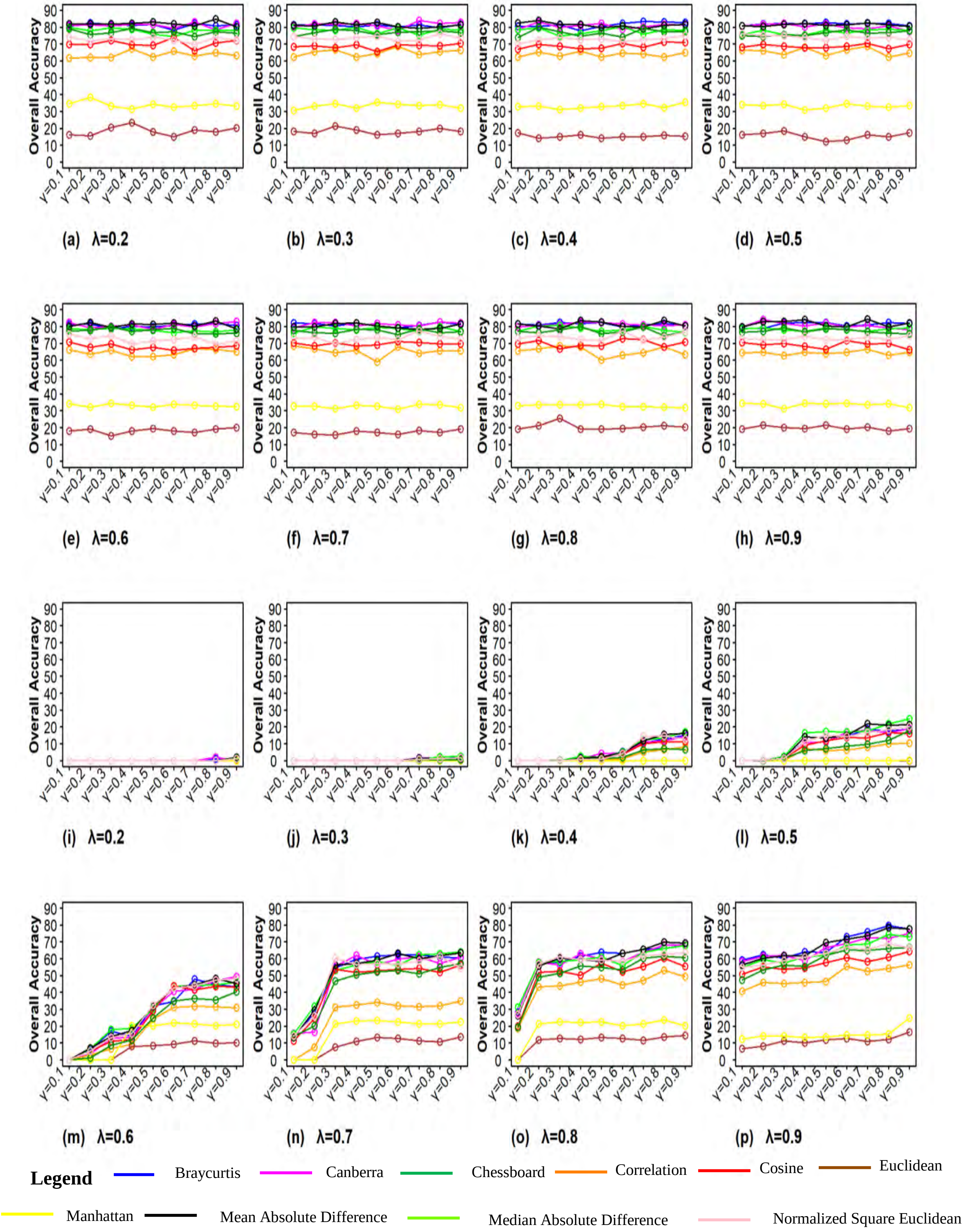

Figure 3. Comparison of Overall Accuracy in Discontinuity Adaptive Prior (DA) (H1) figure 3 (a-h) where DA (H2) figure 3 (i-p) using base classifier NC for applying different distance measures and m=1.1

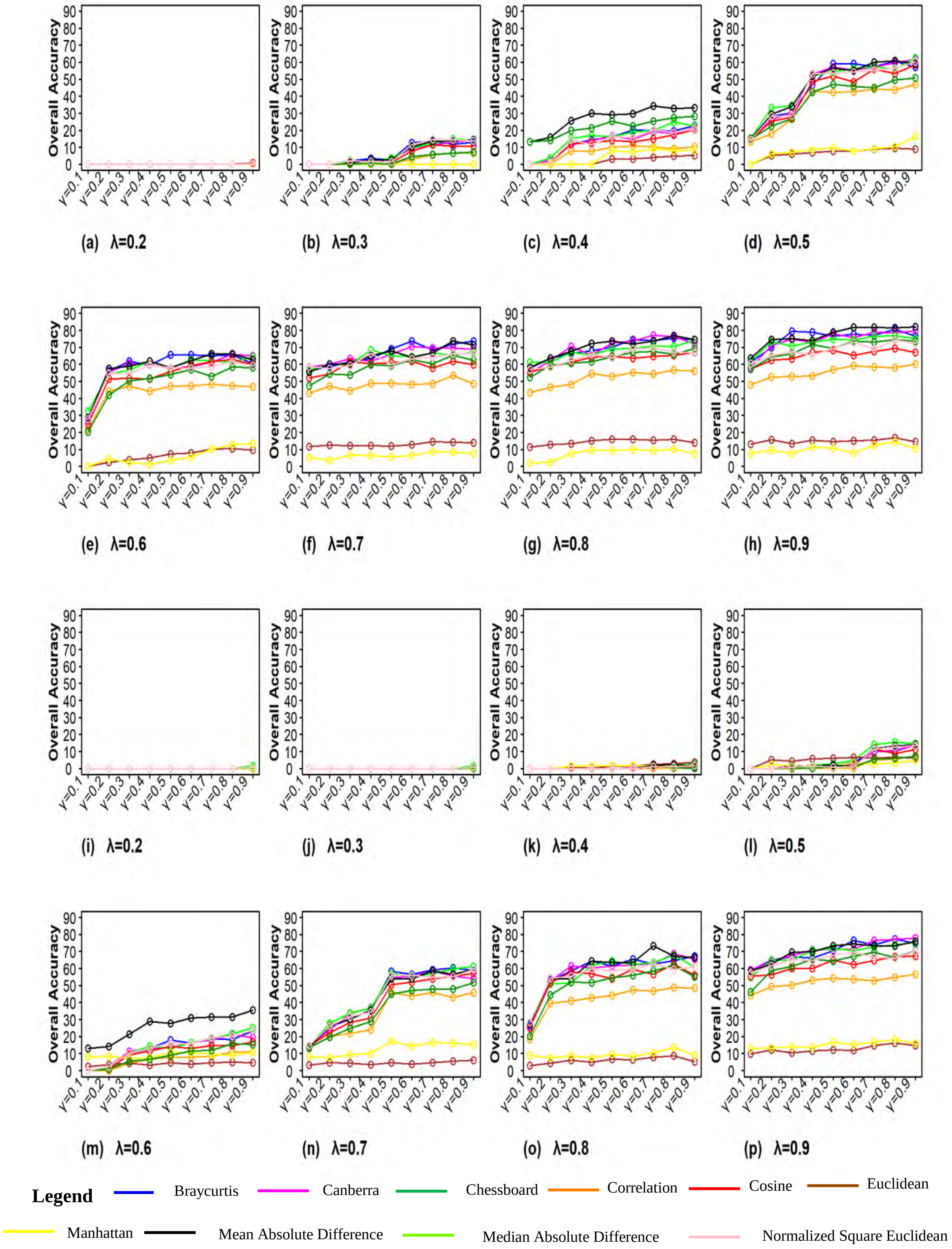

(a) λ=0.2 (b) λ=0.3 (c) λ=0.4 (d) λ=0.5

(e) λ=0.6 (f) λ=0.7 (g) λ=0.8 (h) λ=0.9

(i) λ=0.2 (j) λ=0.3 (k) λ=0.4 (l) λ=0.5

(m) λ=0.6 (n) λ=0.7 (o) λ=0.8 (p) λ=0.9

Figure 4. Comparison of Overall Accuracy in Discontinuity Adaptive Prior (DA) (H3) figure 4 (a-h) where DA (H4) figure 4 (i-p) using base classifier NC for applying different distance measures and m=1.1

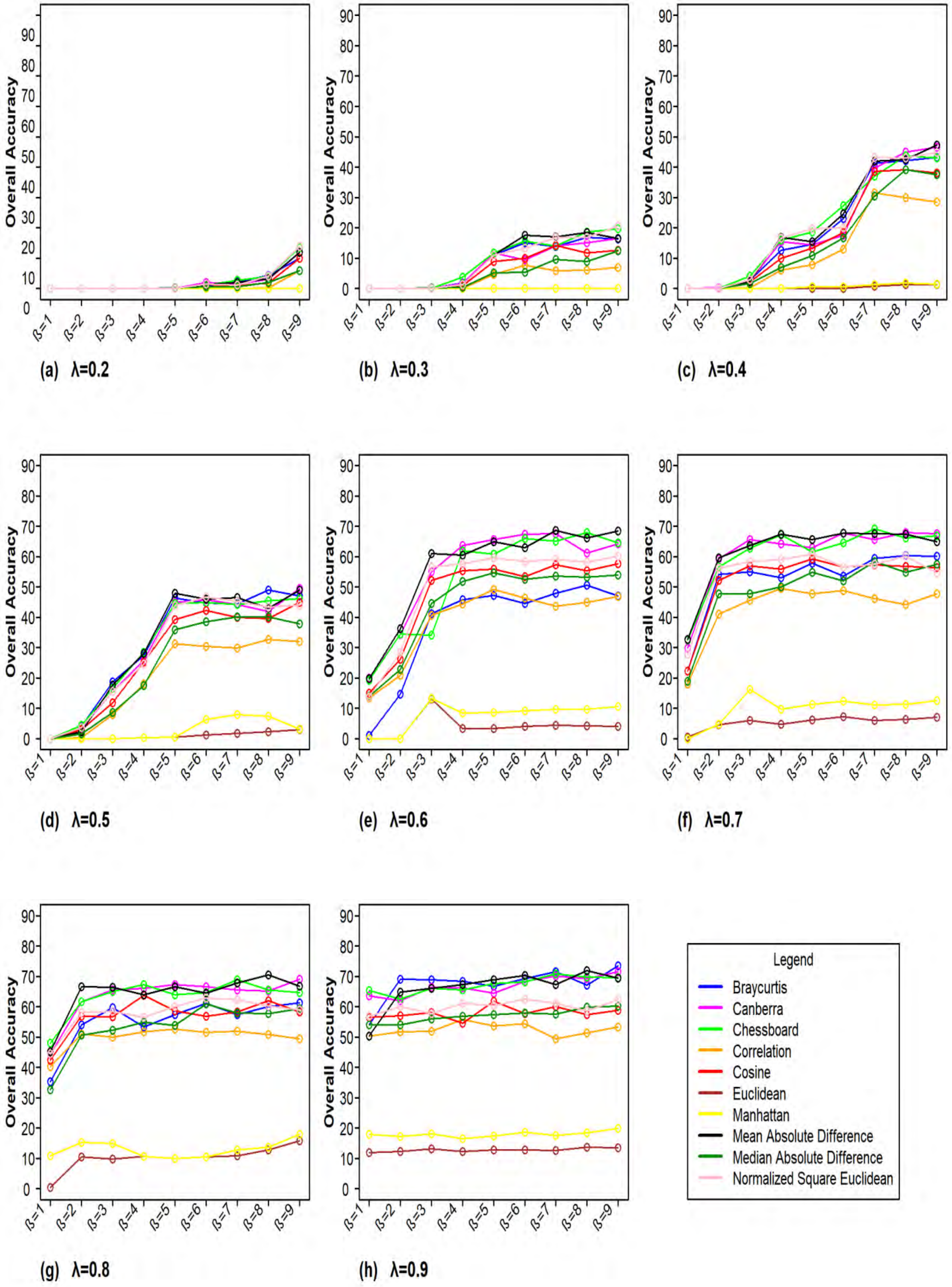

(a) λ=0.2 (b) λ=0.3 (c) λ=0.4 (d) λ=0.5 (e) λ=0.6 (f) λ=0.7 (g) λ=0.8 (h) λ=0.9

Figure 5. Comparison of Overall Accuracy in Smoothing Prior (SP) using base classifier NC for applying different distance measures and m=1.1

Table 3. Maximum overall accuracy for H3 and H4 using NC as a base classifier for the combination of distance measures and γ for different values of λ where m=1.1

	DA(H3)			DA(H4)		
λ	γ	Overall Accuracy (OA)	Distance Measures	γ	Overall Accuracy (OA)	Distance Measures
0.2	0.9	0.83	Cosine	0.9	1.68	Chessboard
0.3	0.8	15.1	Chessboard	0.9	1.52	Chessboard
0.4	0.7	34.24	Mean Absolute Difference	0.9	2.72	Chessboard
0.5	0.9	62.70	Chessboard	0.8	15.63	Chessboard
0.6	0.8	65.93	Canberra	0.9	35.50	Mean Absolute Difference
0.7	0.9	73.61	Bray Curtis	0.9	61.11	Chessboard
0.8	0.7	77.08	Canberra	0.7	73.27	Mean Absolute Difference
0.9	0.9	82.16	Mean Absolute Difference	0.9	77.99	Canberra

Table 4. Maximum overall accuracy for SP using NC as a base classifier for the combination of distance measures and γ for different values of λ where m=1.1

	SP		
λ	β	Overall Accuracy (OA)	Distance Measures
0.2	9	13.78	Normalized Square Euclidean
0.3	9	20.53	Normalized Square Euclidean
0.4	9	47.29	Mean Absolute Difference
0.5	9	49.44	Canberra
0.6	8	67.95	Chessboard
0.7	7	69.21	Chessboard
0.8	8	70.55	Mean Absolute Difference
0.9	9	73.46	Bray-Curtis

Table 5. Maximum overall accuracy of H1, H2, H3, H4, and Smoothing Prior (SP) using base classifier NC for various distance measures and parameters (λ, γ, and β) where 'm'=1.1

Maximum Overall Accuracy	Bray Curtis	Canberra	Chessboard	Correlation	Cosine	Euclidean	Manhattan	Mean Absolute Difference	Median Absolute Difference	Normalized Square Euclidean
H1 (λ/ γ)	83.22 0.4/0.7	83.99 0.9/0.2	80.56 0.8/0.3	68.68 0.7/0.1	73.83 0.2/0.6	25.5 0.8/0.3	38.22 0.2/0.2	84.93 0.2/0.8	80.02 0.4/0.2	77.42 0.8/0.6
H2 (λ/ γ)	79.58 0.9/0.8	74.98 0.9/0.9	74.40 0.9/0.8	56.18 0.9/0.9	64.32 0.9/0.8	16.48 0.9/0.9	24.73 0.9/0.9	78.41 0.9/0.8	66.59 0.9/0.9	68.94 0.9/0.8
H3 (λ/ γ)	80.46 0.9/0.8	79.73 0.9/0.9	76.75 0.9/0.8	60.13 0.9/0.9	69.38 0.9/0.8	16.69 0.9/0.8	14.55 0.9/0.8	82.16 0.9/0.9	74.38 0.9/0.8	74.23 0.9/0.8
H4 (λ/ γ)	77.24 0.9/0.8	77.99 0.9/0.9	75.40 0.9/0.9	56.62 0.9/0.9	67.11 0.9/0.9	16.17 0.9/0.8	18.15 0.9/0.8	75.83 0.9/0.9	70.44 0.9/0.9	70.02 0.9/0.9
SP (λ/ β)	73.46 0.9/9	71.45 0.9/9	70.76 0.9/7	55.79 0.9/4	63.73 0.8/4	15.82 0.8/9	19.82 0.8/9	71.96 0.9/8	60.99 0.8/9	62.81 0.8/6

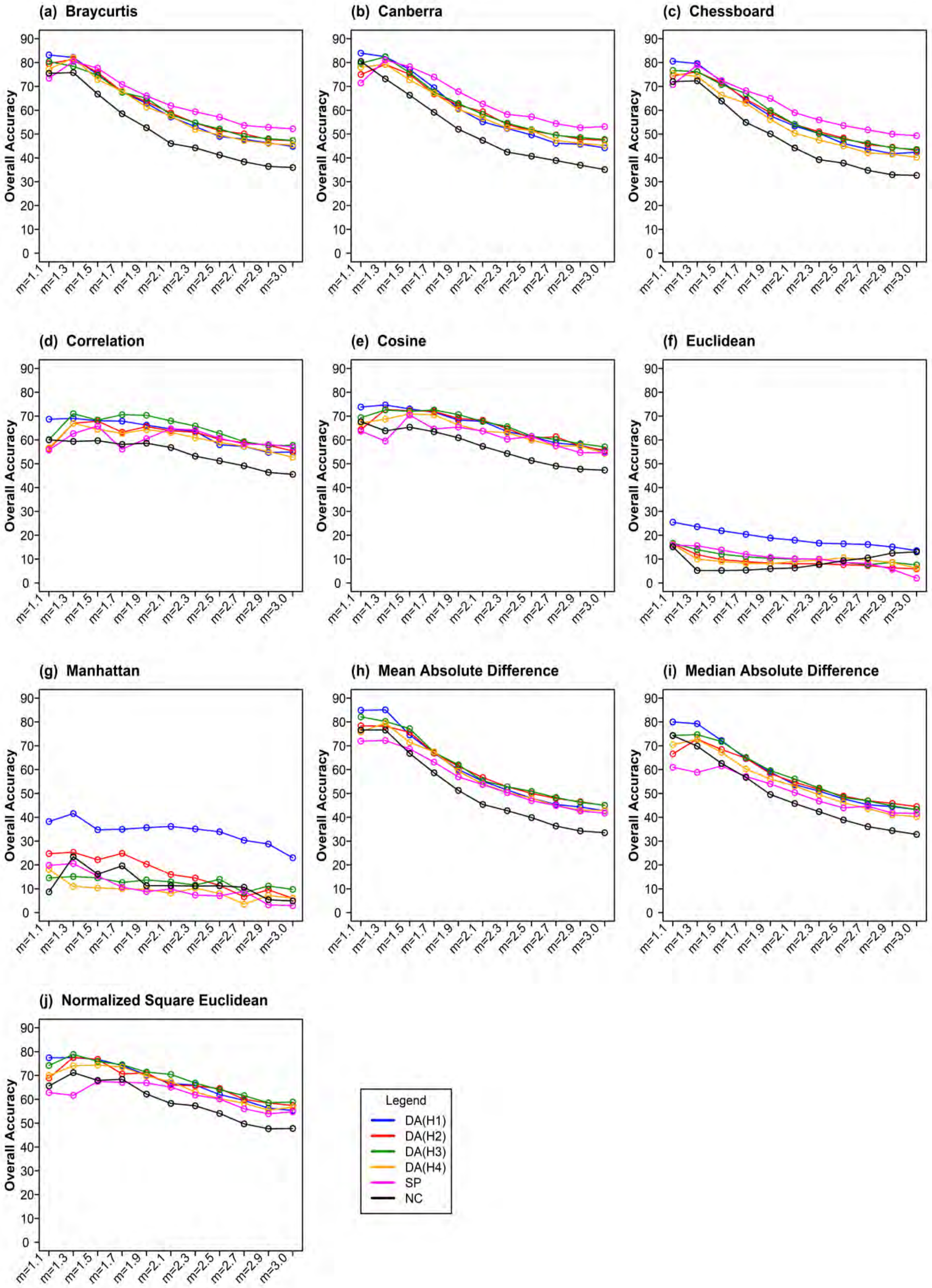

Figure 6. Comparison of Overall Accuracy in Discontinuity Adaptive Prior (DA) (H1, H2, H3, H4), Smoothing Prior (SP) and NC respectively for different m(1.1-3.0) and distance measures (a) Bray Curtis (b) Canberra (c) Chessboard (d) Correlation (e) Cosine (f) Euclidean (g) Manhattan (h) Mean Absolute Difference (i) Median Absolute Difference (j) Normalized Square Euclidean

Table 6. Highest OA occurred for NC and NC-based MRF models for different m value and distance measures

	DA(H1)		DA(H2)		DA(H3)		DA(H4)		SP		NC	
	OA	m	OA	m	OA	m	OA	m	OA	m	OA	m
Bray-Curtis	83.22	1.1	81.37	1.3	80.46	1.1	82.04	1.3	80.44	1.3	75.82	1.1
Canberra	83.99	1.1	79.25	1.3	82.37	1.3	79.30	1.3	81.08	1.3	80.48	1.1
Chessboard	80.56	1.1	76.14	1.3	76.75	1.1	75.4	1.1	79.01	1.1	72.34	1.3
Correlation	69.07	1.3	67.91	1.5	71.00	1.3	67.03	1.3	65.85	1.3	60.03	1.1
Cosine	74.68	1.3	72.80	1.3	72.57	1.3	70.98	1.5	70.46	1.5	67.65	1.1
Euclidean	25.50	1.1	16.48	1.1	16.69	1.1	16.17	1.1	15.82	1.1	15.18	1.1
Manhattan	41.56	1.3	25.31	1.3	15.14	1.3	18.15	1.1	20.60	1.1	23.48	1.3
Mean Absolute Difference	85.09	1.3	78.41	1.1	82.16	1.1	79.52	1.3	72.22	1.3	76.64	1.1
Median Absolute Difference	80.02	1.1	72.85	1.3	74.71	1.3	72.68	1.3	61.55	1.3	74.27	1.1
Normalized Square Euclidean	77.53	1.3	77.65	1.3	78.83	1.3	74.36	1.5	67.50	1.5	71.19	1.3

Table 7. The maximum overall accuracy of different algorithms using NC and NC based DA and SP algorithms concerning m and distance measures

Algorithm	m	Distance Measures	Overall Accuracy (%)
DA(H1)	1.3	Mean Absolute Difference	85.09
DA(H2)	1.3	Bray-Curtis	81.37
DA(H3)	1.3	Canberra	82.53
DA(H4)	1.3	Bray-Curtis	82.04
SP	1.3	Canberra	81.08
NC	1.1	Canberra	80.48

6. Conclusion

Traditional classification methods did not yield information on noisy and nearby pixels. On the other hand, the MRF model method takes care of the noisy and nearby pixels. This paper used Various MRF models, such as SP and DA (H1, H2, H3, and H4), to optimize the approach while considering distance measures and different parameters λ, β, γ, and m). The NC classifier as a base for SP and DA (H1, H2, H3, and H4) compares various distance measures and parameters to achieve the best technique. With $\gamma = 0.8$, $\delta = 10^4$, $m = 1.3$, and $\lambda = 0.2$, DA (H1) provided the highest overall accuracy of 85.09 % for Mean Absolute Difference distance measures. This study will also help find the optimized parameters (γ, β, m, and λ) and distance measures for MRF models (SP and DA) by applying NC as a base classifier to obtain the highest accuracy and classify the images perfectly.

Acknowledgment

The authors would like to express their sincere gratitude to the Department of Mining Engineering, Indian Institute of Technology (Indian School of Mines), Dhanbad for their help and support, and also to the Indian Institute of Remote Sensing Dehradun for their kind co-operation during the course of this study.

References

Agarwal S., C. Burgess and K. Crammer (2009). Advances in ranking. In *Workshop, Twenty-Third Annual Conference on Neural Information Processing Systems, Whistler, BC.*

Baccour L. and RI John (2014). Experimental analysis of crisp similarity and distance measures. In *2014 6th International Conference of Soft Computing and Pattern Recognition (SoCPaR)* (pp. 96-100). IEEE.

Bezdek J. C., R. Ehrlich and W. Full (1984). FCM: The fuzzy c-means clustering algorithm. *Computers & geosciences*, *10*(2-3), 191-203.

Binaghi E. and A. Rampini (1993). Fuzzy decision making in the classification of multisource remote sensing data. *Optical Engineering*, *32*(6), 1193-1204.

Binaghi E., PA Brivio, P. Ghezzi and A. Rampini (1999). A fuzzy set-based accuracy assessment of soft classification. *Pattern recognition letters*, *20*(9), 935-948.

Bray J. R. and JT Curtis (1957). An ordination of the upland forest communities of southern Wisconsin. *Ecological monographs*, *27*(4), 326-349.

Davé R. N. and R. Krishnapuram (1997). Robust clustering methods: a unified view. *IEEE Transactions on fuzzy systems*, *5*(2), 270-293.

Fisher P. (1997). The pixel: a snare and a delusion. *International Journal of Remote Sensing*, *18*(3), 679-685.

Geman S., & Geman D. (1984). Stochastic relaxation, Gibbs distributions, and the Bayesian restoration of images. *IEEE Transactions on pattern analysis and machine intelligence*, (6), 721-741.

Hasnat A., S. Halder, D. Bhattacharjee, M. Nasipuri and DK Basu (2013). Comparative study of distance metrics for finding skin color similarity of two color facial images. *ACER: New Taipei City, Taiwan*, 99-108.

Krishnapuram R. and JM Keller (1993). A possibilistic approach to clustering. *IEEE transactions on fuzzy systems*, *1*(2), 98-110.

Li S. Z. (1995). On discontinuity-adaptive smoothness priors in computer vision. *IEEE Transactions on Pattern Analysis and Machine Intelligence*, *17*(6), 576-586.

Rawat A., D. Kumar, RS Chatterjee and H. Kumar (2022a). A GIS-based liquefaction susceptibility mapping utilising the morphotectonic analysis to highlight potential hazard zones in the East Ganga plain. Environmental Earth Sciences, 81(13), 1-16.

Rawat A., D. Kumar, RS Chatterjee and H. Kumar (2022b). Reconstruction of liquefaction damage scenario in Northern Bihar during 1934 and 1988 earthquake using geospatial methods. Geomatics, Natural Hazards and Risk, 13(1), 2560-2578.

Saha A., VGK Villuri and A. Bhardwaj (2022). Development and Assessment of GIS-Based Landslide Susceptibility Mapping Models Using ANN, Fuzzy-AHP, and MCDA in Darjeeling Himalayas, West Bengal, India. Land, 11(10), 1711.

Scollar I., B. Weidner and TS Huang (1984). Image enhancement using the median and the interquartile distance. Computer vision, graphics, and image processing, 25(2), 236-251.

Suman S., D. Kumar and A. Kumar (2022). Study the Effect of the MRF Model on Fuzzy c Means Classifiers with Different Parameters and Distance Measures. Journal of the Indian Society of Remote Sensing, 1-13.

Senoussaoui M., P. Kenny, T. Stafylakis and P. Dumouchel (2013). A study of the cosine distance-based mean shift for telephone speech diarization. IEEE/ACM Transactions on Audio, Speech, and Language Processing, 22(1), 217-227.

Singh P. P. and RD Garg (2017). On sphering the high resolution satellite image using fixed point based ICA approach. In Proceedings of International Conference on Computer Vision and Image Processing (pp. 411-419). Springer, Singapore.

Smits P. C. and SG Dellepiane (1997, August). Discontinuity adaptive MRF model for remote sensing image analysis. In IGARSS'97. 1997 IEEE International Geoscience and Remote Sensing Symposium Proceedings. Remote Sensing-A Scientific Vision for Sustainable Development (Vol. 2, pp. 907-909). IEEE.

Solberg AHS, T Taxt and AK Jain (1996), A Markov Random Field Model for classification of multisource satellite imagery in IEEE Transcation on Geoscience and Remote Sensing Vol. 34, PP. 100-113.

Székely G. J., ML Rizzo and NK Bakirov (2007). Measuring and testing dependence by correlation of distances. The annals of statistics, 35(6), 2769-2794.

Tso B. and RC Olsen (2005). A contextual classification scheme based on MRF model with improved parameter estimation and multiscale fuzzy line process. Remote Sensing of Environment, 97(1), 127-136.

Vassiliadis S., EA Hakkennes, JSSM Wong and GG Pechanek (1998, August). The sum-absolute-difference motion estimation accelerator. In Proceedings. 24th EUROMICRO Conference (Cat. No. 98EX204) (Vol. 2, pp. 559-566). IEEE.

Zhang B., S. Li, X. Jia, L. Gao and M Peng (2011). Adaptive Markov random field approach for classification of hyperspectral imagery. IEEE Geoscience and Remote Sensing Letters, 8(5), 973-977.

Journal of Geomatics Vol. 17, No. 1, April 2023

Spatiotemporal analysis of land surface temperature owing to NDVI: A case study of Vadodara District, Gujarat

Sharmistha Bhowmik* and Bindu Bhatt
The Maharaja Sayajirao University of Baroda, Vadodara
*Email: sharmib24031988@gmail.com

(Received: January 15, 2022; in final form Feb 20, 2023)

DOI- *https://doi.org/10.58825/jog.2023.17.1.83*

Abstract: The expeditious extension of LULC in the name of development is the root cause of global warming. Replacement of natural resources due to the expansion of manmade erections is accountable for the increase in LST of Earth's topography. The impression of change in LULC is reflected in LST. To seize the rising temperature, the lamentation of a new plan of action for urbanization is of utmost requisite. This paper examines the change in LULC and its spatiotemporal impact on LST in Vadodara, which is situated on the bank of river Vishmamitri river. Vadodara an arid region has three main seasons and these are summer, monsoon, and winter. The climate is characterized by hot summer and dryness in the non-rainy seasons. May is the hottest month while January is the coldest month. The annual rainfall of the district is 475.2 mm. Hence, to analyze we used multi-spectral and multi thermal Landsat TM and ETM+ satellite images to monitor the evaluation of LULC and its impact on LST from 2001(pre-monsoon) to 2021(pre- monsoon). The study explores to what extent observed LST can be examined by vegetation cover measured through NDVI from2001 to 2021. To achieve this an analysis of co-relation is performed between LULC and LST and by using spectral indices comprising NDVI with the help of software like ArcGIS 10.2 and Erdas Imagine 2014. It had been observed that a considerable increase in LST in Vadodara was 58.338°C (Max) and 21.9014°C (Min) in 2001(pre-monsoon) to 60.844 °C (Max) and 24.6784 °C (Min) in 2021(pre-monsoon) which is just about 2°C increase in Max and 3 degrees increase in Min for LST in past 20 years. It was also observed that there is an inverse relationship between LST and NDVI. The value of NDVI is observed that change from 0.380711(H) and -0.59322(L) in 2001 to 0.551(H) to -0.351193(L)in 2021. Moreover, SMI places a vital role to investigate and verify the relation between LST and NDVI. Henceforth, to verify SMI was also calculated and it was noticed that places with high LST value and low NDVI value contained less soil moisture and places with less LST value and high NDVI values contained more soil moisture. Thus, it can be concluded that, if urban planners and decision-makers implement suitable land-use strategies then Earth's topography can be protected from adverse effects of urban heat by planting adequate and appropriate trees in bare soil and beside the impervious areas, thus the expansion of UHI can also be controlled. Moreover, with the help of SMI values, it will also be beneficial for the agricultural sector.

Keywords: Land Use Landcover, Land Surface Temperature (LST), NDVI (Normalized Difference Vegetation Index), SMI (Soil Moisture Index).

1. Introduction

The most important role it plays in the transmission of which is an essential component in the physics of land surface processes (Jin et al., 1997; Yuvaraj, 2020). Therefore, the spatial and temporal distributions of LST reveal the changes in climatic factors and the characteristics of the land surface (Yuvaraj, 2020). By, accurately studying and analyzing the combined factor of Land Surface Temperature with physical properties such as vegetation and soil moisture, we can access valuable metrics of surface state. Vegetation can effectively influence LST by selectively absorbing and reflecting solar radiation energy and regulating latent and sensible heat exchange (Yuvaraj, 2020). Land surface temperature, which is a significant parameter of the urban climate system, can be derived from satellite observations to monitor long-term environmental changes (Guillevic et al., and biophysical elements. They can also be related to energy fluxes of certain landscape phenomena or processes (Feizizadeh and Blaschke, 2012; Quattrochi and Luvall, 1999; Sobrino et al., 2006).

The technical term remote sensing was first coined by Evelyn Pruitt at the United States office research in 1958 (Estes energy and water from the ground to the atmosphere is that of the land surface temperature (LST),

2012; Li et al., 2013; Voogt and Oke, 2003). Land Surface Temperature measurement is one of the desirable goals of satellite-based remote sensing in the TIR part of the electromagnetic spectrum (Shah et al., 2012). Using thermal infrared (TIR) remote sensing, environmental characteristics can be gathered, examined, and modeled (Feizizadeh and Blaschke, 2012). It makes it possible to figure out land surface temperature (LST), a crucial element in many environmental processes like global warming or urban heat (Feizizadeh and Blaschke, 2012). It's important to emphasize here that two key ways that TIR data help us understand land surface processes better: In addition to observed point data, surface temperature values can be associated with specific landscape

and Jenson 1998; Yadav et al., 2016). The science and art of learning about an object, location, or p or phenomenon by analyzing data collected by a device that isn't in direct contact with the subject under study is referred to as remote sensing (Lillesand and Kiefer, 1979; Tomlinson et al., 2011). Usage is growing within the fields of meteorology and climatology and works in unison with the use of Geographical Information Systems (GIS) for spatial analysis (Chapman and Thornes, 2003; Dyras et al., 2005; Tomlinson et al., 2011). However, the identification of the patterns and analyses of spatial and temporal changes would help immensely in the planning for proper infrastructural facilities (Igbokwe et al., 2013).This could be done effectively and efficiently with the help ofspatial and temporal technologies such as GIS and Remote sensing, along with collateral data such as surveys of existingmaps, etc. (Barnes et al., 2001). Remote sensing also provides a sound database for generating baseline information on natural resources and a prerequisite for planning and implementing, and monitoring any developmental program (Yadav et al., 2016). Further, the application of the Geographical Information System (GIS) inanalyzing the trends and estimating the changes that have occurred in different themes helps in the management decision-making process (Yadav et al., 2016).

In general, NDVI values range from -1 to 1 (GIS Geography, 2018). Vegetation is healthier when the NDVI values are high. Low NDVI means there is little to no vegetation present (GIS Geography, 2018). The proportion of the field capacity and the remaining soil moisture to the difference between the current soil moisture and the permanent wilting point is known as the soil moisture index (SMI) (Saha et al., 2018). Soil moisture is the total amount of water present in the upper 10 cm of soil and it represents the water on the land surface that resides in the pores of the soil which is not in rivers, lakes, or groundwater and which and which depends on the weather conditions, soil type, and associated vegetation, among others (Gonzalez, 2021). Surface temperature is also regulated by soil moisture levels because evaporation is a more efficient cooling mechanism than sensible heating (Bateni and Entekhabi, 2012). To explore the changes in LST under different vegetation coverconditions the relation between summer LST with NDVI and SMI of pre-monsoon 2001 and 2021 was selected to investigate the impacts.

2. Study Area

Vadodara district is part of the great Gujarat plain. Vadodaradistrict with a 7548 sq. km area is located in the central part of the mainland of Gujarat between 21º49’19” and 22º48’37” north latitude and 72º51’05” and 74º16’55” east longitude (figure 1). Vadodara district is bounded in the north and northeast by Anand, Panchmahals, and Dahod districts in the east and the southeast by Madhya Pradesh and Maharashtra, in the southeast by Narmada district and in the south and the west by Bharuch district. The western and southern portion of the Vadodara district is comprised of Mahi and Narmada Doab which is an alluvial plain region with gently undulating terrain. The central portion of the district is comprised of an undulating plain with a low-level plateau and a few relict hills. The existence of a low-level stabilized dune with rolling topography is noticed in the central area between the Unch river and the Orsang river. The eastern and northeastern portion of the district is hilly terrainwith few ridges, flat-topped plateaux, and isolated relict hills.

3. Materials and Methods

3.1 Data Acquired

Landsat 7 ETM+ and Landsat 8 OLI_TIRS were used to calculate LST, NDVI, and SMI for the study purpose (figure 2).The digital data sets used in the present study were created bythe USGS and were acquired in GeoTIFF (Nasar and Minallah, 2020). The optical bands of satellite Landsat 7 and 8 were utilized in developing NDVI and SMI. Georeferencing was done using the UTM projection method for Landsat images (WGS 1984, Zone 43N). Moreover, the nearest-neighbor algorithm was used for resampling with the size of a pixel of30m*30m. ERDAS Imagine and ArcGIS 10.6 were used to analyze the satellite data and acquire the concluding product during the whole study.

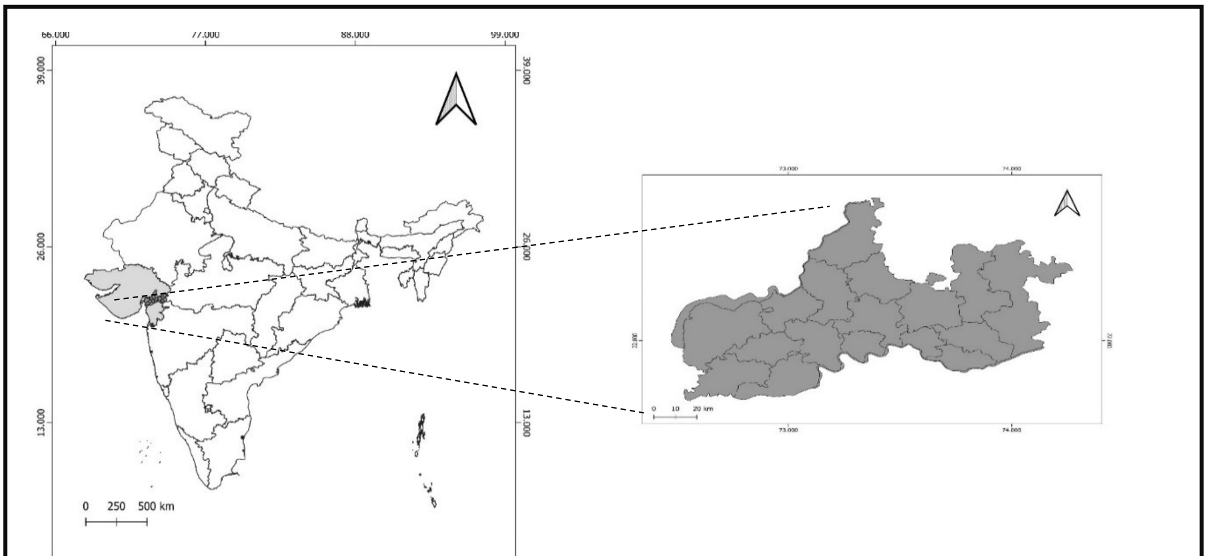

Figure 1. Location Map of The Study Area

3.2 Calculating LST, NDVI, and SMI

3.2.1 Converting Digital Numbers (DN) to Top of Atmospheric Spectral Radiance (TOA):

The algorithm's initial stage is the input of Band 10. The program uses algorithms from the USGS website to retrieve the top of atmospheric (TOA) spectral radiation after band 10 is entered in the background (Lλ):

$$L\lambda = M_L * Q_{cal} + A_L - O_i, \quad (1)$$

Where Q_{cal} is the Band 10 image, A_L is the band-specific additive rescaling factor, M_L represents the band-specific multiplicative rescaling factor, and $O_i$is the Band 10 correction (Avdan and Jovanovska, 2016; Barsi et al., 2014).

The TIRS band data should be converted from spectral radiance to brightness temperature (BT) using the thermal constants provided in the metadata file after the digital numbers (DNs) are translated to to reflection. The tool's algorithm converts reflectance to BT using the following equation (Avdan and Jovanovska, 2016).

$$BT = \frac{K_2}{1_n\,[(K_1/\,L_\lambda)+1]} - 273.15 \quad (2)$$

Seen from metadata, where $K_1$and K_2 stand for the band-specific thermal conversion constants. The radiant temperature is corrected by adding absolute zero (about 273.15°C) to obtain the figures in Celsius (Xu and Chen, 2004).

3.2.2 Calculating NDVI

Since NDVI can be used to infer overall vegetation condition, it is crucial to estimate it since the amount of vegetation present is a crucial element.

$$NDVI = \left(\frac{NIR-RED}{NIR+RED}\right) \quad (3)$$

In contrast to other wavelengths, healthy vegetation (chlorophyll) reflects greener and near-infrared (NIR) light. It does, however, absorb more red and blue light (GIS Geography, 2022).

3.2.3 Calculating the Proportion of Vegetation

The proportion of vegetation (Vegetation Fraction) is defined as the percentage of vegetation occupying the ground area invertical projection (Twumasi et al., 2021). The proportion of vegetation P_V is closely related to NDVI values for vegetation and soil. In this study, PV was estimated following the NDVI traditional method (Rouse et al., 1974; Twumasi et al., 2021). The NDVI algorithm makes use of the fact that dense or less green vegetation reflects more visible light and less near-IR, while green vegetation reflects less visible light and more NIR Dutta 2016).

$$P_v = \left[\frac{NDVI-NDVI_s}{NDVI_v-NDVI_s}\right]^2 \quad (4)$$

where $NDVI_v$ and $NDVI_s$ are Maximum and Minimum $NDVI$ respectively, representative of NDVI of Vegetation and NDVI of soil respectively (Bendib et al., 2017; Carlson and Ripley, 1997).

3.2.4 Calculating Land Surface Emissivity

Since LSE is a proportionality factor that scales blackbody radiance (Plank's Law) to predict emitted radiance and represents the effectiveness of transporting thermal energy across the surface into the atmosphere, it is the key component in the computation of LST (MuñozJiménez-Juan C. et al., 2006).

The emissivity calculation formula looks like this:

$$\varepsilon\lambda = \varepsilon v\lambda \mathrm{P}v + \varepsilon s\lambda\,(1 - \mathrm{P}v) + C\lambda \quad (5)$$

Where C denotes the surface roughness assumed as a constant value and $\boldsymbol{v}$ and $\boldsymbol{s}$ are the vegetation and soil emissivities, respectively (Avdan and Jovanovska, 2016).

3.2.5 Calculating LST (Land Surface Temperature)

The "surface" of the Earth would feel warm when touched in that area can be defined as LST. The "surface" is anything a satellite observes when it peers through the atmosphere to the earth. It might be ice and snow, grass on a lawn, a building's roof, or the leaves in a forest canopy. LST and the air temperature listed in the daily weather report are different" .

$$LST = \frac{T_B}{1+\left(\lambda\sigma T_B/(hc)\right)ln\varepsilon} \quad (6)$$

where: $h\ is$ Plank's constant (6.626 1034 Js), $\sigma\ is$ the Boltzmann constant (1.38 1023 J/K), $c\ \ is$ the velocity of light in a vacuum (2.998 108 m/sec), $\lambda\ is$ the effective wavelength (10.9 mm for band 10 in Landsat 8 data), and ε is the emissivity are all constants. (Guha et al., 2018; Weng et al., 2004)

3.3 Calculating SMI

Soil moisture is always an important factor in agriculture, certainly in semi-arid and arid circumstances (Arnold, 1999; Enkhjargal Natsagdorj, 2021) Determination of SMI (Soil Moisture Index) is an effective factor in biological processes and soil profile evolution. In addition, soil moisture affects vegetation distribution (Mohamed et al., 2020). The SMI has been retrieved directly according to (Moawad, 2012) using LST as follows for Landsat 8:

$$SMI = \left(\frac{LST_{max}-LST}{LST_{\max} - LST_{min}}\right) \quad (7)$$

where LST_{max}, LST_{min}, LST and are the maximum, minimum, and value of the recovered LST in turn, and SMI stands for Soil Moisture Index.

The SMI has been retrieved directly according to (Dupigny-Giroux et al., 1999; Enkhjargal Natsagdorj, 2021) for Landsat 7 as follows:

$$SMI = \frac{NIR}{VisBlue} \quad (8)$$

where band 1 is $VisBlue$ and band 4 is NIR.

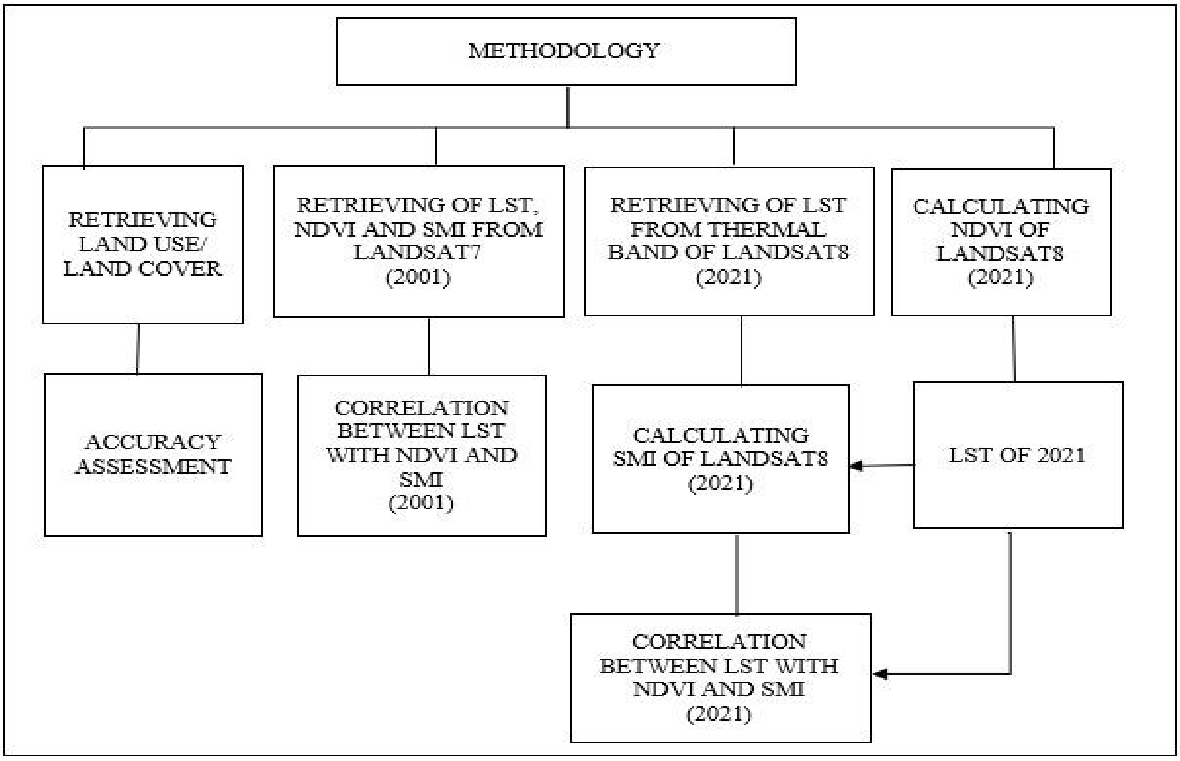

Figure 2. Flowchart of Methodology

4. Results

The increasing population has changed the land cover pattern through overexploitation of land resources for their livelihood because the population residing near forests depends on valuable timber for forest and agriculture (Bhattacharjee and Nayak 2003; Das and Joshi 2013). The pressure of increasing population and unplanned land use practices has a great impact on natural land cover. The change in land use and land cover also disturbs the other natural components of soil fertility, soil erosion, ecology, biodiversity, air quality, and water regime of the distributed area (Singh and Singh, 2016).

Kappa for 2001 was 0.91, for 2006 it was 0.92, 0.90 for 2011, 0.92 for 2016 and 0.94 for 2021.

4.1 LULC Analysis

LULC of 2001, 2006, 2011, 2016, and 2021 is described below in figure. 3, and meta data are available in Table 1. Change detection of LULC is also performed and metadata are available in Table 2.

Table 1. LULC types and their area in sq. km.

LULC Type	2001 area sq. km.	2006 area sq. km.	2011 area sq. km.	2016 area sq. km.	2021area sq. km.
Bare Soil	5223.92	4682.18	3724.76	3273.58	2710.19
Fallow land	3211.36	3392.53	3428.11	3533.49	3366.08
Settlement	1087.62	1357.71	1780.86	1998.91	2365.61
Vegetation	807.36	892.76	1394.94	1511.85	1869.46
Water body	466.92	472.00	468.51	479.35	485.84

Table 2. Change in area of LULC type

LULC Type	2001 to 2006 area changed	2006 to 2011 area changed	2011 to 2016 area changed	2016 to 2021 area changed
Bare Soil	-541.74	-957.42	-451.18	-563.39
Fallow land	181.17	35.58	105.38	-167.41
Settlement	270.09	423.15	218.05	366.70
Vegetation	85.40	502.18	116.91	357.61
Water body	5.08	-3.49	10.84	6.49

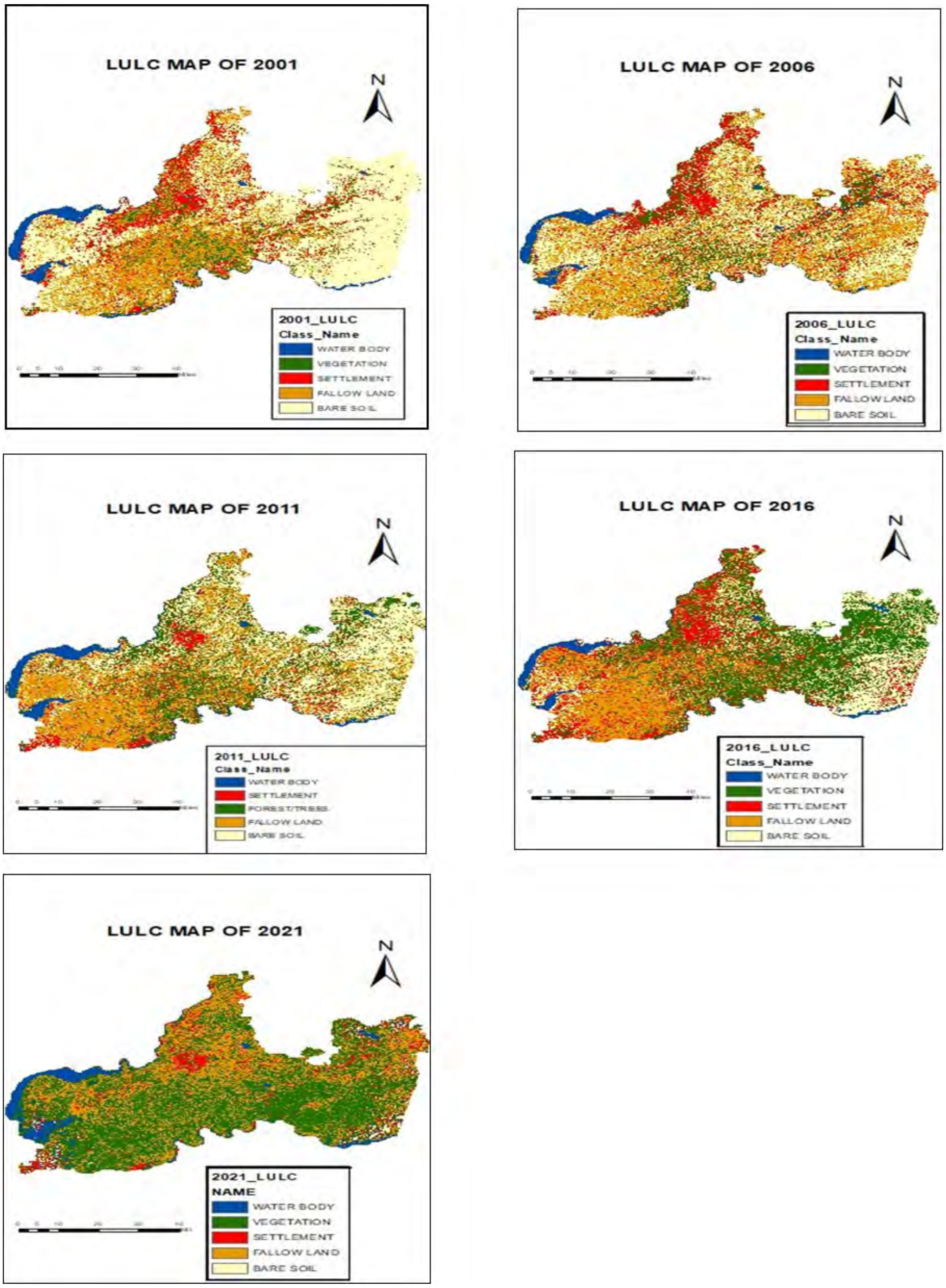

Figure 3. LULC Map of 2001, 2006, 2011, 2016, and 2021.

From the LULC maps, it can be analyzed that blue color represents water bodies, red represents settlements or built-up, vegetation is represented by green color, brown color represents fallow land and off-white color represents bare soil. From 2001 to 2006 bare land decreased, as it was replaced by settlements, especially in the urban area, and it was also replaced by fallow lands in the eastern zone of the district. Forest, big trees were replaced by settlements in urban areas. However, the existence of small shrubs and plants were noticed around settlements, roads, and other built-up areas. From 2016 to 2011 too bare land decreased and it was replaced by fallow land and settlements. Here also, small trees or plants was observed to have replaced bare soil, which were planted near new settlements and along the roadside. The same trend was observed from 2011 to 2016 and from 2016 to 2021, but, fallow lands which decreased, was replaced by vegetation. In the year 2021 vegetation is observed to be higher than in all other years, firstly because of the increasing trend of plantation and moreover due to the high amount of rainfall in 2020 post-monsoon. Rainwater increases soil moisture which may have helped in the growth of bushes and shrubs. Water bodies more or less remained constant.

4.2 Analysis of LST, NDVI, and SMI

4.2.1 LST

The distribution of LST in figure 4 illustrates that black color represents high temperature, grey represents medium temperature and white represents low temperature. The high temperature was observed in barren lands and in settlement areas. Whereas, forested areas and areas covered with vegetation and water bodies registered low temperatures

4.2.2 NDVI

The distribution of NDVI is illustrated in figure 5 Black represents high NDVI with a value near +1, grey represents medium temperature whereas white represents low NDVI with a value near -1. High NDVI was observed in agricultural lands, as well as forested areas. Whereas, barren areas and areas with fallow land, built-up areas, and water bodies prevail in low NDVI.

4.2.3 SMI

The distribution of SMI in figure 6 illustrates a value near 1 with black representing high SMI, greyresenting medium SMI, and white representing low SMI with a value near 0. High SMI was observed in agricultural lands, as well as forested areas. Low SMI prevails in the settlement and fallow land areas.

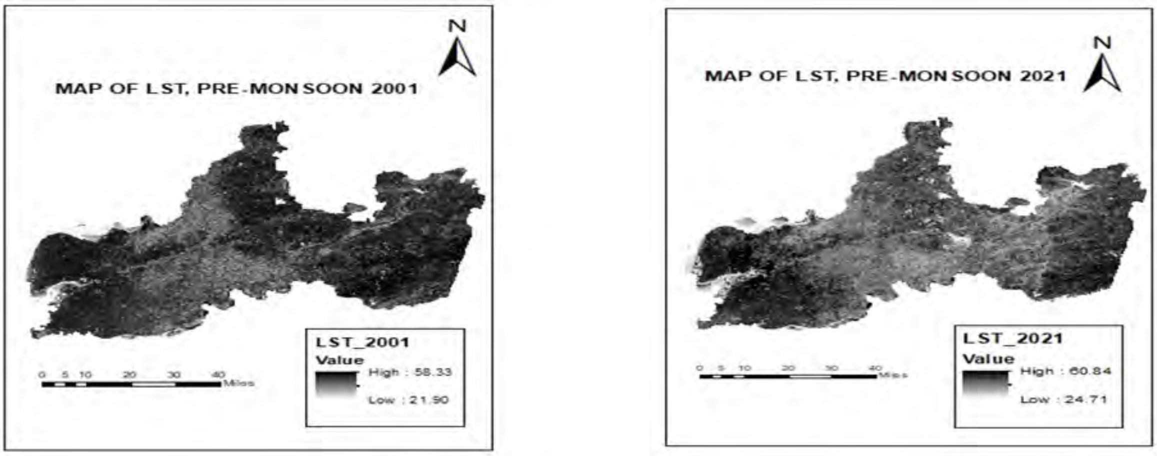

Figure 4. LST Map of 2001 and 2021

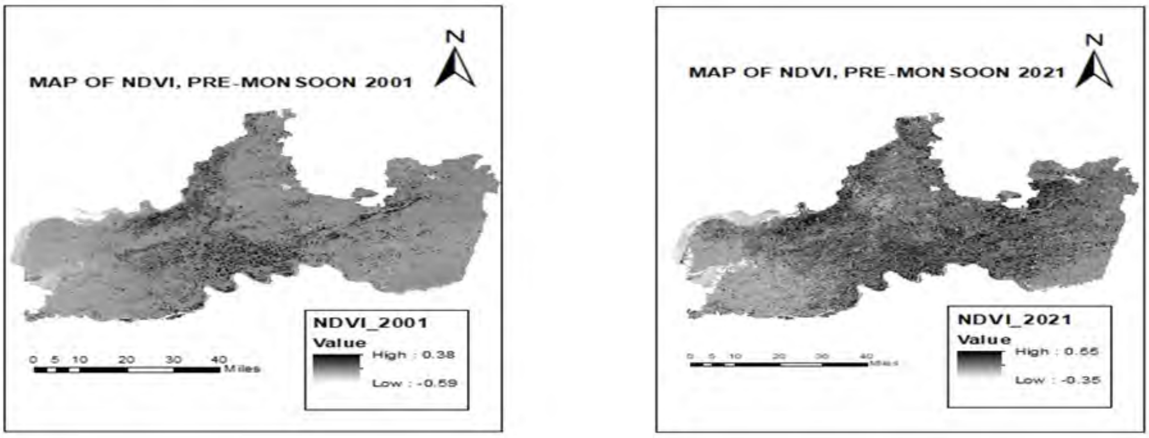

Figure 5. NDVI Map of 2001 and 2021

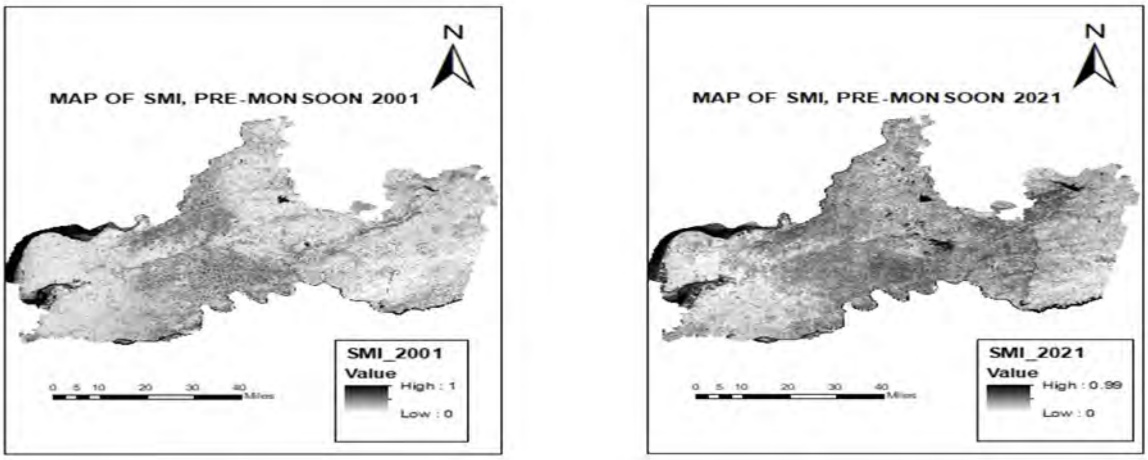

Figure 6. SMI Map of 2001 and 2021

4.3 Correlation between LST with NDVI and SMI

In 2001 high value of LST was observed to be 58.33 ℃ and the low value was 21.90 ℃. In 2021 the high value of LST changed to 60.84 ℃ and the low value changed to 24.71 ℃. In the case of NDVI in 2001 the high value was recorded as 0.38 and the low value as -0.59 and in 2021 the high value changed to 0.55 and the low value changed to -0.35. The high value of SMI was 1 and the low value was 0 in 2001. The high value of SMI was 0.99 and the low value was 0 in 2021. In 2001 mean LST was 36.33° C and mean NDVI was -0.23 and the mean value of SMI was 0.51 whereas in 2021 mean LST increased to 39.76. On the other hand, the mean value of NDVI increased from -0.23 to 0.19. Moreover, the mean value of SMI increased to 0.68. This study has analyzed the Land Surface Temperature of the Vadodara district of Gujarat in the years 2001 (pre-monsoon) and 2021 (pre-monsoon). The results indicated that the eastern zone with barren hilly rugged hills and fallow lands in the southwestern zone is distributed by high Land Surface Temperature (LST) and the central zone and the northeastern zone are distributed by low LST owing to the existence of high vegetation as agriculture is practiced in settlement areas as well as areas adjacent to rivers and water bodies. It is also noticed that vegetation and water body is inversely related to LST and built-up and bare soil has a positive relationship with LST. Furthermore, it is crucial to note that LST is impacted by urban growth and that vegetation is seen as a key role in reducing the intensity of urban heat islands. The Correlation is depicted in figure 7.

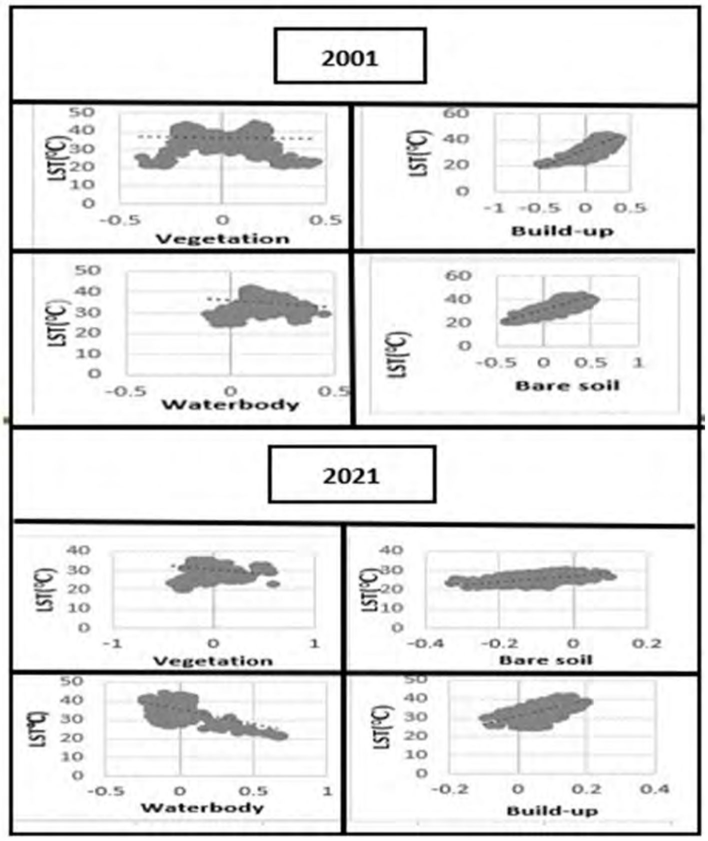

Figure 7. Correlation between LST with vegetation, built-up, water-body and bare soil (2001, 2021)

5. Conclusion

The LST distribution of the Vadodara district was characterized by a warmer western and eastern zone and a cooler zone adjacent to water bodies and areas occupied by vegetation. Mean LST over the period of 20 years increased by just 3ºC. For the study purpose, LST NDVI and SMI had been utilized. Normalized difference vegetation index (NDVI) is a vegetation identifier in the area that is purposefully utilized in the study to find the relationship with LST (Deng et al., 2018). It was observed that the value of NDVI increased from 2001 to 2021 in the Vadodara district. It was also analyzed that Soil Moisture Index was high where there existed high vegetation. A value close to zero indicates water deficiency and a value near 1 indicates a forested area that has more moisture compared to the rest of the land cover. Wet soil increases evaporate fraction, lowering the surface temperature and thereby decreasing the longwave radiation emitted by the surface. (Ballinas and Barradas, 2016) explains that 24 large trees can reduce air temperature by two degrees (Rushayati et al., 2018). The initiatives taken by the Gujarat government have helped to increase the vegetation cover over the period. Social forestry programs/schemes for like planting in strip lands like, along the roadside, railway side, and canal banks, planting in degraded lands, government wastelands, check to gaze in villages, fruit tree plantations through farmer's participation, Rehabilitation of Degraded Farm Land (RDFL) helped in increasing the ratio of vegetation cover in Vadodara district (Principal Chief Conservator of Forest and Head of the Forest Force (HoFF), 2020). It was also observed that Drip Irrigation was created in Gaucher Land and Barren Hillocks Land. Narmada Irrigation Project has helped in the adoption of horticulture crops, fruits, and vegetables by farmers. About 10 hectares of land have been collectively dedicated to growing grapes in Savli village in the Vadodara district, and the early results are comparable to those of any other region of the nation (Thakkar, 2013). Trees and vegetation lower surface and air temperature by lowering surface and air temperatures by providing shade and evapotranspiration. The Soil Moisture index is an important parameter for the production of vegetation. Hence, if proper care is taken for mother earth by increasing plantations Global Warming can be controlled. May the study prove useful for urban planners to mitigate the accelerating LST by reducing some of the impacts of urban development.

Acknowledgment

The authors are grateful to SHODH- ScHeme of Developing High quality research, Education Department, Gujarat State for the fellowship provided.

References:

Arnold J.E. (1999). *SOIL MOISTURE*. https://weather.msfc.nasa.gov/landprocess/

Avdan U. and G. Jovanovska (2016). Algorithm for automated mapping of land surface temperature using LANDSAT 8 satellite data. *Journal of Sensors, 2016*. https://doi.org/10.1155/2016/1480307

Ballinas, M. and V.L. Barradas (2016). The Urban Tree as a Tool to Mitigate the Urban Heat Island in Mexico City: A Simple Phenomenological Model. *Journal of Environmental Quality*, *45*(1). https://doi.org/10.2134/jeq2015.01.0056

Barnes K., J. Morgan, M. Roberge and S. Lowe (2001). Sprawl Development: Its Patterns, Consequences, and Measurement. *Annals of Physics*, *54*.

Barsi J. A., J.R. Schott, S.J. Hook, N.G. Raqueno, B.L. Markham and R.G. Radocinski (2014). Landsat-8 thermal infrared sensor (TIRS) vicarious radiometric calibration. *Remote Sensing*, *6*(11). https://doi.org/10.3390/rs61111607

Bateni S. M. and D. Entekhabi (2012). Relative efficiency of land surface energy balance components. *Water Resources Research*, *48*(4). https://doi.org/10.1029/2011WR011357

Bendib A., H. Dridi and M.I. Kalla (2017). Contribution of Landsat 8 data for the estimation of land surface temperature in Batna city, Eastern Algeria. *Geocarto International*, *32*(5). https://doi.org/10.1080/10106049.2016.1156167

Bhattacharjee P.R and P. Nayak (2003). Socio-economic rationale of a regional development council for the Barak Valley of Assam. *Journal of NEICSSR*, *27(1)*, 13–26. https://www.researchgate.net/publication/267765309_A_remote_sensing_study_for_land_cover_change_in_south_Assam_India

Carlson T. N. and D.A. Ripley (1997). On the relation between NDVI, fractional vegetation cover, and leaf area index. *Remote Sensing of Environment*, *62*(3). https://doi.org/10.1016/S0034-4257(97)00104-1

Chapman L. and J.E. Thornes (2003). The use of geographical information systems in climatology and meteorology. *Progress in Physical Geography*, *27*(3). https://doi.org/10.1191/0309133303767888464

Das P., & S. Joshi. (2013). A remote sensing study for land cover change in south Assam, India. *Earth Science India*, *6 (lll)*, 136–146. https://www.researchgate.net/publication/267765309_A_remote_sensing_study_for_land_cover_change_in_south_Assam_India

Deng, Y., S. Wang, X. Bai, Y. Tian, L. Wu, J. Xiao, F. Chen and Q. Qian. (2018). Relationship among land surface temperature and LUCC, NDVI in typical karst area. *Scientific Reports*, *8*(1). https://doi.org/10.1038/s41598-017-19088-x

Dupigny-Giroux, L. and J. E. Lewis. (1999). A Moisture Index for Surface Characterization over Semi-Arid Area. *Photogrametric Engineering Remote Sensing*, *65*(8), 937–945. https://www.asprs.org/wpcontent/uploads/pers/1999journal/aug/1999_aug_937-945.pdf

Dutta R. (2016). *Review of Normalized Difference Vegetation Index (NDVI) as an Indicator of Drought*.

Dyras I., H. Dobesch, E. Grueter, A. Perdigao, O.E. Tveito, J.E. Thornes, F. van der Wel and I. Bottai (2005).

The use of Geographic Information Systems in climatology and meteorology: COST 719. *Meteorological Applications*, *12*(1). https://doi.org/10.1017/S1350482705001544

Enkhjargal Natsagdorj. (2021). *Soil moisture analysis using remotely sensed data in the agricultural region of Mongolia* [GHENT UNIVERSITY]. https://www.researchgate.net/publication/351225146_Soil_moisture_analysis_using_remotely_sensed_data_in_the_agricultural_region_of_Mongolia

Estes J. and Jensen. (1998). Development of remote sensing digital image processing systems and raster GIS. *The History of Geographic Information Systems. Longman, New York*, 163–180.

Feizizadeh B. and T. Blaschke (2012). Thermal remote sensing for land surface temperature monitoring: Maraqeh County, Iran. *International Geoscience and Remote Sensing Symposium (IGARSS)*. ttps://doi.org/10.1109/IGARSS.2012.6350808

GIS Geography. (2018). What is NDVI (Normalized Difference Vegetation Index)? *Web Page GIS Geography*.

GIS Geography. (2022). *What is NDVI (Normalized Difference Vegetation Index)?* https://gisgeography.com/ndvi-normalized-difference-vegetation-index/

Gonzalez R.R. (2021). *Landsat 8 satellite data-based estimation of soil moisture in McMurdo Dry Valleys, Antarctica*. https://run.unl.pt/bitstream/10362/113892/1/TGEO0270.pdf

Guha, S., H. Govil, A. Dey and N. Gill (2018). Analytical study of land surface temperature with NDVI and NDBI using Landsat 8 OLI and TIRS data in Florence and Naples city, Italy. *European Journal of Remote Sensing*, *51*(1). https://doi.org/10.1080/22797254.2018.1474494

Guillevic P. C., J.L. Privette, B. Coudert, M.A. Palecki, J. Demarty, C. Ottlé and J.A. Augustine (2012). Land surface temperature product validation using NOAA's surface climate observation networks-scaling methodology for the visible infrared imager radiometer suite (VIIRS). *Remote Sensing of Environment*, *124*. https://doi.org/10.1016/j.rse.2012.05.004

https://www.business-standard.com/article/economy-policy/narmada-water-changing-crop-pattern-in-the-region-105021601093_1.html

Igbokwe J.I, I.C. Ezeomedo and J. Ejikeme (2013). Identification of Urban Sprawl Using Remote Sensing and GIS Technique: A Case Study of Onitsha and Its Environs in South East Nigeria. *Environmental Science, Mathematics*, *2*, 41–49.

Jin, M, R. E. Dickinson and A.M. Vogelmann (1997). A comparison of CCM2-BATS skin temperature and surface-air temperature with satellite and surface observations. In *Journal of Climate* (Vol. 10, Issue 7).

Li, Z. L., B.H. Tang, H. Wu, H. Ren, G. Yan, Z. Wan, I.F. Trigo and J.A. Sobrino (2013). Satellite-derived land surface temperature: Current status and perspectives. In *Remote Sensing of Environment* (Vol. 131). https://doi.org/10.1016/j.rse.2012.12.008

Lillesand, T.M. and R.W. Kiefer (1979). Remote sensing and image interpretation. *Remote Sensing and Image Interpretation*. https://doi.org/10.2307/634969

Moawad B.M. (2012). *Geoscience general tool package*. https://www.sciencedirect.com/science/article/pii/S1110982318304551#b9045

Mohamed E. S., A. Ali, M. El-Shirbeny, K. Abutaleb and S. M. Shaddad (2020). Mapping soil moisture and their correlation with crop pattern using remotely sensed data in arid region. *Egyptian Journal of Remote Sensing and Space Science*, *23*(3). https://doi.org/10.1016/j.ejrs.2019.04.003

MuñozJiménez- Juan C., S. José A., G. Alan, S. Donald and W.T. Gustafson. (2006). Improved land surface emissivities over agricultural areas using ASTER NDVI. *Remote Sensing of Environment*, 474–487.

Nasar U and M. Minallah (2020). Exploring the Relationship between Land Surface Temperature and Land Use Change in Lahore Using Landsat Data. *Pakistan Journal of Scientific and Industrial Research Series A: Physical Sciences*, *63*(3). https://doi.org/10.52763/pjsir.phys.sci.63.3.2020.188.200

Principal Chief Conservator of Forest & Head of the Forest Force (HoFF), G. of G. (2020). *Schemes*. https://forests.gujarat.gov.in/schemes-details.htm

Quattrochi, D. A. and J. C. Luvall (1999). Thermal infrared remote sensing for analysis of landscape ecological processes: Methods and applications. *Landscape Ecology*, *14*(6). https://doi.org/10.1023/A:1008168910634

Rouse J.W., R.W. Haas, J.A. Schell, D.W. Deering and J.C. Harlan (1974). *Monitoring the Vernal Advancements (Greenwave Effect) and Retrogradation of Natural Vegetation*. https://ntrs.nasa.gov/citations/19740022555

Rushayati, S. B., A.D. Shamila and L.B. Prasetyo (2018). The Role of Vegetation in Controlling Air Temperature Resulting from Urban Heat Island. *Forum Geografi*, *32*(1). https://doi.org/10.23917/forgeo.v32i1.5289

Saha A., M. Patil, V.C. Goyal and D.S. Rathore (2018). *Assessment and Impact of Soil Moisture Index in Agricultural Drought Estimation Using Remote Sensing and GIS Techniques*. https://doi.org/10.3390/ecws-3-05802

Shah D. B., M.R. Pandya, H.J. Trivedi and A.R. Jani (2012). Estimation of minimum and maximum air temperature using MODIS data over Gujarat. In *Journal of Agrometeorology* (Vol. 14, Issue 2).

Singh R.P. and N. Singh. (2016). Normalised Difference Vegetation Index (NDVI) Based Classification to Access the Change in Land Use/Landcover (LULC) in Lower Assam, India. *School of Environmental Science*. https://www.researchgate.net/publication/315943042_Normalized_Difference_Vegetation_Index_NDVI_Based_Classification_to_Assess_the_Change_in_Land_UseLand_Cover_LULC_in_Lower_Assam_India

Sobrino J. A., J.C. Jiménez-Muñoz, P.J. Zarco-Tejada, G. Sepulcre-Cantó and E. de Miguel(2006). Land surface temperature derived from airborne hyperspectral scanner thermal infrared data. *Remote Sensing of Environment*, *102*(1–2). https://doi.org/10.1016/j.rse.2006.02.001

Thakkar M. (2013, March 1). Narmada water changing crop pattern in the region. *Business Standard*.

Tomlinson C. J., L. Chapman, J.E. Thornes and C. Baker (2011). Remote sensing land surface temperature for meteorology and climatology: A review. In *Meteorological Applications* (Vol. 18, Issue 3). https://doi.org/10.1002/met.287

Twumasi Y. A., E.C. Merem, J.B. Namwamba, O.S. Mwakimi, T. Ayala-Silva, D.B. Frimpong, Z.H. Ning, A.B. Asare-Ansah, J.B. Annan, J. Oppong, P.M. Loh, F. Owusu, V. Jeruto, B.M. Petja, R. Okwemba, J. McClendon-Peralta, C.O. Akinrinwoye and H.J. Mosby (2021). Estimation of Land Surface Temperature from Landsat-8 OLI Thermal Infrared Satellite Data. A Comparative Analysis of Two Cities in Ghana. *Advances in Remote Sensing*, *10*(04). https://doi.org/10.4236/ars.2021.104009

Voogt, J. A. and T.R. Oke (2003). Thermal remote sensing of urban climates. *Remote Sensing of Environment*, *86*(3). https://doi.org/10.1016/S0034-4257(03)00079-8

Weng, Q., D. Lu and J. Schubring (2004). Estimation of land surface temperature-vegetation abundance relationship for urban heat island studies. *Remote Sensing of Environment*, *89*(4). https://doi.org/10.1016/j.rse.2003.11.005

Xu H. Q. and B.Q. Chen (2004). Remote sensing of the urban heat island and its changes in Xiamen City of SE China. *Journal of Environmental Sciences*, *16*(2).

Yadav, K. K., N. Gupta and V. Kumar (2016). Remote Sensing and Geographical Information System (GIS) and Its Applicationn in Various Fields. *American String Teacher*, *66*(1).

Yuvaraj R. M. (2020). Extents of Predictors for Land Surface Temperature Using Multiple Regression Model. *Scientific World Journal*, *2020*. https://doi.org/10.1155/2020/3958589

The Study of Heavy Metal Contamination in Industrial Soils of Aurangabad Using GIS Techniques

V.B. Kadam[1*], A.V. Tejankar[1], and S.K. Sirsat[2]
[1] Department of Geology, Deogiri College, Aurangabad, Maharashtra, India-431005
[2]Department of Geology, Government Institute of Science, Aurangabad, Maharashtra, India-431004
*Email: kadamvishranti@gmail.com

(Received: 18 March 2022, Accepted in final form: 20 November 2022)

DOI- *https://doi.org/10.58825/jog.2023.17.1.73*

Abstract: The main objective of the present study is to assess the level of contamination, source identification, and health risk assessment of heavy metals in the industrial soils of Aurangabad. A total of 15 Soil samples were collected with a sampling density of 3–5 composite soil samples from 0–10 cm surface soil, analyzed heavy metals (Ni, Pb, Cd, Zn, Cr, Mn, Fe, and Cu) using atomic absorption spectroscopy. The geographical information system (GIS) technology like Kriging and inverse distance weighted interpolation (IDW) was used for the preparation of spatial distribution maps. A significant spatial relationship was found for Ni, Cd, Zn, Pb, and Cu in the soils using a GIS-based analysis, suggesting that these metal contaminants in the industrial area had common sources. Assess the risks of contamination for heavy metals in the soil were assessed based on a geo-accumulation index (Igeo) and contamination factor (CF). According to the Igeo and CF, most of the samples vary between 0 to 1, unpolluted to moderately polluted except Cd values. Most of the measured heavy metals showed the highest availability in top soils collected from around the steel and metal industries of the Waluj MIDC area. Also, based on the outcomes of the health risk assessment, particular attention should be paid to Ni, Pb, Cd, Zn, Cr and Cu in the industrial soils of Aurangabad. This study is socially beneficial for prevailing human health hazards in such industrially populated regions.

Keywords: Geo-accumulation index, GIS, Heavy metals, Pollution, Soil

1. Introduction

Soil contamination is now a global problem, owing primarily to intensive industrialization, urbanization, and transportation (Nazzal et al., 2015; Wieczorek et al., 2020). Soil pollution by potentially heavy metals represents one of the major problems for the sustainable development of urban areas. The amounts of heavy metals in soil are harmful to human health and they enter the human body, affecting directly or indirectly by ingestion and inhalation. The heavy metal concentrations of groundwater (Deshpande et al., 2013) and soils (Bikkad et al., 2008) have been studied in Aurangabad. According to Maharashtra pollution control boards (MPCB-2020) suggests that different Action plans for the Responsible Stake Holders were studied. Many kinds of research on the fate and transport of heavy metals in soil, as well as the remediation of polluted soils, have all been solving this issue extensively (Ma et al., 2015, Hou et al., 2016). For regional soil quality assessment, a growing number of researchers have used integrated geographical information systems (GIS) and multivariate analysis in recent years (Ali et al., 2016; Huang et al., 2015, Hou et al., 2017, Lin et al., 2016; Mihailovic et al., 2015, Moore et al., 2016; Zhou et al., 2016). This can be attributed in part to the use of specialized software that can handle enormous spatial data sets in GIS. GIS and GIS-based geo- statistics have proven to be effective tools. (Hooker & Nathanail, 2006).

Consequently, attempts to carry out a detailed survey of Aurangabad's urban soils using a systematic sampling technique have been limited. Furthermore, only a few studies have used a GIS-based technique to analyze heavy metal contamination in an urban environment, and there has not been a GIS-based investigation of soil quality in Aurangabad.

The main objective of the present study is to assess the heavy metal contamination of the topsoil based on a geo-accumulation index (Igeo), contamination factor (CF), correlation matrix and, to assess the possible sources and hotspots of heavy metal contamination in industrial soil samples in the study area using GIS techniques. The spatial distribution maps deciphering different zones of heavy metal concentration in the soil were generated in the GIS environment.

2. Materials and methods

2.1 The study area and sampling sites

The study area belongs to the City of Aurangabad coordinates 19° 53' 47"N, 75° 23' 54"E (Figure 1). In Aurangabad, the geological formations from the Deccan basaltic flow of the upper cretaceous to the lower Eocene age. The lava flows are overlain by thin alluvial deposits. The basaltic flows represent Deccan trap-rocks, which are two distinct units. The uppermost is vesicular basalt and amygdaloidal basalt. The bottom-most is massive basalt. The soil of the study area, mainly from an igneous rock, is a black and calcareous type having different depths (Deshpande, 2012). Aurangabad consists of three industrial areas, namely Waluj- Chikhalthana- Shendra Industrial Zone. For smaller-scale site-specific soil contamination investigations, sample locations are often chosen based on professional judgment, to determine the soil contamination within the 15 number sampling locations. As shown in figure 1, the three major MIDC (Maharashtra industrial development corporation) areas, Aurangabad have been selected for soil sampling sites, collecting multiple sub-samples to render composite samples are chosen randomly at the depth of 0-10 cm using a stainless-steel spatula. At each sampling location, composite samples are typically obtained from several sub-sampling points and combined (Li et al., 2004). Because the distribution of heavy metals in the soil is extremely varied from the micro to mesoscale, this technique is widely used.

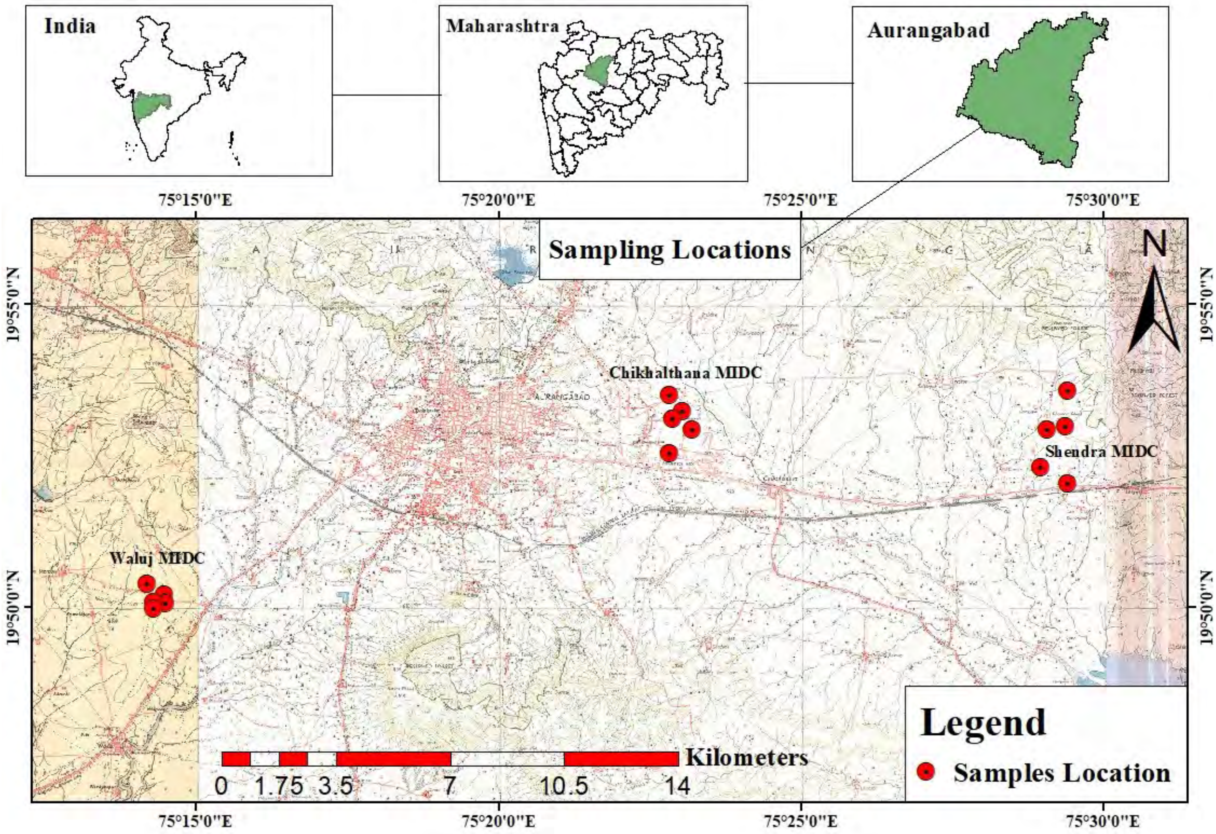

Figure 1. Location map of the study area and sample location

2.2 Heavy metal analysis

The soil samples were analyzed for heavy metal concentrations using a strong acid digestion method (Siaka et. al, 1998). Approximately 1 gm of the soil samples were weighed and placed into pre-cleaned 250 ml Beakers separately. Concentrated hydrochloric acid (HCl) and concentrated nitric acid (HNO3) acid were added in a ratio of 3:1. The mixtures were heated until they were completely transparent. After cooling, the resultant solution was filtered using Whatman filter paper no. 42 and into a 50 ml dilute to 50 ml volumetric flask and diluted to mark volume using double distilled water. Metal concentrations of the solutions were measured using an Atomic Absorption Spectrometer (Chemito Analyst Instrument 300).

2.3 Geo-accumulation Index

The geo-accumulation Index (Table 1), a quantitative measure of the degree of pollution in soil, the method assesses the degree of metal pollution in terms of seven enrichment classes based on the increasing numerical values of the index.

This index is calculated by following equation (1)

$$I_{geo} = log_2\left(\frac{C_n}{1.5\times B_n}\right)\text{-------}\ (1)$$

Where Cn is the concentration of a given element in the soil and Bn is the average background value described by Stoffers et al. (1986). The constant 1.5 factor is used because of to minimize the effect of possible variations in the background values due to lithogenic effects. The following descriptive classification is known for the index of geo-accumulation by (Salomons and Forstner, 1984).

Table 1. Classification of samples in terms of enrichment factor and geo-accumulation

I-geo Value	Class	Qualification of material
< 0	0	Unpolluted
0-1	1	From unpolluted to moderately polluted
1-2	2	Moderately polluted
2-3	3	From moderately polluted to strongly polluted
3-4	4	strongly polluted
4-5	5	From strongly polluted to extremely polluted
>5	6	Extremely polluted

2.4 Contamination Factor (Cf)

The assessment of soil contamination was accomplished using the contamination factor. The CF is the single element index of the environment and all four classes are recognized. In the version suggested by Hakanson (1980), they enable the ratio of the concentration of that heavy metal in the sample to the respective mean values or background concentration of the metal for the natural environment. Mathematically, this factor is given by following equation (2).

$$CF = \frac{Csample}{Cbackground} \text{------- (2)}$$

The following terminologies are used to describe the contamination factor according (Hakanson (1980):

CF <1 low contamination factor
1≤CF<3 moderate contamination factor
3≤CF<6 considerable contamination factor
CF≥6 very high contamination factor

2.5 GIS and spatial analysis

The heavy metal concentrations were used as the input data to study the distribution of metals in the urban soils. A geo-statistics method Kriging and inverse distance weighted (IDW) method was adopted for the interpolation of geographical data for assessed heavy metal (Table 2).

The Spatial distribution maps that were obtained were then overlaid in GIS with other geographical features such as roads. Arc GIS 10.3 was used to conduct the spatial analysis for the current study. GIS was used in this study in the following aspects: (a) to locate the sampling locations in the study area (Figure 1). (b) To generate spatial distribution maps showing polluted areas of heavy metal contamination in soils (Figure 2-9).

Table 2. Using Interpolation Techniques for Various heavy metals

Element	Interpolation Techniques
Nickel (Ni)	IDW method
Lead (Pb)	IDW method
Cadmium (Cd)	IDW method
Zinc (Zn)	IDW method
Chromium (Cr)	Kriging method
Manganese (Mn)	IDW method
Iron (Fe)	IDW method
Copper (Cu)	Kriging method

3. Results and Discussion

3.1. Heavy metal concentrations in soil

Assessment of heavy metal concentrations with Ni, Pb, Cd, Zn, Cr, Mn, Fe, and Cu in the industrial soils of Aurangabad was assessed and their spatial distribution was compared with heavy metal concentration in the earth's crust (Mason & Moore, 1982), (Table 3). The Ni varied from 66.32 - 161.23 ppm, Pb varied from 9.56 -18.23 ppm, Cd varied from 0.15 -0.80 ppm, Zn 61.20 - 140.30 ppm, Cr 113.10 - 168.08 ppm, Mn varied from 1262.32 -1834.16 ppm, Fe varied from 79500.4000 -86600.3000 ppm, and Cu varied from 90.02 -134.74 ppm. The heavy metal concentration in the industrial soil is in descending order as Fe>Mn>Cr>Ni>Zn>Cu>Pb>Cd. The obtained results of the studied area of heavy metals were higher than the background values of the volcanic rocks according to Mason & Moore (1982).

Based on these values it is expected that Ni, Cd, Cr, Fe, And Cu are dominated by natural sources whereas Pb and Zn are likely to be affected by Anthropogenic sources (Ramdani et al., 2018). Fe is abundant in natural soils, it has been used as an indicator of lithogenic origin in multivariate statistical analysis results (Kinniburgh et al., 1976). Depending on the location, different heavy metals may be attributed to natural sources. For instance, Li et al. ascribed Cd, Co, and Cr concentrations to natural sources, whereas, Shan et al. ascribed Cu, Ni, and Cr concentrations to natural sources. Facchinelli et al. also made this conclusion for Crand Ni concentrations. It is concluded that multivariate statistical analysis techniques are effective at determining heavy metal lithogenic origins (Hou et al., 2017). The higher amount of Fe and Mn have come from steel, Iron, and poor disposal of spare parts (metallurgical sources). A study by Kubier et al. (2019) reveals that Cd comes into soil due to combustion emissions, sewage sludge, traffic, metal industry and mining, where as Cu and Zn are added from the deterioration of automobile parts (Orosun et al., 2020). Cr is one of the toxic elements found naturally from the process of weathering minerals in the earth's crust or because of industrial waste reaching the soil (Hammam et al., 2022). However, a high concentration of them causes a reduction of plants and affects human health. Waluj Industrial and Chikalthana area mainly contain Pb, Zn, Cd, Cu and Cr are like higher concentrations from an industrial process. Therefore, the source of contamination generated by metal Industries through metal emission.

The study revealed a positive correlation between Fe and 3 heavy metals (Mn, Cd, and Ni) based on the observations of the correlation matrix (Table 4). The Pearson correlation coefficient matrix identified that the pairwise linear regression, Fe concentrations positively correlated with Mn and Ni, it mentioned that the natural geogenic source. On the other hand, Fe negative or negligible correlation with Pb, Zn and Cr which replicates the anthropogenic origin (Ali et al., 2016). Cu exhibited a highly significant positive relationship with Pb (0.208), Ni (0.260), and Cr (0.025) indicating the anthropogenic source with geogenic composition. The result suggested that Cu, Pb, and Zn may come from the same source and the local industrial activities contributed greatly to the soil contamination Usually, heavy metals correlate well with the observed similarities in their spatial distributions.

Table 3. Descriptive statistics of metal concentration (ppm) with Background values of volcanic rocks

	Nickel (Ni) (ppm)	**Lead (Pb)** (ppm)	**Cadmium (Cd)** (ppm)	**Zinc (Zn)** (ppm)	**Chromium (Cr)** (ppm)	**Manganese (Mn)** (ppm)	**Iron (Fe)** (ppm)	**Copper (Cu)** (ppm)
Minimum	66.32	9.56	0.15	61.20	113.10	1262.32	79500.4000	90.02
Maximum	161.23	18.23	0.80	140.30	168.08	1834.16	86600.3000	134.74
Mean	103.5187	13.4707	0.3293	93.3060	129.2393	1390.4040	75024.233360	115.7520
Std. Deviation	26.66098	2.97833	0.22195	18.53857	19.77934	174.32496	21178.2629569	9.75255
Background Values (Mason &Moore 1982)	**76**	**7.8**	**0.15**	**86**	**114**	**1280**	**77600**	**110**

Table 4. Pearson correlation coefficient matrix for heavy metals and others properties in the industrial urban soil of Aurangabad

	Nickel (Ni)	**Lead (Pb)**	**Cadmium (Cd)**	**Zinc (Zn)**	**Chromium (Cr)**	**Manganese (Mn)**	**Iron (Fe)**	**Copper (Cu)**
Nickel (Ni)	1							
Lead (Pb)	-0.126	1						
Cadmium (Cd)	-0.055	-0.022	1					
Zinc (Zn)	-0.162	-0.092	-0.044	1				
Chromium (Cr)	-0.146	0.377	-0.444	0.551*	1			
Manganese (Mn)	0.246	-0.312	0.165	-0.234	-0.329	1		
Iron (Fe)	0.344	-0.335	0.055	-0.047	-0.052	0.121	1	
Copper (Cu)	0.260	0.208	0.104	-0.086	0.025	-0.102	0.219	1
*. Correlation is significant at the 0.05 level (2-tailed).								

Table 5. Descriptive Statistics of Igeo Index for Industrial soil

	Minimum	**Maximum**	**Mean**	**Std. Deviation**	**Skewness**
Nickel (Ni)	0.0023	0.0056014	0.0036	0.00095	1.222
Lead (Pb)	0.032	0.0601274	0.04443	0.00982332	0.663
Cadmium (Cd)	1.338	7.134815	2.9372	1.97951	1.412
Zinc (Zn)	0.002	0.00381	0.003	0.000503	1.100
Chromium (Cr)	0.002	0.0026	0.002	0.00031	1.417
Manganese (Mn)	0.0002	0.000225	0.0002	0.0000214	2.028
Iron (Fe)	0.000000003	0.000003	0.000003	0.00000071	-3.607
Copper (Cu)	0.0015	0.002235	0.00192	0.00016174	-0.887

Table 6. Descriptive Statistics of Contamination Factor for Industrial soil

	Minimum	Maximum	Mean	Std. Deviation	Skewness
Nickel (Ni)	0.873	2.122	1.363	0.351	1.222
Lead (Pb)	1.226	2.337	1.727	0.382	0.663
Cadmium (Cd)	1.000	5.333	2.196	1.480	1.412
Zinc (Zn)	0.712	1.631	1.085	0.216	1.100
Chromium (Cr)	0.992	1.474	1.134	0.174	1.417
Manganese (Mn)	0.986	1.433	1.0863	0.136	2.028
Iron (Fe)	0.001	1.116	0.967	0.273	-3.607
Copper (Cu)	0.818	1.225	1.0523	0.089	-0.887

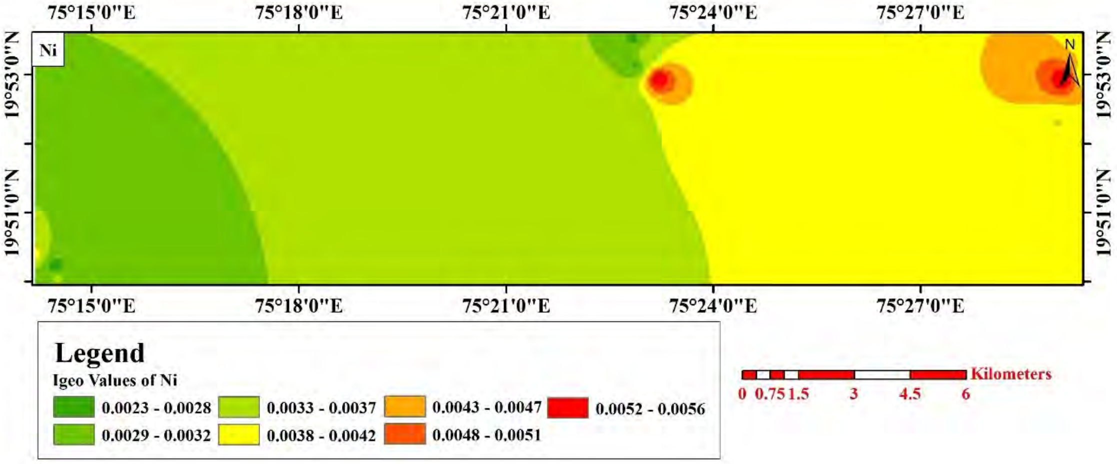

Figure 2. Spatial distribution map of Ni

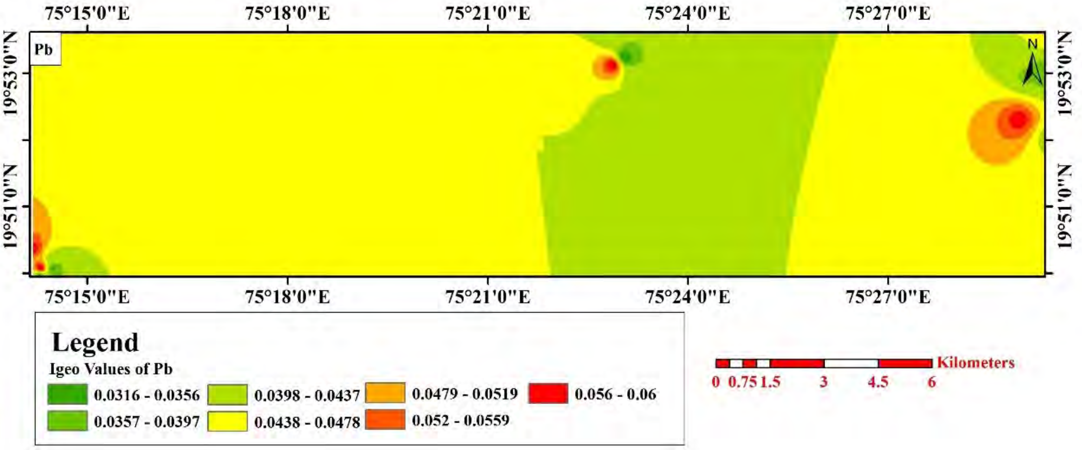

Figure 3. Spatial distribution map of Pb

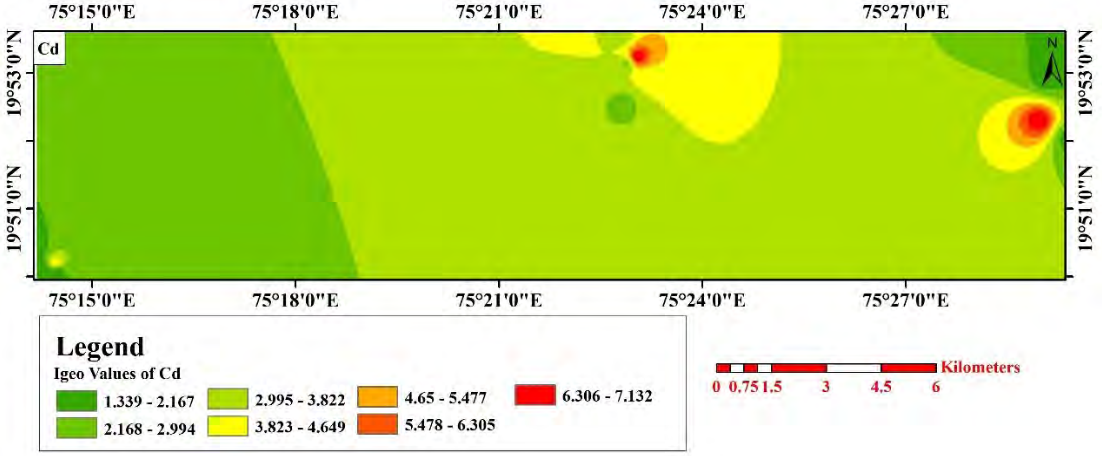

Figure 4. Spatial distribution map of Cd

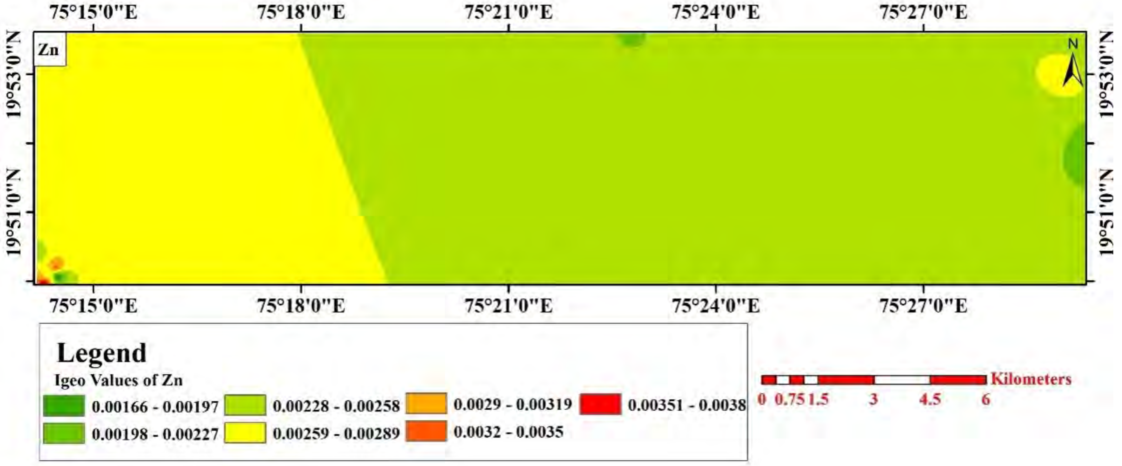

Figure 5. Spatial distribution map of Zn

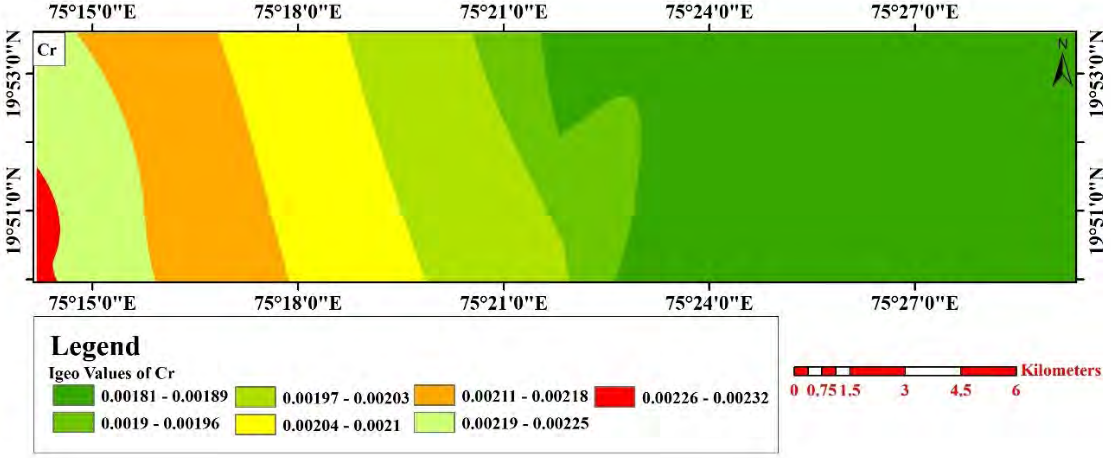

Figure 6. Spatial distribution map of Cr

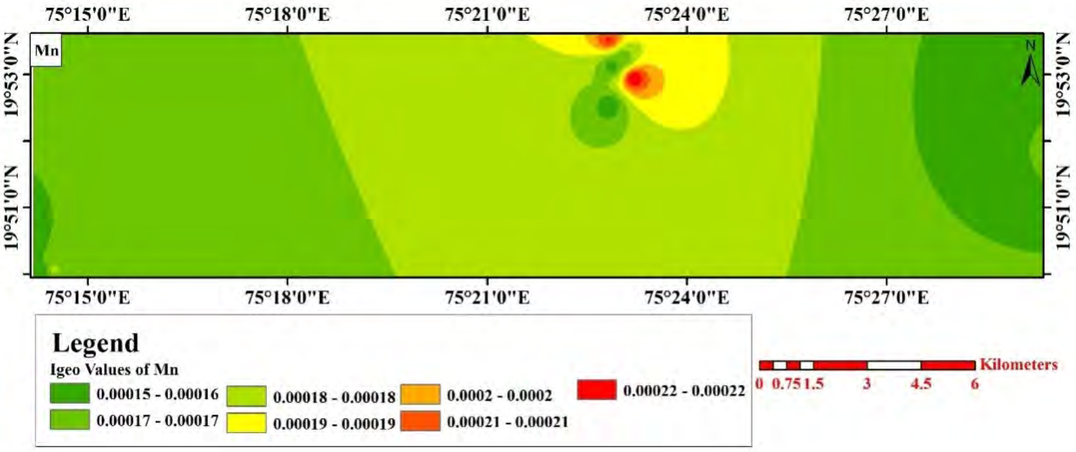

Figure 7. Spatial distribution map of Mn

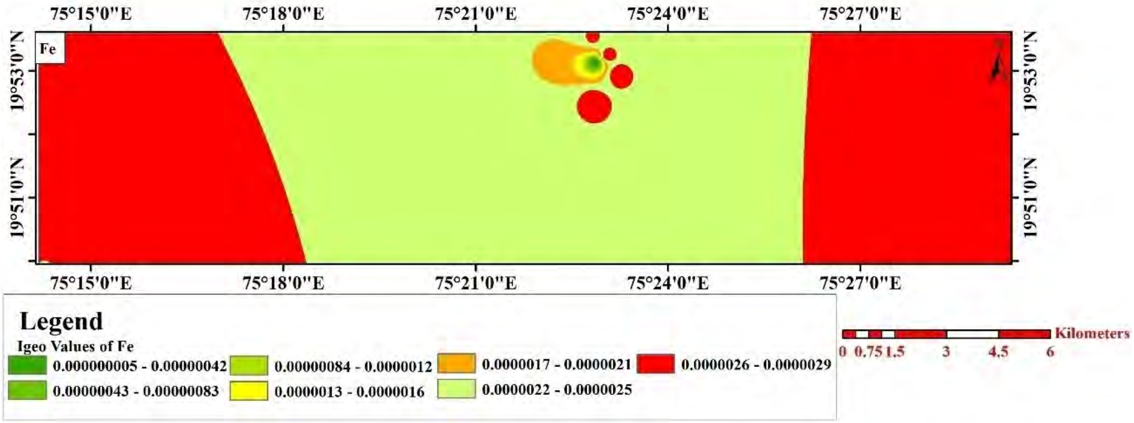

Figure 8. Spatial distribution map of Fe

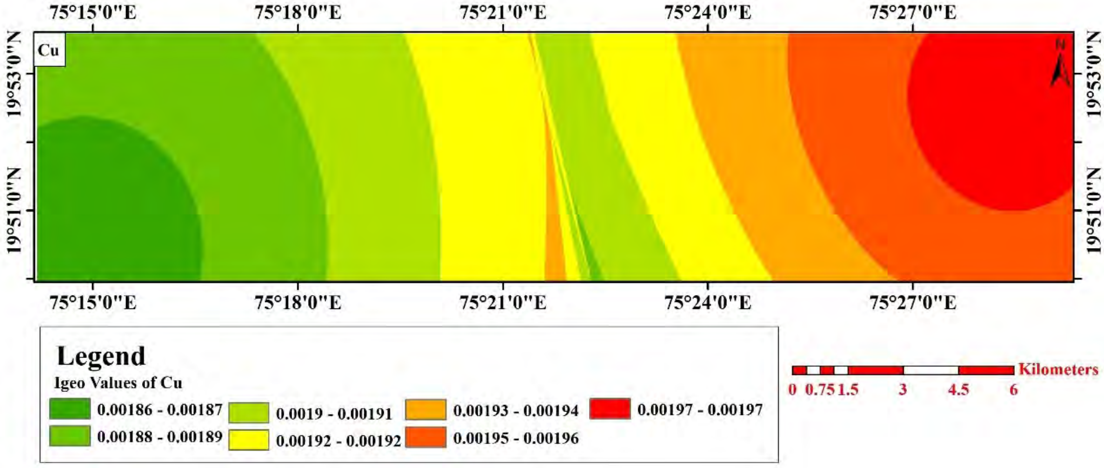

Figure 9. Spatial distribution map of Cu

3.2 Assessment of contamination risk using geo-accumulation index and contamination factor

In the present study, the contamination of soils was assessed based on the I-geo and CF. The I-geo values indicated moderately polluted by Ni, Pb, Cd, Cr, Zn, Mn, Fe, and Cu in the industrial soil. I-geo (Ni) varied from 0.0023 to 0.0056, I-geo (Pb) varied from 0.032 to 0.060, I-geo (Cd) varied from 1.338 to 7.135, and I-geo (Zn) varied from 0.002 to 0.0038, I-geo (Cr) varied from 0.002 to 0.0023, I-geo (Mn) varied from 0.0002 to 0.000225, I-geo (Fe) varied from 0.000000003 to 0.000003, and I-geo (Cu) varied from 0.0015 to 0.0022 (Table 5). The results indicate that there was no significant pollution observed in Ni, Pb, Cr, Zn, Mn, Fe, and Cu. As per the Igeo values (Igeo 1-2 Class 2), the study area belongs to unpolluted to moderately polluted for the assessed Seven heavy metals as shown in Table 5. However, there are some noticeable Igeo values of Cd (Samples I-2,10,11,12,13) indicating an extremely polluted (Igeo >5- Class 6) region.

Similarly, CF values of soil samples of the studied area are less than 1 which indicates a low contamination factor for Ni, Pb, Cr, Zn, Mn, Fe, and Cu (Table 6). The CF values of Cd is in 1≤CF<3 means moderate contamination factor but soil samples(I2,11,12) show the highest CF in between 3-5 (3≤CF<6 considerable contamination factor) present in the studied area it indicating high anthropogenic activity in the study area.

The results of Igeo and CF values of Waluj industrial soil samples show maximum values as then the Chikalthana and Shendra industrial areas. Industrial activity or anthropogenic sources like metal plating, automotive, fossil fuel combustion, and other waste is the main source of contamination of heavy metals Ni, Pb, Zn, Cd, and Cr in soil. Although the Igeo values are shown the maximum amount of Fe, Mn, and Cu heavy metals, hence it is indicating that the Shendra MIDC soil samples are less contaminated or the source of geogenic origin. This result indicates that the studied soil samples are unpolluted to moderately polluted with assessed heavy metal.

3.3 Spatial analysis using GIS

The spatial distributions of I-geo for heavy metals (Ni, Pb, Cd, Cr, Zn, Mn, Fe, and Cu) in the study area using GIS methods are illustrated in (Figure 2-9). The I-geo for heavy metals was first interpolated with the Kriging and IDW method. In general, a spatial distribution map was built up to determine the highly affected areas as well as the pollution source and several hot spots of high metal concentrations correlated to one other more than two faraway points. The lotus pond green colour represents the minimum Igeo values of soils related to the heavy metals analyzed, while the Igeo maximum values of soils are represented by the Mars Red colour. Based on the Igeo values the results shown in the spatial distribution map on the western parts of the area have the highest level of contamination while the eastern parts are clear of toxic levels of both essential trace constituents and toxic heavy elements.

This result may indicate that further monitoring of these heavy metals is required and the prevention of additional enrichment of these elements in soils requires regular protection measures.

4. Conclusion

The current study highlights the assessment of soil contamination by heavy metals in the Aurangabad industrial area. This study demonstrated the effective use of the Spatial distribution maps for predicting the hot-spot areas and assessing the potential sources of pollutants of heavy metals in the study area. Furthermore, the geo-accumulation index and contamination factor provided unconventional results in classifying the study area in significant correlation, reflecting the impacts of anthropogenic especially industrial activities.

The contamination of the soils of the study area was assessed based on the geo-accumulation index obtained for assessed heavy metals indicated unpolluted to moderately polluted. Significant contamination factors observed in the study area indicated very low contamination except for Cd. This indicates, that there were many hotspots contaminated with Cd, Cu, Pb, Fe, Mn and Cr, suggesting human causes such as long periods of industrial activities in the study area are responsible for the heavy metal pollutants.

The soil in the study area could be considered Partially or moderately polluted by heavy metals because mean values were greater than the corresponding background values of volcanic rocks. The increased levels of heavy metals in the study area are a major concern for the suitability of land management practices. Fe, Mn, and Zn concentrations are mainly inherited from parent materials, and Ni, Pb, Cr, Cd, and Zn could be affected by both geogenic and anthropogenic sources including the steel and metal industries, automotive, municipal, or industrial waste, sewage discharge, aerial pollution, etc.

The results emphasize that investigation of heavy metals might be better used for establishing environmental quality to identify the pollution source and to minimize or reduce soil contamination in the study area. Hence, this study is socially beneficial for prevailing human health hazards in such industrially populated regions.

Acknowledgment

The author V. Kadam is very grateful for the financial support from the Chhatrapati Shahu Maharaj Research Training and Human Development Institute (SARTHI), Pune (an Autonomous institute of the Government of Maharashtra) for CSMNRF-2019 fellowship funding for the Ph. D. The author would thankful to Dr. Amit Bhatpude, Junior Geologist, Groundwater Surveys and Development Agency, Aurangabad, and also grateful to the Head, Department of Geology, Government Institute of Science, Aurangabad for providing the AAS analysis facilities.

Conflict of interest

All authors declare no conflicts of interest in this paper.

References

Ali MH, ARA Mustafa and AA El-Sheikh (2016). Geochemistry and spatial distribution of selected heavy metals in surface soil of Sohag, Egypt: a multivariate statistical and GIS approach, Environmental Earth Sciences, 75, 1257.

Bikkad S.B. and SR Mirgane (2008). Assessment of heavy metals in groundwater of Aurangabad Industrial areas. Current World Environment, 3(1), 131-134.

Deshpande G.G. (2012). Geology of Maharashtra. Geological Society of India, Bangalore, pp. 156-157.

Deshpande SM, KR Aher and AA Bhatpude (2013). Heavy metal concentrations in groundwaters of Chikalthana Area of Aurangabad,India. Journal of Applied Geochemistry, 15(2), 201-212.

Hakanson L (1980). An ecological risk index for aquatic pollution control. A Sedimentological approach. Water Research, 14(8), 975-1001.

Hammam AA, WS Mohamed, SEE Sayed, DE Kucher and ES Mohamed (2022). Assessment of Soil Contamination Using GIS and Multi-Variate Analysis: A Case Study in El-Minia Governorate, Egypt. Agronomy, 12(5), 1197. https:// doi.org/10.3390/agronomy12051197

Hooker PJ and CP Nathanail (2006). Risk-based characterization of lead in urban soils, Chemical Geology, 226 (3–4), 340-351.

Hou D, Q Gu Q, F Ma and S O'Connell (2016). Life cycle assessment comparison of thermal desorption and stabilization/solidification of mercury contaminated soil on agricultural land. Journal of Cleaner Production, 139, 949-956.

Hou D, D O'Connor, P Nathanail, L Tian and Y Ma (2017). Integrated GIS and multivariate statistical analysis for regional-scale assessment of heavy metal soil contamination: A critical review. Environmental Pollution, 231, 1-13.

Huang Y, T Li, C Wu, Z He, J Japenga, M Deng and X Yang (2015). An integrated approach to assess heavy metal source apportionment in peri-urban agricultural soils. Journal of Hazardous Materials, 299, 540-549.

Kinniburgh D, M Jackson and J Syers (1976). Adsorption of alkaline earth, transition, and heavy metal cations by hydrous oxide gels of iron and aluminum. Soil Science Society of America Journal, 40(5), 796-799.

Kubier A, RT Wilkin and T Pichler (2019). Cadmium in soils and groundwater: A review. Applied Geochemistry, 108, 1-16.
https:// doi.org/10.1016/j.apgeochem.2019.104388

Li X., S Lee, S Wong, W Shi and I Thornton (2004). The study of metal contamination in urban soils of Hong Kong using a GIS-based approach, Environmental Pollution, 129(1), 113-124.

Lin WC, YP Lin and YC Wang (2016). A decision-making approach for delineating sites which are potentially contaminated by heavy metals via joint simulation. Environmental Pollution, 211, 98-110.

Ma F, C Peng, D Hou, B Wu, Q Zhang, F Li and Q Gu (2015). Citric acid facilitated thermal treatment: an innovative method for the remediation of mercury contaminated soil. Journal of Hazardous Materials, 300, 546-552.

Maharashtra Pollution Control Board (MPCB) (2020). R-2 Revised Action Plan for Industrial Cluster in Severally Polluted Areas, July, Aurangabad.

Mason B and CB Moore (1982). Principle of geochemistry, 4th ed., Willey, New York.

Mihailovic A., L Budinski-Petkovic, S Popov, J Ninkov, J Vasin, N Ralevic and MV Vasic (2015). Spatial distribution of metals in urban soil of Novi Sad, Serbia: GIS based approach. Journal of Geochemical Exploration, 150, 104-114.

Moore F, V Sheykhi, M Salari and A Bagheri (2016). Soil quality assessment using GIS-based chemometric approach and pollution indices: Nakhlak mining district, Central Iran. Environmental Monitoring and Assessment, 188, 1-16.

Nazzal YH, NSN Al-Arifi, MK Jafri, HA Kishawy, H Ghrefat, MM El-Waheidi, A Batayneh and T Zumlot (2015). Multivariate statistical analysis of urban soil contamination by heavy metals at selected industrial locations in the Greater Toronto area, Canada. Geologia Croatica, 68(2), 147–159.

Orosun MM, SA Oniku, A Peter, RO Orosun, NB Salawu and L Hitler (2020). Magnetic Susceptibility measurements and heavy metal pollution at an automobile station in Ilorin, North-Central Nigeria. Environmental Research Communications, 2(1), 015001.

Ramdani S, A Amar, K Belhsaien, S Hajjajji, S Ghalem, A Zouahri and A Douaikb (2018). Assessment of heavy metal pollution and ecological risk of roadside soils in Tlemcen (Algeria) using Flame-Atomic Absorption Spectrometry, Analytical Letters, 51(15), 2468-2487.

Salomons W and U Forstner (1984). Metals in the Hydrocycle. Springer-Verlag, Berlin Heidelberg, pp. 349.

Stoffers P, GP Glasby, CJ Wilson, KR Davis and P Walter (1986). Heavy metal pollution in Wellington Harbour. New Zealand Journal of Marine and Freshwater Research, 20(3), 495-512.

Siaka M, CM Owens and GF Birch (1998). Evaluation of some digestion methods for the determination of heavy metals in sediment samples by flame-AAS. Analytical Letters, 31(4), 703–718.

Wieczorek K, A Turek, M Szczesio and WM Wolf (2020). Comprehensive Evaluation of Metal Pollution in Urban Soil of a Post-Industrial City- A Case of Lodz, Poland. Molecules, 25(18), 4350.

Zhou J, K Feng, Z Pei, F Meng and J Sun (2016). Multivariate analysis combined with GIS to source identification of heavy metals in soils around an abandoned industrial area, Eastern China. Ecotoxicology, 25, 380-388.

Journal of Geomatics Vol.17, No.1, April 2023

Analysis of sea ice concentration and thickness over Barents Sea using standard logistic curve model

Dency V. Panicker[1], Bhasha Vachharajani[1]*, Rohit Srivastava[1] and Sandip R. Oza[2]
[1]Pandit Deendayal Energy University, Gandhinagar, Gujarat, INDIA
[2]Space Applications Centre, ISRO, Ahmedabad, Gujarat, INDIA
*Email: bhasha.vachharajani@sot.pdpu.ac.in

(Received: 2nd September 2022, Accepted in final form: 19 March 2023)

***DOI:** https://doi.org/10.58825/jog.2023.17.1.74*

Abstract: As marginal, the Barents Sea plays a major role in the process of Atlantification, and large seasonal variability in sea ice is observed over the region. Current sea ice concentration and thickness obtained from satellite help one understand the variation in sea ice is seasonal. During summer, the concentration and thickness of sea ice are seen to fall, and during winters, it is seen to rise. In order to understand the difference in these variabilities and to analyse the future state of sea ice, a standard logistic curve model is considered. The standard logistic curve model is applied to sea ice parameters during summer and winter to quantify the sea ice growth and decay processes over the Barents Sea.The model yields predicted values based on the adjustment parameter (b) used.Results show that the predicted sea ice concentration performs well with the satellite sea ice concentration values. The model is run on the timeframe grouped into two, with each set having an average of ten years from 2000-2020. For the decay process, the fitted sea ice concentration decay curves derived from the standard logistic curve model are in good agreement with the observed data for the two timelines, with r^2 = 0.88 and 0.87, respectively. Similarly, for the growth process, the relevant fitted decay curves derived from the standard logistic curve model are also in good agreement with the observed data during the above different time periods withr^2= 0.80 and 0.78, respectively. Further, the model is implied to sea ice thickness, and the result obtained by the logistic curve model is found to be consistent with the satellite sea ice thickness with r^2 = 0.75 for the years 2011–2020. Particularly, both the rapid sea ice increase pattern during the growth process and the remarkable decrease pattern during the decay process are successfully characterized by the corresponding fitted curves. The introduction of calculated adjustment parameters into the model helps in accurately determining the sea ice variables, which brings us closer to conservation tools that mitigate therisks associated with rapid sea ice loss.

Keywords: Sea ice concentration, Sea ice thickness, Barents Sea, Logistic curve model, Growth process, Decay process

1. Introduction

Earth's overall temperature warmed by 0.8 °C (Intergovernmental Panel on Climate Change, 2018) since the late 19th century, while the Arctic has warmed by 2 - 3 °C over the same span (Allen et al., 2018). Similarly, Antarctica, the coldest, windiest, and driest continent on Earth, has also experienced prominent decadal and interannual variation in mean annual temperature anomalies. The increase in temperature has caused a total ice sheet loss (Turner et al., 2019) from 40 ± 9 Gt/y in 1979–1990 (Schröder et al., 2018) to 252 ± 26 Gt/y in 2009–2017 (e.g., King & Turner, 1997). With an increase in temperature, pronounced seasonality, and the year-round presence of ice and snow, the Arctic and Antarctica may face different futures in response to topographical and geographical reasons (Meredith et al., 2019). The temperature hike due to warming is of great concern as the poles are important components of the global climate system and their changes have highly impacted ocean hydrology, atmospheric circulation, and climate change (Kim et al., 2014). Overall, one of the most visible signs of warming changes over the poles is the declining sea ice cover. Sea ice concentration and extent, which are clear indicators of sea ice cover, have decreased in all months over the past 30 years (Parkinson, 2019). Particularly during summer, the sea ice is seen to be thinning. As the thinner ice dominates the thicker ice, the younger ice type is seen to be more prevalent than the multiyear ice (Meier et al., 2014).

Due to the diverging nature (decline in sea ice occurs at different rates in different regions and seasons) of the Arctic, unlike the Antarctic in terms of its ocean influence, many scientists have projected the Arctic to be ice-free in most late summers as soon as the 2030s (Wang et al., 2009; Holland et al., 2006; Boé et al., 2010; Eisenman & Wettlaufer, 2008; Notz et al., 2009). The future of Arctic sea ice cover is of enormous climatic and economic significance (ACIA, 2005). The daily sea ice concentration data from the NSIDC shows that the sea ice concentration varies significantly between 2007 and 2012. The maximum (higher) values of sea ice concentration was reducing, while the minimum (lower) values of concentration were found to be increasing (Vázquez et al., 2016). The highest decreasing rates are mainly focused on the Beaufort, Chukchi, and East Siberian Seas (Chen & Zhao, 2017; Zhao et al., 2017). In the summer of 2010, there was a very low sea ice concentration (30%) that appeared at high Arctic latitudes, even lower than that of the surrounding pack of ice at lower latitudes (Cavalieri & Parkinson, 2012). The extent of perennial sea ice in the Arctic decreased rapidly, and in the East Arctic Ocean, it continued to be depleted with area-wise reduction of 70% from October 2005 to April 2006 (Nghiem et al., 2006). Along with concentration and extent, sea ice thickness is another key characteristic of the sea ice cover. Sea ice that are thick enough can survive the summer melt season and may last for many years. For ice to thicken, the ocean must lose heat to the atmosphere. But this thicker sea ice deteriorates the coupling between the ocean and atmosphere systems (Vella & Wettlaufer, 2008). Thicker sea ice is a strong thermal insulator; as a result, it limits heat transfer from the ocean to the atmosphere in winter and also its thermodynamic growth (Petty et al., 2018; Rösel et al., 2018). By the end of winters, thicker ice gets developed, decreasing the transmission of solar radiation to the surface ocean and reducing the potential primary productivity (Mundy et al., 2005; Katlein et al., 2015). Also, this thick sea ice is more likely to survive the melt season, increasing the average age of sea ice.

While investigating the influence of oceans over sea ice, the Barents Sea is found to be a hotspot for Arctic climate change (King et al., 2017; Lind et al., 2018; Schlichtholz, 2019; Skagseth et al., 2020), with pronounced upper ocean warming and a retreating sea ice cover over the past two decades (Sorokina et al., 2016; Screen et al., 2018). The Barents Sea is one of the marginal shelf seas of the Arctic Ocean, which surrounds the Arctic Basin. The sea is located in the European sector of the Arctic and is influenced by both Atlantic and Arctic waters. Most of the sea ice in the Barents Sea is formed locally, with a fraction imported from the Arctic Basin through the straits between Svalbard and Novaya Zemlya. The marginal ice zone in the western Barents Sea extends south to 75 -78° N in early spring and retreats to about 80-82° N in late summer. This trend has been seen extending to higher latitudes during the last 10 years (Tronstad et al., 2007). It is expected that ice cover in the Barents Sea will continue to reduce in the future also due to (i) increase in Arctic air temperature, (ii) recent increase of cyclonic activity in northern north Atlantic and associated ocean heat anomalies, and (iii) depletion of sea ice in the eastern Arctic Ocean and thus less import of thick ice into the Barents Sea region (Smedsrud et al., 2013). Additionally, air-sea temperature differences in the Barents Sea are extremely large, ocean heat release reaches values of 300-500 Wm^{-2} (Simonsen and Haugan, 1996). The Barents Sea dominates the seasonal Arctic heat budget and has the most vigorous ocean air exchange in the Arctic, making it a centre of influence on the high latitude climate system (Serreze et al., 2007). Studies suggest that the decrease in sea ice over the Barents Sea in early winter also affects cyclonic pathways in the downstream region (Inoue et al., 2012) and results in a warm Arctic pattern. The Barents Sea ice extent in winter has decreased since 1850 (Shapiro et al., 2003), and the retreat observed during recent decades has been the largest decrease in the Arctic (Parkinson & Cavalieri, 2008).

The decline in sea ice is faster than what most models have forecasted, leading to possible near-ice-free summer conditions in the coming decades. This is due to a combination of factors, including the complexity of the Arctic climate system and the difficulty of modeling the interactions between different components of the system (Walsh et al., 2017). Most climate models have predicted a decline in Arctic sea ice extent and thickness in response to increasing greenhouse gas concentrations in the atmosphere. However, the actual decline has been more rapid than what the models have projected. For example, the minimum Arctic sea ice extent in September 2020 was the second-lowest on record (Diebold et al., 2020), despite most models predicting that such low extents would not be reached until the 2030s. According to climate change experiments based on phase 5 of the Climate Model Intercomparison Project (CMIP5), the warm Arctic anomalies will continue in the future (Yang and Christensen, 2012). Additionally, a new generation of atmosphere-ocean coupled reanalysis, the National Centers for Environmental Prediction Climate Forecast System Reanalysis (NCEP CFSR), has been produced. The NCEP CFSR has benefited from advances in operational weather forecasting and previous reanalysis improvements (Bengtsson et al., 2007). The NCEP CFSR assimilates the oceanic field, including sea ice concentration. Therefore, it is expected that the predictability of the sea ice and its relation to the atmosphere and ocean variability can be examined. Similar to such models, is the Community Earth System Model (CESM), which is used to simulate the interactions between the atmosphere, oceans, land surface, and sea ice. It is used to make projections of future sea ice conditions under different climate scenarios (Danabasoglu et al., 2020). For short-term (daily to seasonal) timescale prediction, the Arctic Regional Ocean Model (AROM) is generally used (Ren et al., 2021). The Pan-Arctic Ice-Ocean Modeling and Assimilation System (PIOMAS) is used to track changes in Arctic sea ice over time and make predictions about future sea ice conditions (Zhang and Rothrock, 2003). These models are continually being refined and improved as more data becomes available and our understanding of the complex processes that govern sea ice behaviour increases. Similar to these models, one such model that can help in assessing the growth and future of sea ice conditions is the standard logistic curve model (Hui, 2006). This model had been used originally to analyse the growth of population, where the carrying capacity denoted the population size at which the population growth rate equals zero. But now, the model is being used in various fields of science (Meyer, 1994). As the model made space in every aspect of science (Bony et al., 2006), the carrying capacity now represented merely the value of a state variable at which its growth rate equals zero in a system. Researchers in the past have used this logistic curve model to understand the sea ice conditions over Antarctica (Tietsche et al., 2013) and Arctic (Bitz and Lipscomb, 1999). Over the Arctic, the model was used to study the seasonal cycle of Arctic sea ice volume.

The paper illustrates and discusses the use of the standard logistic curve model to understand the behaviour of sea ice during summers and winters. This study aims to explore and characterize a quantitative statistical model in order to better quantify and simulate the sea ice growth and decay processes in the Barents Sea during 2000-2020. The paper aims to study sea ice concentration and sea ice thickness, obtained through the model, to analyse how the sea behaves during various seasons; summer and winter. Here, the evolution of sea ice over the region, that is, from the freeze onset to its maximum attainment, is considered. These parameters further help in projecting the future of the Arctic sea ice. The model operates based on the threshold value allotted to the adjustment parameter. The model can operate on two types of adjustment parameters: one by fixing it and the other by varying it.

Here the major goal revolves around finding which value of the adjustment parameter can better fit with the satellite sea ice values, therefore offering an opportunity for predicting sea ice state on seasonal timescales. The current model aims at providing valuable information on how sea ice parameters evolve and how it will be affected by changing climate. This model can be used for long-term climate studies, short-term operational forecasts (within the duration of one year or so), and seasonal forecasts (such as during the decay and growth phases of sea ice).

2. Datasets and Methodology

For the current study, consistent monthly sea ice concentration (SIC) and sea ice thickness (SIT), of the Barents Sea of the Arctic region are considered.

2.1 Datasets

SIC data is selected from National Snow and Ice Data Center (NSIDC) (Stroeve et al., 2018) for the years 2000-2020. The spatial resolution of the data is 0.22° x 0.22°. The SIC data is retrieved based on the NASA TEAM algorithm in terms of the brightness temperature data. The accuracy of total sea ice concentration is within ± 5 % of the actual sea ice concentration in winter, and ± 15 % in the Arctic during summer when melt ponds are present on the sea ice. Accuracy tends to be best within the consolidated ice pack when the sea ice is relatively thick and ice concentration is high. Accuracy decreases as the proportion of thin ice increases (Cavalieri et al., 1996). However as the time range considered for this study is limited to just 20 years, such a decline in accuracy is irrelevant in the current case. Additionally, SIT data have also been taken from NSIDC (Kurtz and Harbeck, 2017) CryoSat-2, but for the span of 2010-2020. The spatial resolution of the SIT data is 0.22° x 0.22°. The CryoSat-2 data set contains estimates of Arctic Sea ice thickness and SIC, ice freeboard and surface roughness, as well as snow density and depth, derived from the ESA CryoSat-2 Synthetic Aperture Interferometric Radar Altimeter (SIRAL). Quality assessment of this data is done through comparison with NASA's Operation IceBridge data. Freeboard error for a 0.22° grid cell from the associated surface elevation retrieval error is estimated as ±0.065 m in comparison with IceBridge data (Kurtz and Harbeck, 2017). The shape files for the Barents Sea are extracted from Marine Regions Database. Marine Regions are generally used to create a standard, relational list of geographic names, coupled with information and maps of the geographic location of these features.

2.2 Methodology

To understand the state of sea ice prevailing over the region, satellite-observed monthly SIC and SIT are considered. After the extraction of these datasets from the aforementioned sources, they are put through pre-processing. The data is pre-processed to extract the cryospheric variables, latitudes, and longitudes. The data is further re-projected into a different coordinate system (npstere-north polar stereographic projection) corresponding to the spatial resolutions of both the datasets. Firstly, the spatio-temporal analysis of SIC is carried out. For the spatial analysis, the years 2000–2004 were considered as the background years from which the averages of 2005–2009, 2010–2014, and 2015–2019 were subtracted. The maps of the long-term average 2000–2004 SIC from 2005–2009, 2010–2014, and 2015–2019 at each location for each month were generated. However, the variability in SIC for the month of December, January, February, and March is displayed and thoroughly discussed in the upcoming section. For temporal variation of the parameter, monthly whisker plots are generated. Here, each month is represented as a box with whiskers extending the minimum and maximum values. The median is shown by a horizontal line inside the box, and the quartiles by a vertical line inside the box. Lastly, SIT is also analysed across the domain in a similar manner. The only difference between the two analyses is that SIC is carried out for all the months of the year, whereas SIT is only performed for the winter months due to the lack of availability of SIT data during the summer months. Further, SIC and SIT during the winter months, specifically January, February and March are intensely examined. Histograms with bins are considered for the ease of understanding. SIC is averaged over Barents Sea for the entire span of each month. The binning technique is used to reduce the amount of data. By using the trial-and-error method, a suitable bin size of 70 was found, which removed the insignificant lower values and helped in the representation of the growth of SIC. The selected bin size clearly depicted the intensification of SIC from lower values to higher concentrations. However, for SIT, along with the knowledge of the number of pixels lying within a particular thickness, Gaussian density plots are also extracted. In the case of SIT, the Gaussian distribution gave a better understanding as it shows the continuous distribution of data around its center. Additionally, here the mean, median and mode are equal, giving a better knowledge of the shift in the variable during each month. Furthermore, for the quantitative analysis of the variability of sea ice, the logistic growth model is used to understand the seasonal sea ice growth and decay over the Barents Sea. For better clarity and transparency of the research methodology adopted in the paper, a flow chart is illustrated in Figure 1. The logistic curve model mentioned in the flow chart, used to predict the cryospheric parameters (SIC and SIT) is elaborately explained in Section 2.2.1.

2.2.1 Standard logistic curve model

In 1838, the Logistic function was first proposed by Pierre François Verhulst in the context of population growth. Verhulst derived the logistic equation to describe the growth of the biological population (Kyurkchiev and Markov, 2015). Interestingly, Sweilam et al. (2012) assert that the logistic equation is described by a first-order ordinary differential equation. Their study resonates further with Murphy et al., 2016 who noted that the logistic equation is formalized by the differential equation. Later various modifications were made to the function to fit into various spheres of science. The mathematical equation of the standard logistic curve model is as follows:

$$Y = \frac{L}{1+be^{-kt}} \qquad (1)$$

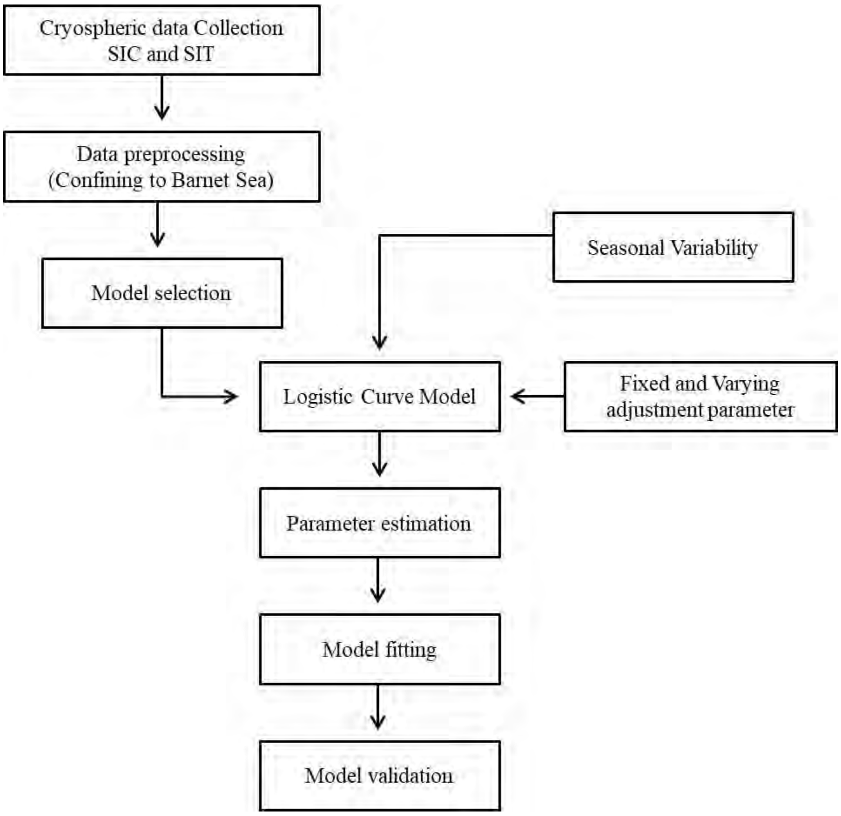

Figure 1. Flow chart describing the methodology used

In Eq. (1), 'Y' refers to the observed temporal SIC or SIT at any month (t), 'L' is the carrying capacity (in summers it is seen varying but, during winters as the Arctic region is completely frozen, L = 100% for SIC and L = 3 m for SIT), 'b' stands for the adjustment parameter, which is to be calculated from the existing parameter value given, 'e' refers to the natural logarithm base, and 'k' represents the Logistic growth rate at which the ice concentration/thickness approaches L. This model has the ability to describe the growth stage, such as formation, development, maturity, and limit, of sea ice. The carrying capacity is determined by calculating the maximum occurrences of the highest value of SIC and SIT obtained over any pixel in the Barents Sea during winter and summer in the background years (2000–2004). During winter (October–March), SIC is found to have maximum value of 100% in 2000–2004, whereas during summer (April-September), L=87%. Similarly for SIT, L = 3 m during winters. Here, only the winter season is considered, as this dataset is unavailable during summer months.

During winter the equation for SIC becomes:

$$Y = \frac{100}{1+be^{-kt}} \qquad (2)$$

And for summers the equation is, simplified as:

$$Y = \frac{87}{1+be^{-kt}} \qquad (3)$$

For SIT, eq. (1) becomes:

$$Y = \frac{3}{1+be^{-kt}} \qquad (4)$$

Using these equations, the values of b and k are calculated for each season. Further, in order to evaluate the performance of the model, statistical methods, viz., regression analyses, are performed which aid in computing its slope, intercepts, standard error, and p-value.

3. Results and discussion

3.1 Spatio-temporal variations of monthly SIC over Barents Sea

The two decades 2000–2010 and 2010–2020 are divided into four lustrums: 2001–2005, 2006–2010, 2011–2015, and 2016–2020. The first five years are considered to be the base (background years), and the other successive three sets of five years are compared with it to understand the deviation of sea ice conditions from its initial stage. Or, in other words, anomalies in all the latter three sets are found by comparing them with the average of the former span (2001–2005). Values below zero indicate that the present duration consists of more SIC than the base duration. If the values are positive (above zero), the current period could not build more SIC compared to the base. In the case of October, November, and December, the period is divided into 2000–2004, 2005–2009, 2010–2014, and 2015–2019. This is done so as to place October-December first in every winter season (for example, the timeline is taken as October 2000, November 2000, December 2000, January 2001, February 2001, and March 2001). Analyses have been carried out for all the months; however, spatial maps of SIC during December, January, February, and March are displayed in Figure 2.

During December, the contrast is predominantly found over the Barents Sea. The regions above and east of Svalbard greatly experience a disparity. The difference indicates that during 2005–2009 (Figure 2a), the sea lost immense ice. This significant variation is also found above and to the east of Novaya Zemlya. As we move towards the right, as shown in the subsequent plots, it is clearly observed that the deviation has built up. The regions around Svalbard and portions below Franz Josef have highly lost sea ice during the time span of 2010–2014 (Figure 2b). Apart from the Barents Sea, the difference is observed over the Kara and White Seas. During 2015–2019 (Figure 2c), the sea again failed to recover its lost sea ice conditions, making the contrast appear more intense. The Arctic Circle and the region near Svalbard also show a positive anomaly. December is an important month in the life cycle of Arctic sea ice in general, as it marks the beginning of the winter season in the Arctic region. During this month, the Arctic sea ice starts to freeze and form as the temperature drops. This process continues throughout the winter months, and by the end of winter, sea ice covers a large portion of the Arctic Ocean. The variation of sea ice near the land region makes one understand the land is yet to lose the heat it has absorbed during the summers. The land passes on its heat to the water nearby, causing the ice to melt away. As the latent heat capacity of water is quite high when compared to land/soil, the water tends to hold the heat for a prolonged period, which is thereafter passed to the nearby portions through the process of conduction with the help of wind and currents. This ultimately causes the ice to melt drastically. Recent winter warmings, when coupled with such transfer of heat (causing a decrease in albedo), inhibits the growth of sea ice. This prevailing situation not only hampers the growth of existing sea ice but also prevents the development of fresh ice.

During January (Figures 2d, 2e, and 2f), the range of SIC anomalies is seen shifting. The highest value is +80, and the lowest is -20. This clearly indicates that the recent fifteen years; 2006–2020 (Figures 2d, 2e, and 2f), have not gained sea-ice over the Barents as much as during the years 2001–2005. The contrast is somewhat similar to that during December, but here the anomaly has experienced a horizontal shift (the nearing of higher difference towards higher latitudes, more towards the Svalbard region). The region of the sea, south of Svalbard and north of Novaya Zemlya, experiences tremendous sea ice loss. Even the region south of Barents shows a huge contrast that was not observed during December, especially the area around Kolguyev island, over the White Sea, and around the Kanin Peninsula. During 2011–2015 (Figure 2e), the contrast remained similar, with little intensification around the islands of Svalbard and Novaya Zemlya. Sections over the Arctic Circle are also found to have positive anomalies, meaning the base period, 2001–2005, had more sea ice compared to 2011–2015. The lateral (spatial) spread of positive differences in SIC is greater during this period. By 2016–2020 (Figure 2f), the contrast reaches up to +80 near the northwest and southeast sectors of the sea. The plot during this span is extremely alarming, as nowhere over the sea has there been a visible effort by the atmospheric conditions to promote the growth of sea ice. The incapability of the atmospheric environment to favour the development of sea ice may be potentially due to the development of sea level pressure patterns in January. Researchers have already confirmed that the variation or the developments of such pressure patterns are due to changes in moisture which occur due to atmospheric transport from remote areas other than the Arctic (Zhao et al., 2022). Unlike December and January, February shows a different behaviour. The values from 2006 to 2010 (Figure 2g) were found to be significantly lower than those from 2001 to 2005. However, as the years progressed to 2011–2015, the differences were found to be less (Figure 2h) than they were between 2001 and 2005. However, as the years passed to reach 2011–2015, the difference was found to be less. And finally, by 2016–2020 (Figure 2i), the sea has lost tremendous amount of concentration, making the early years, 2001–2005, higher in value. February is typically one of the coldest and snowiest months in the region, and SIC is generally at its highest during this time. However, there has been a significant decline in Arctic SIC in recent years due to climate change and other factors. This decline has also affected the Barents Sea, and the sea ice concentration may vary from year to year depending on these factors.

In most cases, the timeline of sea ice melt is determined by whether the circulation patterns are strong or weak. March has always been a key period in the lifecycle of sea-ice growth. This month has the highest percentage of SIC in the sea ice life cycle during all the considered years. During 2006-2010 (Figure 2j), the contrast in SIC is similar to that during January, except for the fact that the south portion of the sea does not experience much difference, e.g., the White Sea. However, the area near Novaya Zemlya Island is seen to develop extreme anomalies (positive) with the passage of years. By 2011–2015 (Figure 2k), SIC shows significant variation in positive anomalies to the east of Svalbard and Novaya Zemlya. By 2016–2020 (Figure 2l), the existing fluctuation is seen deepening. Overall, majority of the sea remains within the ~0 anomalies, stating that the years 2006–2020 are not much different from 2001–2005 in the formation or decay of sea-ice over the Barents Sea. March is often depicted as the winter peak month. Though recently it has been known that winter warming is quite high compared to summers. It is recorded that almost 50% of sea-ice reduction occurred in the month of March from 1979–2020. Additionally, during this month, significant ocean heat transport at the Barents is observed (Wang et al., 2019). Large amounts of heat get transported to the Barents Sea by Atlantic waters and by the Norwegian coastal current inflows. Unlike other months that have been discussed so far (December, January, February, and March), during April the scenario is different. The entire sea experiences an anomaly greater than zero. The entire west of Novaya Zemlya experiences a contrast. This variation is further observed near Kolguyev Island, the Kanin Peninsula, and also over the White Sea with the passage of time. Additionally, during 2006–2010, the area around Svalbard is found to be extremely devoid of any major anomalies. In fact, the south of the island experiences some negative anomalies ranging ~-15 proving that the years 2006–2010 have seen some development of sea ice when compared to the years 2001–2005. By 2011–2015, the constant was noticeable around Svalbard but not extremely significant. However, the west boundary of Novaya Zemlya is seen to intensify SIC to a greater extent. By 2016–2020, this depth of anomaly/variability will have further thickened. It is understood from the plots that the sea did not experience a favourable situation during the successive years for the ice to grow.

The whisker plot (Figure 3) illustrates the variation in the life-cycle of SIC over the Barents Sea during the span of 2000–2020. The range of SIC lies between 0 and 70%. As observed over the Arctic Sea, the Barents Sea also experiences its minimum sea-ice condition during September (highlighted in pink) and maximum during March (highlighted in blue). Months: April–September can be demarcated as the decay phase and October–March as the growth phase of sea ice. The diamond dots in the graph illustrate outliers, which are greatly observed during the decay process. The range during April is fairly broad, with a mean greater than 40%. The wideness in the range of SIC is seen to be decreasing thereafter. Correspondingly, the mean value is also found to be dropping. By June, the drop in SIC is significant, with the range falling below 10% by the month of September. The range, median, and mean are the lowest for this month, which is as expected. After September, SIC is seen to gradually build up. By December, the range in SIC is seen to be highly fluctuating, covering a wide range of concentrations. Soon in January, the median and mean values of SIC are seen to be greater than those during December; however, there is no noticeable incline in the range of SIC. Nevertheless, during January and also during February, the median remained the same. This indicated that during both months the values were almost the same, which divided the distribution between the lower half and the higher half. By March, which is also known as winter maxima, the median and mean are at their highest.

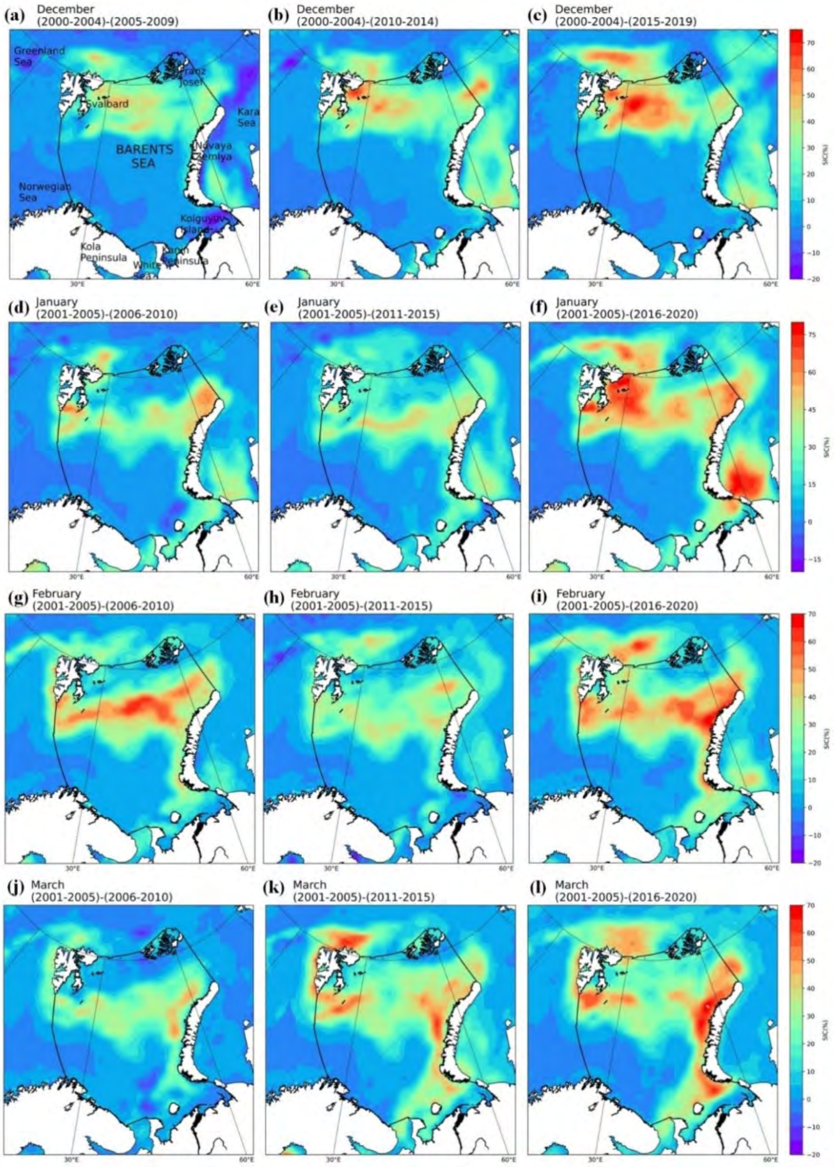

Figure 2. Spatial anomaly of SIC over Barents Sea during December in 2005-2009, 2010-2014, and 2015-2019 during a), b) and c) December d), e), and f) January g), h), and i) February j), k), and l) March

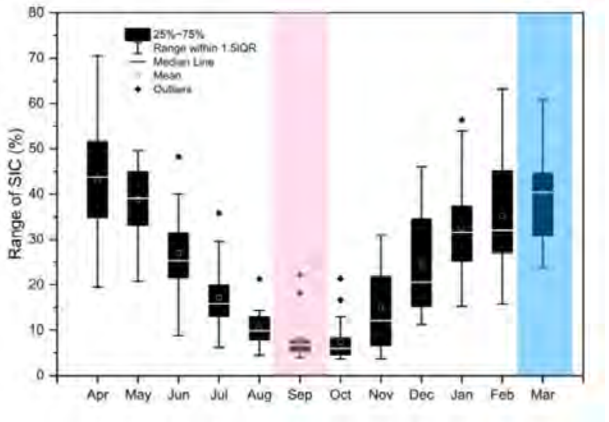

Figure 3. Temporal variability of SIC over the Barents Sea during summer (April-September) and winter (October-March) for the span of 2000-2020

3.2 Spatio-temporal variations of monthly SIT over Barents Sea

The spatial anomaly plot over Barents demonstrates the difference in SIT averages of 2016–2020 from 2011–2015. Unlike the anomaly plot of SIC, where two decades were divided into quadrants of five years each, in this case, the span is limited to 2011–2020 due to the unavailability of SIT data. From the anomaly plot, the general observation noted is that the central region of the Barents Sea remains devoid of many fluctuations (the range within zero). During December (Figure 4a), the horizontal section connecting Svalbard and Franz Josef is observed to have a positive anomaly of +0.35 m, stating that the years 2010–2014 had more SIT compared to that during 2015–2019. Additionally, the region west of Kara also experiences a difference. However, it is clearly evident that the south of Barents Sea remains devoid of any contrast, meaning the thickness has remained almost the same during the considered span over the region. By January (Figure 4b), the difference that had been observed around Svalbard during December had now intensified. The southeast corner of Novaya Zemlya also shows a variation, meaning all these places have lost tremendous ice during January 2016–2020. Even though it is alarming to notice that high positive anomalies are observed over the Arctic region, by February (Figure 4c), the entire east side of the Barents Sea had lost excessive sea ice. Kolguyev Island and the Kanin Peninsula, along with a few sections of the Arctic Circle, now show fluctuations. Regions at higher latitudes show positive anomalies, indicating that the sea gains back its lost thickness during 2016–2020. March (Figure 4d), which is also known as the month with maximum SIT, shows an equal contribution of both positive and negative anomalies. The inner sea consists of more positive values, whereas the outside of it has more negative values. The peripheral changes will definitely contribute to the sea making more sea ice. Therefore, by April, the sea had more negative anomalies. This clearly indicates that during April 2016–2020 (Figure 4e), the thickness of sea ice was definitely more compared to that during 2011–2015. However, by May (Figure 4f), the region closer to the land area—Svalbard, Franz Josef, Kolguyev Island, etc.—had gradually experienced positive values. From the plots, it can be substantiated that during 2016–2020, during the onset of winter (December, January, and February); the sea could not build up ice that was lost during summers. In March, April, and May, significant improvement is seen during the span. The probable reason might be the role played by atmospheric forcing, which has acted in favour of sea-ice growth. Still, it can be overlooked that the growth is quite low and hardly reaches 1 m. All the negative anomalies over the sea fall within the range of -0.35 to -0.25 m. The values are very low when compared to the ice, sea losses. However, in the larger picture, such small development in SIT can add a lot of importance to the cryospheric conditions over the region.

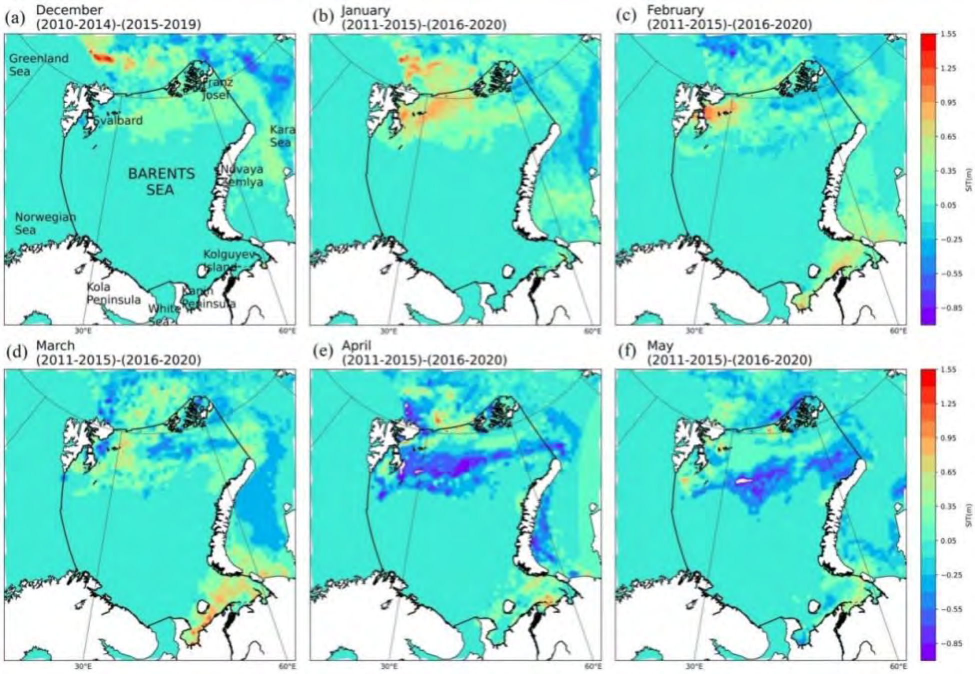

Figure 4. Spatial anomaly of SIT over Barents Sea during a) December b) January c) February d) March e) April and f) May 2010-2020

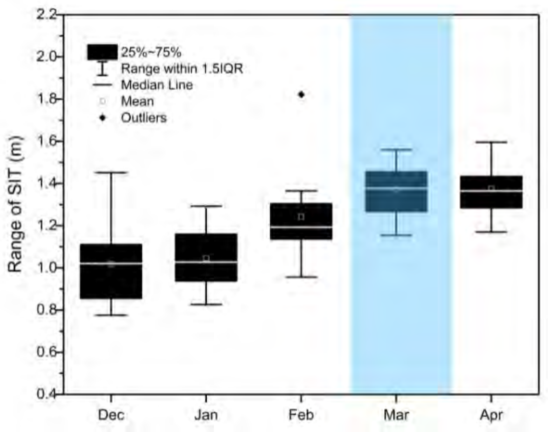

Figure 5. Temporal variability of SIT over the Barents Sea during December-May for the span 2010-2020

The temporal variation in SIT over the Barents Sea is depicted in Figure 5. The range over the sea varies between 0.7 and 1.6 m, including some outliers that go beyond 1.6 m. The plot clearly shows how the range increases as the winter months progress. The winter maximum is observed in the month of March. However, in Figure 5, the range during March and April seems to be almost the same, indicating that the developed thickness could not vanish away immediately with the onset of summer. Even the median in March is found to be higher than that in April. This indicates that the majority of pixels will have higher values of SIT during the next month. SIT data during the summer months is not available, therefore the transformation of the sea ice during those periods could not be observed. Anyway, the trend of its decay would be very similar to that of SIC, which has already been understood in the previous section.

3.3 Variability in Sea Ice Concentration with respect to Sea Ice Thickness

The histogram plot of SIC in Figure 6a has a range of 87–97%. Here the SIC values are obtained by averaging the data over all the years of each pixel of the respective month. For example, if we consider January, all the SIC values of January months are combined (averaged) for 2010–2020 (11 years), and later they are binned at 70 counts. The outputs obtained are displayed in Figure 6a. From the plot, it is evident that during January, February, and March, the lines overlap with each other. During January, SIC is observed to have a low percentage compared to the other two winter months, February and March. Due to the binning applied to the variable (SIC), the maximum count observed is ~5. However, the SIT plot (Figure 6b) shows a significant rise in thickness by a value of ~0.5 m with the passage of each month. The range of SIT here lies between 0.2 and 3.5 m. Figure 6b represents two Y axes, with one Y axis denoting the number of points (counts) having a particular thickness, the other Y axis showing the density of SIT, and the X axis representing SIT in metres (m). The density plot here represents the distribution of SIT. The highest peak, with a thickness of 1.2 m, is obtained in January.

During February, the maximum peak slightly shifts to attain the value of 1.5 m. The shift in peak helps one understand the increase in the depth of sea ice, which is obtained as a result of favourable conditions (especially during winters). Furthermore, the highest value had fallen to 1.7 m by March. Here, the density distribution during January and February is observed to be almost the same, which is thereafter followed by a slight decline during March. It is worth noting that the SIT of about 2 m in March over the Barents Sea is seasonal. FYI or MYI refers to thick ice greater than 2 m in thickness. In the analysed plots displayed in Figure 6a, the frequent appearances of SIC within the range of 90–100% are seen to be in proper agreement with the shift of thick sea ice (Figure 6b).The winter monthly variation of SIC with respect to SIT over Barents for the span of 11 years is illustrated in Figure 6c. From the plot, it is evident that the range of SIC varies between 0-50 % and that of SIT varies between 0.2-2m. SIT and SIC own a high linear correlation and also have noticeable seasonal variation characteristics. When SIC increases, SIT also increases, and vice versa. Over the Barents Sea, the $r^2_{(SIC,\ SIT)} = 0.62$ ($p < 0.05$), indicating a strong relationship between the two quantities.

3.4 Numerical Logistic Curve Model

3.4.1 Logistic SIC decay process averaged over summer months (April-September)

From the literature, it is clearly evident that atmospheric changes highly influence the development of cryospheric features (e.g., Qin and Ding, 2010). The Earth's climate system is a complex and dynamic system, and changes in one component can have far-reaching effects on others, thereby influencing the sea ice conditions. This underscores the importance of understanding and monitoring the entire system to accurately predict future trends and mitigate the impacts of climate change.

However, here, the work revolves around understanding the standard numerical logistic curve model for predicting the fate of sea-ice conditions. Figure 7 shows the decay of sea ice during the summer months, i.e., from April to September. The time series of model-predicted SIC and satellite-observed SIC is drawn so as to understand the closeness of these parameters. The predicted SIC is calibrated by the numerical formula of the logistic curve model using the methodology discussed in the aforementioned section. From the visual observation, it is clearly evident that the calculated b matches well with the satellite-derived SIC.

.

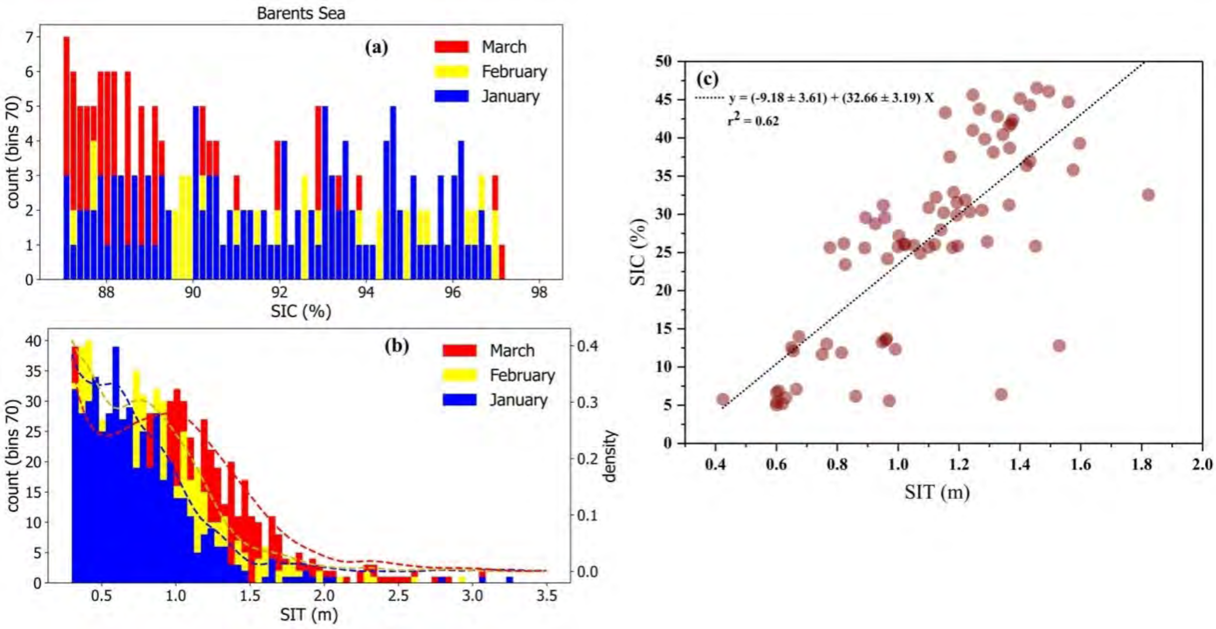

Figure 6. Histogram of a) Sea Ice Concentration and b) Sea Ice Thickness during January, February and March and c) Linear regression analysis of Sea Ice Concentration (SIC) with respect to Sea Ice Thickness (SIT) over Barents Sea during winter months (October-April) for the span 2010-2021

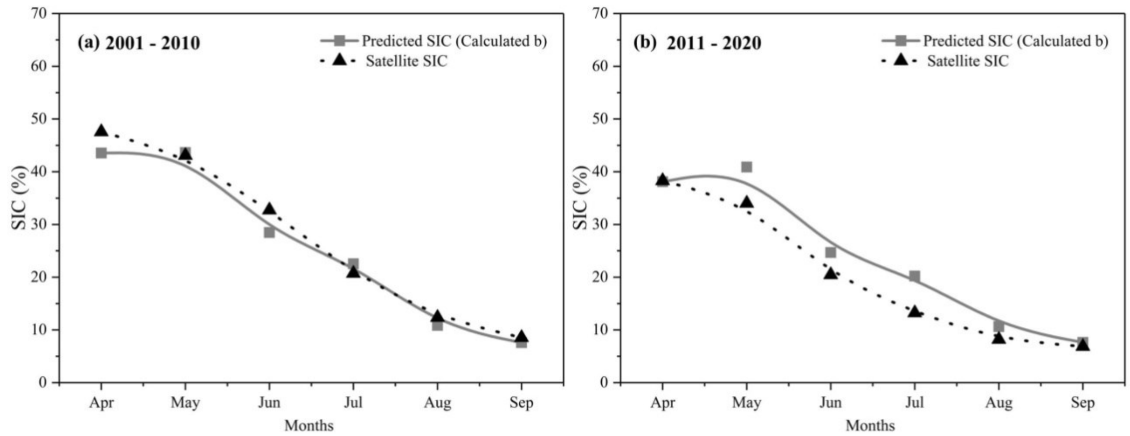

Figure 7. Temporal variability of SIC over Barents Sea during summer (April-September) for the span a) 2001-2010 and b) 2011-2020.

For the years 2001–2010 (Figure 7a), it is seen that the predicted SIC is seen to overlay with satellite data for several months. Apart from that, the percentage difference is calculated to understand the extent of the difference between the two SICs. Here, points during April, May, and July are an exact match. The percentage difference between the predicted SIC for these three months and the satellite-derived SIC is found to be 8.82%, 1.27%, and 8.49%, respectively. The highest difference between the values was noted in the month of June (13.98%), which is not significantly visible in Figure 7. However, the predicted SIC clearly shows the summer life cycle of SIC. It is highest in the month of April, with a range of 50–40%, and gradually declines by September, which is also recorded as the month of sea-ice minimum. However, the regression analyses performed in the subsequent sections add to our understanding of the method and its closeness to the satellite-drawn observations. During the recent decade, 2011-2020 (Figure 7b) predicted SIC and satellite SIC are seen to line up well with each other, as in the case of 2001-2010 (Figure 7a). The two datasets clearly show the decay of sea ice from April to September. April is the month with the highest value, and September is the month with the lowest value, which is the existing trend of sea ice over the region during the summer phase. Figure 7b shows the real scenario prevailing over the region, with the highest difference between the two SICs in the month of July and the lowest in August. The highest closeness was observed at 0.49% in the month of August. The match between the starting and ending values of the sea ice decay life cycle clearly demonstrated that the trend could be correctly determined to a greater extent well in advance. The highest difference between the two was with value reaching 41.73% in the month of July. The difference observed in this case is phenomenally high, which might be due to other atmospheric forcings that are not currently incorporated in the numerical logistic curve equation. July, being the mid-month of summer, might have experienced tremendous warming during the recent decade, which has made the sea undergo significant melting beyond the predicted decay. During May and June, the match between the two values was also high, with values of 18.35% and 18.68%, respectively. August also has the second-largest SIC difference, with 25.90%. Figure 7 clearly states that during this period, the predicted SIC works fine over the region.

3.4.2 Logistic SIC decay process averaged over winter months (October-March)

Similar to the summer months (Figure 7), the standard logistic curve is also applied to the winter months (Figure 8). Sea ice grows from October to March, with the maximum amount occurring in March. From Figure 8, it is evident that during both decades, predicted SIC is in line with satellite-obtained SIC except for few differences during few months. During the growth stage (winter phase), the lowest range of SIC (minimum SIC) is observed in the month of October and the maximum in the month of March. In Figure 8a, the predicted SIC is found to show the highest similarity with the satellite SIC during March and December, with a percentage difference of just 2.98% and 4.62%, respectively, between the two. However, the largest difference between the two quantities was seen during the month of November, with a percentage dissimilarity of 32.59%, which is not quite high but the highest amongst all the other winter months. Further, the second largest difference between the two SICs is observed in the month of February with a value of 12.00%, followed by January with a value of 10.61%.

During the recent decade 2011–2020 (Figure 8b), the trend line of the predicted SIC is seen to match well with the satellite-obtained SIC. This nature of the time series during this decade indicates that the predicted SICs can be used to know the health of sea ice well in advance. However, the percentage differences between predicted SIC and satellite SIC is more during this span than during the previous span (2001–2010). The difference between the two SICs is the smallest during October, January, and February, with values of 5.97%, 0.31%, and 1.97%, respectively. For all the other months, the percentage difference is quite higher than 10%. However, here also, the highest is observed in the month of November, with a value of 38.97%. Apart from Figures 6 and 7, which give a visual interpretation of the closeness of SICs, regression analyses in the upcoming section provide a better understanding of the calibration of the standard logistic curve model in predicting the cryospheric variable, SIC.

3.4.3 Regression analyses between predicted and satellite SIC during summer and winter months

In order to validate the efficacy of the standard logistic curve during summer when sea ice undergoes decay, regression analyses are performed between the predicted SIC and satellite SIC, and the results are displayed in Figure 9. Similar to the previous section, where the model was applied over the span of each decade, i.e., 2001–2010 and 2011–2020, here too the regression analyses are performed on similar timelines. Figure 9 gives information about the closeness of the predicted and satellite-obtained SICs. The obtained coefficient of determination gives an understanding of the fit of predicted data with satellite-derived SIC. The calculation of the p-value here gives an understanding of the confidence level (in this case; 95%) that prevails between the two datasets. For years 2001–2010 (Figure 9a), r^2 = 0.88 between predicted SIC and satellite SIC. The coefficient of determination being greater than 0.5 indicates predicted SIC is significant with satellite SIC. Similarly, during the span of 2011–2020 (Figure 9b), the coefficient of determination is greater than 0.5, with r^2 = 0.87. The marginal difference between the two predicted SICs with the satellite SIC was low during the previous decade of 2001–2010 compared to the latter period of 2011–2020.

Similar to summers, in order to validate the functioning of the model during winter, regression analyses are performed between predicted SIC and satellite SIC. Here also, the coefficient of determination value during 2001–2010 (Figure 10a) reveals that the predicted value fits well with the satellite SIC. The r^2 value in the former case is 0.80 with level of significance $p<0.05$, indicating that the confidence level is greater than 95%. However, during 2011–2020 (Figure 10b), r^2 = 0.78 of the satellite SIC with the predicted SIC In this case, the range of r^2 is ~0.7, stating that the method can be adopted to determine SIC.

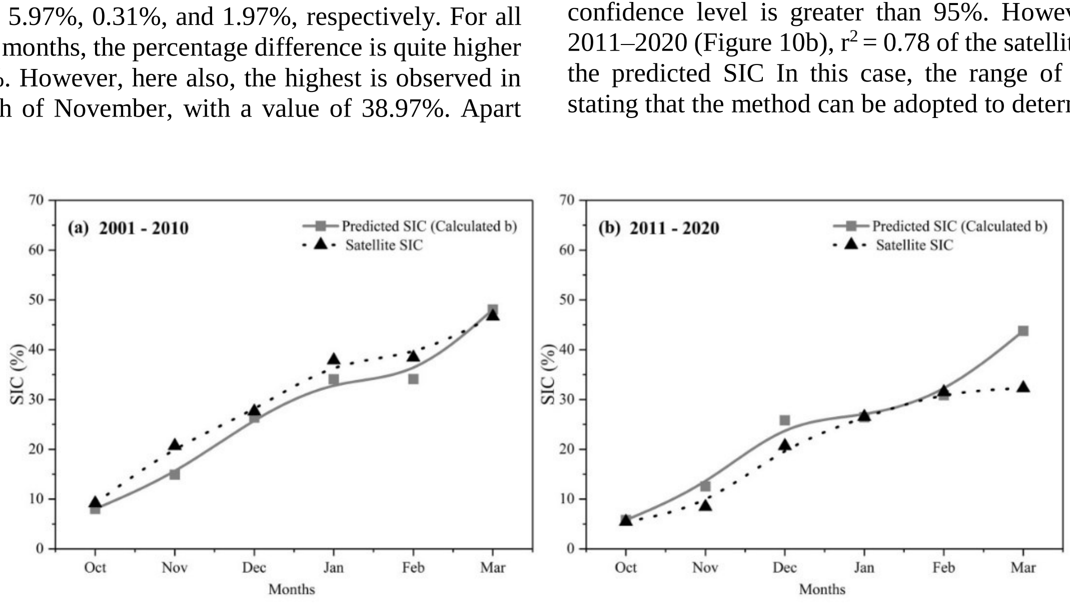

Figure 8. Temporal variability of SIC over Barents Sea during winter (October-March) for the span a) 2001-2010 and b) 2011-2020.

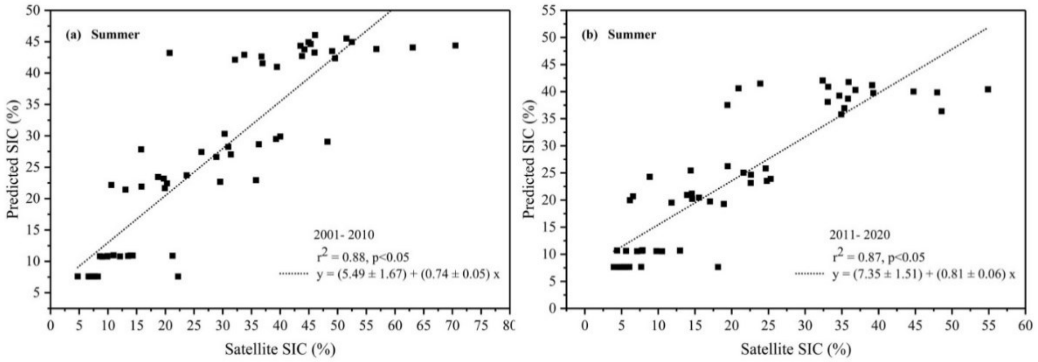

Figure 9. Correlation between predicted and satellite SIC during summer (April - September) for the span a) 2001-2010 and b) 2011-2020

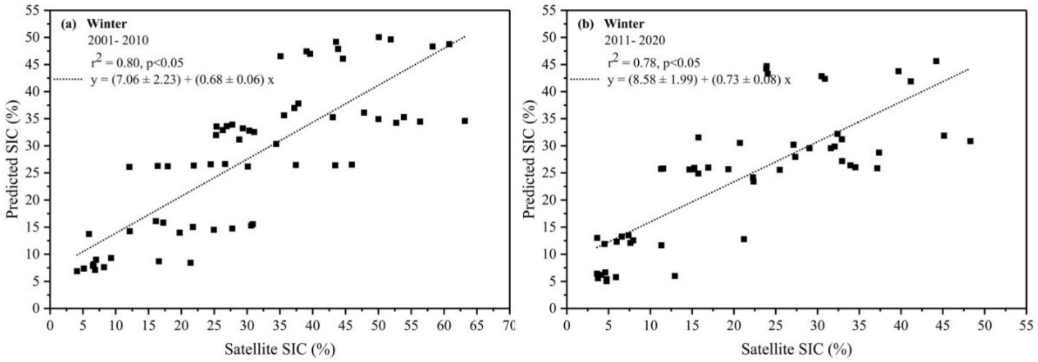

Figure 10. Correlation between predicted and satellite SIC during winter (October-March) for the span a) 2001-2010 and b) 2011-2020.

3.4.4 Evolution of SIT and regression analyses between predicted and satellite SIT during December – April

Apart from the implication of the logistic curve on the parameter SIC, we have tried to understand the further scope of this model by applying it to another sea-ice parameter, namely SIT. Looking at the general behaviour of thickness, the parameter is found to range between 0 and 2 m, which is also well noted in the aforementioned section. Here, however, the model-obtained SIT is tested with the satellite-derived SIT to understand the closeness of the derived SIT. In terms of the trend line, the predicted SIT exhibits similar patterns to that of satellite SIT, indicating that the model works well on this cryospheric parameter as well. Additionally, the degree of closeness in the predicted SIT is seen to be good compared to that of the satellite SIT. From Figure 11a, it is evident that October is the month with the lowest SIT and March–April with the highest. However, when observing the satellite SIT, it is clearly evident that March has the highest SIT; the SIT during March is greater than that during April. While with the predicted SIT, April is found to show the highest value, indicating the development of sea-ice growth even during the onset of summer. This information may be misleading at times. While checking the difference in the value between predicted SIT and satellite SIT, March and April had a difference of about 2.95% and 6.93%, respectively. The highest difference between the two SITs was observed in the months of November and December, with values of 21.17% and 19.42%, respectively. The difference in November is not much, which still indicates an appreciable match. Further computation of the percentage difference between the predicted SIT and the satellite-obtained SIT revealed that the majority of the values were insignificant. For the months of October, January, and February, the differences between the SITs were 13.06%, 16.35%, and 14.81%, respectively. Despite these differences between the two entities, the predicted values of SIT are more reliable.

After observing the trend followed by the predicted SIT, it is vital to validate the closeness of modelled data with satellite data. This is done by performing linear regression analyses between the predicted SIT and the satellite SIT. Figure 11b displays the results of analyses performed between these SITs during December and May for the years 2011–2020. From Figure 11b, $r^2 = 0.75$ for calculated SIT with satellite-derived SIT. The coefficient of determination values state that the calculated SIT matches well with the satellite SIT. From the above observations, it can be stated that the standard logistic curve model works fine for each month. Also, the model can be extended to incorporate more cryospheric parameters, as it is now proven that SIC and SIT work fine with the model.

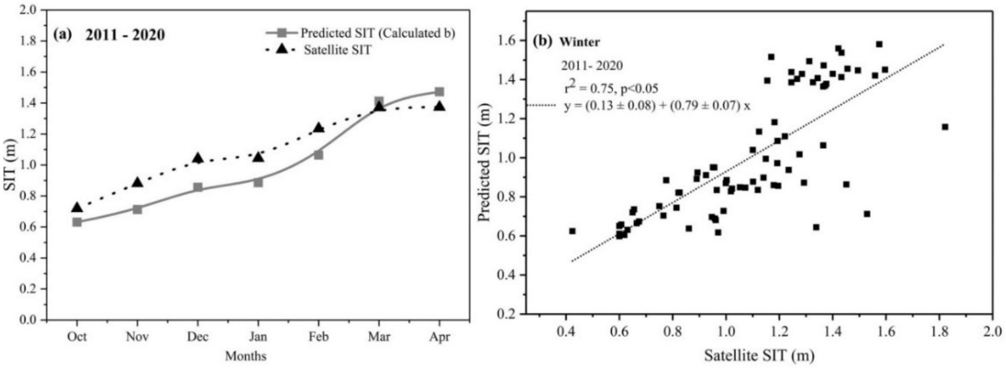

Figure 11. a) Temporal variability of SIT and b) correlation between predicted and satellite SIT over the Barents Sea during winter (October-April) for the span 2011-2020

4. Conclusions

With the recently discovered process of Atlantification taking place over the Arctic region, the marginal Barents Sea has now gained special attention from researchers, as this sea serves as a gateway for the Atlantic water to merge into the Arctic region. This study paves a new quantitative statistical approach for a better understanding of the seasonal sea ice processes. The statistical approach used here is the standard logistic curve model, which is proven to be an outstanding tool for both the summer and winter seasons. The sea ice patterns show high monthly variability over the Barents Sea. In general, the sea ice grows from mid-September to mid-March and decays from mid-March to mid-September. In order to understand the existing nature of sea ice, two cryospheric parameters namely SIC and SIT are considered. The SIC over the region is seen to peak in winter and decrease to its lowest in summer. During the considered period, the Barents SIC is seen decreasing 87–97% with the passage of time. However, the decline is better explained by the parameter, SIT. Additionally, SIT revealed that there is intensification in thickness with each month's shift. The peak of SIT shifts from 1.2 to 1.5 m during January and February and from 1.5 to 1.7 m during February and March. The standard logistic curve model is selected to quantify the sea ice growth and decay processes during the two seasons. For the summer months, the fitted SIC derived from the standard logistic curve model is in good consistent with the average satellite data every ten years (decade); 2001-2010 and 2011-2020. The rapid decline in the SIC pattern from mid-May to September is successfully characterized by the fitted (modelled) curves. For the winter months, the fitted SIC derived from the standard logistic curve model is in good dependence with the average true (satellite) data during the above-mentioned different time periods. The gradual increase in SIC from November to March is well reflected by these fitted curves. Further, mathematical validation of modelled obtained data is done with the satellite SIC with the help of regression analyses. The coefficient of determination (r^2) values obtained for predicted SIC and satellite SIC during summer for the years 2001-2010 and 2011-2020 are 0.88 and 0.87 respectively. Whereas during winter, these values correspond to 0.80 and 0.78 are for the above-mentioned years. Additionally, SIT is also predicted using this model. In this case, the duration is kept confined to December - April for the year 2011-20. During these months, the fitted SITs derived from the model are in good support with the average satellite data during the decade. The same has been proven mathematically by deriving the coefficient of determination (r^2) values between the predicted SIT and the satellite SIT. The correlation co-efficient value is 0.75 which is obtained between modelled SIT and satellite SIT for the months December - April for the years 2011-20. From the observations, it is clear that the model can be used to understand the state of sea condition to a large extent. This enhancement in the values is mostly due to considering individual ‘b’ values for each month, which compensates for the varying nature of sea ice features.

This study promotes the understanding of sea ice - both in the x-y plane; SIC and z-plane; SIT in the marginal - Barents Sea. The modelled results are not only seen to match with the satellite data but are also seen to yield good r^2 values, stating it can also be used to foresee the future scenario of the sea. Additionally, developing a numerical model like this helps in predicting sea ice behaviour well into the future. Additional development of the model by incorporating the external driving forces of sea ice - atmospheric and oceanic variables will help in accurately computing the future cryospheric conditions at the micro scale and macro scale. Future work may be to investigate more sea ice parameters using the same standard logistic curve model over different spatial and temporal domains.

References

ACIA - Arctic Climate Impact Assessment (2005). Arctic climate impact assessment - Scientific report. Cambridge University Press.

Allen MR, OP Dube, W Solecki, F Aragón-Durand, W Cramer, S Humphreys, M Kainuma, J Kala, N Mahowald, Y Mulugetta, R Perez, M Wairiu and K Zickfeld (2018). Framing and Context. In: Global Warming of 1.5°C. An IPCC Special Report on the impacts of global warming of 1.5°C above pre-industrial levels and related global greenhouse gas emission pathways, in the context of strengthening the global response to the threat of climate change, sustainable development, and efforts to eradicate poverty.

Bengtsson L, P Arkin, P Berrisford, P Bougeault, CK Folland, C Gordon, K Haines, KI Hodges, P Jones, P Kallberg, N Rayner, AJ Simmons, D Stammer, PW Thorne, S Uppala and RS Vose (2007). The need for a dynamical climate reanalysis. Bulletin of the American Meteorological Society, 88(4), 495-502. https://doi.org/10.1175/bams-88-4-495

Bitz CM and WH Lipscomb (1999). An energy-conserving thermodynamic model of sea ice. Journal of Geophysical Research: Oceans, 104(C7), 15669-15677. https://doi.org/10.1029/1999jc900100

Boé J, A Hall and X Qu (2010). Sources of spread in simulations of Arctic Sea ice loss over the twenty-first century. Climatic Change, 99(3-4), 637-645. https://doi.org/10.1007/s10584-010-9809-6

Bony S, R Colman, VM Kattsov, RP Allan, CS Bretherton, J Dufresne, A Hall, S Hallegatte, MM Holland, W Ingram, DA Randall, BJ Soden, G Tselioudis and MJ Webb (2006). How well do we understand and evaluate climate change feedback processes? Journal of Climate, 19(15), 3445-3482. https://doi.org/10.1175/jcli3819.1

Cavalieri DJ, CL Parkinson, P Gloersen, and HJ Zwally. (1996), updated yearly. Sea Ice Concentrations from Nimbus-7 SMMR and DMSP SSM/I-SSMIS Passive Microwave Data, Version 1. [sea ice thickness]. Boulder, Colorado USA. NASA National Snow and Ice Data Center Distributed Active Archive Center. https://doi.org/10.5067/8GQ8LZQVL0V [28/09/2021].

Cavalieri DJ and CL Parkinson (2012). Arctic Sea ice variability and trends, 1979–2010. The Cryosphere, 6(4), 881-889. https://doi.org/10.5194/tc-6-881-2012

Chen P and J Zhao (2017). Variation of sea ice extent in different regions of the Arctic Ocean. ActaOceanologicaSinica, 36(8), 9-19. https://doi.org/10.1007/s13131-016-0886-x

Danabasoglu G, JF Lamarque, J Bacmeister, DA Bailey, AK DuVivier and J Edwards (2020). The Community Earth System Model Version 2 (CESM2). Journal of Advances in Modeling Earth Systems, 12, e2019MS001940. https://doi.org/10.1029/2019MS001940

Diebold FX and GD Rudebusch (2020). Probability Assessments of an Ice-Free Arctic: Comparing Statistical and Climate Model Projections. Federal Reserve Bank of San Francisco Working Paper 2020-02. https://doi.org/10.24148/wp2020-02

Eisenman I and JS Wettlaufer (2008). Nonlinear threshold behavior during the loss of Arctic Sea ice. Proceedings of the National Academy of Sciences, 106(1), 28-32. https://doi.org/10.1073/pnas.0806887106

Holland MM, CM Bitz and B Tremblay (2006). Future abrupt reductions in the summer Arctic Sea ice. Geophysical Research Letters, 33(23). https://doi.org/10.1029/2006gl028024

Hui C (2006). Carrying capacity, population equilibrium, and environment's maximal load. Ecological Modelling, 192, 317-320.

Inoue J, ME Hori and K Takaya (2012). The role of Barents Sea ice in the wintertime cyclone track and emergence of a Warm-Arctic cold-siberiananomaly. Journal of Climate, 25(7), 2561-2568. https://doi.org/10.1175/jcli-d-11-00449.1

Intergovernmental Panel on Climate Change. (2018). Global warming of 1.5°C. An IPCC special report on the impacts of global warming of 1.5°C above pre-industrial levels and related global greenhouse gas emission pathways, in the context of strengthening the global response to the threat of climate change, sustainable development, and efforts to eradicate poverty. World Meteorological Organization.

Katlein C, S Arndt, M Nicolaus, DK Perovich, MV Jakuba, S Suman, S Elliott, LL Whitcomb, CJ McFarland, R Gerdes, A Boetius and CR German (2015). Influence of ice thickness and surface properties on light transmission through arctic sea ice. Journal of Geophysical Research: Oceans, 120(9), 5932-5944. https://doi.org/10.1002/2015jc010914

Kim B, S Son, S Min, J Jeong, S Kim, X Zhang, T Shim and J Yoon (2014). Weakening of the stratospheric polar vortex by Arctic sea-ice loss. Nature Communications, 5(1). https://doi.org/10.1038/ncomms5646

King JC and J Turner (1997). Antarctic Meteorology and climatology. Cambridge University Press. https://doi.org/10.1017/cbo9780511524967

King J, G Spreen, S Gerland, C Haas, S Hendricks, L Kaleschke and C Wang (2017). Sea-ice thickness from field measurements in the northwestern Barents Sea. Journal of Geophysical Research: Oceans, 122(2), 1497-1512. https://doi.org/10.1002/2016jc012199

Kurtz N and J Harbeck.(2017). CryoSat-2 Level-4 Sea Ice Elevation, Freeboard, and Thickness, Version 1. [sea ice thickness]. Boulder, Colorado USA. NASA National Snow and Ice Data Center Distributed Active Archive Center. https://doi.org/10.5067/96JO0KIFDAS8 [28/09/2021]

Kyurkchiev N and S Markov (2015). On the Hausdorff distance between the heaviside step function and Verhulst logistic function. Journal of Mathematical Chemistry, 54(1), 109-119. https://doi.org/10.1007/s10910-015-0552-0

Lind S, RB Ingvaldsen and T Furevik (2018). Arctic warming hotspot in the northern Barents Sea linked to declining sea-ice import. Nature Climate Change, 8(7), 634-639. https://doi.org/10.1038/s41558-018-0205-y

Meier WN, GK Hovelsrud, BE Van Oort, JR Key, KM Kovacs, C Michel, C Haas, MA Granskog, S Gerland, DK Perovich, A Makshtas and JD Reist (2014). Arctic Sea ice in transformation: A review of recent observed changes and impacts on biology and human activity. Reviews of Geophysics, 52(3), 185-217. https://doi.org/10.1002/2013rg000431

Meredith M, M Sommerkorn, S Cassotta, C Derksen, A Ekaykin, A Hollowed, G Kofinas, A Mackintosh J Melbourne-Thomas, MMC Muelbert, G Ottersen, H Pritchard and EAG Schuur (2019). Polar Regions. In: IPCC Special Report on the Ocean and Cryosphere in a Changing Climate.

Meyer P (1994). Bi-logistic growth. Technological Forecasting and Social Change, 47, 89-102.

Mundy C, D Barber and C Michel (2005). Variability of snow and ice thermal, physical and optical properties pertinent to sea ice algae biomass during spring. Journal of Marine Systems, 58(3-4), 107-120. https://doi.org/10.1016/j.jmarsys.2005.07.003

Murphy H, H Jaafari and HM Dobrovolny (2016). Differences in predictions of ODE models of tumor growth: A cautionary example. BMC Cancer, 16(1). https://doi.org/10.1186/s12885-016-2164-x

Nghiem SV, Y Chao, G Neumann, P Li, DK Perovich, T Street and P Clemente-Colón (2006). Depletion of perennial sea ice in the east Arctic Ocean. Geophysical Research Letters, 33(17). https://doi.org/10.1029/2006gl027198

Notz D (2009). The future of ice sheets and sea ice: Between reversible retreat and unstoppable loss. Proceedings of the National Academy of Sciences, 106(49), 20590-20595. https://doi.org/10.1073/pnas.0902356106

Parkinson CL (2019). A 40-y record reveals gradual Antarctic sea ice increases followed by decreases at rates far exceeding the rates seen in the Arctic. Proceedings of the National Academy of Sciences, 116(29), 14414-14423. https://doi.org/10.1073/pnas.1906556116

Parkinson C L and DJ Cavalieri (2008). Arctic Sea ice variability and trends, 1979–2006. Journal of Geophysical Research, 113(C7). https://doi.org/10.1029/2007jc004558

Petty AA, MM Holland, DA Bailey and NT Kurtz. (2018). Warm Arctic, increased winter sea ice growth?. Geophysical Research Letters, 45(23). https://doi.org/10.1029/2018gl079223

Qin D and Y Ding (2010). Key issues on Cryospheric changes, trends and their impacts. Advances in Climate Change Research, 1(1), 1-10. https://doi.org/10.3724/sp.j.1248.2010.00001

Ren S, X Liang, Q Sun, H Yu, LB Tremblay, B Lin, X Mai, F Zhao, M Li, N Liu, Z Chen and Y Zhang (2021). A fully coupled Arctic sea-ice–ocean–atmosphere model (ArcIOAM v1.0) based on C-Coupler2: model description and preliminary results. Geoscientific Model Development, 14(3), 1529-1556. https://doi.org/10.5194/gmd-14-1529-2021

Rösel A, P Itkin, J King, D Divine, C Wang, MA Granskog, T Krumpen and S Gerland (2018). Thin sea ice, thick snow, and widespread negative Freeboard observed during N-ICE2015 north of Svalbard. Journal of Geophysical Research: Oceans, 123(2), 1156-1176. https://doi.org/10.1002/2017jc012865

Schlichtholz P (2019). Subsurface ocean flywheel of coupled climate variability in the Barents Sea hotspot of global warming. Scientific Reports, 9(1). https://doi.org/10.1038/s41598-019-49965-6

Schröder L, M Horwath, R Dietrich and V Helm (2018). Four decades of surface elevation change of the Antarctic ice Sheetfrom multi-mission satellite altimetry. https://doi.org/10.5194/tc-2018-49

Screen JA, C Deser, DM Smith, X Zhang, R Blackport, PJ Kushner, T Oudar, KE McCusker and L Sun (2018). Consistency and discrepancy in the atmospheric response to Arctic sea-ice loss across climate models. Nature Geoscience, 11(3), 155-163. https://doi.org/10.1038/s41561-018-0059-y

Serreze MC, MM Holland and J Stroeve (2007). Perspectives on the Arctic's shrinking sea-ice cover. Science, 315(5818), 1533-1536. https://doi.org/10.1126/science.1139426

Shapiro I, R Colony and T Vinje (2003). April sea ice extent in the Barents Sea, 1850–2001. Polar Research, 22(1), 5-10. https://doi.org/10.3402/polar.v22i1.6437

Simonsen K and PM Haugan (1996). Heat budgets of the Arctic Mediterranean and sea surface heat flux parameterizations for the nordic seas. Journal of Geophysical Research: Oceans, 101(C3), 6553-6576. https://doi.org/10.1029/95jc03305

Skagseth Ø, T Eldevik, M Årthun, H Asbjørnsen, VS Lien and LH Smedsrud (2020). Reduced efficiency of the Barents Sea cooling machine. Nature Climate Change, 10(7), 661-666. https://doi.org/10.1038/s41558-020-0772-6

Smedsrud LH, I Esau, R Ingvaldsen, T Eldevik, P Haugan, C Li, V Lien, A Olsen, A Omar, O Otterå, B Risebrobakken, A Sandø, V Semenov and S Sorokina (2013). The Role of the Barents Sea in the Arctic Climate System. Reviews of Geophysics, 51, 415-449.

Sorokina SA, C Li, JJ Wettstein and NG Kvamstø (2016). Observed atmospheric coupling between Barents Sea ice and the Warm-Arctic cold-siberian anomaly pattern. Journal of Climate, 29(2), 495-511. https://doi.org/10.1175/jcli-d-15-0046.1

Stroeve J and WN Meier (2018). Sea Ice Trends and Climatologies from SMMR and SSM/I-SSMIS, Version 3. [sea ice concentration]. Boulder, Colorado USA. NASA National Snow and Ice Data Center Distributed Active Archive Center. https://doi.org/10.5067/IJ0T7HFHB9Y6. [28/09/2021].

Sweilam NH, MM Khader and AM Mahdy (2012). Numerical studies for fractional-order logistic differential equation with two different delays. Journal of Applied Mathematics, 2012, 1-14. https://doi.org/10.1155/2012/764894

Tietsche S, D Notz, JH Jungclaus and J Marotzke (2013). Assimilation of sea-ice concentration in a global climate model – physical and statistical aspects. Ocean Science, 9(1), 19-36. https://doi.org/10.5194/os-9-19-2013

Tronstad S, O. Pavlova and R Ingvaldsen (2007). Havklima (marine climate), in Forvaltningsplan Barentshavet. 1. Rapport fra overva˚kingsgruppen, edited by K. Sunnana˚, Chapter 4.1., pp. 12 – 15, Inst. Mar. Res., Bergen, Norway.

Turner J, GJ Marshall, K Clem, S Colwell, T Phillips and H Lu (2019). Antarctic temperature variability and change from station data. International Journal of Climatology, 40(6), 2986-3007. https://doi.org/10.1002/joc.6378

Vázquez M, R Nieto, A Drumond and L Gimeno (2016). Extreme sea ice loss over the Arctic: An analysis based on anomalous moisture transport. Proceedings of the 1st International Electronic Conference on Atmospheric Sciences. https://doi.org/10.3390/ecas2016-d003

Vella D and JS Wettlaufer (2008). Explaining the patterns formed by ice floe interactions. Journal of Geophysical Research, 113(C11). https://doi.org/10.1029/2008jc004781

Walsh JE, WL Chapman and F Fetterer (2017). Sea ice extents continue to set new records: Arctic, Antarctic, and global results. EOS, Transactions American Geophysical Union, 98. https://doi.org/10.1029/2017eo068607

Wang M and JE Overland (2009). A sea ice free summer Arctic within 30 years? Geophysical Research Letters, 36(7). https://doi.org/10.1029/2009gl037820

Wang Q, X Wang, C Wekerle, S Danilov, T Jung, N Koldunov, S Lind, D Sein, Q Shu and D Sidorenko (2019). Ocean heat transport into the Barents Sea: Distinct controls on the upward trend and Interannual variability. Geophysical Research Letters, 46(22), 13180-13190. https://doi.org/10.1029/2019gl083837

Yang S and JH Christensen (2012). Arctic Sea ice reduction and European cold winters in CMIP5 climate change experiments. Geophysical Research Letters, 39(20). https://doi.org/10.1029/2012gl053338

Zhang J, DA and Rothrock (2003). Modeling global sea ice with a thickness and enthalpy distribution model in generalized curvilinear coordinates. Monthly Weather Review, 131(5), 845-861. https://doi.org/10.1175/1520-0493(2003)131<0845:MGSIWA>2.0.CO;2

Zhao J, D Barber, S Zhang, Q Yang, X Wang and H Xie (2017). Record low sea-ice concentration in the central Arctic during summer 2010. Advances in Atmospheric Sciences, 35(1), 106-115. https://doi.org/10.1007/s00376-017-7066-6

Zhao X, K Huang, JS Fu and SF Abdullaev, S. F. (2022). Long-range transport of Asian dust to the Arctic: Identification of transport pathways, evolution of aerosol optical properties, and impact assessment on surface albedo changes. Atmospheric Chemistry and Physics, 22(15), 10389-10407. https://doi.org/10.5194/acp-22-10389-2022

Area Estimation of Mango and Coconut Crops using Machine Learning in Hesaraghatta Hobli of Bengaluru Urban District, Karnataka

Zubair Ahmed, P.P. Nageswara Rao*, and P. Srikanth
Karnataka State Remote Sensing Applications Centre, Doora Samvedi Bhavana, Doddabettahalli, Bengaluru
*Email: ppn1953@gmail.com

(Received: 30 October 2022, Accepted in final form: 19 March 2023)

DOI: *https://doi.org/10.58825/jog.2023.17.1.75*

Abstract: Timely and accurate estimation of acreage and production of horticulture crops is necessary for deciding how much, where and when to export these commodities in the national and global markets. Remote sensing has been one of the methods adopted, in addition to conventional sampling methods, for improving the estimates. Parametric image classification algorithms have been used by many researchers for identification and area estimation of horticulture crops. But these algorithms result in several unclassified pixels leading to over/underestimates. This study has been undertaken to estimate the area of two horticulture crops (i.e., mango and coconut) of Hesaraghatta *hobli* of Bengaluru urban district using Convolutional Neural Network (CNN) on Google Colaband Random Forest (RF) algorithms on Google Earth Engine (GEE). Remotely sensed data acquired by the Multi-Spectral Instrument (MSI) onboard Sentiel-2A satellite was used. Spectral signatures of horticulture crops and other associated cover types have been generated to identify the cover types and for selecting appropriate band combinations. Two different band combinations were used for area estimation of selected horticulture crops: i) Near-InfraRed (NIR), Red, and Green all three having a spatial resolution of 10 m, ii) Red edge-3, Short-Wave InfraRed1 (SWIR1) and Short-Wave InfraRed2 (SWIR2) having 20 m spatial resolution. Area estimates of horticulture crops and associated cover types were validated with respect to ground truth and statistical reports from Karnataka State Directorate of Horticulture (KSDH). It was found that the CNN model performed better than RF using NIR, Red, and Green band combination with an overall accuracy of 84%, but it failed to give similar accuracies with Red edge 3, SWIR1, and SWIR2 band combination. We attempted transfer learning using the trained CNN model at two different study areas far away from the study area and found encouraging results.

Keywords: Mango, Coconut, Area estimation, Machine learning, Convolutional Neural Network, Random Forest (RF)

1. Introduction

Horticultural crops serve as a source of income and provide employment opportunities for the farmers of the country. But these crops experience lot of fluctuation in their production owing to weather and climate variations. Therefore, timely estimates of area and production of horticulture crops are necessary for taking appropriate decisions in their marketing and export. Several researchers from Indian Agricultural Statistics Research Institute (IASRI), Directorate of Economics and Statistics (DES), Ministry of Agriculture& Farmers Welfare, National Sample Survey Organization (NSSO) and the State-level Horticulture Universities have developed innovative statistical techniques for estimating area and production but they are time consuming and costly.

Remote sensing (RS) and geographic information system (GIS) are the emerging technologies for generating quicker and easier estimates of acreage and production. Per-pixel based classification algorithms have been extensively used for estimating acreage and production of horticulture crops (Yadav et al., 2002; Nageswara Rao et al., 2004; Paul et al., 2018). Ray et al. (2018) have also tried several image analysis techniques for horticulture crop assessment under the national project called Coordinated Horticulture Assessment & Management using GeoiNformatics (CHAMAN). Advanced geospatial technologies have been applied for expansion of horticulture in the north eastern region of India (Handique et al., 2021).

Realising that the per-pixel methods do not consider the spatial relationships of neighbouring pixels associated with them which in turn results in mixed pixels and inconsistency in the estimates, several researchers tried Object-Based Image Analysis (OBIA) algorithms in the image segmentation phase followed by a variety of classification algorithms for analysis (Lu and Weng, 2007; Blaschke, 2010; Duro et al., 2012., Handique et al., 2020; Stephen et al., 2022). Baharami et al. (2021) have tried several ML algorithms to estimate crop biophysical parameters. Other researchers have tried to improve the accuracy and quality of remotely-sensed information by incorporating ancillary data in the classification process (McIver and Friedl, 2002) including expert systems and neural networks (Qiu and Jensen, 2004). However, there are not many successful studies on identification and area estimation of horticulture crops in our country. Therefore, there is a need for developing an effective methodology of incorporating spectral, spatial and ancillary information.

ML and Artificial Neural Networks (ANN) have taken over statistical modelling techniques in various fields, because of their high performance and capability to solve complex problems, by virtue of their capability to execute a particular task (Khemani, 2013). ANN has been used to classify various types of remotely sensed data and produced results better than those of traditional statistical classification methods (Jiang et al., 2004). In recent years, several researchers have used the Convolutional Neural Networks (CNN) for performing object detection, image segmentation and pattern recognition (Verma and Jana, 2019; Chouhan et al., 2022; Singh et al., 2022) and for mapping Rabi crops using multispectral temporal images of Sentinel-2A/2B sensors (Snighal et al., 2022). CNN is a deep learning algorithm and it considers shape, texture, size, and spatial relationships of objects to extract information from images.

In this study, the CNN, a widely used approach in the field of object recognition and Random Forest (RF) that is computationally less expensive and does not require a graphical processing unit (GPU), were used to develop a methodology to accurately identify and estimate the area of perennial horticulture crops (Mango and Coconut).

2.1 Study area

The Hesaraghatta *Hobli*, a sub-division below the district, in the state of Karnataka (Figure 1) was selected for the study. It is a semi-arid administrative unit having an area of 54 sq.km. It is located at an elevation of 915 meter above mean sea level (msl) and mean annual rainfall of 920 mm. This study area was selected because it has several varieties of fruit crops like Mango, Guava, Banana, Sapota, Papaya, etc developed and promoted by the Indian Institute of Horticulture Research (IIHR) of Indian Council of Agriculture Research (ICAR). The farmers of the study area are very progressive in developing horticulture as an enterprise. IIHR is encouraging farmers to maintain biodiversity in their farming systems so that their economy is climate-resilient. The study area truly represents the heterogeneity that is worth applying AI for object recognition and information extraction from remotely sensed data.

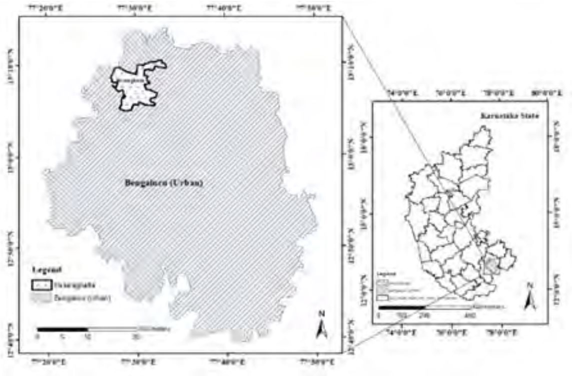

Figure 1. Location of Hesaraghatta hobli shown in the north-western corner of Bangalore Urban District

2.2 Data Sources and Software Used

Spatial data used in the study have come from different sources (Table1). We have used GEE-based cloud computing that gave access to data, algorithms to process, analyse and visualize the spatial data. The GEE had enabled us to handle several gigabytes of raw images without much financial investment on high-performance hardware and software systems. The Tensor Flow (TF), the front end Application Programming Interface (API) developed by Google has several pre-trained models. Google Colab was used as platforms to perform ML. TF, an open source framework developed by Google for predictive analytics, was used to perform deep learning. An open-source API called Keras with user-friendly interface written in Python was used to construct deep learning model on TF. Python-for-Remote Sensing-and GIS (Pyrsgis) library was used to read, write, and export geospatial data in Geotiff format. Skimage library was used for pre-processing of data.

Table 1. Sources of data used in the study

Data Sources	Data product & Date	Spatial / radiometric resolution
Sentinel-2A Multispectral Instrument (MSI)	L-2A, On UTM projection, WGS 84 datum. 23-01-2022	12 spectral bands, 10 mand 20 m / 16 bit
LULC maps from KSRSAC	Vector layers (.shp)2021	1:10,000 scale
Administrative boundaries from K-GIS website.	Vector layers (.shp)	1: 10,000 scale
Ground Truth	April 20 & 25, 2022	Geotagged Photographs
Karnataka State Horticulture Department (KSHD)	Crop Area Statistics	Printed reports

2.3 Spectral signatures of horticulture and associated cover types

Spectral signatures of mango, coconut, scrubland, eucalyptus and other plantations (Figure 2) were generated using the spectral reflectance observed in visible (B,G,R), Red edge, NIR, and SWIR bands of Sentinel-2A MSI. These signatures are very valuable in the selection of appropriate spectral bands during subsequent analysis. We observed significant overlap in spectral reflectance of mango, scrubland and eucalyptus in the wavelength range from 496.6 nm to 740.2 nm and at 864.8 nm. Good separability was observed at 835.1 nm, 1613.7 nm and 2202.4 nm. Coconut and other plantations showed significant overlap with each other from 496.6 nm to 703.9 nm and fairly good separability in other wavelengths. While the open land and fallow cropland signatures were overlapping at 560 nm and 740.2 nm, good separability was observed in other wavelengths. Signatures of grapes overlapped at 664.5 nm and that of fallow land in the 835.1 nm to 864.8 nm.

2.4 Generation of false colour composites (FCCs)

With respect to spectral signatures and in order to get familiarise with the spectral and spatial relationships in the study area, two FCCs were prepared: FCC1 using Near infrared (NIR), Red, and Green bands of spatial resolution 10 meters (m) coloured with red, green, and blue, FCC2 with Rededge-3, Short-Wave Infrared1 (SWIR1), and Short-Wave Infrared2 (SWIR2) resampled to spatial resolution of 10 m coloured with red, green, and blue respectively. These two FCCs (Figure 3 a and b) were used as input to CNN and RF for classification and area estimation of mango and coconut horticulture crops.

2.5 Generation of training samples

In order to enable the algorithm to perform the semantic segmentation (i.e., associating a label or category with every pixel in an image), we have used the land use land cover (LULC) vector map prepared by Karnataka State Remote Sensing Applications Centre (KSRSAC) for year 2021. The map has various LULC classes including mango and coconut in the form of polygons as labelled dataset (Figure 4). The LULC vectors were converted from shape file to Geotiff format with a spatial resolution of 10 metres(m) and used as training sets for analysing FCC1 and FCC2. Since the random access memory (permitted by Colab is only 12 GB), we resorted to patch based approach to generate training samples from the satellite images (Figure 5). In all 768 grids of size 64*64 pixels were used for training and validating the CNN. Each patch of image and its corresponding interpreted LULC map (mask) were used as instances in the model. In case of RF, 84 training and 35 validation samples (total 119) of minimum size of sixteen homogeneous pixels were created based on ground truth.

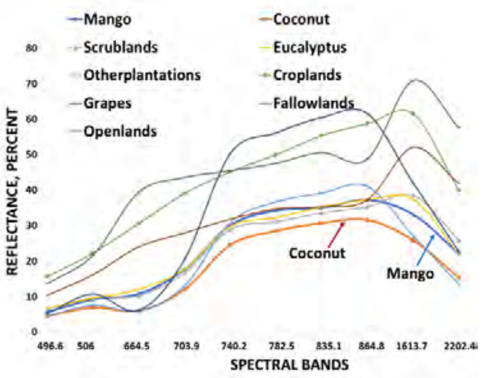

Figure 2. Spectral signature of horticulture crops and associated LULC types of study area

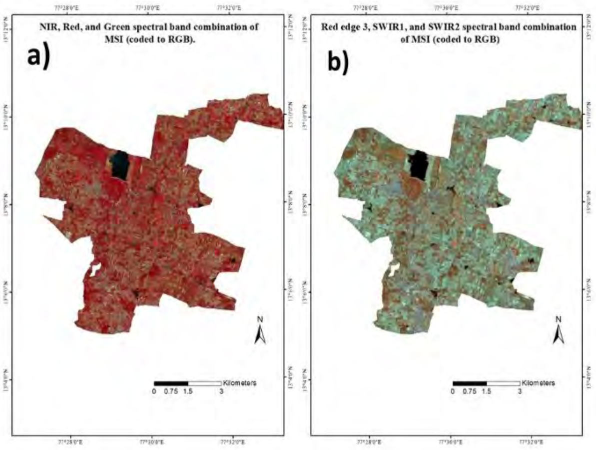

Figure 3. a) False Colour Composite (FCC)-1(all spectral bands of 10m spatial resolution) and b) FCC - 2 (all spectral bands of 20m spatial resolution)

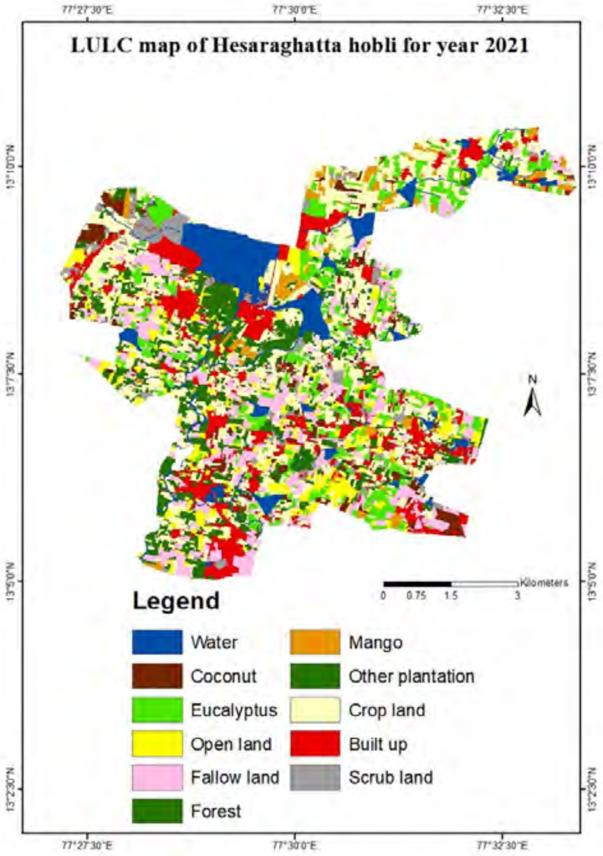

Figure 4. Reference human interpreted map of Mango, Coconut crops and associated LULC type (Source: KGIS project of KSRSAC)

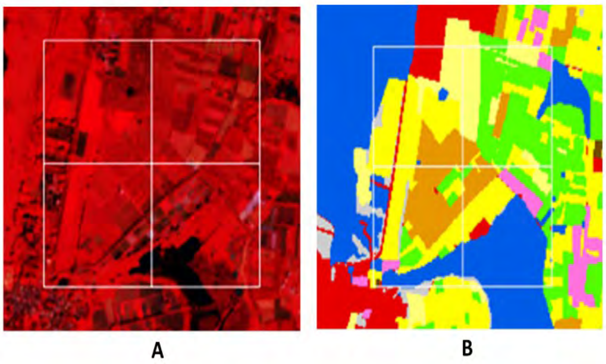

Figure 5. (A) Sample test image of size 64*64*3 and (B) Reference interpreted map (Mask) of size 64*64.

2.6 Area estimation of horticulture crops

Area estimation using RF: The ground truth collected during April 20 & 25, 2022 at 119 locations was separated into two sets of samples for training and validation. The corresponding images were extracted from MSI-Level-2A satellite data: one dataset was used to train the RF and separate dataset for evaluating accuracy of trained RF model. Sequence of steps followed for area estimation of the horticulture crops is given in Figure 6.

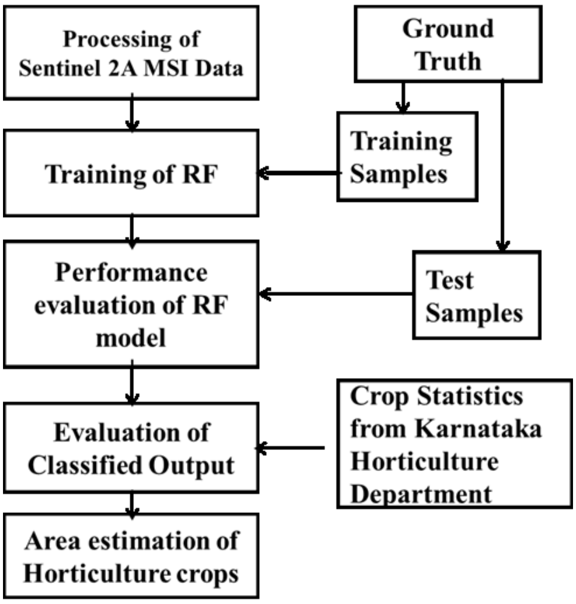

Figure 6. Methodology for area estimation of horticulture crops using RF

Area estimation using CNN: Image chips (from Sentinel - 2A MSI) and mask chips (from the visually interpreted LULC maps) were generated as explained in section 2.5. Pre-processing was carried out using MinMaxScaler of sklearn and converted the masks to categorical features using keras.utils. The data was split into training and validation datasets using sklearn.model_selection. Adam optimizer to minimise the loss, Rectified Linear Unit (ReLu) as the activation function, and several epochs to train the CNN were adopted. The Visual Geometry Group 16 (VGG16) as backbone with pre-trained ImageNet weights in U-net architecture was tried (Ronneberger et al., 2015; Shelhamer et al., 2017; Siddique et al., 2017). In the study, U-net architecture was adopted because it can extract multi-scale spatial and spectral information from remotely sensed images by performing convolution, max-pooling operation and decoding by utilising up-sampling and skip connections (Ge et al., 2021). It has achieved higher accuracies in multi-class classification tasks than other statistical and ML algorithms (TeluguntLa et al., 2018; Belgiu et al., 2016). A moving window of size 64*64 pixels with a minimal overlap of 2 pixels was used with the trained CNN model on the whole image to obtain the classified map. The final classification map was visualised using Matplotlib library and exported using a geospatial python module called Pyrsgis. Only when the validation accuracy exceeded 80%, the model was used for prediction. After training and validating the model, it was also used to perform transfer learning (i.e., testing the efficiency of the model outside the study areas). Sequence of steps followed is in figure 7.

2.7 Accuracy Assessment

Overall classification accuracy in case of RF was assessed as per Congalton and Green (1999) wherein a confusion matrix was created to evaluate and understand the performance of the classifier with both band combinations (FCC1 & FCC2). The diagonal values in the confusion matrix correspond to number of pixels classified correctly. Kappa co-efficient, producer's and user's accuracy were also evaluated from the confusion matrix. In case of CNN, accuracy graph was generated for train and validation data to evaluate the performance of the model and loss graph was generated to evaluate how far is the predicted output with respect to expected output for both band combinations. More details are available in Helber et al. (2017). A comprehensive review of assessing the labeling results can be found in Liu et al. (2018).

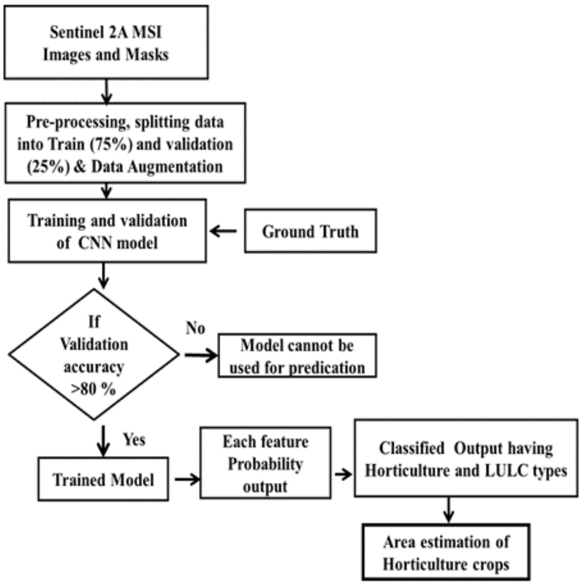

Figure 7. Methodology for area estimation of horticulture crops using CNN

3. Results and discussion

It was observed that the CNN performed better (Table 2 & Figure 8) than RF on FCC1 (10 m spatial resolution) with an overall accuracy of 84% (Figure 9). It seems this algorithm efficiently incorporates the spatial relationships among pixels along with their spectral reflectance in the classification. In case of FCC-2, the performance of CNN was not that good as seen from training and validation accuracy (Figure 10). Hence no further experiments were conducted on FCC2 with CNN. However, the RF performed better (Figure 11) than CNN on FCC2 (20m spatial resolution) with an overall accuracy of 97.65% (Table 3). The CNN was not able to generalise the smaller features within the scene (due mixed pixels) due to coarse resolution, hence resulted in lower accuracy and greater loss.

Table 2. Overall Classification accuracy of RF and CNN using FCC1 and FCC2 of MSI data

Algorithm Used		Overall accuracy (%)	Kappa coefficient
RF	FCC1	82.30	0.80
	FCC2	97.65	0.96
CNN	FCC1	84.00	0.81
	FCC2	50.55	0.48

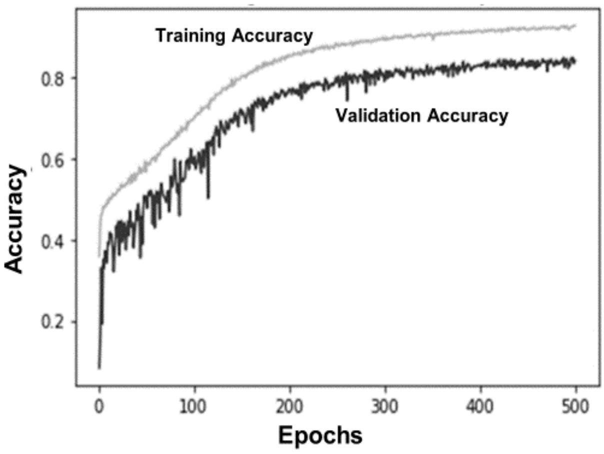

Figure 8. Training and Validation accuracy assessment graphs of CNN on FCC1

Validation of predicted classes (Figure 12) obtained using different band combinations of MSI with RF and CNN algorithms was done with respect to ground truth. As evident from Table 3, mango was identified with an accuracy of 77.7% using CNN (applied on FCC1) and RF (applied on FCC2). Validation accuracy of 100% for coconut was observed with CNN applied on FCC1 while the RF gave an accuracy of 75% and 87.5% for both band combinations. Accuracy of 57-90% was observed for other cover types with both the classifiers.

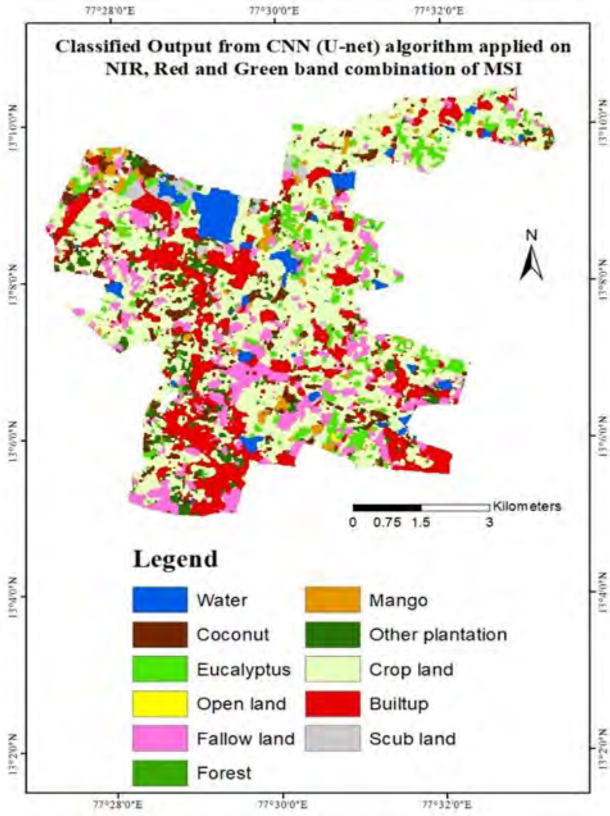

Figure 9. Classified Output using CNN (on U-net architecture) algorithm applied on FCC1

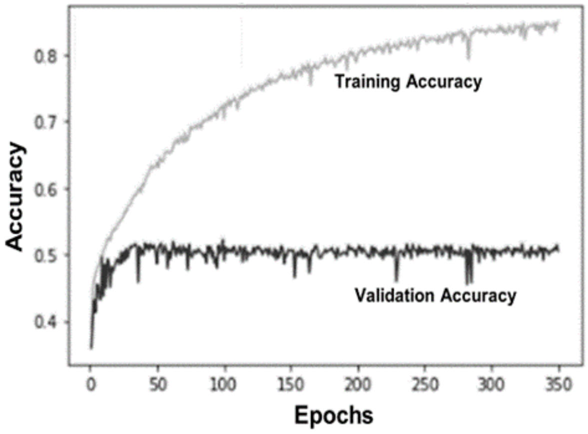

Figure 10. Training and Validation accuracy assessment graph of CNN on FCC2

Table 3. Horticulture Crop Accuracy Assessment using RF and CNN on FCC1 and FCC2

Horticulture / Associated cover types		Accuracy Using RF (%)	Accuracy Using CNN (%)
Mango	FCC1	44.4	77.7
	FCC2	77.7	
Coconut	FCC1	75.0	100
	FCC2	87.5	
Eucalyptus	FCC1	80.0	90
	FCC2	90.0	
Scrub land	FCC1	57.1	71.4
	FCC2	71.4	

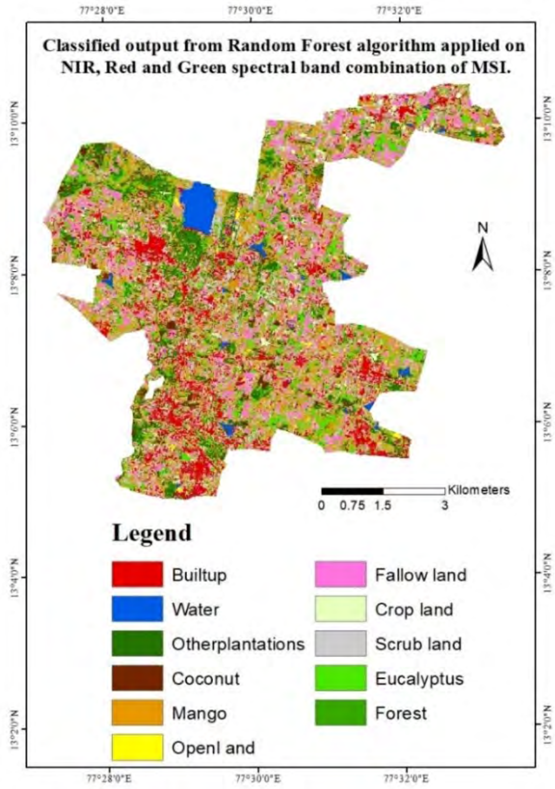

Figure 11. Classified output using RF algorithm applied on FCC1

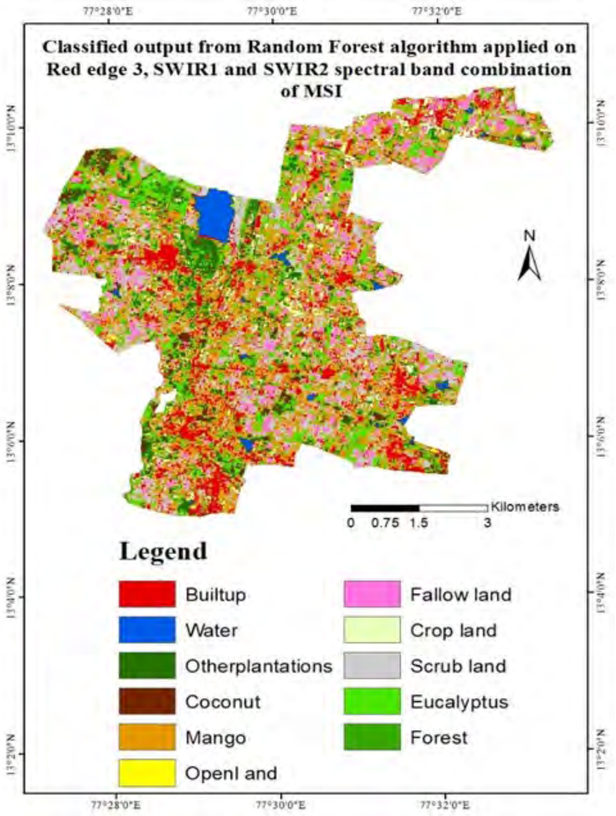

Figure 12. Classified output using RF algorithm applied on FCC2 of MSI data

As evident from Table 4, the area estimation of mango using RF classifier with both band combinations were found to be overestimated, whereas area estimation using CNN (applied on FCC1) was found to be better than RF because of no mixed pixels. The area estimates of coconut were in the range of 314-357 ha using RF with both band combinations, whereas area estimates using CNN with FCC1 data was found to be 310 ha. The relative deviations (RD) are very high because the data supplied by the KSHD are older than RS data and not updated. Our efforts to get exact data from KSHD corresponding to MSI data did not succeed.

It is very encouraging to note that the trained CNN model was found to perform reasonably good transfer learningon two different study areas viz., Kundanahobli of Devanahalli taluk of Bengaluru rural district and Bommathanahalli panchayath of Pavagada taluk of Tumkur district (location maps of these study areas not shown due to space constraint). In the first case, where spatial and spectral variabilities are similar to the study area, the model did better classification of all LULC cover types including mango and coconut horticulture crops. In second case where spatial and spectral variabilities are quite different from that of Hesaraghatta hobli (the present study area), the trained CNN model gave better classification for the cover types which were large in size (in terms of area and contiguity of classes), whereas model failed to identify smaller sporadically distributed fields. This assessment was made based on visual comparison of the predicted output with Google satellite imagery as a reference. Quantification of transfer learning, in terms of overall accuracy, omission and commission errors shall be done in our future research studies.

Table 4. Area estimates using RF on FCC1 and FCC2 and using CNN on FCC1of MSI Data

Crop Cover type		Crop Area (ha)			RD1 %	RD 2 %
		RF	CNN	KSHD@		
Mango	FCC1	1221	125	64	(+) 94.7	(+) 48.8
	FCC2	1652	-		(+) 117.4	
Coconut	FCC1	357	310	118	(+) 66.94	(+) 61.9
	FCC2	314	-		(+) 62.42	

@Karnataka State Horticulture Directorate
Relative Deviation with RF (RD1)={(RS-KSHD) / RS)} * 100., Relative Deviation with CNN (RD2)

4. Conclusions

The CNN-based classification allowed better object detection and improved classification accuracy with 10 meter spatial resolution data. In case of coarse resolution data (20 meter), the CNN algorithm showed good learning accuracy but resulted in low validation accuracy which clearly shows that there was lot of spectral mixing of horticulture gardens which are smaller than the spatial resolution of the sensor. However, the CNN model did well in identifying the built up, water bodies, fallow and other croplands which are large in spatial extent. While the RF-based classification performed well on the coarse resolution (20 m) data, though there were mixed pixels.

The study clearly shows that the ML algorithms provide a means of obtaining rapid and automatic estimation of horticultural crops like mango and coconut that are economically important. The new methods of information extraction from remotely sensed images help in the development of intelligent horticulture information systems to take appropriate decisions in export/import of these commodities and improving the efficiency of their supply chain. It would also help the state-level functionaries (e.g., KSDH) to update their area statistics without much waiting for receiving the information through their administrative hierarchy. The modern algorithms such as ML and deep learning (DL) provide better opportunities for efficiently processing the 'big data having very high spatial (a few centimeters) and temporal resolution (any time) going to be collected by several start-ups using Unmaaned Aerial Vehicles (UAVs).

Acknowledgements

Authors are very grateful to Dr. D.K. Prabhuraj, Director, Karnataka State Remote Sensing Applications Centre (KSRSAC), Bengaluru for providing the laboratory facilities, guidance and encouragement in conducting the research. The authors sincerely thank two anonymous reviewers for their valuable comments and useful suggestions.

References

Baharami H, S Homayouni, A Safari, S Mirzaei, M Mahdianpari and O Reisi-Gahrouei (2021). Deep Learning-Based Estimation of Crop Biophysical Parameters Using Multi-Source and Multi-Temporal Remote Sensing Observations. Agronomy, 11(7), 1363-1385. https://doi.org/10.3390/agronomy1107136

Belgiu M and L Drăguţ (2016). Random forest in remote sensing: A review of applications and future directions. ISPRS Journal of Photogrammetry and Remote Sensing, 114, 24-31.

Blaschke T (2010). Object-Based Image Analysis for Remote Sensing. ISPRS Journal of Photogrammetry and Remote Sensing, 65(1), 2-16.

Chouhan A, A Sur and D Chutia (2022). Aggregated Context Network for Semantic Segmentation of Aerial Images. IEEE International Conference on Image Processing (ICIP), Bordeaux, France, October 16-19, 2022, pp. 1526-1530. https://doi.org/10.1109/ICIP46576.2022.9898016

Congalton RG and K Green (1999). Assessing the Accuracy of Remotely sensed data: Principles and Practices. Lewis Publishers, Boca Raton, London and New York.

Duro DC, SE Franklin and MG Dube (2012). A Comparison of Pixel-based and Object-based Image Analysis with Selected Machine Learning Algorithms for the Classification of Agricultural Landscapes using SPOT-5 HRG Imagery. Remote Sensing of Environment. 118, 259-272.

Ge S, J Zhang, Y Pan, Z Yang and S Zhu (2021). Transferable deep learning model based on the phenological matching principle for mapping crop extent. International Journal of Applied Earth Observation and Geoinformation, 102, 102451. https://doi.org/10.1016/j.jag.2021.102451

Handique BK, C Goswami, P Jena, F Dutta, R Samiam, I Nongrum, D Jha, PLN Raju, CR Deka, R Sarma, K Sarmah, HK Dutta, S Deb, B Yari, S Maibam, H Thanpuii, R Sailo, V Muansangi, D Katiry, T Medo, NP Sharma, B Lepcha, A Roy, BK Bhattacharya, JG Patel, CP Singh, KR Manjunath, MM Kimothi, S Mamatha, P Kumar, P Tahlani and SS Ray (2021). Applications of Advanced Geospatial Technology for Expansion of Area under Horticultural Crops in North-eastern Region of India. Journal of Indian Society of Remote Sensing, 50, 331-345.

Handique BK, C Goswami C, C Gupta, S Pandit, S Gogoi, R Jadi, P Jena, G Borah and PLN Raju (2020). Hierarchical Classification for Assessment of Horticultural Crops in Mixed Cropping Pattern Using UAV-Borne Multi-Spectral Sensor. The International Archives of the Photogrammetry, Remote Sensing and Spatial Information Sciences, XLIII-B3-2020XLIII-B3-2020, pp. 67-74.

Helber P, B Bischke, A Dengel and D Borth (2019). EuroSAT: A novel dataset and deep learning benchmark for land use and land cover classification. IEEE Journal of Selected Topics in Applied Earth Observations and Remote Sensing, 12(7), 2217-2226.

Jiang D, X Yang, N Clinton and N Wang (2004). An Artificial Neural Network Model for Estimating Crop Yields using Remotely Sensed Information. International Journal of Remote Sensing, 25(9), 1723-1732.

Khemani D (2013). A First Course in Artificial Intelligence, McGraw Hill Education (India) Private Ltd, Chennai.

Liu Y, B Fan, L Wang, J Bai, S Xiang and C Pan (2018). Semantic labeling in very high resolution images via a self-cascaded convolutional neural network. ISPRS Journal of Photogrammetry and Remote Sensing. 45 (Part A), 78-95.

Lu D and Q Weng (2007). A Survey of Image Classification Methods and Techniques for Improving Classification Performance. International Journal of Remote Sensing, 28(5), 823-870.

McIver DK and MA Friedl (2002). Using Prior Probabilities in Decision-tree Classification of remotely sensed data. Remote Sensing of Environment, 81, 253-261.

Nageswara Rao PP, HM Ravishankar, U Raj and K Nagajothi (2004). Production estimation of horticulture crops using IRS-1D LISS-III data. Journal of the Indian Society of Remote Sensing, 32(4), 393-398.

Paul NC, PM Sahoo, T Ahmad, RN Sahoo, G Krishna and SB Lal (2018). Acreage estimation of mango orchards using hyperspectral satellite data. Indian Journal of Horticulture, 75(1), 27-33.

Qiu F and JR Jensen (2004). Opening the black box of neural networks for remote sensing image classification. International Journal of Remote Sensing, 25(9), 1749-1768.

Ray SS, S Mamatha, MM Kimothi, P Kumar, S Sehgal, KR Manjunath, BK Bhattacharya, KN Chaudhary, U Raj, K J Hebbar, CS Murthy, R Kameswara, PLN Raju, BK Handique, C Goswami, HP Sharma, KK Singh, AK Upadhyay and M Saxena (2018). Horticultural crops assessment and development using remote sensing. In K.L. Chadha, S.K. Singh, J. Prakash, V.B. Patel (Eds.), Shaping the future of horticulture, Kruger Brentt (1st ed.), pp. 609–623.

Ronneberger O, P Fischer and T Brox (2015). U-net: Convolutional networks for biomedical image segmentation. Medical Image Computing and Computer-Assisted Intervention (MICCAI), Springer, LNCS, 9351: 234-241.

Siddique N, S Paheding, CP Elkin and V Devabhaktuni (2021). U-net and its variants for medical image segmentation: A review of theory and applications. IEEE Access, 9, 82031-82057.

Singh G, S Singh, G Sethi and V Sood (2022). Deep learning in the mapping of agricultural land use using

Sentinel-2 satellite data. Geographies, 2(4), 691-700. https://doi.org/10.3390/geographies2040042

Shelhamer E, J Long and T Darrell (2017). Fully Convolutional Networks for Semantic Segmentation. IEEE Transactions on Pattern Analysis and Machine Intelligence. 39 (4), 640–651.

Snighal M, A Payal and A Kumar (2022). Study of CNN deep learning model for temporal remote sensing data processing to map rabi crops. Journal of Geomatics, 16(2), 167-175.

Stephen S, D Haldar and NR Patel (2022). Impact of various Vegetation Indices on Mango orchard mapping using Object-Based Image Analysis. Journal of Geomatics, 16(2), 159-166.

Teluguntla P, PS Thenkabail, A Oliphant, J Xiong, MK Gumma, RG Congalton, K Yadav and A Huete (2018). A 30-m landsat-derived cropland extent product of Australia and China using random forest machine learning algorithm on Google Earth Engine cloud computing platform. ISPRS Journal of Photogrammetry and Remote Sensing, 144, 325-340.

Verma D and A Jana (2019). LULC classification methodology based on simple Convolutional Neural Network to map complex urban forms at finer scale: Evidence from Mumbai. arXiv preprint arXiv:1909.09774.

Yadav IS, NK Srinivasa Rao, BMC Reddy, RD Rawal, VR Srinivasan, NT Sujatha, C Bhattacharya, PP Nageswara Rao, KS Ramesh and S Elango (2002). Acreage and production estimation of mango orchards using Indian remote sensing (IRS) satellite data. Scientia Horticulture, 93(2), 105–123.

Studies on the variability of mean winds in the mesosphere and lower thermosphere region (MLT) over Kolhapur (16.8ºN, 74.2ºE)

G.P. Naniwadekar[1,2]*, S.Gurubaran[3],A.P.Jadhav[3], R.N.Ghodpage[4], P.T.Patil[4], D.S.Burud[5]
[1]Sou.S.M.Lohia Junior College, Kolhapur, India
[2]Physics Department, Shivaji University, Kolhapur, India
[3]Indian Institute of Geomagnetism, Navi Mumbai, India
[4]M.F. Radar Facility, Indian Institute of Geomagnetism, Shivaji University Campus, Kolhapur, India
[5]Sh. M. M. Patel Institute of Sciences and Research, KadiSarva Vishwavidyalaya, Gandhinagar, India
*Email: naniwadekargouri@gmail.com

(Received: 9th November 2022, Accepted in final form: 10 April 2023)

DOI: *https://doi.org/10.58825/jog.2023.17.1.78*

Abstract: We present the study of mesospheric winds in the 78–98 km height range using observations by a partial reflection radar station (MF–radar) situated at Kolhapur (16.8° N, 74.2° E), India. The sequential wind profiles over the period of 2014–2019 obtained from this radar operated at 1.98 MHz are used for this study. To delineate the behaviour of the winds in the mesosphere and lower thermosphere (MLT) region, we use wind data providing horizontal wind velocities averaged for an hour. Details of the seasonal, annual, and inter-annual variations and also the climatology of mean motion in zonal (East-West) and meridional (North-South) components in the MLT region over the aforementioned period are presented. The zonal wind below 90 km has been observed with eastward flow for the period of solstices and westward flow at equinoxes, showing strong semi-annual oscillations (SAO). While above 90 km, annual oscillations (AO) are seen to be dominant. Annual oscillations (AO) are observed in the mean meridional wind, with poleward motion during winter and equatorward motion during the remaining seasons. At higher altitudes (above 92 km), the poleward motion weakens and the equatorward wind flow becomes strong.

Keywords: Wind profiles, MF (medium frequency) radar, low latitude, MLT region, Annual Oscillation, Semi-annual Oscillation.

1. Introduction

The Earth's tilt with the ecliptic plane and its rotation about its axis are responsible for the unequal heating of the atmosphere between the poles and the equator, resulting in large-scale circulation. Due to this, the wind in the mesosphere-lower thermosphere region (MLT) is expected to flow northward during the day and southward during the night. Similarly, there is an inter-hemispheric flow with trans-equatorial motion from the summer hemisphere to the winter hemisphere at low to mid-latitudes (Patil et al. (2007), for example). The neutral wind flow represents zonal and meridional wind components in a three-dimensional trajectory along with the vertical component. These components can be observed by the MF radar using echoes from the MLT region. The MLT region extends from 60 to 110 kilometres and is part of the middle atmosphere. Atmospheric waves, tides, gravity waves, and planetary waves are well known to affect the dynamical structure of the MLT region (Gurubaran & Rajaram, 2000). Most of them are produced at tropospheric heights and propagate in the upper atmospheric region. As the wave propagates, its amplitudes rise in an exponential way with the falling atmospheric density (e.g., Andrews et al., 1987). Considering the dominating influence of waves in the MLT region, extensive averaging is used to revive the mean wind from the radar observations. As the Coriolis frequency is smaller at low latitudes, many long-period wave modes exist in the equatorial region. Complexities arise owing to the interactions such waves undergo with the mean flow.

Zonal winds in the MLT region exhibit certain dynamical features involving long term atmospheric oscillations like the quasi-biennial oscillations (QBO) with period of around 2 years and semi-annual oscillations (SAO) with period of 6 months (Veryard & Ebdon, 1961; Reed et al., 1965; Hirota, 1978; Andrews et al., 1987). In the equatorial region, the middle atmospheric part is found with long-period waves whose propagation mechanism is studied with the help of satellite data obtained from board Nimbus-7, the Microwave Limb Sounder (MLS), and the Limb Infrared Monitor of the Stratosphere (LIMS) as a part of the UARS (Upper Atmospheric Research Satellite) mission (Salby et al., 1984; Delisi & Dunkerton, 1988; Hitchmann & Leovy, 1986; Canziani et al., 1994). Ground based observations with high temporal resolution have been of great help in understanding the propagation mechanism of long-period oscillations has been studied using equatorial radar (Vincent, 1993; Rajaram & Gurubaran, 1998).

MF radars are known to provide information on the varaibilities of the MLT region with enhanced resolution in time and height (Woodman & Guillen, 1974; Vincent & Lesicar, 1991; Harris & Vincent, 1993; Palo & Avery, 1996). Continuous monitoring of the MLT winds with MF radars is possible at heights above 80 km (Ratnam et al., 2001). The medium-frequency (MF) radar facility in Kolhapur (16.8^0 N, 74.2^0 E) was established in 1999 and has been operated since then by the Indian Institute of Geomagnetism. The system was subsequently upgraded during 2013 with further enhancement of the altitude coverage and improved sensitivity and data quality. The operating frequency of radar systems installed at both the stations

Kolhapur and Tirunelveli (8.7°N, 77.8°E) is 1.98 MHz (Rajaram & Gurubaran, 1998). The mode of operation and the experimental details of these systems are available in the literature (Vincent & Lesicar, 1991). This study is important to understand the various characteristics of wind motions across the MLT region over low latitudes and would contribute to the study of the overall dynamics of this low-to-mid latitude region at various temporal and spatial scales.

2. Observations and Data Analysis

The Kolhapur MF radar is a conventional spaced antenna arrangement that operates at 1.98 MHz and has 32 kW of ultimate power. The Spaced Antenna Technique is the most powerful and economical method for the study of neutral wind patterns, especially in the MLT region. The MF radar probes the most weakly ionised part of the atmosphere by transmitting and receiving radio waves vertically in the height range 70 to 98 km. The radio waves transmitted upward are partially reflected back to the ground due to the presence of an irregularity in the refractive index of the atmosphere. Thus, scattering and reflection processes are responsible for the radar signals returning from the atmosphere.

Figure 1 is the schematic representation of the MF radar system. The main parts of the system are the transmitter, the receiver, and the data acquisition system. The transmitting antenna array is consists of four centre-fed half-wave dipoles, each ~75 m in length, arranged in a square. The receiving antennas are placed in a form of equilateral triangle as shown in figure 1. The height of the transmitting antenna is 30 m, which is one-fourth of the transmitting wavelength above the ground plane. Three receiving antennas are positioned at the vertices of a regular triangle with 180-metre spaces and shaped as an inverted-V type. The radar system is monostatic because the transmitters and receivers are collocated. The operational frequency of the transmitter is 1.98 MHz and offers a constant phase difference. The transmitters are specified with 32 kW of power and a pulse length of 25 µs, along with a 4.5 km height resolution. The pulse repetition frequency is 80 Hz. The receiving and data acquisition system is controlled by the computer controller, which analyses the raw data. In the end, the data after analysis is stored in binary form by the computer controller.

The method of data retrieval is based on the movement of scatterers over the receivers. These movements are being characterized by the Full Correlation Analysis (FCA) method (Briggs et al., 1984). To estimate the background wind vector, three fading signals from the three receiving antennas with different time delays are used. For each of the three fading signals, the auto- correlation and cross-correlation functions were determined by applying the FCA method. This wind vector, known as apparent velocity, is produced without taking into account random variations in the pattern and generally overstates the background wind speed. To determine true velocity, it is adjusted for arbitrary variations in the diffraction pattern. This technique calculates the wind velocities using the ground diffraction pattern generated due to the scattering of transmitted radio signals.

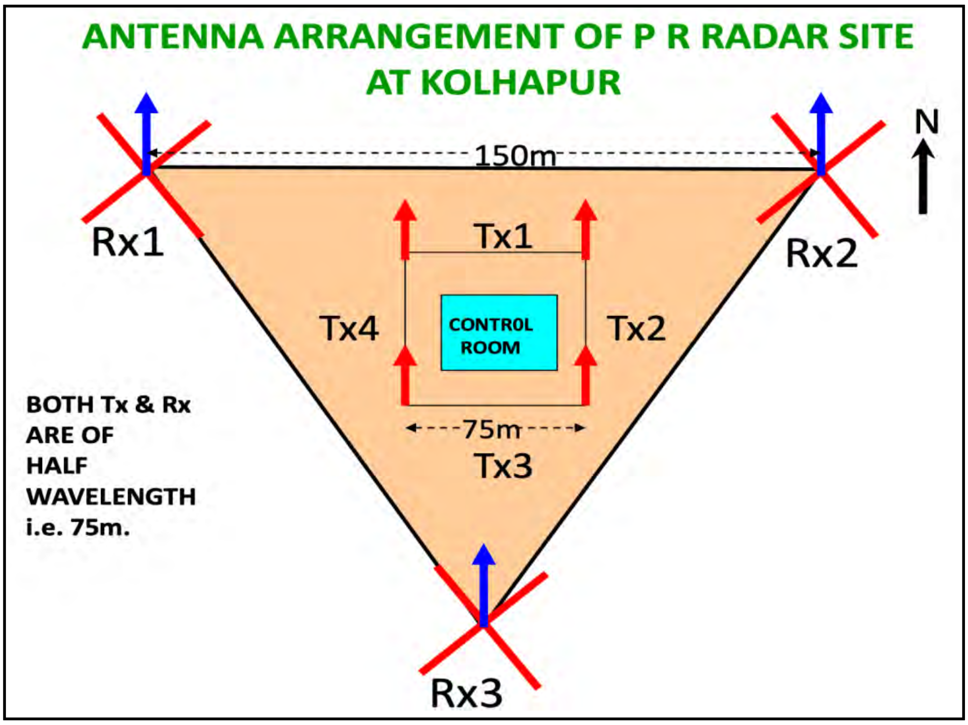

Figure 1. Schematic diagram of the medium-frequency radar system installed at Kolhapur

The full correlation analysis of Briggs is adopted to derive various atmospheric parameters and retrieve information on the spatial and temporal characteristics of the ground diffraction pattern. This radar samples the two components of the horizontal wind between heights of 68 and 110 km with a spatial and temporal resolution of 2 km and 2 min, respectively. Hourly mean winds for each height are utilized in this work for further analysis. Sharma et al. (2018) presented the first results on mean winds observed over Kolhapur, but with limited data sets. For the present work, the height region is restricted to 78–98 km due to poor data quality below 80 km. Recently, Gaikwad et al. (2019) reported the day-to-day variability of the MLT region over Kolhapur caused by planetary-scale waves.

The data for the period July 2014–June 2019 were chosen for the present work. For the purpose of analysis, hourly wind observations are further averaged using the methodology adopted in Rajaram & Gurubaran (1998). The present study is restricted to examining the seasonal variation of mean MLT winds over Kolhapur. For the present purpose, the seasons are considered to be: Summer - from May to August, winter - from November to February; Spring equinox, March and April; Fall equinox, September and October.

3. Results

Mean winds are one of the parameters that are used to describe the state of the atmosphere and its dynamics. Here, we present results from the analysis of wind data obtained from the radar system in terms of mean zonal and Meridional wind components over the altitude of 78–98 km and for the period July 2014 to June 2019.

3.1 Mean Zonal Winds

3.1.1 Composite seasonal variations of mean zonal winds over Kolhapur:

Figure 2 depicts the time–height contours showing prevailing zonal wind patterns over the chosen period. For this analysis, we use the monthly mean wind velocities to represent the monthly variations over the five-year period**.**

In Figure 2, the contours of the mean flow with positive values represent the eastward component of the zonal winds, while the negative values represent the westward component. The plots clearly highlight the altitude dependence of the mean zonal flow. The winds are largely westward during the equinoxes (March-April and September-October) at lower altitudes (86 km) and eastward during the solstice's months at higher altitudes (> 86 km). At lower altitudes, the flow is weaker during the summer months. Large eastward wind speeds exceeding 20 m/s are noticed during the winter months of December and January at altitudes below 84 km. The largest westward wind speeds are 35 m/s during the equinox months. In general, at lower altitudes, the westward wind flow is stronger than the eastward wind flow, while at higher altitudes, the eastward wind flow is stronger. An important feature to be noted is that at lower elevations, we observe a semi-annual type of variation, while at higher elevations (above 90 km), the variation is typically annual. Hereafter, we denote the semi-annual type of variation as SAO and the annual type as AO. At lower heights, SAO is stronger and becomes weaker with increasing altitude. The study emphasizes that AO is stronger at higher altitudes.

3.1.2 Averaged Seasonal Variations in Mean Zonal Wind over Kolhapur

Figure 3 reveals the seasonal component of the zonal wind averaged over 5 years, i.e., July 2014 to June 2019. Altitude profiles clearly show the eastward and westward winds in winter and summer, respectively. Winds are stronger westward during the spring equinox compared to the fall equinox. The wind directions during different seasons are more distinct and clear at altitudes below 90 km. At higher altitudes, winds change direction and exhibit opposite behaviour to those at lower altitudes. The averaged wind velocities vary from -30 m/s to 15 m/s (Figure 4). The winds are larger in magnitude at lower altitudes, and a clear seasonal dependence of the wind velocities can be seen.

3.1.3 Long term variations in mean zonal wind

The monthly mean MLT wind over Kolhapur for the period 2014–2019 is presented in contour form with a time-height cross-section of monthly averaged zonal winds in the altitude range 78–98 km. The contour plot confirms the dominance of the SAO at a lower height and the AO at higher heights. There is an inter-annual variability superimposed on the wind fields on the annual and semi-annual time scales. Also, the westward maximum occurring in the Spring equinox (March-April) is stronger as compared to that occurring in the fall equinox (September-October). Similarly, the eastward motion observed during the December-January solstice period is stronger than that observed during the June-July summer solstice period. Largest eastward and westward wind speeds are observed during the December–January months of 2016–2017 and during the following spring equinox months of March–April, respectively. Considering the dominance of SAO at lower altitudes, the MLT region over Kolhapur behaves very much like a low latitude/equatorial site with its characteristic SAO. On the other hand, the motion at higher altitudes, with its characteristic annual oscillation, resembles that observed at mid-latitudes.

3.2 Mean Meridional winds

3.2.1 Composite seasonal variations of mean meridional winds over Kolhapur

The monthly composite seasonal variations of mean meridian wind over Kolhapur in the altitude region of 78–98 km representing the chosen five-year period are plotted in Figure 5, with positive values representing northward motion and negative values representing southward motion. From this plot, it can be seen that at lower heights (90 km), the wind motion tends to reflect an annual variation, but at higher altitudes (> 90 km), the motion is largely southward (largest speeds in the range of 15–25 m/s) but for a weak northward (pole ward) motion (speeds in the range of 0–5 m/s) during the winter months. As was expected, the wind motion is northward during the winter, while during the summer, the wind flows in the opposite direction, as the radar site is situated in the Northern Hemisphere.

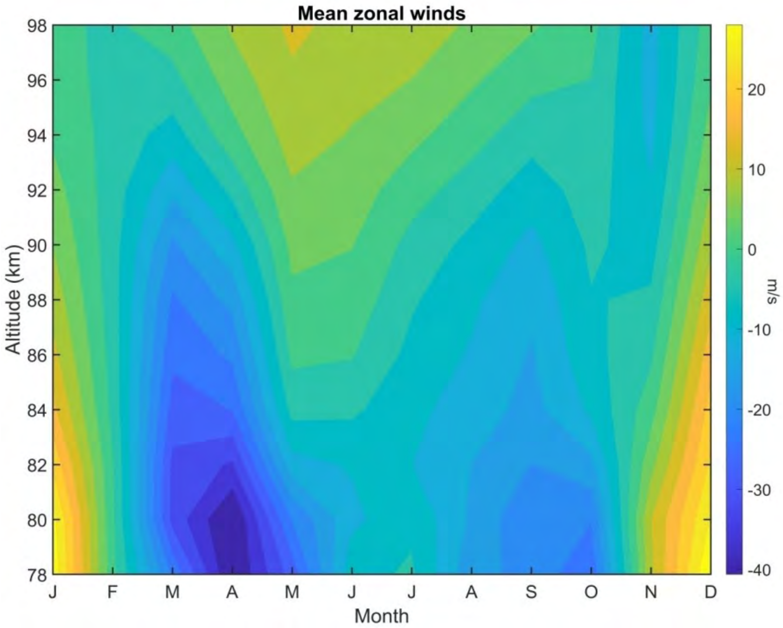

Figure 2. Composite seasonal behaviour of the zonal winds in the altitude 78 - 98 km over Kolhapur.

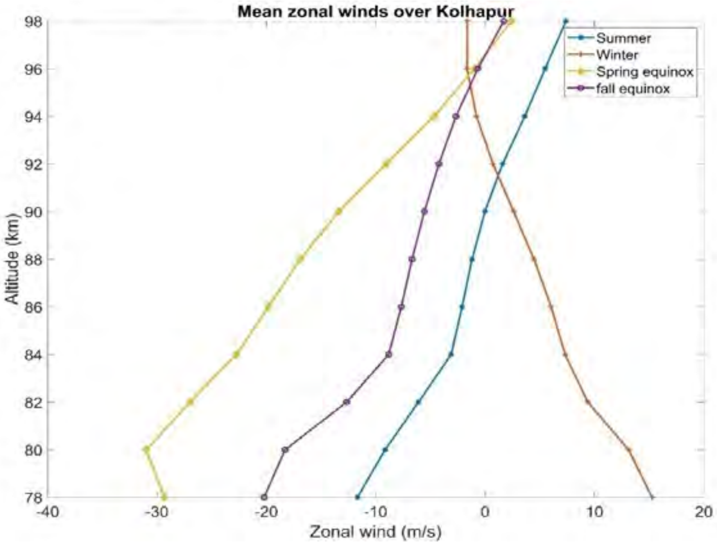

Figure 3. Seasonally averaged zonal wind over Kolhapur for the year 2014-2019

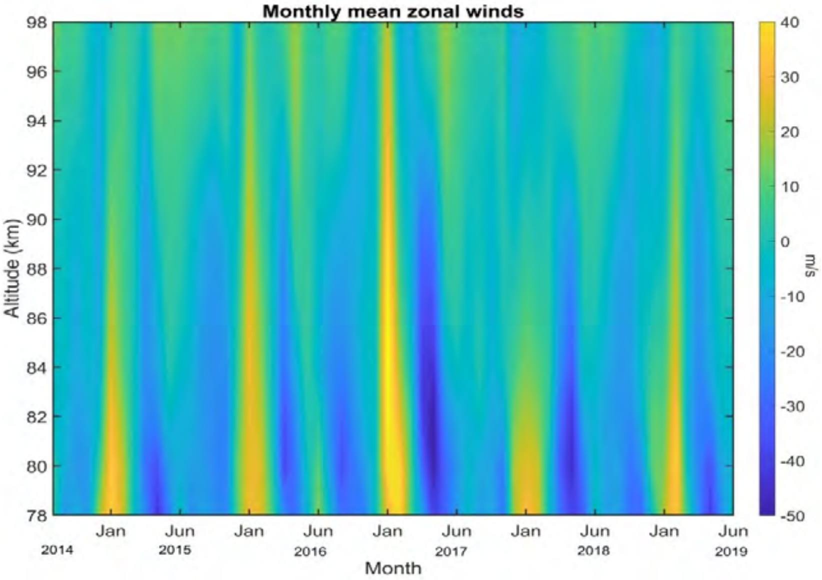

Figure 4. The time-height representation of monthly averaged zonal winds during 2014-2019 for heights 78-98 km

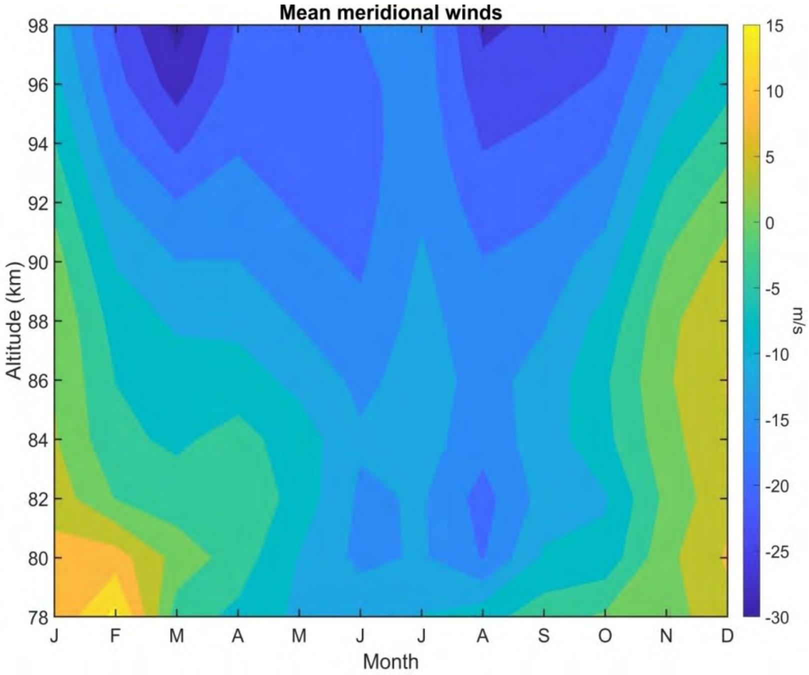

Figure 5. Composite seasonal behaviour of the Meridional winds in the altitude range of 78-98 km over Kolhapur

3.2.2 Averaged Seasonal Variations in Mean Meridional Wind over Kolhapur

Figure 6 plots the seasonal mean flow in the meridional direction for 5 years. Unlike zonal wind vertical profiles, meridional winds do not show much variation with respect to altitude. Seasonal variations have a considerable impact on wind magnitudes. The mean winds vary seasonally between -20 m/s and 5 m/s. The southward winds during the spring equinox become more southward as summer approaches and then turn northward during the winter. This shows the effect of seasons on the meridional component of winds and pole-to-pole circulation.

3.2.3 Long term variations in mean meridional winds

Figure 7 represents the monthly mean meridian winds across the altitude range of 78–98 km from July 2014 to June 2019. The contour plot depicted herein clearly shows the annual oscillation (AO) in the mean meridian wind during the chosen years. Throughout the winter, it has been noted that the meridional wind advances northward, and at nearly all other times, the wind motion is southward. Above 94 km in height, it is observed that the wind constantly flows in the southward direction. The largest southward motions are indeed observed at these heights. The wintertime northward wind speeds are in the range of 10-15 m/s, which are somewhat weaker than the 25–30 m/s southward wind speeds observed during the summer months on the monthly time scales. A persistent feature has been that during the month of January every year, a strong poleward wind motion occurs below 84 km. The northward motion seems to occur one month earlier at higher altitudes.

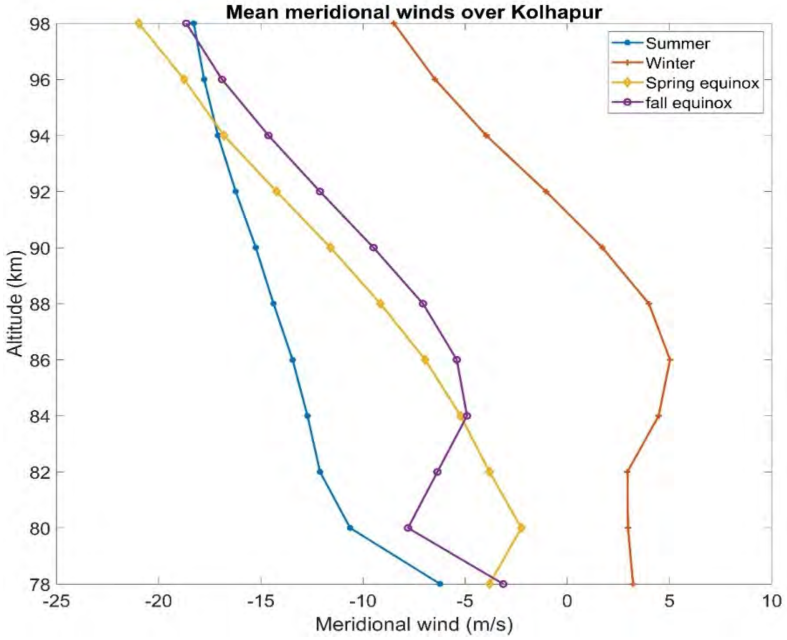

Figure 6. Seasonally averaged meridional wind over Kolhapur for the year 2014-2019

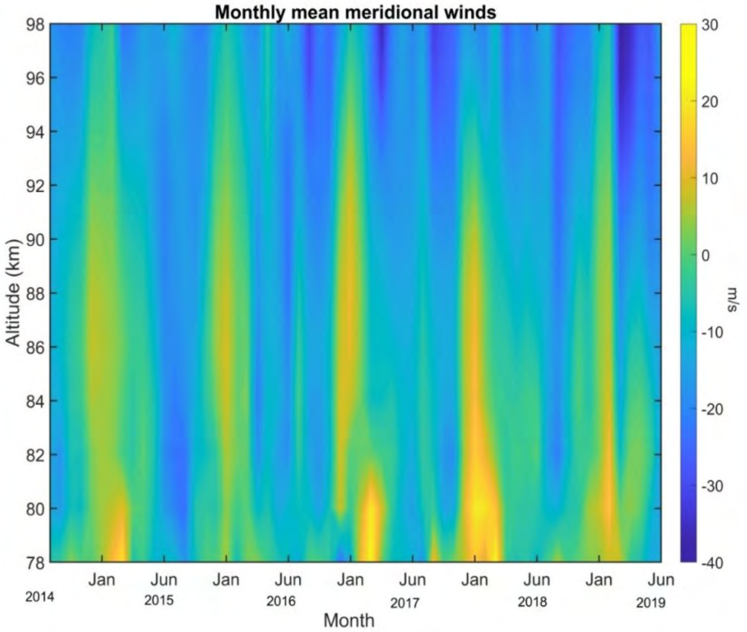

Figure 7. The time-height representation of monthly averaged meridional winds during 2014-2019 for heights 78-98 km

4. Discussion and Conclusion

Medium-frequency (MF) radars are among the powerful tools yielding valuable information about the dynamic processes occurring in the low-latitude and equatorial mesosphere. The data used in this work is from the MF radar operated at Kolhapur. The analysis carried out was for the period July 2014 to August 2019. The main goal of the current analysis was the study of mean wind variations and the seasonal variation over Kolhapur. In particular, MLT mean zonal and meridional winds are examined on monthly time scales, and the seasonal variations and the altitudinal dependence of the seasonal transitions in mean winds are brought out in this work.

The semi-annual variation in the mean zonal wind, especially at lower altitudes, is a distinct feature that is reported. The SAO is characterised by westward flow during equinoxes and eastward flow during solstices, a well-known feature reported from equatorial sites (Rajaram & Gurubaran, 1998, for example). On the other hand, at higher altitudes, an annual type of oscillation is observed. There is a tendency for interannual variability in the occurrence of SAO. For example, the westward motions during the April equinox period of 2017 and the eastward motions during the December/January winter solstice of 2016/2017 were more intense than during the previous and subsequent years. An interannual variation of this kind is a defining trait of the MLT zone near the equator. The seasonal asymmetry in SAO, for example, in the westward flow between the two equinoxes or in the eastward flow between the two solstices, is also a notable feature reported in this work.

The mean meridional wind flow, in contrast to the mean zonal wind, indicates the presence of inter-hemispheric flow that is caused by the uneven solar heating of the two hemispheres. A northward move in the winter and a southern motion at other times define the yearly cycle of meridional flow. In the annual meaning, there is also a separate time-mean flow. More crucially, as one rises in height, the southerly (equatorward) wind becomes stronger. It is clear that the meridian winds consistently rely on altitude over the course of all the years, with little inter-annual variation in this behaviour.

The seasonal variation in the monthly mean meridional wind component follows a consistent pattern year after year: northward motion during winter months and southward motion during summer months. These observations are similar to the previous outcomes reported from Tirunelveli by Rajaram & Gurubaran (1998) and from Gadanki by Ratnam et al. (2001). SAO in mesosphere as well as in stratosphere display seasonal variation and exhibit similar behaviour. The first cycle of the stratospheric SAO, which starts with the westward phase in the winter of the Northern Hemisphere, is more powerful than the second cycle, which starts with the westward phase in the winter of the Southern Hemisphere. Variations in extratropical planetary wave forcing, which are stronger in the northern winter than the southern winter, are the source of this asymmetrical behaviour (Hitchman & Leovy, 1986; Delisi & Dunkerton, 1988). Burrage et al. (1996) used data from the UARS (Upper Atmospheric Research Satellite) program to discover interannual variations for the first time. The current study provides compelling evidence supporting this conclusion. . With four years (1993-1996) of MF radar data, Rajaram & Gurubaran (1998) previously noticed this distinctive characteristic over Tirunelveli.

In summary, a comprehensive overview of mean winds over Kolhapur using a 5-year database is presented here with distinct features that resemble more of the behaviour reported for equatorial sites. Though this is the case for the zonal wind, the meridional wind over Kolhapur behaves like that over mid-latitude sites. In particular, the annual mean Meridional wind at the highest altitudes sampled by the radar reveals a large southward component and if this prevailing wind feature exists at mid-latitudes needs to be seen. With the help of a comparatively longer database, the present analysis brings out some supplementary structures.

Acknowledgements

The Indian Institute of Geomagnetism (IIG), Navi Mumbai, an autonomous organization under the Department of Science and Technology (DST), New Delhi, Government of India, provided assistance for the scientific effort detailed in this article. MF Radar observations were carried out as part of a scientific collaboration programme (MoU) between the IIG, Navi Mumbai, and Shivaji University, Kolhapur.

References

Andrews DG, JR Holton and CB Leovy (1987). Middle atmosphere dynamics, Academic Press.

Briggs BH (1984). The analysis of spaced sensor records by correlation techniques, Middle Atmosphere Program: Handbook for MAP., 13, 166-184.

Burrage MD, RA Vincent, HG Mayr, WR Skinner, NF Arnold and PB Hays (1996). Long-term variability in the equatorial middle atmosphere zonal wind, Journal of Geophysical Research: Atmospheres, 101(D8), 12847-12854.

Canziani PO, JR Holton, E Fishbein, L Froidevaux and JW Waters (1994). Equatorial Kelvin waves: a UARS-MLS view, Journal of the Atmospheric Sciences, 51(20), 3053-3076.

Delisi DP and TJ Dunkerton (1988). Seasonal Variation of the Semiannual Oscillation, Journal of the Atmospheric Sciences, 45(19), 2772–2787.

Gaikwad HP, AK Sharma, OB Gurav, GA Chavan, DP Nade, PT Patil, SS Nikte and GP Naniwadekar. (2019). Seasonal, annual and interannual variability in MLT Quasi Two Day Waves over low latitude region Kolhapur (16.8^{O} N; 74.2^{O} E), Advances in Space Research, 63(7), 2100-2117.

Gurubaran S and R Rajaram (2000). Signatures of equatorial electrojet in the mesospheric partial reflection drifts over magnetic equator, Geophysical Research Letters, 27(7), 943-946.

Harris TJ and RA Vincent (1993). The quasi-two-day wave observed in the equatorial middle atmosphere, Journal of Geophysical Research: Atmospheres, 98(D6), 10481-10490.

Hirota I (1978). Equatorial Waves in the Upper Stratosphere and Mesosphere in Relation to the Semiannual Oscillation of the Zonal Wind, Journal of the Atmospheric Sciences, 35(4), 714–722.

Hitchman MH and CB Leovy (1986). Evolution of the Zonal Mean State in the Equatorial Middle Atmosphere during October 1978-May 1979, Journal of the Atmospheric Sciences, 43(24), 3159-3176.

Palo SE and SK Avery (1996). Observations of the quasi-two-day wave in the middle and lower atmosphere over Christmas Island, Journal of Geophysical Research: Atmospheres, 101(D8), 12833-12846.

Patil PT, S Gurubaran, R Rajaram, AK Sharma and RV Bhonsle (2007). Mesospheric winds from 70 to 98 km altitude over low latitude station Kolhapur by a partial reflection radar, Bulletin of the Astronomical Society of India, 35, 561-568.

Rajaram R and S Gurubaran (1998). Seasonal variabilities of low-latitude mesospheric winds, Annales Geophysicae, 16, 197-204.

Ratnam MV, DN Rao, TN Rao, S Thulasiraman, JB Nee, S Gurubaran and R Rajaram (2001). Mean winds observed with Indian MST radar over tropical mesosphere and comparison with various techniques, Annales Geophysicae, 19(8), 1027–1038.

Reed RJ (1965). The quasi-biennial oscillation of the atmosphere between 30 and 50 km over Ascension Island, Journal of the Atmospheric Sciences, 22(3), 331-333.

Salby ML, DL Hartmann, PL Bailey and JC Gille (1984). Evidence for equatorial Kelvin modes in Nimbus 7 LIMS, Journal of the Atmospheric Sciences, 41(2), 220-235.

Sharma AK, HP Gaikwad, MV Ratnam, OB Gurav, L Ramanjaneyulu, GA Chavan and S Sathishkumar (2018). Diurnal, monthly and seasonal variation of mean winds in the MLT region observed over Kolhapur using MF radar, Journal of Atmospheric and Terrestrial Physics, 169, 91-100.

Veryard RG and RA Ebdon (1961). Fluctuations in tropical stratospheric winds, Meteorology Magazine, 90, 125-143.

Vincent RA (1993). Long-period motions in the equatorial middle atmosphere, Journal of Atmospheric and Terrestrial Physics, 55(7), 1067-1069, 1071-1080.

Vincent RA and D Lesicar (1991). Dynamics of the equatorial mesosphere: First results with a new generation partial reflection radar, Geophysical Research Letters, 18(5), 825-828.

Woodman R F and A Guillen (1974). Radar Observations of Winds and Turbulence in the Stratosphere and Mesosphere, Journal of the Atmospheric Sciences, 31(2), 493-505.

Journal of Geomatics Vol. 17, No. 1, April 2023

Static-PPP Performance using Multi-GNSS (Single, Dual and Triple) Frequency Observations

Ashraf Farah[1, 2,*]
[1] College of Engineering, King Saud University, Riyadh, KSA
[2] College of Engineering, Aswan University, Aswan, Egypt
*Email: afarah@ksu.edu.sa

(Received: 16 May 2022; Accepted in final form: 12 December 2022)

DOI- *https://doi.org/10.58825/jog.2023.17.1.80*

Abstract: Precise Point Positioning (PPP) is relatively modern GNSS positioning technique that proved its efficiency comparing with traditional Differential positioning technique for more than three decades. PPP requires only one receiver collecting observations at unknown station, while Differential technique requires two receivers collecting observations simultaneously one at known-position station and the other at unknown station. Extensive mitigation of different GNSS errors is essential for PPP-collected observations. Static-PPP accuracy depends on different factors such as; used GNSS system; single (GPS(G) or GLONASS(R) or BeiDou(C) or Galileo(E)) or mixed-GNSS systems (GPS/GLONASS or GPS/GLONASS/BeiDou or GPS/GLONASS/BeiDou/Galileo), observations type (single or dual or triple frequency), satellites geometry and observations duration. This research investigates static-PPP accuracy variation on three different-latitude IGS stations based on different factors; used GNSS system (single or mixed), observations type (single or dual or triple frequency) and satellites geometry. It can be concluded that GRCE combination provides 3D-accuracy of (8 cm) using single frequency observations, (1.5 mm) using dual frequency observations and (1 mm) using triple frequency observations. GRCE combination provides a convergence time of only four minutes (8 epochs) for dual frequency observations.

Keywords: Multi-GNSS, Static-PPP, Single frequency, Dual frequency, Triple frequency

1. Introduction

GNSS users consider Differential Positioning the sole accurate positioning technique for many decades. Differential positioning provides the highest accuracy with many limitations. The limitations mainly encompasses; the need for a reference station (known coordinates), the distance limitation between the rover and reference station, and the need for simultaneous observations between the reference and rover stations. Differential positioning's limitations increase its cost over autonomous positioning (Hofmann-Wellenhof and Lichtenegger, 2008). Single Point Positioning (SPP) where observations are collected only at the unknown station, computes the unknown position without applying any corrections to errors faced by GNSS signals. SPP is not suitable for engineering applications because the accuracy is too bad. The need was essential for a cost-effective positioning technique that provides acceptable accuracy for many GNSS applications. Precise Point Positioning (PPP) technique met the requirements of this need (Chen and Gao, 2005; Leandro, 2009; Farah, 2013; Farah, 2014).

PPP is a cost-effective standalone positioning technique, requires a single GNSS receiver. PPP uses un-differenced, differenced single and dual frequency pseudorange and carrier-phase observations along with precise satellite orbit and clock products to produce decimeter to sub-centimeter positioning in real-time and post-processing (Bisnath and Gao, 2008; Cai, 2009; Soycan, 2012; Ding et al., 2018; Du et al., 2021).

Researches continue their effort during more than two decades to increase the accuracy provided by PPP. PPP accuracy depends mainly on used GNSS systems (single or mixed), observations type (single or dual or triple frequency), duration of observations, satellites geometry and processing software capabilities. PPP's achieved accuracy could benefit from advancement and modernization of satellite constellations. Since start of 2021, PPP users could depend on four different GNSS constellations; (GPS, GLONASS, BeiDou and Galileo). PPP accuracy could improve a lot by depending not only in one constellation but different mixed constellations such as (GPS/GLONASS or GPS/GLONASS/BeiDou or GPS/GLONASS/BeiDou/Galileo). Those different mixed constellations provide different types of observations (single or dual or triple) frequency observations. Capabilities of PPP- processing software affect resulted PPP-accuracy for different types of observations and different GNSS systems. Many online PPP-processing services are there for PPP users (CSRS-PPP, GAPS, APPS and magicGNSS) (Farah, 2016) and Net_Diff service (Net_Diff, 2021).

2. NET_DIFF Online PPP/RTK Service

Net_Diff (Github, 2021) is software for GNSS Download, Positioning and Analysis. It enables users to perform SPP/PPP/PPP-AR/DSPP/DPPP/RTK/PPP-RTK (Yize, 2018; Hamed et al., 2019). All the signals of the current GPS/GLONASS/BeiDou/Galileo/QZSS/IRNSS are supported from single-frequency to triple-frequency. It can also be applied in SPP/PPP with BeiDou augmentation information (authorized user). It supports data analysis, including coordinate plotting, coordinate comparison, satellite number, PDOP, satellite sky view, satellite visibility, cycle-slip, troposphere, ionosphere, observation minus correction, positioning residuals plotting and KML file writing. It provides GNS observation data and products download from many public FTP servers.

Net_Diff provides online PPP/RTK Service (Net_Diff, 2021). For GPS/GLONASS/BeiDou/ Galileo/QZSS, the single-frequency indicates L1/G1/B1/E1/L1; dual-frequency indicates L1L2/ G1G2/B1B3/E1E5a/L1L2; triple-frequency indicates L1L2L5/G1G2G3/B1B2B3/ E1E5aE5b/L1L2L5. Table 1 presents PPP processing parameters used in Net_Diff. software. The advantages of Net_Diff. service over other PPP-services is its ability to process observations from all available systems (GPS/GLONASS/BeiDou/Galileo/QZSS/IRNSS) with different combinations between those systems as well as its ability to process different-frequency observations (single/dual/triple). Those two advantages are ideal for research purposes.

Table 1. PPP processing parameters used in Net_Diff. service

Reference System	ITRF2008
Coordinate format	ENH (UTM)
Satellite orbit and clock ephemeris source	CODE final 30 sec. for clock 15 min for orbits
Satellite phase center offset	IGS ANTEX
Receiver phase center offset	IGS ANTEX
Tropospheric model	Saastamoinen
Meteorological model	GPT
Mapping function	Global Mapping Function (GMF)
Ionospheric model	Final Global Ionospheric Maps (GIM) from IGS
Mask angle	10º
Observation type	Code + Phase
System	GPS/GLONASS/BeiDou/Galileo/ QZSS/IRNSS
Frequency	Single/Dual/Triple
Processing mode	Static
Estimation method	Kalman Filter

3. Test Study Scope

The study investigates static-PPP accuracy under different parameters.

Table 2. Tested IGS stations' geographic coordinates (IGS, 2021).

IGS Station	Latitude (Deg. Min. Sec)	Longitude (Deg. Min. Sec)	Ellips. Height (m)
DGAR	S 07° 16' 10.86"	E 72° 22' 12.86"	-64.746
GAMG	N 35° 35' 24.25"	E 127° 55' 10.77"	927.965
MAR7	N 60° 35' 42.19"	E 17° 15' 30.38"	74.300

Those parameters are; used system (single or mixed), observation type (single or dual or triple) frequencies and satellite geometry. Single system includes (GPS or GLONASS or BeiDou or Galileo). Mixed systems include (GPS/GLONASS or GPS/GLONASS/BeiDou or GPS/GLONASS/BeiDou/ Galileo). Seven days during GPS week (2156) (2-8, May, 2021) were processed from three different-latitude IGS stations (IGS, 2021) (Table 2) with 30 sec. observation interval. The different processed observation files were extracted from stations' rinex files using TEQC software (TEQC, 2021). Table 3 presents average number of visible satellite, average PDOP and average GDOP for the tested three stations during the tested week

Table 3. Average (no. visible satellites, PDOP, GDOP) for tested IGS stations during GPS week (2156).

IGS Station	System	Average no. visible satellites	Average PDOP	Average GDOP
DGAR	G	9	1.811	2.035
	R	6	2.988	3.377
	C	11	2.037	2.435
	E	7	2.196	2.468
	GR	16	1.345	1.695
	GRC	27	1.002	1.445
	GRCE	35	0.876	1.402
GAMG	G	8	1.935	2.221
	R	6	2.895	3.332
	C	9	2.824	3.436
	E	6	2.461	2.841
	GR	15	1.392	1.808
	GRC	25	1.154	1.711
	GRCE	31	0.992	1.630
MAR7	G	9	1.870	2.112
	R	7	2.128	2.430
	C	4	9.629	11.160
	E	7	2.146	2.420
	GR	17	1.297	1.664
	GRC	21	1.145	1.637
	GRCE	29	0.977	1.559

4. Study Results

4.1 Single Frequency Static-PPP Positioning

3D-position error from true coordinates of Static-PPP precision for different single frequency observations from different; single systems (GPS(G), GLONASS(R), BeiDou(C) and Galileo(E)) and mixed systems (GPS/GLONASS (GR) GPS/GLONASS/BeiDou (GRC) and GPS/GLONASS/BeiDou/Galileo (GRCE)) starting from DOY 122 down to DOY 128 of GPS week 2156 resulting from this study are presented graphically (Figure 1) for the three tested IGS stations.

4.2 Dual Frequency Static-PPP Positioning

3D-position error of Static-PPP precision for different dual frequency observations from different; single and mixed systems (G, R, C, E, GR, GRC, GRCE) for DOY 122 down to DOY 128 of GPS week 2156 resulting from this study are presented in (Figure 2) for the three tested IGS stations.

4.3 Triple Frequency Static-PPP Positioning

3D-position error of Static-PPP precision for different triple frequency observations from different; single and mixed systems (G, R, C, E, GR, GRC, GRCE) for DOY 122 down to DOY 128 of GPS week 2156 resulting from this study are presented (Figure 3) for the three tested IGS stations.

4.4 Convergence Time Effect

The convergence time of static-PPP solution is affected by number of used satellites and used observations which are dependent on used systems. More GNSS systems mean more observed satellites and more observations. To show the effect of using multi-GNSS on convergence time, the 3D accuracy difference from true coordinates was plotted (Figure 4) for station (DGAR) on (GPS day 21560) based on dual frequency observations solution. Table 4 presents 3D-Convergence time (10 cm-3D accuracy comparing with true coordinates) from Static-PPP solutions using dual-frequency observations from different systems for station (DGAR) for (GPS day 21560).

Table 4. 3D Convergence time (10 cm-3D accuracy comparing with true coordinates) from Static-PPP solutions using dual-frequency observations from different systems for station (DGAR) for (GPS day 21560).

IGS Station	System	Convergence time (hh:mm:ss)
DGAR	G	00:15:30
	R	04:43:30
	C	00:12:30
	E	01:48:00
	GR	00:23:00
	GRC	00:07:30
	GRCE	00:04:00

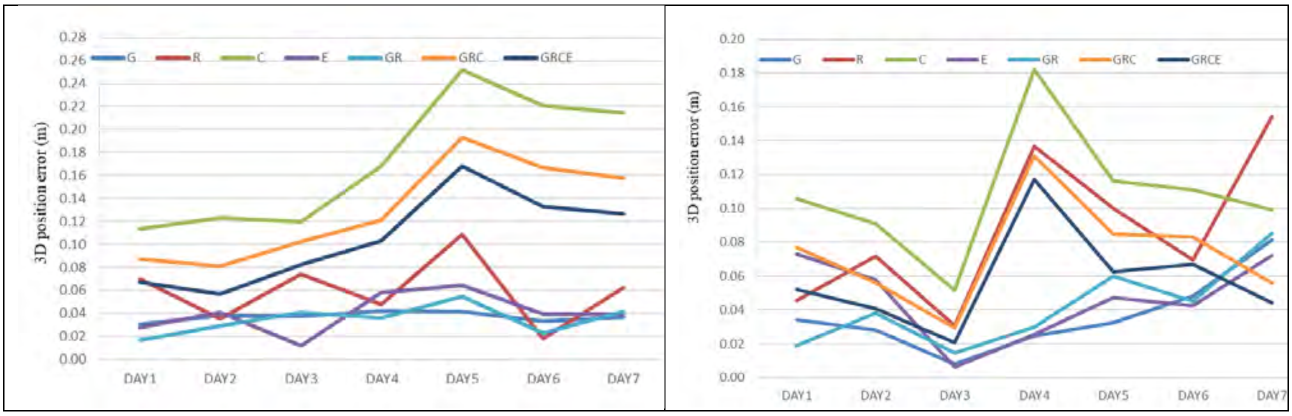

a) DGAR **b) GAMG**

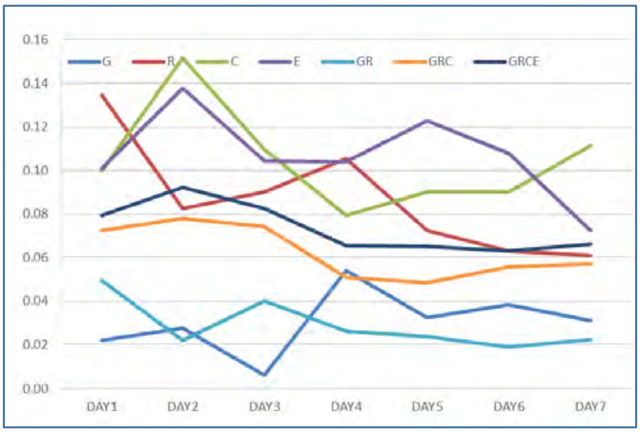

c) MAR7

Figure 1. Static-PPP 3D-Position precision using single-frequency for GPS week (2156) of station

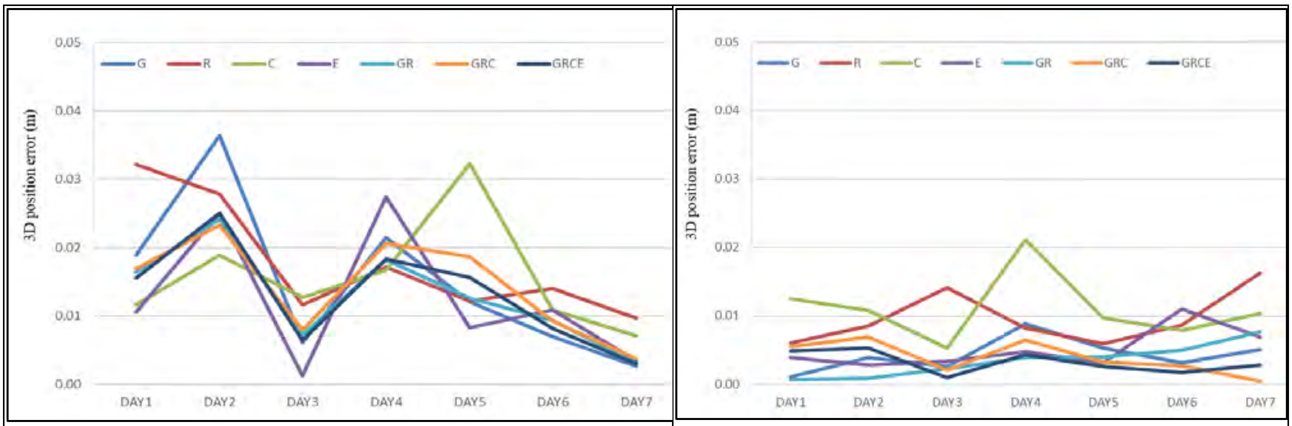

a) **DGAR** b) **GAMG**

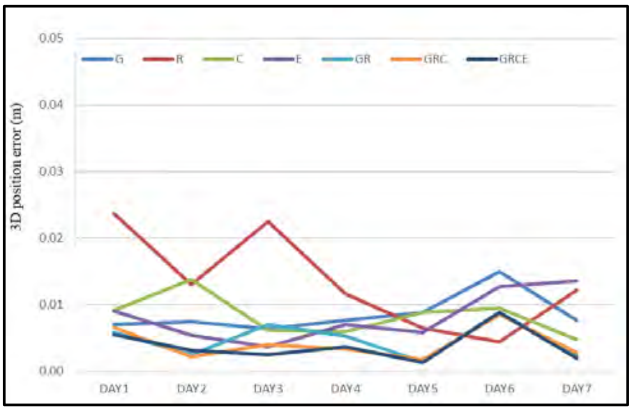

c) **MAR7**

Figure 2. Static-PPP 3D-Position precision using dual-frequency for GPS week (2156) of station

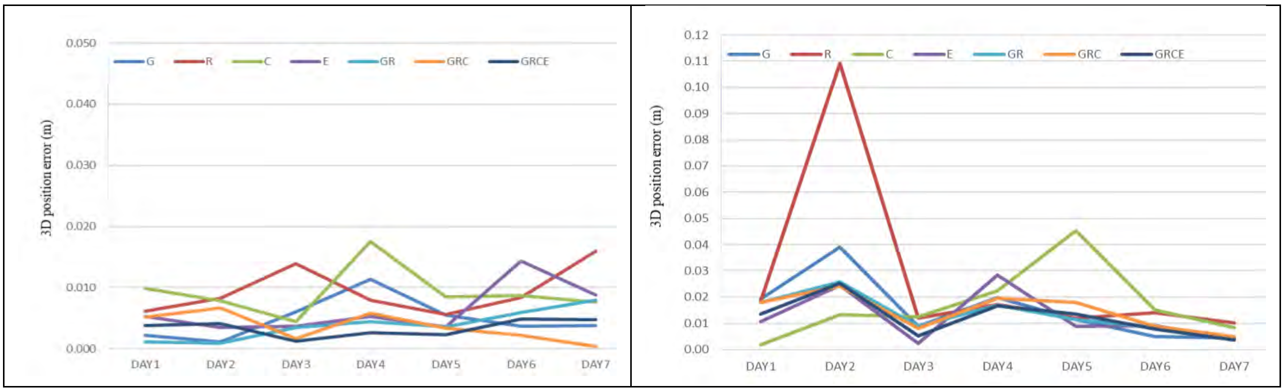

a) **DGAR** b) **GAMG**

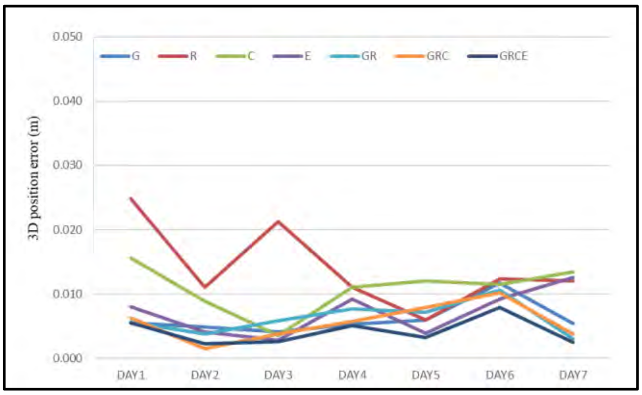

c) **MAR7**

Figure 3. Static-PPP 3D-Position precision using triple-frequency for GPS week (2156) of station

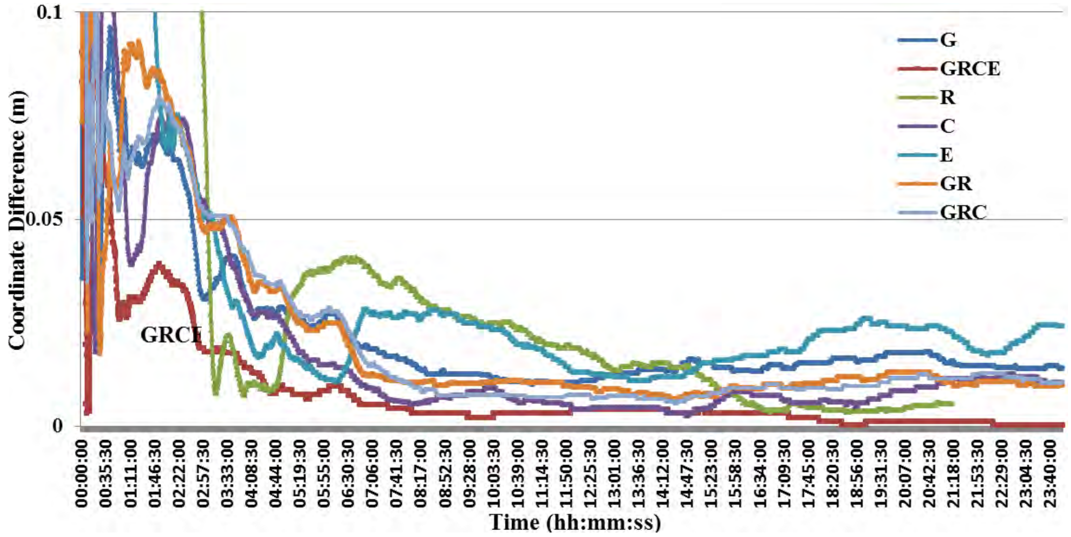

Figure 4. 3D coordinate difference from Static-PPP solution with true coordinates (meters) using dual-frequency observations from different systems for station (DGAR) for (GPS day 21560).

5. Discussion

This research presents a study for static-PPP performance under multi-GNSS systems using different types of observations (single & dual and triple) frequency. The study uses 7-days of observations for three different-latitude IGS stations. Tables 5, 6 and 7 present average Static-PPP accuracy 3D-differences from true coordinates for (GPS week 2156) for three tested stations using single frequency, dual frequency and triple frequency observations respectively.

Table 5. Average Static-PPP 3D-Position accuracy differences from true coordinates using single frequency Observations (GPS week 2156) for three tested stations.

IGS Station	**System**	3D-position error (m)
DGAR	G	0.019
	R	0.046
	C	0.172
	E	0.026
	GR	0.020
	GRC	0.129
	GRCE	0.105
GAMG	G	0.031
	R	0.084
	C	0.106
	E	0.039
	GR	0.040
	GRC	0.075
	GRCE	0.057
MAR7	G	0.027
	R	0.083
	C	0.101
	E	0.106
	GR	0.026
	GRC	0.061
	GRCE	0.073

Table 6. Average Static-PPP 3D-Position accuracy differences from true coordinates using dual frequency Observations (GPS week 2156) for three tested stations.

IGS Station	System	3D Position error (m)
DGAR	G	0.002
	R	0.006
	C	0.005
	E	0.007
	GR	0.001
	GRC	0.002
	GRCE	0.001
GAMG	G	0.002
	R	0.008
	C	0.010
	E	0.003
	GR	0.003
	GRC	0.004
	GRCE	0.002
MAR7	G	0.008
	R	0.012
	C	0.005
	E	0.006
	GR	0.002
	GRC	0.001
	GRCE	0.001

Table 7. Average Static-PPP 3D-Position accuracy differences from true coordinates using triple frequency Observations (GPS week 2156) for three tested stations.

IGS Station	System	3D Position error (m)
DGAR	G	0.005
	R	0.018
	C	0.011
	E	0.006
	GR	0.004
	GRC	0.002
	GRCE	0.000
GAMG	G	0.004
	R	0.008
	C	0.006
	E	0.004
	GR	0.004
	GRC	0.003
	GRCE	0.000
MAR7	G	0.006
	R	0.013
	C	0.006
	E	0.005
	GR	0.004
	GRC	0.003
	GRCE	0.000

Figure 1 present static-PPP precision variation using single frequency observations from different single and combined GNSS constellations during different days of GPS week 2156 for three different-latitude IGS stations. Table 5 presents average Static-PPP accuracy 3D-position differences from true coordinates using single frequency Observations (GPS week 2156) for three tested stations. From Table 3, it can be concluded that GPS provides the best PDOP comparing with other single systems for the three tested stations. GLONASS and Galileo provide similar consistent PDOP on average basis. BeiDou provides varying PDOP based on tested stations. GPS provides the best accuracy for static-PPP using single frequency observations comparing with other single systems. GR combination worsens the accuracy provided by GPS alone, while the attained accuracy is better than GLONASS alone. GRC combination provides better accuracy than GLONASS alone or BeiDou alone. Galileo alone provides better accuracies than GLONASS alone for the two mid-latitude stations (DGAR, GAMG). BeiDou alone provides the worst accuracy comparing with other single systems. Combining Beidou with other systems such as GRC or GRCE worsen the accuracy provided by GR. GPS provides average 3D-accuracy under or equal to 3 cm while GRCE provides 3D-accuracy under 10 cm. Those findings are constrained with this study's circumstances (visibility & PDOP). Varying circumstances could lead to different output accuracies from single and combined systems.

Figure 2 present static-PPP precision 3D-position variation using dual frequency observations from different single and combined GNSS constellations during different days of GPS week 2156 for three different-latitude IGS stations. Table 6 presents average Static-PPP 3D-accuracy differences from true coordinates using dual frequency Observations (GPS week 2156) for three tested stations. GPS provides the best accuracy for static-PPP using dual frequency observations comparing with other single systems for the two mid-latitude stations (DGAR, GAMG). GLONASS and BeiDou provide similar accuracies for the two mid-latitude stations. GR combination provides better accuracy than GPS alone or GLONASS alone. GRC combination provides better accuracy than any single system or GR combination. GRCE provides the best accuracy comparing with any single system or GR or GRC combinations. GRCE provides the 3D-accuracy of about 1mm.

Figure 3 present static-PPP precision 3D-position variation using triple frequency observations from different single and combined GNSS constellations during different days of GPS week 2156 for three different-latitude IGS stations. Table 7 presents average Static-PPP 3D-accuracy differences from true coordinates using triple frequency Observations (GPS week 2156) for three tested stations. Triple frequency observations provide similar performance to dual frequency observations. GPS provide the best accuracy comparing with any single system. Different combinations provide better accuracy than any single system. GRCE provides the best accuracy of less than 1 mm.

Figures 4 presents 3D coordinate difference from Static-PPP solution with true coordinates (meters) using dual-frequency observations from different systems for station (DGAR) for (GPS day 21560). Table 4 presents Convergence time (10 cm-3D accuracy comparing with true coordinates) from Static-PPP solutions using dual-frequency observations from different systems for station (DGAR) for (GPS day 21560). It can be concluded that GPS and BeiDou provide similar convergence time of about 15 minutes. GLONASS provide the longest convergence time of a single system with about 5 hours. Galileo provides a convergence time of about 2 hours. GR combination improves convergence time to 23 minutes. GRC combination improves the convergence time to about 8 minutes. GRCE combination gives the best convergence time of about 4 minutes (8 epochs of observations). Those attained convergence time depend on processing of 30 sec observation interval of the three tested IGS stations.

6. Conclusions

This research investigates static-PPP accuracy using different observations (single, dual and triple) from single system (G, R, C and E) and combined systems (GR, GRC and GRCE). It can be concluded that the attained accuracy directly depends on the used system constellation status which directly affects number of visible satellites and DOP values. Combined systems could improve satellite geometry and DOP values which remedy the deficiencies in one system and improve the attained accuracy from combined systems.

Under constraints of this study (tested stations & GPS week 2156) and the constellation status of tested systems, it can be concluded that GPS provides the best accuracy comparing with other single systems for different types of observations. Combining GPS with other systems could worsen the attained accuracy comparing with GPS-single system.

GRCE combination provides 3D-accuracy of (8 cm) using single frequency observations, (1.5 mm) using dual frequency observations and (1 mm) using triple frequency observations.

Static-PPP positioning using Combination of systems improves the convergence time remarkably. GRCE combination provides a convergence time of only four minutes (8 epochs) for dual frequency observations.

References

Bisnath S. and Y. Gao (2008). Current State of Precise Point Positioning and Future Prospects and Limitations. *International Association of Geodesy Symposia*, Vol. 133 pp. 615-623, 2008.

Cai C (2009). "Precise Point Positioning Using Dual-Frequency GPS and GLONASS Measurements." *Calgary: UCGE Reports* No. 20291, pp. 40-52.

Chen K and Y Gao (2005). "Real-Time Precise Point Positioning Using Single Frequency Data," *Proceedings of the 18th International Technical Meeting of the Satellite Division of The Institute of Navigation (ION GNSS 2005)*, Long Beach, CA, September 2005, pp. 1514-1523.

Ding, W., B. Tan, Y. Chen, F. N. Teferle & Y. Yuan (2018). Evaluation of a regional real-time precise positioning system based on GPS/BeiDou observations in Australia. Advances in Space Research, 61(3), 951–961.

Du, Y., J. Wang, C. Rizos and Ahmed El-Mowafy (2021). "Vulnerabilities and integrity of precise point positioning for intelligent transport systems: overview and analysis". Satellite Navigation 2, 3 (2021). https://doi.org/10.1186/s43020-020-00034-8.

Farah, A. (2013). "Effect analysis of GPS observation type and duration on convergence behavior of static PPP". *Journal of Geomatics*, vol.7, no.2, October 2013.

Farah, A. (2014). “Assessment study of static-PPP convergence behavior using GPS, GLONASS and mixed GPS/GLONASS observations”. *Artificial Satellites Journal of Planetary Geodesy*, Vol. 49, No. 1 2014 DOI: 10.2478/arsa- 2014-0005

Farah, A. (2016). “Accuracy evaluation for online Precise Point Positioning Services”. *Journal of Geomatics*, vol.10, no.1, April 2016.

GitHub (2021). Net_Diff processing software. https://github.com/YizeZhang/Net_Diff/.
Accessed (10/8/2021).

Hamed M., A. Abdallah and A. Farah (2019). “Kinematic PPP using Mixed GPS/GLONASS Single-Frequency Observations”. Journal of Artificial Satellites, Vol. 54, No.3, September 2019.

Hofmann-Wellenhof B and H Lichtenegger (2008). “Global Navigation Satellite Systems.” NewYork: *SpringerWien*, pp. 33-58.

IGS (2021). IGS network. https://igs.org/network/. Accessed (2-9-2021).

Leandro R. F. (2009). “Precise point positioning a new approach for positioning, atmospheric studies, and signal analysis.” *Fredericton, New Brunswick, Canada*, Technical Report No. 267, http://www.gmat.unsw.edu.au/snap/gps/glossary.
Accessed: August, 2014.

Net_Diff (2021). The online PPP/RTK processing service of Net_Diff. http://129.211.69.159:8090/Main.aspx. Accessed (10/8/2021).

Soycan, M. (2012). “A quality evaluation of precise point positioning within the Bernese GPS Software Version 5.0”. *Arabian Journal for Science and Engineering,* Vol. 37 No. 1, 147–162.

TEQC (2021). TEQC-UNAVCO tutorial. http://facility.unavco.org/software/teqc/doc/ UNAVCO_Teqc_ Tutorial.pdf. Accessed (4/10/2021).

Yize, Z. (2018). "Research on Real-time High Precision BeiDou Positioning Service System." *Acta Geodaetica et Cartographica Sinica* 47(9): 1293-1293.

Journal of Geomatics Vol. 17, No. 1, April 2023

Quantifying Spatio-Temporal Land Surface Temperature and Biophysical Indices for Sustainable Management of Watershed: A Study of Vishwamitri Watershed of Gujarat

Bindu Bhatt[1]*, Shashikant A. Sharma[2], Janak P Joshi[3], Shashikant Patel[4],
[1]Department of Geography, The Maharaja Sayajirao University of Baroda, Vadodara 390002, Gujarat.
[2]Space Application Centre, ISRO, Ahmedabad-380015, Gujarat
[3]VSCDL, Vadodara, Gujarat
[4]Punjab Remote Sensing Centre, Ludhiana-141004.
*Email: bindoobhatt@gmail.com

(Received: June 13, 2022; in final form Apr 17, 2023)

DOI- *https://doi.org/10.58825/jog.2023.17.1.82*

Abstract: Spatio-Temporal Analysis of the nexus between vegetation dynamics and climatic parameters like surface temperature is essential in environmental and biophysical studies and for monitoring and management of watersheds. This study explored the spatio-temporal distribution of land surface temperature (LST), Normalised Difference Water Index (NDWI), and Normalized Difference Vegetation Index (NDVI) and the relationship between them in the Vishwamitri watershed of Gujarat for the Pre Monsoon and Post Monsoon of the Year 2001 and 2016 using Landsat dataset. The findings of the study showed that the LST of the Vishwamitri watershed. The mean LST value of the year 2001 was 46.19°C in the pre-monsoon season and 39.27°C in the post-monsoon season. Mean LST values for the year 2016 were 49.34°C in pre-monsoon and 35.21°C in the post-monsoon season as observed. The spatial distribution of NDVI and LST reflects an inverse relationship. A strong positive correlation between LST with NDVI is observed over highly dense built-up areas. In summary, the LST is greatly controlled by surface characteristics. The results of this study illustrate there has been a dynamic change in vegetation cover of the watershed in all seasons. There was also a negative correlation between LST and NDVI in the studied years. The study concludes that there has been a degradation of vegetation and intensification of LST in the year 2016 as compared with the year 2001. This study can be used as a reference for land use and environmental planning in a tropical city.

Keywords: LST, Biophysical Indices, Watershed, Vishwamitri Watershed

1. Introduction

The world is currently experiencing different environmental changes which are caused by both nature-induced and anthropogenic activities. India, like other parts of the world, is highly vulnerable to the impacts of these environmental changes. The country faces various problems in managing natural resources. Long-term degradation of vegetation is one of the major environmental challenges in various parts of the country. Serious vegetation degradation is highly influenced by human activities such as the conversion of vegetated and wetlands into agricultural, as well as residential and commercial areas (Chen et al., 2006).

Watersheds have been viewed as useful systems for planning and implementing natural resources and ecological development for many centuries. Urbanization accelerates the ecological stress by warming the local or global cities to a large extent (Foley et al., 2005; Fu, P. and Weng Q., 2016; Grimm et al. 2008; Liu H. et al. 2018; Liu Y. et al 2018; Peng J et al. 2018; Guha, S., and Govil, H. 2020). Presently, many urban areas are suffering from huge land conversion and resultant new heat zones (Patz et al.2005).

Population growth, widespread industrialization, and migration of the rural population to urban areas lead to urban population growth and expand the urban sprawls. Rapid urbanization also causes a drastic decrease in green cover, and water bodies, and a rapid increase in impervious areas. All this together modify the microclimate regime of an area. Urban growth and sprawl is a global phenomenon and has a significant influence on the biophysical environmental effects leading to severe ecological and environmental problems. Rapid and unplanned urbanization leads to changes in the land use/ land cover (LULC) of the area, especially reduction in vegetation cover, which in turn increased the built-up areas. Hence, impervious areas have increased and impervious surfaces can be considered a key indicator of the urban environment (Arnold and Gibbons, 2016). Natural vegetation and permeable soils have been replaced by impervious surfaces such as asphalt, bricks, and concrete, which lead to more sensible heat than heat flux. It could be argued that UHIs represent the most significant form of irreversible anthropogenically forced climatic change not only at the local scale but also at the regional and even global scale (Arnfield, 2003).

Such alterations are the main factors for global environmental change upsetting sustainable development. Land cover and land use (LCLU) changes induced by human and natural processes play a major role in global as well as regional-scale patterns of the climate.

The urban heat island (UHI) effect indicates the higher air and land surface temperature (LST) in urban areas in comparison to the surrounding rural area, generated by high levels of near-surface energy emission, solar radiation absorption of ground objects, and low rates of evapotranspiration (Buyantuyev and WuJ 2010).

Land surface temperature (LST) refers to the temperature of the soil, water, buildings, and the vegetation canopy on the land surface (Zhang and Liao 2014), is a key parameter for describing thermal conditions (Walawender, et. al. 2014) and is a common research topic in local and global environmental studies (Liu And Weng 2013). LST plays an important role in a variety of scientific studies, such as those on hydrology, ecology, and global climate change (Zhang and He. 2013). LST is calculated from emitted radiation measured by either ground or satellite-based instruments. Generally, remote sensing techniques require less time and a cheaper cost than field methods to investigate numerous phenomena on the land surface. Because of its repetitive nature and increasing spatial resolution, satellite imagery is becoming more and more a viable and preferred alternative to ground-based measurements of land surface characteristics (Alemu, 2019).

Increased LST in certain urban pockets in comparison to its surroundings consequent to the increase in paved surfaces is known as the urban heat island (UHI) phenomenon (Gallo and owen 1998). It is also observed that the vegetation and water body patches are having relatively low temperatures, which acts as a heat sink (Joshi and Bhatt 2012). The relationship between the LST and NDVI has been widely documented in the literature (Chen et. al, 2006; Weng, 2001 & Weng et.al, 2006).

The land surface temperature can be obtained from direct ground measurement (Chen et. al, 2006). With the availability of satellite remote sensing, thermal bands retrieved from the satellite can be used to estimate surface temperature. Several studies used the Land sat ETM+ imagery to develop LULC maps as well as for deriving the surface temperature. Accurate mapping of LST is becoming more significant in providing information about surface physical and the use of satellite images has become the predominant way to monitor LST on local and regional scales. Remote sensing-based indices have the advantages of being used effectively, being parameter-free, and being efficient in the applications of land surface information extractions.

In the earlier years, NOAA-AVHHR data and recently MODIS, LANDSAT, and ASTER data have been used for deriving land surfaces biophysical parameters such as vegetation abundances, built-up indices, and land surface temperature (*LST*) in many studies; which are good indicators of the situation of an urban ecosystem to investigate the urban heat formation (Gallo et. al 1993 Lu and Weng 2009; Sobrino et. al, 2014; Tooke et.al,2008; Zhang et al, 2009.). The distinctive LST patterns are associated with the thermal characteristics of the land cover types (Weng, 2001 and Lo et. al., 1997). It is necessary to further study the temperature changes by LULC for studying the effect of urbanization on the local thermal environment.

Numerous studies had been made to examine the effect of the vegetation on the LST, which showed that there was a negative correlation between LST and urban vegetation abundance measured by the Normal Difference Vegetation Index (NDVI) and the percent cover of urban vegetation (Sundara 2012; Mallik et.al, 2008; Gao, 1996). However, in India studies focusing on the relationship between urban vegetation and LST using Land sat ETM+ imagery are relatively scant.

Chen et al (2006) stated that appropriate indices such as the Normalized Difference Vegetation Index (NDVI), Normalized Difference Build-Up Index (NDBI), and Modified Normalized Difference Water Index (MNDWI) can be used to classify Landuse/land cover. The study consequently intends to quantify the dynamics of LST NDVI, NDWI 2001, and 2016 for the Vishwamitri watershed.

2. Study Area

The Vishwamitri River originates from Pavagadh hill at about 22º 28´ N latitude and 73 º 45´ E longitude at an elevation of more than 700 m with 601 sq. km. The watershed has two distinct regions upper half is comprised of industrial units along highways and wasteland parcels along the river. Whereas and lower part has high meandering under influence of rapid urbanization. The catchment area comprises 102 villages of Savali, Waghodia, and Vadodara Taluka of Vadodara District and Halol Taluka (Panchmahal District) with more than 12 lakh populations. The watershed is under the influence of the growing Vadodara city, the urbanization has resulted in the land cover change to a non-agriculture area. This change will make the shrinkage of the river channel and the floodplains, the green cover alongside the rivulets. Thus the chances of the development of the urban heat island are inevitable if goes unmonitored.

3. Objective

Analysis of the interaction between vegetation and waterbody's dynamics and climatic parameters like surface temperature is essential in environmental and ecological studies and for monitoring natural resources. The study of the health of the resource and its implication on other biophysical parameters is of utmost importance This study explores the interaction of spatio-temporal distribution of land surface temperature (LST), vegetation, and water distribution, using indices of Normalized Difference Vegetation Index (NDVI), Normalized Difference Water Index (NDWI) respectively. The study also addresses the temporal change during pre and post-monsoon for the years 2001& 2016 in the Vishwamitri watershed (Figure 1).

The present study aims to calculate the LST from Landsat dataset, NDVI and NDWI. Datasets of two different seasons (pre-monsoon, and post-monsoon) in the Vishwamitri watershed using a total of 12 Landsat satellite images for the years 2001 and 2016. Meanwhile, the LULC map has been generated using the Landsat dataset. The main aims of the study were (1) to analyze the seasonal variation of the spatial distribution pattern of the LST in the study area, (2) to determine the seasonal variation of LST, NDVI, and NDWI relationship for the study area, and (3) to explore the seasonal variation of

LST, NDVI and NDWI relationship on different LULC types.

4. Methodology

For the present study, the methodology involves the preparation of NDVI and Land surface temperature maps and correlation analysis between LST and NDVI, and NDWI. The methodology involves the stages from Satellite data acquisition, LST retrieval, Land Use / Land cover Map generation, Assessment of NDVI, Assessment of NDWI, and determination of the relationship between, LST, NDVI, and NDWI over the study area.

4.1 Satellite image acquisition and processing

Landsat 8 Operational Land Imager (OLI) and Thermal Infrared Sensors (TIRS) data of 2016; Landsat 5 Thematic Mapper (TM) data of 2001 freely downloaded from the United States Geological Survey (USGS) (https://earthexplorer.usgs.gov) Data Centre. Landsat 8 TIRS dataset has two TIR bands (bands 10 and 11) in which band 11 has uncertainty in calibration. Thus, only TIR band 10 (100 m resolution) has been recommended for the present study. Landsat 5 TM data has only one TIR band (band 6) of 120 m resolution that has been used for the present study. The spatial resolution of visible to near-infrared (VNIR) bands of the two types of Landsat datasets is 30 m which has been used for the NDVI and NDWI Indices generation.

4.2 Land surface temperature (LST) retrieval

Land surface temperature is the temperature at the interface of the earth's surface with its atmosphere. The LST gives the relative information of the surface heat disseminated at any given point in time.

4.3Retrieval of LST from Satellite Image (Landsat TM)

The at-sensor spectral radiance is the amount of energy received by the satellite sensor. Spectral Radiance (L_λ) has been computed through the Conversion of the Digital Number (DN) into the radiance using equation.1. Digital Number (DN) of a pixel in an image is a numerical value that represents the brightness of that pixel in the image. In this step, each pixel of the Landsat images was converted from Digital Numbers (DN) to Spectral radiance (L_λ) using the following formula (Fathian et al., 2015; Wang et al., 2015).

$$L_\lambda = \left(\frac{L_{Max\lambda} - L_{Min\lambda}}{QCAL_{Max} - QCAL_{Min}}\right) * (QCAL - QCAL_{Min}) + L_{Min\lambda} \quad \ldots\text{(Equation.1)}$$

where;

L_λ = Spectral Radiance at the sensor's aperture in watts/(sq.m)

$LMAX_\lambda$ = the spectral radiance that is scaled to $QCAL_{Max}$ in watts/(sq. m)

$QCAL_{Min}$ = the minimum quantized calibrated pixel value (corresponding to $L_{MIN\lambda}$) in DN

$QCAL_{Max}$ = the maximum quantized calibrated pixel value (corresponding to LMAXλ) in DN

Next, Thermal radiance values were converted from spectral radiance to brightness temperature using the thermal constants with the equation.2. (Sobrino et al., 2004): The brightness temperature presumes that the Earth's surface is a completely black body i.e spectral emissivity is 1.

$$BT = \frac{K2}{\ln\left(\frac{K1}{L_\lambda} + 1\right)} - 273.15 \qquad \ldots (Equation. 2)$$

Where;

BT= The ToA brightness temperature in°C

K_2 = Calibration constant 2 from metadata

K_1 = Calibration constant 1 from metadata

L_λ = Spectral radiance in watts/(sq. m)

$$LST = \frac{BT}{1 + (\lambda * BT/\rho) * \mathrm{Ln}\varepsilon} \qquad \ldots. (Equation. 3)$$

Where,

BT= Satellite rightness temperature (Kelvin),

λ= Wavelength of emitted radiance (11.5 μm),

ε= Land surface emissivity,

$\rho = h * c/\sigma$= 1.438*10-2mK (σ= Boltzmann constant= 1.38*10-23 J/K, h= Planck's constant= 6.626*10-34Js, c= velocity of light= 2.998*108 m/s).

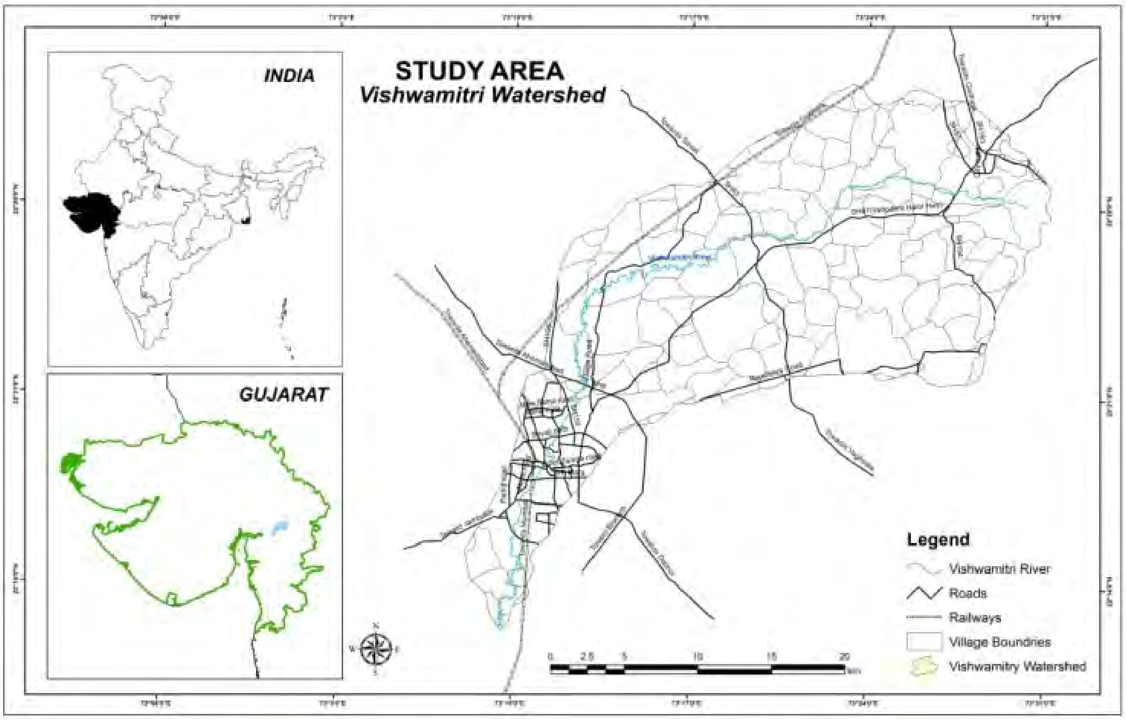

Figure 1. Study area

4.3 Calculation of Normalized Difference Vegetation Index (NDVI)

The Normalized Difference Vegetation Index (NDVI) is essential to estimate the amount of above-ground green vegetation cover. It is calculated from measurements of red and near-infrared reflectance using equation.4.

$$NDVI = \frac{NIR - RED}{NIR + RED} \quad \ldots (Equation.4)$$

where; NIR and RED are the near-infrared and red band pixel values respectively. The value of NDVI ranges between -1.0 and 1.0.

4.4 Calculation of Normalized Difference Water Index (NDWI)

The NDWI is the most suitable index for water body mapping. Water bodies have strong absorbability and low radiation in the range from visible to infrared wavelengths. The index uses the green and NIR bands of the remote sensing images based on this phenomenon. The NDWI can enhance the water information effectively in most cases. It is sensitive to built-up land and often results in over-estimated water bodies. NDWI was calculated as follows using an equation.5 (McFeetemrs, 1996)

$$NDWI = \frac{Green - NIR}{Green + NIR} \quad \ldots (Equation.5)$$

5. Results and discussion

Spato-Temporal variation of LST

Figure 2 illustrates the LST variation in the study area for the pre-monsoon and Post-monsoon years 2001 and 2016. LST represents the temperature of an object within a pixel, which may include several land cover types. LST maps are prepared to show the spatial distribution of LST within the study area. The maximum LST was observed as 49.41 °C and the minimum LST was observed as 35.85°C in the pre-monsoon of the year 2001; similarly, 42.33°C maximum and 31.21°C LST in the post-monsoon season was observed in the year 2001 (Figure 2). Spatial distribution of LST for pre-monsoon of the year 2016 shows the maximum and minimum LST is 53.43°C and 35.39°C respectively (1st May); whereas for post-monsoon of the year 2016 shows the maximum is 38.45°C and minimum is 29.03°C (29th October). The results also show that there are variations in the LST of the area due to variations in land use/land cover classes of the study area. The different cover has different conductivity of the heat owing to which a regional flow of thermal energy can be seen. The statistics showing the minimum & maximum values of LST are given in Table 1.

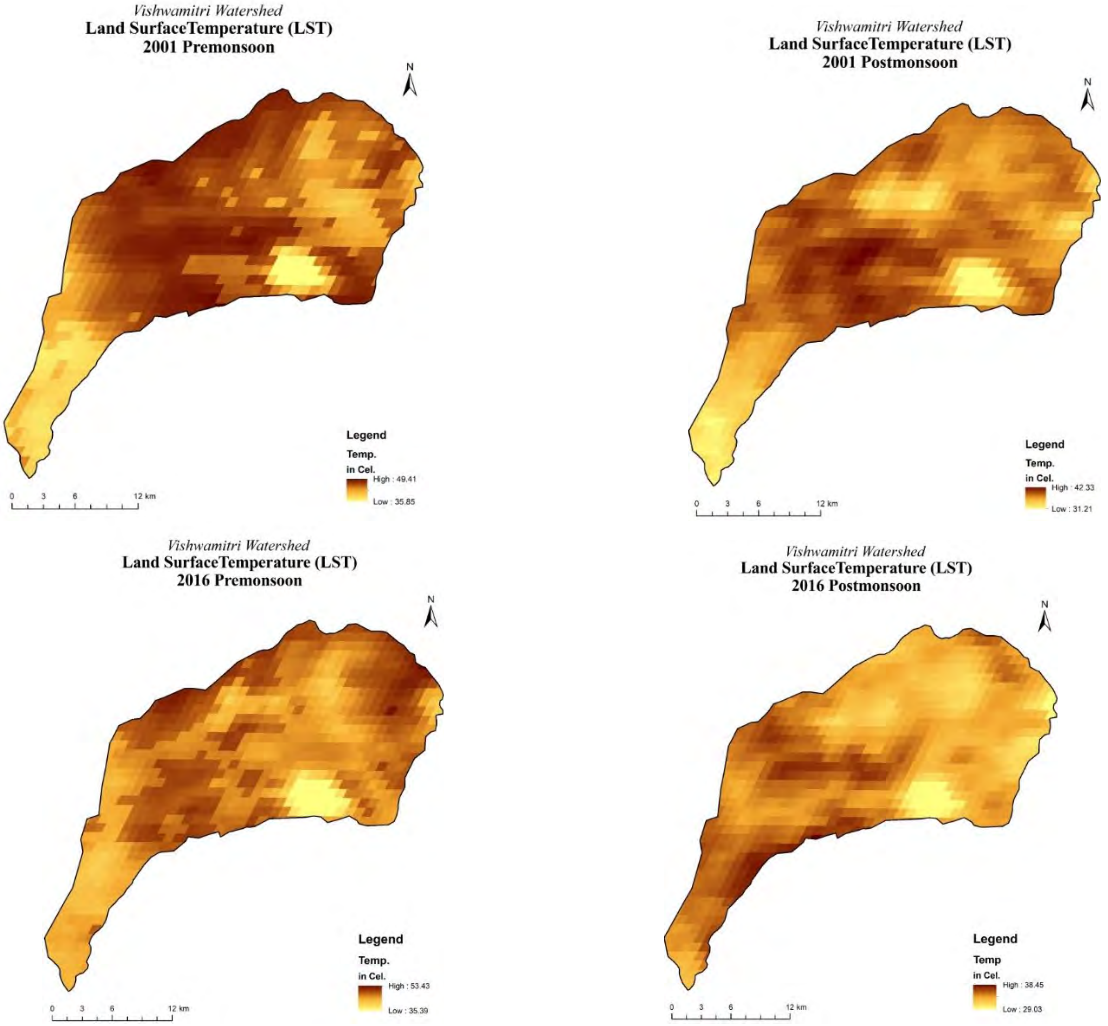

Figure2. Spatial and Temporal Variation of the LST

Table 1 . Variation of LST.

Year	**Season**	**Temperature(°C)**		
		Max.	**Min.**	**Mean**
2001	Pre-monsoon	49.41	35.85	46.19
	Post-monsoon	42.33	31.21	39.27
2016	Pre-monsoon	53.43	35.39	49.34
	Post-monsoon	38.45	29.03	35.21

It is observed that the pre-monsoon maximum temperature is 53.43^{0}C which has increased by 4.02 ^{0}C. The surface temperature of the region for the same period of the year suggests that the temperature is warmer in the Pre-monsoon as compared to the Post monsoon. The scenario of the Landuse also suggests the agricultural practice of current fallow and harvested land also leads to warmer surfaces. The increase in the temperature is accounted for based on the dry surface or the surface covering having a high affinity to hold heat like road and concrete structures.

Spatial and Temporal Variation of the NDVI:

Many vegetation indices have been developed to assess vegetation conditions. Among them, the normalized difference vegetation index (NDVI), which was proposed by Rouse et al. (1973), is applied in the study. Normalized Difference Vegetation Index (NDVI) is an index that describes the vegetation proportion by measuring the difference in the near-infrared portion of the electromagnetic spectrum which is strongly reflected by green vegetation and the red portion of the spectrum which is absorbed by vegetation.

The values of NDVI indicates the variations of green and healthy vegetation type in the given area. The higher the NDVI value the denser the vegetation and the lower the NDVI the less dense or absent vegetation cover. The normalized difference vegetation index (NDVI) was derived for the years 2001 and 2016 for pre-monsoon and post-monsoon.Given the changes occurring in cities and the fact that they will continue to expand, the study of urban land cover changes and their impacts on thermal patterns and NDVI values has a critical interest, Since the urban thermal environment is related to the reduction of evapotranspiration from the surface vegetation cover, it is useful to recognize the relationship between surface vegetation cover and water availability.

The Normalized Difference Indexes are commonly used to characterize the land cover types and in this study, they were used to evaluate the relationship between land cover types and heat formation.

The NDVI gradually increased in especially post-monsoon season in the period between the years 2001 and 2016 as shown in table 2 and figure 3. for the entire region. One of the reasons can be the availability of water from the Narmada branch canal. The mean NDVI was 0.25 observed in the year 2001 pre-monsoon period, which slowly increased to 0.28 in 2016, and the post-monsoon mean NDVI increased from 0.43 to 0.51 from the year 2001 to 2016 (Table 2).

Areas, where NDVI exhibited standard trends, were primarily located near the foothills and along the young stage of the Vishwamitri River. NDVI from 2001 to 2016, decreased continuously over the impervious area, although significant fluctuations were observed during this period.

4.4 Spatial and Temporal Variation of the NDWI

Normalized different water indices (NDWIs) derived from satellite images are commonly and successfully utilized in surface water body detection and mapping. NDWI has been calculated to draw to the wetland index in the watershed. The minimum and maximum and mean NDWI index found in the watershed varies from - 1 to 1. In recent times, several researchers are applying image processing methods for the extraction of water features from satellite data. Gao, (1996) developed the Normalized Difference Water Index from a near-infrared channel and a short-wave infrared channel; which is more sensitive to monitor changes in the water content of leaves. One such important method is the normalized difference water index (NDWI) which could be used for the extraction of water features from Land sat imageries (McFeetemrs, 1996).

The results from NDWI are indices that have a range of values of -1 for non-water bodies and 1 for water bodies.
The spatial variation of the NDWI is analyzed for extracting the water bodies from the watershed area. Ajwa Lake, Sur sager Lake, and Narmada canal were extracted over the watershed in the years 2001, and 2016 (Figure 4). Whereas other water bodies viz., Vadadala, Dhanora, Bodidra, and Pratapura are the lakes where there is seasonal fluctuation in boundaries, especially in pre-monsoon and post-monsoon seasons. Table 3 illustrates the maximum, minimum, and mean NDWI values of the study area for pre-monsoon and post-monsoon seasons of the years 2001 and 2016.

Table 2. Variation of NDVI

Year	**Season**	**Max**	**Min**	**Mean**
2001	Pre-monsoon	0.54	-0.20	0.25
	Post monsoon	0.76	-0.19	0.43
2016	Pre-monsoon	0.56	0.04	0.28
	Post monsoon	0.77	-0.20	0.51

Table 3 . Variation of NDWI

Year	Season	Max	Min	Mean
2001	Pre-monsoon	0.66	-0.58	0.31
	Post-monsoon	1	0.32	0.52
2016	Pre-monsoon	0.17	-0.50	-0.21
	Post-monsoon	0.17	-0.49	-0.23

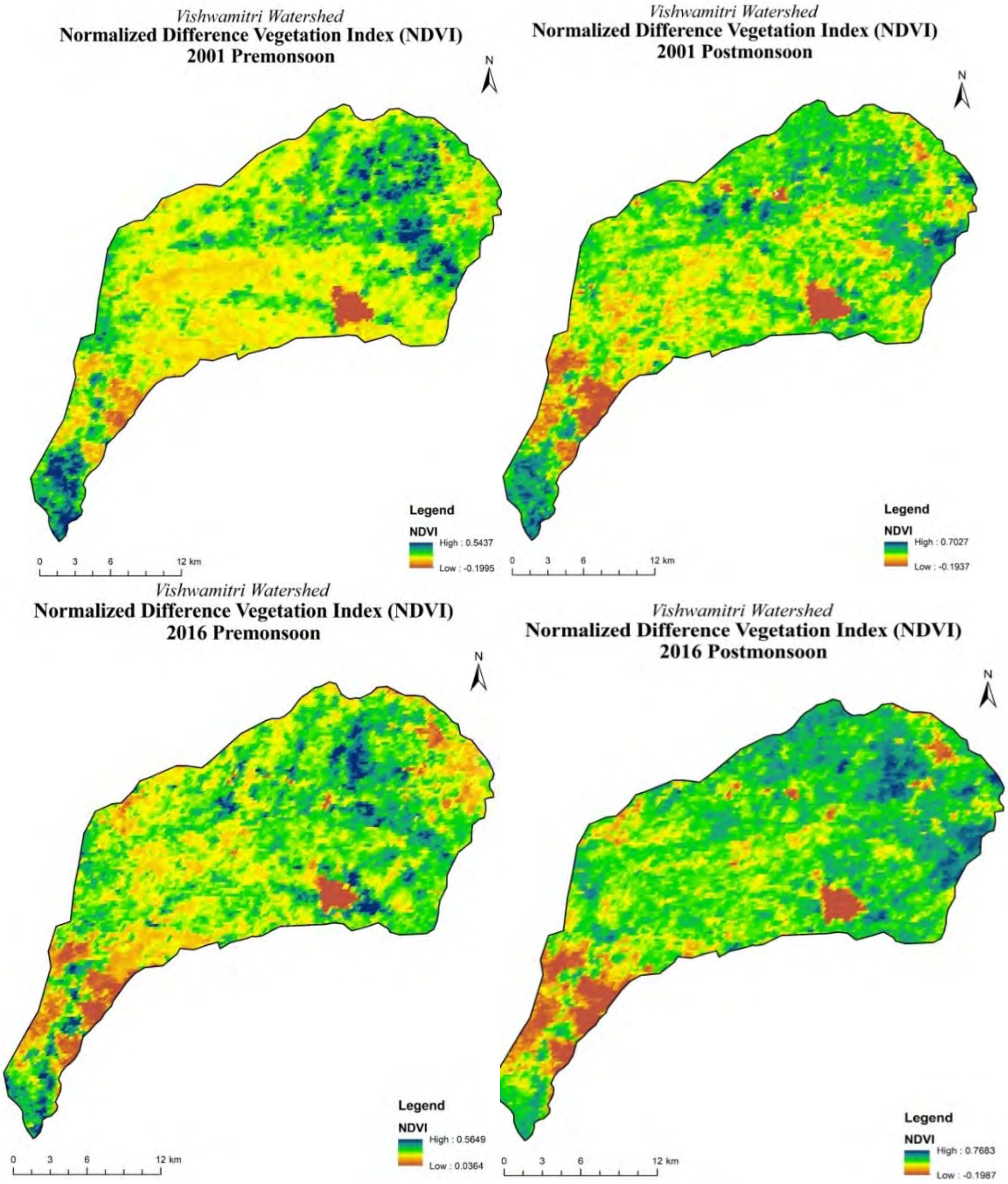

Figure 3. Spatial and Temporal Variation of NDVI

Relationship of LST with NDVI, and NDWI

Land surface temperature (LST) is sensitive to vegetation cover. As shown in table 4, the biophysical indices(NDVI and NDWI) have a negative correlation with LST. In general, it is observed that urban and water body classes of LULC are negatively correlated with NDVI in 2001. Negative relationships between LST and NDVI have been reported in other studies using thermal sensors for urban and rural environments (Dousset and Gourmelon 2003; Lo et al., 1997). Thus, it can be attributed to the fact that higher levels of latent heat fluxes may correspond to the areas characterized by vegetation cover in comparison to areas with sparse or no vegetation cover and low surface moisture availability. Table 4 describes the correlation of LST and biophysical indices for the year 2001.

Whereas the correlation of LST with NDWI shows that the NDWI is effective to water surfaces, this index was originally designed for use in non-urban settings. The threshold of NDWI values eliminated rooftop pixels and other non-water surfaces from the areas contained within the residential parcels themselves. NDVI shows a higher negative correlation with LST in the pre-monsoon period, and NDWI shows a lower negative correlation with LST in the pre-monsoon season for the year 2001. Similarly for the Post monsoon season of the year 2001 NDVI reflects a higher negative correlation with LST as compared to the NDWI.

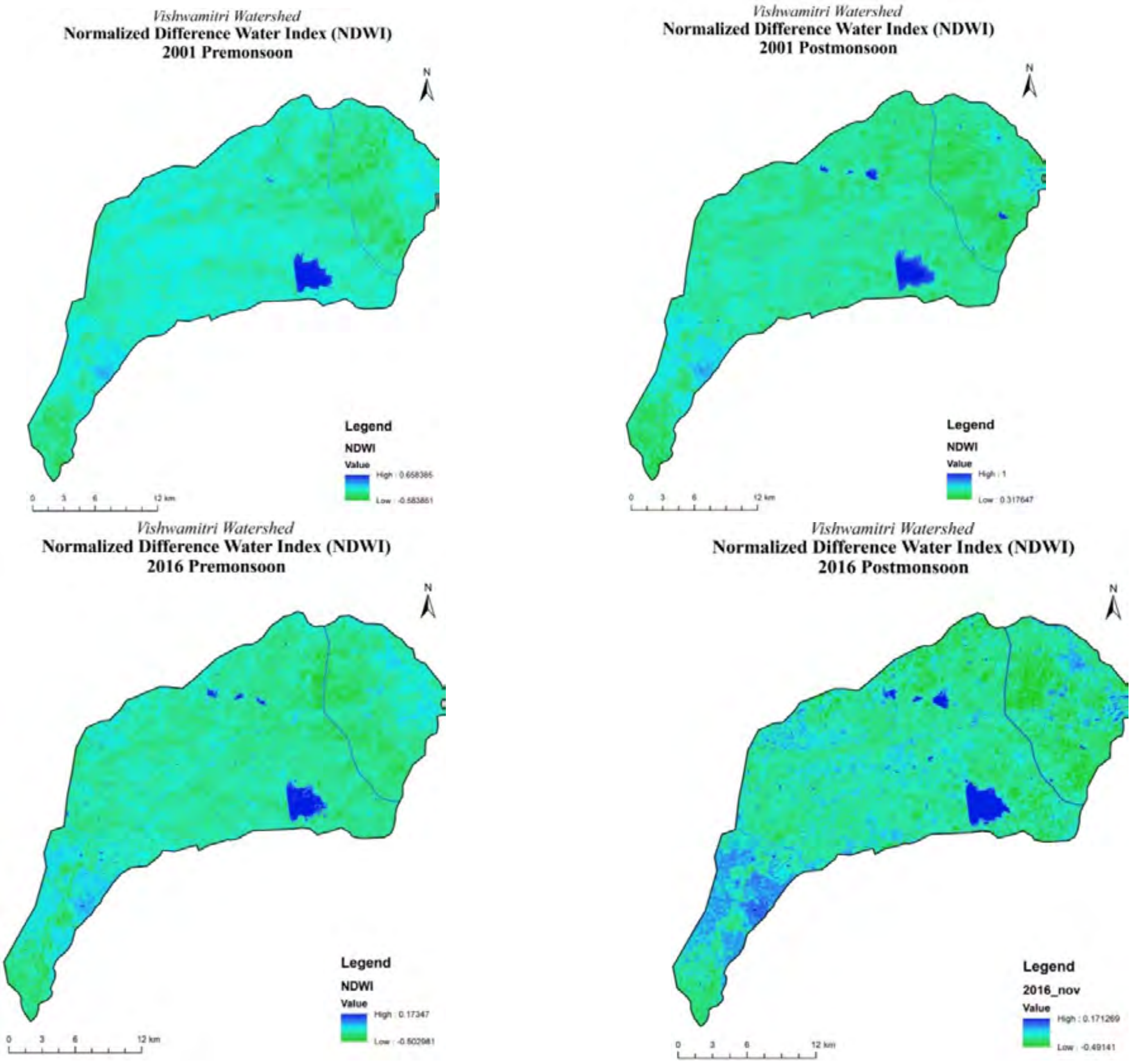

Figure 4. Spatio-temporal Variation of NDWI

Table 4. Correlation of LST and biophysical indices (2001)

2001	Pre Monsoon			Post Monsoon		
Indices	LST	NDVI	NDWI	LST	NDVI	NDWI
LST	1			1		
NDVI	-0.158	1		-0.155	1	
NDWI	-0.023	-0.512	1	-0.005	-0.551	1

The NDVI shows a strong negative correlation with LST in the post-monsoon period, and NDWI is less Negative correlation with LST in the pre-monsoon season. In the year 2016, NDVI shows a strong negative correlation with LST in the post-monsoon period, and NDWI is less Negative correlation with LST in the pre-monsoon season as indicated in table 5.

Table 5. Correlation of LST and biophysical indices for the year 2016

2016	Pre-Monsoon			Post-Monsoon		
Indices	LST	NDVI	NDWI	LST	NDVI	NDWI
LST	1			1		
NDVI	-0.259	1		-0.472	1	
NDWI	-0.003	-0.247	1	0.182	-0.447	1

Land use/ land cover (LULC) map derivation

The mapped land-use change and the land-use statistics of the catchment are derived using the Landsat dataset (Figure 5). The land-use pattern indicates that the expansion of Vadodara city is sinking the flood plains of the river and the vegetation cover adjoining the river. Also due to the non-perennial nature of the river, the current fallow usage is considerably high owing to which the pre and post-monsoon interaction of the usage has its impact in defining the micro biophysical variation of the region. As noticeable in figure 6. In the period of the study, it is evident that the area under the built-up has almost doubled, reducing the open land, current fallow, and vegetation coverage.

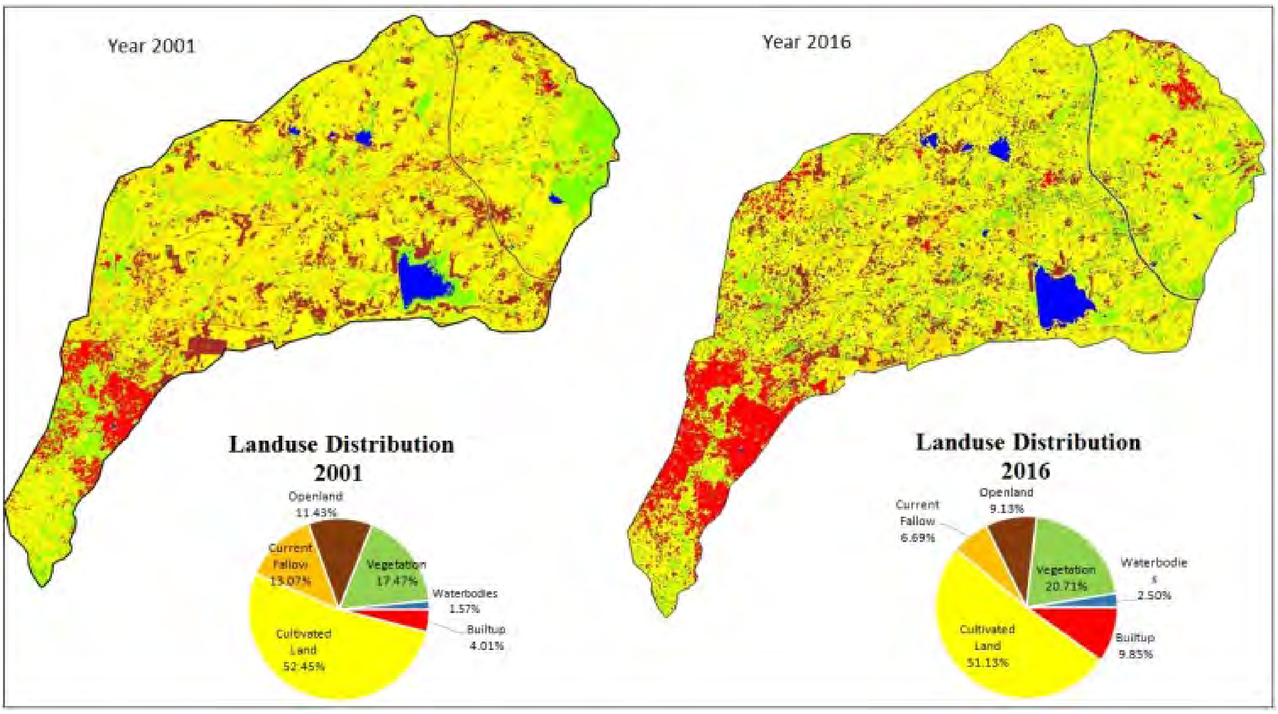

Figure 5: Landuse of the Vishwamitri River catchment area.

Pre - Monsoon and Post – Monsoon composite Characteristics

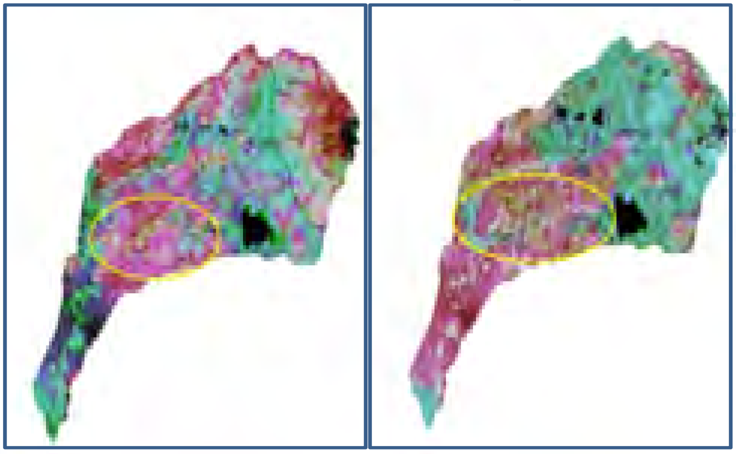

Figure 6: Landcover Variation in the Vishwamitri River catchment area. The central catchment area is showing a high variation of cropping as the water deficit

Conclusion:

A strong positive correlation between LST with NDVI is observed over the highly dense built-up area. A strong negative correlation between LST and NDVI implies that the higher the biomass a land cover has, the lower the surface temperature. On the other hand, the strong positive correlation between LST and NDVI implies that the lower the biomass of a land cover, the higher the surface temperature. Because of this causal relationship between LST and NDVI, the type of LULC influences LST through NDVI and consequently, it affects the microclimate of an area. The foregoing discussion reveals that NDVI effectively differentiates between the vegetation and non-vegetation land cover classes. A negative correlation between LST and NDVI means wherever there is high NDVI the surface temperature is low.

The results suggest that the bareness of the surface plays an important role in the overall surface temperature range. In biosphere interaction, water bodies and vegetation cover act as heat sinks preventing higher temperature fluctuation in the region. Normally, water bodies, vegetation, and damp soil are less warm compared to bare soil and built-up area. Consequently, there is a positive relationship between LST with urbanization. The period chosen was in line with the development the region is undergoing. The large-scale usage transformations are underway. The Middle basin region is relatively dry and post-monsoon and also it shows heterogeneity in land usage. This shows the disparity in the region. Also, the expanding city limits and disparity will be exerting tremendous pressure for transformation.

For sustainable management in the Vishwamitri watershed area, to adopt climatic changes, interventions are required for increasing the density of the vegetation and water body conservation. Especially, the central portion of the catchment area is required to be addressed as it is agricultural land but in the absence of water, the land becomes moistureless thus productivity is decreased. Owing to the less yield this land will be subjected to non-agricultural use which indeed will promote concretization. Also, the land serves as the hinterland for the city for the vegetable need, thus agro-technological inputs can be enhanced to promote horticulture. Along with the area planning approach to deal with provisioning of the water resource. The check dam and groundwater recharge well can be adapted to facilitate the region in maintaining soil moisture and healthy growth of the vegetation.

Dense built-up at the lower catchment and its expansion can pose a threat to becoming an urban heat island formation. Tree cutting, and conversion of wetlands and agricultural land into built-up areas have adverse effects on the micro-climate of the area which may result in several pockets of heat zones UHI over some time. Development of the region should be along with the usage of material having an emissivity of energy and higher reflection toward the infrared radiation.
Planning is essential to distribute suitable agricultural practices to incorporate the current fallow and open land with some biomass productivity. Climate change impact can be addressed by conservation of the hydrology. The river size and the wet perimeter are significantly less, to mitigate the rising temperature change. So water bodies are to be conserved also vegetation growth should be enhanced. Prior attention is needed to address the micro-climate changes of the area for sustainable management.

Based on the bio-physical indicators an areal regionalization concept has to be adapted by looking at the microclimatic impact. This region will cater as the environmental planning unit. Also, effective restoration of the vegetation and waterscapes will help the region to cope with future climate adversity. Thus leading to the climate resilience planning of the region.

The retrieved satellite LST was effectively validated with in-situ observations. The application of robust geospatial technology with freely available data such as Landsat has the potential to be effective in monitoring urban growth patterns, hot spot detection, and spatial-temporal climatic changes. The effective use of this technology for determining the normalized difference in water index, urban index, moisture index, drought index, and vegetation index has immensely enhanced the capability of human beings to further explore remote sensing data for quick and accurate results. This study shows that the watershed can be subdivided functionally for efficient ecologically sustainable planning and resource management.

Acknowledgement:

We would like to express our gratitude to NRDMS (DST) for financial support (NRDMS 01/138/015(G). Authors cordially acknowledge USGS for supplying necessary satellite imagery.

References

Alemu, M.M. (2019). Analysis of Spatio-temporal Land Surface Temperature and Normalized Difference Vegetation Index Changes in the Andassa Watershed, Blue Nile Basin, Ethiopia[J]. Journal of Resources and Ecology, 2019, 10(1): 77-85.

Arnfield, A.J. (2003): “Two decades of urban climate research: a review of turbulence, exchanges of energy and water, and the urban heat island”, International Journal of Climatology, Vol. 23, pp.1-26.

Arnold, C. L., Jr., and C.J. Gibbons (2016) ‘‘Impervious surface coverage: The emergence of a key environmental indicator,’’ J. Amer. planning Assoc., vol. 62, no. 2, pp. 243–258, https://doi.org/10.1080/01944369608975688.

Buyantuyev, A. and Wu, J. (2010). Urban heat islands and landscape heterogeneity: Linking spatiotemporal variations in surface temperatures to land-cover and socioeconomic patterns. Landscape Ecology, 25, 17–33. https://doi.org/10.1007/s10980-009-9402-4.

Chen X.L., H.M. Zhao, P.X. Li and Z.Y. Yin (2006), Remote sensing image-based analysis of the relationship between urban heat island and land use/cover changes. Remote Sens of Environment 104(2): p. 133-146. https://doi.org/10.1016/j.rse.2005.11.016.

Dousset B. and F. Gourmelon (2003). Satellite multi-sensor data analysis of urban surface temperatures and land cover, Photogrammetry and Remote Sensing 58 pp. 43–54 Environment, 106, 375–386. doi:10.1016/S0924-2716(03)00016-9.

Fathian F, Prasad A D, Dehghan Z, et al. 2015. Influence of land use/land cover change on land surface temperature using RS and GIS techniques. International Journal of Hydrology Science and Technology, 5(3):195-207. https://doi.org/10.1504/IJHST.2015.071348.

Foley J.A., R. DeFries, G. P. Asner, C. Barford, G. Bonan, S.R. Carpenter, F.S. Chapin, M.T. Coe, G. C Daily and H. K. Gibbs (2005) Global consequences of land use. Science 309:570–574.

Fu P. and Q. Weng (2016) A time series analysis of urbanization-induced land use and land cover change and its impact on land surface temperature with Landsat imagery. Remote Sens Environ 175:205–214

Gallo, K.P., A.L. McNab, T.R. Karl, J.F. Brown, J.J. Hood and J.D. Tarpley (1993). The use of NOAA AVHRR data for assessment of urban heat island effect. Journal of Applied Meteorology. 32, pp. 899-908.

Gallo, K.P. and T.W. Owen (1998), Assessment of urban heat island: A multi-sensor perspective for the Dallas-Ft. Worth, USA region. Geocarto International, 13, 35– 41.

Gao, B. (1996), "NDWI—A normalized difference water index for remote sensing of vegetation liquid water from space Remote Sensing of Environment Volume 58, Issue 3, December Pages 257-266 https://doi.org/10.1016/S0034-4257(96)00067-3.

Grimm N.B., S.H. Faeth, N.E. Golubiewski, C.L. Redman, J. Wu, X. Bai, J.M. Briggs and Grimm N (2008) Global change and the ecology of cities. Science 319:756–760.

Guha, S., Govil, H. (2020). Land surface temperature and normalized difference vegetation index relationship: a seasonal study on a tropical city. SN Applied Sciences (2020) 2:1661, https://doi.org/10.1007/s42452-020-03458-8.

Joshi J. P and B. Bhatt. 2012. "Estimating Temporal Land Surface Temperature Using Remote Sensing: A Study Of Vadodara Urban Area, Gujarat." *International Journal of Geology, Earth and Environmental Sciences* 2 (1): 123–30. https://www.cibtech.org/J-GEOLOGY-EARTH,

Liu H, Q. Zhan, C. Yang and J. Wang (2018) Characterizing the spatio-temporal pattern of land surface temperature through time series clustering: based on the latent pattern and morphology. Remote Sens 10:654.

Liu Y, J. Peng and Y. Wang (2018) Efficiency of landscape metrics characterizing urban land surface temperature. Landsc Urban Plan 180:36–53.

Liu H. and Q. H. Weng (2013) Landscape metrics for analysing urbanization-induced land use and land cover changes. Geocarto Int., 28, 582–593.

Lo C.P., D.A. Quattrochi and J.C. Luvall, (1997, Application of high resolution thermal infrared remote sensing and GIS to assess the urban heat island effect, International Journal of Remote Sensing 18 pp. 287–304. https://doi.org/10.1080/014311697219079.

Lu, D. and Q. Weng (2009), Extraction of urban impervious surfaces from an IKONOS image. International Journal of Remote Sensing. 30, 5pp. 1297-1311. https://doi.org/10.1080/01431160802508985.

Mallik J., Y. Kant and B. D. Bharath (2008). Estimation of land surface temperature over Delhi using Landsat-7 ETM+. J. Ind. Geophysics Union, 12(3), 131-140.

McFeetemrs S.K., (1996). The use of the normalized difference water index (NDWI) in the delineation of open water features. Int. J. Rem. Sens. 17, 1425–1432. https://doi.org/10.1080/01431169608948714.

Patz J.A., D. Campbell-Lendrum, T. Holloway and J.A. Foley (2005). Impact of regional climate change on human health. Nat Cell Biol 438:310–317.

Peng J, J. Ma, Q. Liu, Y. Liu, Y. Hu, Y. Li and Y. Yue (2018) Spatial-temporal change of land surface temperature across 285 cities in China: an urban-rural contrast perspective. Sci Total Environ 635:487–497.

Sobrino, J. A., J. C. Jiménez-Muoz and L. Paolini. (2004), Land surface temperature retrieval from LANDSAT TM 5. // Remote Sensing Environment. 90, pp. 434-446. https://doi.org/10.1016/j.rse.2004.02.003.

Sundara K., P. B. and K. Padmakumari. Estimation of Land Surface Temperature to study Urban Heat Island effect using Landsat ETM+ Image. International Journal of Engineering Science and Technology, 4(2), 771-778.

Tooke, T. R.; Coops, N. C.; Goodwina, N. R.; Voogt, J. A. .(2008)Extracting urban vegetation characteristics using spectral mixture analysis and decision tree classifications. 10.1016/j.rse.2008.10.005.

Walawender, J.P., M. Szymanowski M. and M.J. Hajto (2014). Land Surface Temperature Patterns in the Urban Agglomeration of Krakow (Poland) Derived from Landsat-7/ETM+ Data. Pure Appl. Geophys., 171, 913–940.

Wang F, Z. Qin and C. Song (2015). An Improved Mono-Window Algorithm for Land Surface Temperature Retrieval from Landsat 8 Thermal Infrared Sensor Data. Remote Sensing, 7(4): 4268–4289. https://doi.org/10.3390/rs70404268.

Weng Q. (2001). "A remote sensing-GIS evaluation of urban expansion and its impact on surface temperature in the Zhujiang Delta, China", International Journal of Remote Sensing, Vol. 22, pp.1999-2014.

Weng, Q., Lu, D. and B. Liang (2006): "Urban surface biophysical descriptors and land surface temperature variations", Photogrammetric Engineering & Remote Sensing, Vol. 72, pp.1275-1286.

Zhang X.F., C.H. Liao (2014). Remote Sensing Collaborative Inversion and Assimilation Simulation of Ecological Environment Parameters; Science Press: Beijing, China, 2014.

Zhang, Y., I.O.A. Odeh.; C.F. Han (2009), Bi-temporal characterization of land surface temperature in relation to the impervious surface area, NDVI, and NDBI, using sub-pixel image analysis. International Journal of Applied Earth Observation and Geoinformation. 11, (2009), pp. 256-264. https://doi.org/10.1016/j.jag.2009.03.001.

Zhang Z. and G. He. (2013) Generation of Landsat surface temperature product for China, 2000–2010. Int. J. Remote Sens. 34, 7369–7375.

Journal of Geomatics Vol. 17, No. 1, April 2023

Morphometric analysis of Hirehalla Sub-basin of Malaprabha River, Northern Karnataka using geoinformatics techniques

Pradnya Govekar[1]*, J. T. Gudagur[1], Ajaykumar N. Asode[2]
[1]Department of Geology, Karnatak University's, Karnatak Science College, Dharwad, Karnataka, India-580001
[2]Department of Studies in Geology, Karnatak University, Dharwad, Karnataka, India-580003
*Email: pradnyagovekar87@gmail.com

(Received: 30 November 2022, Accepted in final form: 15th March 2023)

DOI: *https://doi.org/10.58825/jog.2023.18.1.9*

Abstract: In the present study, basin morphometry of Hirehalla Sub-basin of Bagalkote District, Karnataka was carried out using remote sensing and geoinformatics techniques. Delineation and calculation of various morphometric parameters of the sub-basin was done in GIS environment. The study was categorized into– Linear, Aerial and Relief aspects. Result obtained from morphometric analysis confirms the highest order of fifth and showing sub-dendritic to dendritic drainage pattern. Values of shape parameters- form factor (0.16), elongation ratio (0.45) and circulatory ratio (0.38), suggests the sub-basin to be elongated in shape. Average bifurcation ratio value (Rb=3.34), indicates the influence of geomorphic features on the basin. From the values of Stream frequency (1.36) and drainage density (1.27) it indicates, permeable subsurface and low relief. Drainage texture value (1.74) suggests the basin is coarse. In addition, a low value of ruggedness number indicates the resistance of sub-basin to erosion.

Keywords: Hirehalla Sub-basin, Morphometric analysis, Drainage density, Bifurcation ratio, RS & GIS, Karnataka

1. Introduction

Morphometry is the measurement and mathematical analysis of the configuration of the Earth's surface, shape and dimension of its landforms (Clarke, 1966; Agarwal, 1998; Reddy et al., 2004). Morphometric analysis helps in understanding the original gradient or unevenness of rock hardness, structural limits, recent diastrophism, and lithological and geomorphological history of the catchment (Strahler, 1957; Morisawa, 1985). The quantification of drainage network and system is vital in river basin studies as it helps in related investigations- to assess the groundwater potential, surface and groundwater resource management, and environmental assessment (Strahler, 1964; Kudnar and Rajasekhar, 2019). Basin morphometry was first studied by Horton (1932, 1945). The morphometric analysis includes describing linear, aerial and relief features present within a basin (Nautiyal, 1994; Nag and Chakraborty, 2003; Fenta et al., 2017). These morphometric aspects have been studied using remote sensing and topographical maps (Mesa, 2006; Singh et al., 2013).

The hydrological setup of the exposed rocks within a watershed can be determined through quantitative morphometric study of the watershed. A basin's drainage map act as a good indicator of the permeability of rocks and their interrelationship between rock types, structures and their hydrological status (Magesh et al., 2013; Sreedevi et al., 2013). Stream network of drainage basin show temporal and spatial changes. Such runoff patterns significantly alter hydrologic systems, such as stream discharge, suspended sediments, dissolved solids and litter, and catchment characteristics (Bogale, 2021). Watersheds, catchments, and drainage basins serve as the fundamental administrative entities for managing the conservation of natural resources. The idea of basin control deals with the connections between lowlands, uplands, geomorphology, land use, soil, and slope. In watershed management, water and soil fortification is the chief issue in demarcating watersheds (Chandrashekar et al., 2015; Siddhiraju et al., 2020).

Morphometric analysis of the basin has been done with various objectives. Many researchers throughout the world have worked on drainage basins of different geologic and geomorphic regimes such as- *to understand the role of geology in influencing the drainage network of a basin* (Krishnamurthy et al., 1996; Sameena et al., 2009; Dubey et al., 2015). *Quantification and prioritization of watershed and sub-watershed* (Biswas et al., 1999; Hajam et al., 2013; Odiji et al., 2021). Assessment of potential flood risk and flood control were studied by Vandana et al., 2013; Withanage et al., 2015; Asode et al., 2016. However, over the last two decades or so before the emergence of science of RS and GIS, delineation of hydrological characteristics of a watershed can be achieved using conventional techniques and topographical maps (Panda et al., 2019). Further, in recent times, studies related to not only the assessment of various terrain and morphometric parameters of the drainage basins but agricultural, land use/land cover, climate change, recharge studies etc are all mostly done using the capabilities of RS and GIS, as they provide a flexible environment and powerful tools to manipulate and analyse spatial data.

In order to investigate the input of landuse and agriculture as well as climate change in Indonesia's Upper Brantas Basin, Setyorini et al., (2017) used GIS tools. For managing the water resources of Lower Kosi River Basin, Rai et al., (2017) performed morphometric analysis using RS data. Harsha et al., (2019) evaluated the morphometry and hypsometry of the Arkavathy River Basin in South India using the capabilities of RS and GIS. Mahala (2019) using ASTER data and GIS tools studied the hydro-morphological characteristics of Kosi and Kangsabati

River Basin. Arefin and Alam (2020) applied RS and GIS techniques for water resource management of Dhaka City, Bangladesh. For the Mississippi Delta agricultural watershed, Risal et al (2020) used LULC data to investigate changes in surface water flows, sediment, and nutrient yield due to seasonal changes in land use and land cover. Ramachandra et al., (2020) identified potential groundwater zones in the western part of Cuddapah Basin with the aid of geospatial techniques.

Therefore, the investigation carried out using toposheet, remote sensing and GIS tools is mainly focused on assessing basin morphometric characters of Hirehalla Sub-basin of Malaprabha River. Further, in order to analyze the characteristics of various morphometric parameters which are necessary for better planning of soil and water conservation, different parameters have been calculated by means of a mathematical calculation.

2. Study area

The present study, Hirehalla Sub-basin forms part of Bagalkote District, Karnataka. Hirehalla Sub-basin is one of the tributaries of River Malaprabha which in turn is tributary of majorly flowing Krishna River. The Sub-basin is covered in Survey of India (SOI) toposheets numbering– 47P/08; 47P/12; 47P/16; 48M/09 and 48M/13 and is geographically bounded between 74^{o} 30’ to 75^{o} 15’ N Longitudes and 15^{o} 45’ to 16^{o} 15’ E Latitudes and covers aerially an area of 288 Km^{2} (Figure 1). The Sub-basin is connected with all seasoned roads. Physiographically, the study area is part of the Northern Plains with varied topography. Major soil types include a variety of red and black soil (CGWB, 2011). Geologically, the study area is comprised of arenites, basalts, granites, limestones and shale (Figure 2).

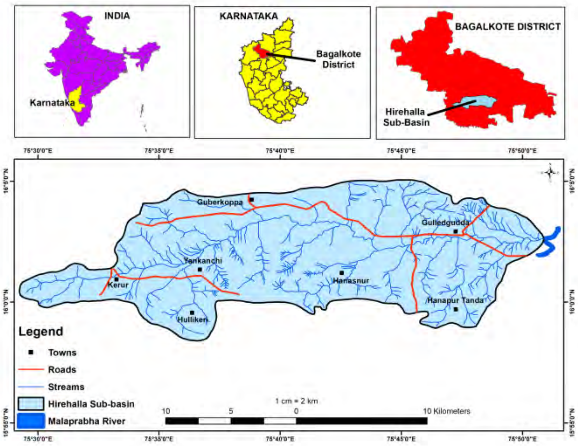

Figure 1. Location map of the study area

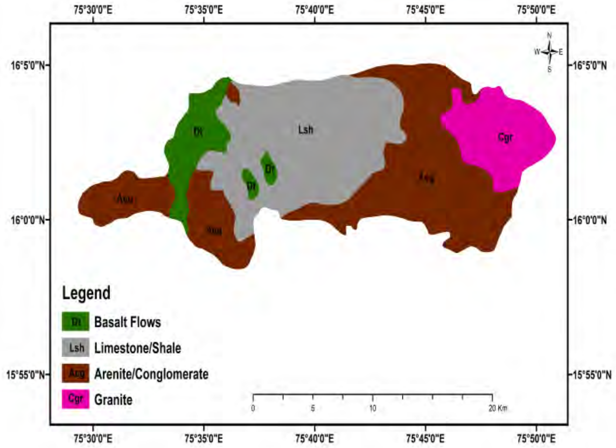

Figure 2. Geological map of the study area (After GSI, 2005)

3. Materials and methods

In this study, the boundary of Hirehalla Sub-basin has been demarcated from Survey of India toposheets numbered- 47P/08, 47P/12, 47P/16, 48M/09 and 48M/13 of 1:50,000 scale. Before demarcation, the toposheets were georeferenced using ground control points then rectified and projected in geographic projection, and re-projected into Universal Transverse Mercator (UTM) projection, WGS 1984, Zone 43 North datum. Table 1 shows the list of Morphometric parameters and their formulae and, the flowchart for the methodology used in this study is shown in figure 3. Its streams were manually delineated and digitized using ArcGIS version 10.3 software. The ordering of streams was done as per Strahler’s system (Strahler, 1957). The drainage map of the sub-basin is shown in figure 4. Shuttle Radar Topography Mission-Digital Elevation Model (SRTM-DEM) data sets of one arc-second (30m) resolution is used in the present study. Spatial analyst tools were used to extract the DEM of the sub-basin. SRTM-DEM data used can be freely downloadable from the USGS Earth Explorer website. This data is then brought into the GIS environment and, slope, topographic elevation and contour maps of the basin are prepared. The study was classified into- linear, aerial and relief aspects. Morphometric parameters such as- stream order, stream number, bifurcation ratio were manually calculated whereas parameters such as stream length, stream frequency, drainage density, shape and, relief parameters were computed using the capabilities of ArcGISv10.3. The geological map of the study area was prepared from District Resource Map of Vijayapur district (then Bagalkote part of Vijayapur) published by the Geological Survey of India in 2005.

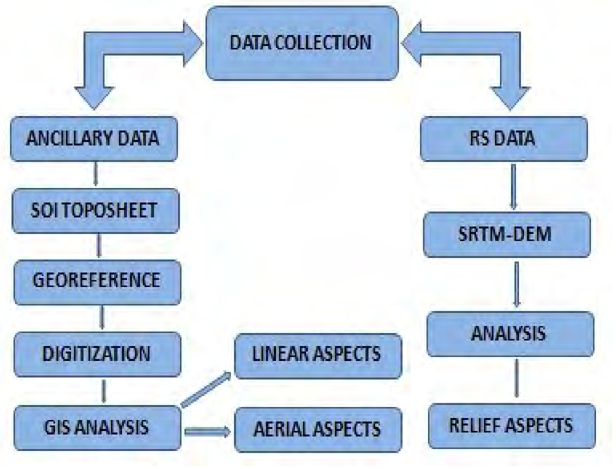

Figure 3. Flowchart of the methodology adopted

Table 1. Standard morphometric parameters and its computational formulae

Sl. No.	Morphometric Parameters	Formula/Definition	Reference
Linear aspects			
1	Stream Order	Hierarchical Rank	Strahler, 1964
2	Stream Number	Total number of stream segments of the order 'u'	Strahler, 1957
3	Bifurcation Ratio	$R_b=N_u/N_{(u+1)}$ where N_u=Total number of stream segments of the order 'u', and $N_{(u+1)}$ = Number of stream segments of the next higher order	Schumm, 1956
4	Stream Length	Total length of the stream segments of that particular order	Horton, 1945
5	Mean Stream Length	$Lsm=\sum L_u/N_u$ where L_u = Total length of the stream segments of that particular order N_u =Total number of stream segments of the order 'u'	Strahler, 1964
6	Stream Length Ratio	$R_l=L_u/L_{(u-1)}$ where L_u= The mean length of all stream segments of a given order (u), and $L_{(u-1)}$ = The mean length of all stream segments of one order less to given order(u)	Horton, 1945
7	Length of Overland Flow	$L_g=1/2D_d$ where D_d = Drainage density of basin	Horton, 1945
Areal aspects			
8	Form Factor	$F_f=A/L_b^2$ where A=Area of the basin (km^2), and L_b=Basin length (km)	Horton, 1932 & 1945
9	Circulatory Ratio	$R_c=4\pi A/P^2$ where A=Area of the basin (km^2), and P=Perimeter of basin (km)	Miller, 1953 & Strahler, 1964
10	Elongation Ratio	$R_e=D/L_b$ $=1.128\sqrt{A}/L_b$ where D=Diameter of a circle of the same area(A) as the basin, A=Area of basin (km^2), and L_b=Basin length	Schumm, 1956
11	Drainage Density	$D_d=\sum L_u/A$ where L_u=Total length of the stream segments of that particular order, and A=Area of the basin (km^2)	Horton, 1932
12	Stream Frequency	$F_s=\sum N_u/A$ where N_u=Total number of stream segments of the order 'u', and A=Area of the basin (km^2)	Horton, 1932
13	Drainage Texture	$T=D_d*F_s$ where D_d=drainage density, and F_s=Stream frequency	Horton, 1945
14	Constant of Channel Maintenance	$C=1/D_d$ where D_d =Drainage density of basin	Schumm, 1956
Relief aspects			
15	Basin Relief	R=(Maximum - Minimum) Elevation	Hadley & Schumm, 1961
16	Relief Ratio	$R_r=R/L$ where R=Basin relief, and L=Basin Length	Schumm, 1956
17	Ruggedness Number	$R_n=R*D_d$ where R=Basin relief, and D_d =Drainage density of basin	Strahler, 1958

4. Results and discussion

4.1 Linear Aspects

4.1.1 Stream order and Stream number

The stream ordering method was first introduced by Horton (1932), which was subsequently modified by Strahler (1957) and is one of the most widely used methods for ranking streams. In the present study Strahler's method of stream ordering is used, where the smallest finger tip tributaries are designated as first order stream. When two such first order streams intersect, a stream of second order is developed. Further, a second order stream is created when two of these first orders meet and, stream of order third is formed when two streams of order two meets and so on. From the above, the sub-basin is found to be in the highest order of five (Table 2). According to Horton (1945), an inverse geometric sequence with an order number is formed by the number of stream segments in each order. In the present study, frequency of stream numbers is highest in the first order streams. It is also noted that with increasing stream order the frequency of stream number decreases (Table 2; Figure 6). This dominant first order streams in the sub-basin imply hilly terrain and compact nature of bed rock lithology (Magesh et al., 2013).

4.1.2 Stream length

Stream length (Lu) is a dimensional property used to understand the characteristic size of the components of a drainage network. Generally, where rock formations are permeable, a smaller number of relatively longer streams are formed, whereas a larger number of smaller streams are formed where rock formations are less permeable (Pakhmode et al., 2003; Subba rao, 2008). In the present study, ESRI ArcGIS version 10.3 software is used to measure the stream length of the basin from river mouth to the drainage divide. The measured stream length of sub-basin was in line with the law proposed by Horton (1945). From the study, it was observed that the total length of the stream decreased with the increasing stream order and was highest in the first order streams (Table 2). This is justified as the plot stream number versus stream length shows positive correlation (straight line) and validates Horton's Law of Stream Length indicating geometrical similarity in the sub-basin of increasing order (Figure 5). This may be due to flowing streams from high elevations, changes in the type of rock and moderate steep slopes as well as possible uplifts across the basin (Singh and Singh, 1997; Vittala et al., 2004; Chopra et al., 2005 and Rudraiah et al., 2008).

4.1.3 Mean stream length

Mean stream length (Lsm) is a characteristic feature of the drainage network component and associated basin surfaces (Strahler, 1964). It is measured by dividing it up into an overall number of segments in that order. Lsm of Hirehalla Sub-basin range from 0.51 to 5.0 Km (Table 2) and it is observed that the Lsm of any given order is higher than that of the lower order and lower than that of the next higher order. This indicates that the order's main stream is more extensive, in comparison to its past tributary streams (Das and Pardeshi, 2018).

4.1.4 Stream length ratio

Horton (1945) defined stream length ratio (Rl) as the ratio of the mean length of the given order to the next lower order of the stream segments. He suggested application of Rl as a tool for assessing the permeability of subsurface formations and that the Rl is likely to be constant at every successive order of the basin. Further, Rl value of any catchment indicates significant changes in the hydrological properties of the subsurface strata over the areas of consecutive stream orders. (Pakhmode et al., 2003). Rl values of Hirehalla Sub-basin range from 0.30 to 0.89 (Table 2). From the table 2 it is noted that, the low values of Rl indicates, that these stream flow over relatively less permeable rocks and the basin at the matured geomorphological stage.

4.1.5 Bifurcation ratio

Schumm (1956) defined a bifurcation ratio (Rb) as the ratio of the number of stream segments in a given order to the number of streams in the next higher order. It is a measure of the degree of distribution of stream network (Mesa 2006). According to Strahler (1964), geological structures donot influence the basin where Rb values are between 3 and 5. In addition, when Rb value exceeds 5 it implies that development of basin is structurally dominated. Further, low value of Rb indicates Elongated basins while high Rb values indicate circular basins (Soni, 2017). In the present investigations, the Rb value varies from 3.83 to 4.50 with an average Rb value of 3.34 (Table 2), suggests the influence of dominant geomorphic control over structural control and implying normal category of basins. Furthermore, the Rb values are similar to the universal value for maturely dissected drainage basins and the stream flows over rocks with consistent erosion resistance for the basin having Rb value of about four (Subba rao, 2008; Singh et al., 2020).

4.1.6 Length of overland flow

Length of overland flow (Lg) is one of the important factors, affecting- both the hydrological and physiographic development of water catchments (Horton, 1945; Ansari et al., 2012). Lg is the length of the stream flow-paths, which is projected to the horizontal from the point of drainage divide to a point on the adjacent stream channel, where its average is equal to half the reciprocal of average drainage density. According to Strahler (1964), the surface runoff is the result of a system of downhill flowpaths from the drainage divide to the nearest channel. A position in the river basin is crucial for these flownets, consisting of a family of orthogonal curves with respect to topographic contours that are local convergence or divergence from parallelism. The Lg value calculated for the current sub-basin is 0.39 (Table 2), which indicates a lower permeability, structural disturbance, steeper slopes and higher surface runoff (Khan et al., 2021).

Table 2: Linear aspects of Hirehalla Sub-Basin

Stream Order	Stream Number	Stream Length	Bifurcation Ratio	Mean Stream Length	Stream Length Ratio	Length of overland flow
1	300	155	4.35	0.51	0.89	0.39
2	69	138	3.83	2.00	0.39	
3	18	54	4.50	3.00	0.30	
4	04	16	4.00	4.00	0.31	
5	01	05	0	5.00	0.00	
Total	**392**	**368**	**3.34 (Avg)**			

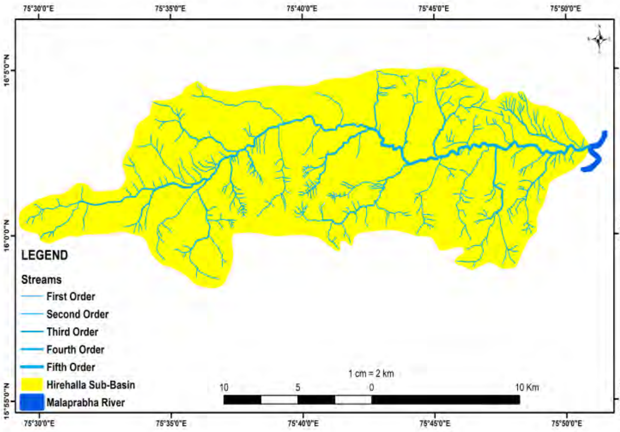

Figure 4. Drainage network map of the Hirehalla Sub-basin

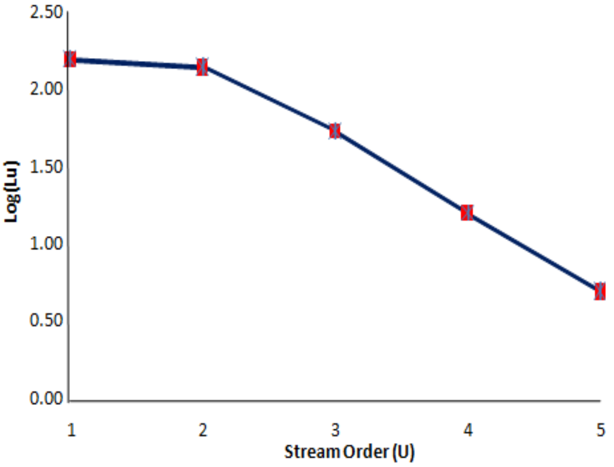

Figure 5. Regression stream length versus stream order

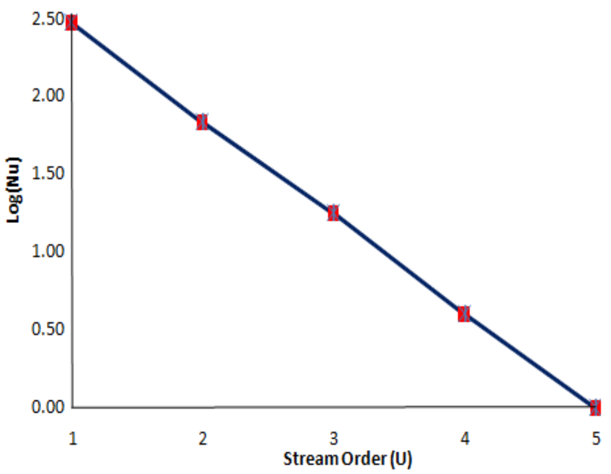

Figure 6. Regression stream number versus stream order

4.2 Aerial aspects

4.2.1 Form factor

Form factor (Ff) is the ratio of the area of the basin and the square of the basin length (Horton, 1932). Further, low value of Ff suggests elongate basin on contrary, high value of Ff suggests circular shape of basin. The computed value of Ff for the present study is 0.16 (Table 3), which indicates Hirehalla sub-basin is elongated with no rapid peak flows from the outlet. In addition, as said earlier the lower value of Ff suggests elongate basin wherein basin experiences low peak flows for longer period but basin with higher value of Ff experiences higher peak flows of smaller period.

4.2.2 Circulatory ratio

Dimensionless circulatory ratio (Rc) is defined as the ratio of basin area to the area of a circle having the same perimeter as the basin. It is observed, low values of Rc indicates elongated basin with highly permeable subsurface and high value of Rc indicates low relief and impermeable subsurface. In addition, where the basin discharge is quite large, Rc value maintained its uniformity in the range of 0.6 to 0.7 while for Rc value of one it implies that the basin is circular in shape (Miller, 1953). The Rc value for Hirehalla Sub-basin is 0.38 (Table 3), indicating that the basin does not have a circular shape. Therefore, discharge is less as compared to circular shaped basins. Additionally, young, mature and old stages of the life cycle of tributary are indicative from Rc values of low, medium and high respectively (Rai et al., 2017).

4.2.3 Elongation ratio

Elongation ratio (Re) is the ratio between the diameter of the circle of the same area as the drainage basin and the maximum basin length (Schumm, 1956). Generally, for a wide range of climate and geologic types the Re value range from 0.6 to 1.0.

Miller (1953) studied that, Re values near to 1.0 are characteristic feature of areas of low relief while where Re values range between 0.6 to 0.8, corresponds to high degree of relief and steep slope. In addition, compared to a elongated basin, the circular basin is more efficient at discharging run-off (Singh and Singh, 1997). The Re value for the present study is 0.45 (Table 3) suggesting the basin to be elongated in shape.

4.2.4 Drainage density

Horton (1932) first coined the term drainage density (Dd) to indicate channel spacing. It is an important factor which describes the climatic conditions, rock types, relief, infiltration capacity, vegetation cover, surface roughness and runoff intensity index. It is an important parameter in the determination of the time of travel by water (Langbein, 1947). Higher values of Dd suggests the area to be having impermeable subsurface, sparse vegetation, high relief and fine drainage texture where as low values of Dd shows areas of highly permeable subsurface, dense vegetation, low relief and coarse drainage texture (Nag, 1998). The main morphological factors controlling drainage density are slope and relative height. The Dd value of the present study is 1.27 Km/Km2 (Table 3), indicating permeable subsoil, coarse texture, dense vegetation cover and low relief (Soni, 2017; (Rai et al., 2017).

4.2.5 Stream frequency

Stream frequency (Fs) or channel frequency is defined as the ratio of the total number of stream segments of all orders per unit area (Horton 1932). The value of channel frequency varies for different. The high value of Fs indicates a larger number of stream availability, high rate of surface run-off and steep slope (Gundekar et al., 2011). The calculated value of Fs for the present study is 1.36 (Table 3). This increase in stream population with respect to an increasing Dd implies positive correlation between Fs and Dd (Das and Pardeshi, 2018).

4.2.6 Drainage texture

Horton (1945) defined drainage texture (Dt) as the total number of stream segments of all orders per basin. According to him, Dt includes drainage density and stream frequency and it is influenced by the infiltration capacity of the basin. Massive, resistant rock shows coarse drainage texture while subsurface underlained by soft or weak rock, show fine drainage texture. In particular, the climate and vegetation in the area determine the texture of the drainage (Dornkamp and King, 1971). Further, Smith (1950) categorized Dt into five classes based on drainage density i.e., Dd <2 (Very Coarse); between 2 and 4 (Coarse); between 4 and 6 (Moderate); between 6 and 8 (Fine) and >8 (Very Fine) drainage texture. The computed values of Dt for the present study is 1.74 (Table 3), indicating coarse drainage texture (Shrivatra et al., 2021).

4.2.7 Constant of channel maintenance

Schumm (1956) used the inverse of drainage density as constant of channel maintenance (C) and defined it as the area of basin surface needed to sustain a unit length of the stream channel. C depends on the duration of erosion and climatic history apart from geology, permeability, vegetation and relief. In the areas of close dissection the values of C is found to be very low. In generally, higher C value indicates higher permeable nature of the subsurface strata of the catchment and vice versa (Gundekar et al., 2011). The calculated value of C for the Hirehalla Sub-basin is 0.78 Km^2/Km (Table 3), that means an area of 0.78

Km^2/km is needed to support one kilometer of stream channel.

4.3 Relief aspects

4.3.1 Basin relief

Basin relief (R) is the difference in altitude between the highest and the lowest point of the basin. Hadley and Schumm (1961) state that relief controls the stream slope which in turn affects flood patterns and sediment transport capacity of the basin. Basin relief of the study area is 189 meters (Table 3; Figure 6-7).

4.3.2 Relief ratio

Schumm (1963) defined relief ratio (Rr) as the maximum relief to horizontal distance along the longest dimension of the basin parallel to the principal drainage line. He suggested that there is a relationship between the hydrological characteristics of a watershed and the relief ratio. In addition, high values of Rr typically indicates hilly region while low values of Rr indicates pediplains and valley. The Rr value of Hirehalla sub-basin is 0.045 (Table 3). This low value of Rr implies the presence of resistant basement and low slope.

4.3.3 Ruggedness Number

Strahler (1958) stated ruggedness number (Rn) as the product of basin relief and drainage density which focuses on the structural complexity and denudational characteristics of the terrain. The higher value of Rn implies structural domination and higher proneness to erosion while low value implies lesser proneness to erosion. From the study, the Rn value was calculated to be 0.241 (Table 3), indicating that the Hirehalla Sub-Basin is resistant to erosion. This smaller Rn values in the present study suggest, a developed river basin with long drainage density, similar lithology, no structural influence and moderate slope which reduces erosional susceptibility (Pande and Das, 2016; Venkatesh and Anshumali, 2019).

Table 3 Aerial and Relief aspects of Hirehalla Sub-Basin

Parameters	Hirehalla Sub-Basin
Area	288 Km^2
Perimeter	97 km
Length	42 km
Form factor (Ff)	0.16
Circulatory ratio (Rc)	0.38
Elongation ratio (Re)	0.45
Drainage density (Dd)	1.27 Km/Km^2
Stream frequency (Fs)	1.36
Drainage texture (Dt)	1.74
Constant of Channel Maintenance (C)	0.78 Km^2/Km
Basin relief (R)	189 m
Relief ratio (Rr)	0.045
Ruggedness number (Rn)	0.024

4.3.4 Slope Analysis

Slope of a basin determines its degree of inclination with respect to the horizontal surface. An understanding of slope is vital in projects related to agriculture, planning and engineering (Sreedevi et al., 2005). In areas of different lithology and varied rate of resistance, morpho-climatic processes determine the slope of an area (Magesh et al., 2011; Gayen et al., 2013; Shrivatra et al., 2021). Slope map of the study area (Figure 8) was generated using SRTM-DEM and classified into five classes (Berhanu et al., 2013). The observation of the slope map of HSB reveals that- 0º-5º (Gentle), 5º-10º (Moderate), 10º-15º (Strong), 15º-20º (Very Strong) and 20º-33º (Steep) slope. Hirehalla Sub-Basin predominantly has gentle slope implying less vulnerable to run-off and erosion.

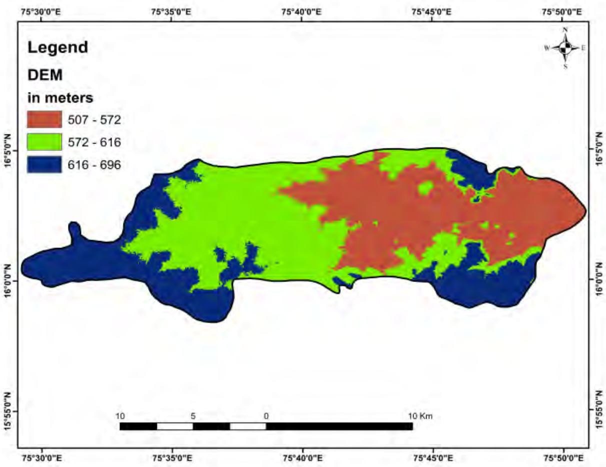

Figure 7. Digital elevation model of Hirehalla Sub-Basin

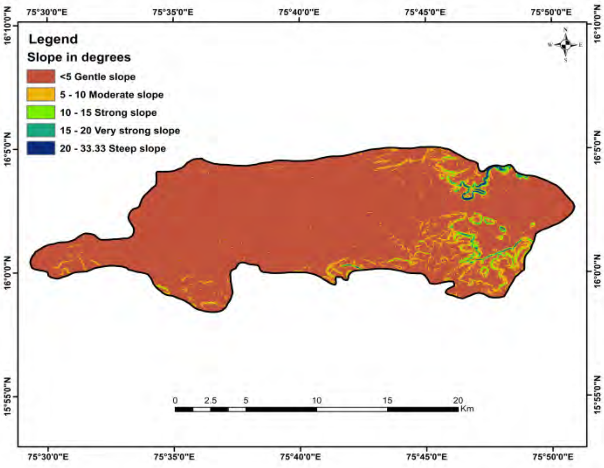

Figure 8. Slope map of Hirehalla Sub-Basin

5. Conclusion

Morphometric analysis of the Hirehalla Sub-Basin of Bagalkote District, Karnataka was carried out using topographical maps, remote sensing data and geoinformatics techniques. From the study following observations were made. Hirehalla Sub-basin geographically covers an area of 288 Km^2 with the highest stream order of five and having dendritic to sub-dendritic drainage patterns. From the values of shape parameters such as form factor (0.16), circulatory ratio (0.38) and elongation ratio (0.45) the sub-basin is asymmetrical (elongated) in shape and shows early stage of maturity. Average bifurcation value (Rb=3.34) ratio emphasis towards geomorphic development of basin. The low values and positive correlation between drainage density (1.27 Km^2/Km) and stream frequency (1.36) indicates the basin to be moderately permeable, gentle slope, low run-off and high water storage capacity. Low values of basin relief and degree of slope, suggest lesser steep, low chances of flood, resistance to erosion and capacities to transport sediments. Thus, the present study of morphometric analysis coupled with RS and GIS provides detailed information about the hydrological and geomorphological conditions of the Hirehalla Sub-basin. Further, there is good scope for future work based on above studies for proposing of location and designing of artificial recharge structures for augmenting the groundwater.

Acknowledgment

The first author PG thanks the Head, Department of Geology, Karnatak University's Karnatak Science College, Dharwad for extending all the laboratory support to carry out this research work. The authors would like to thank the Chief Editor, JoG and anonymous reviewers for their valuable suggestions and comments which helped in improving the quality of the manuscript.

Conflict of Interest

The authors confirm that there is no conflict of interest.

References

Agarwal CS (1998). Study of drainage pattern through aerial data in Naugarh Area of Varanasi District, U.P. *J Indian Soc Remote Sens*, **26(4)**: 169-175.

Arefin R and J Alam (2020). Morphometric study for water resource management using principal component analysis in Dhaka City, Bangladesh: a RS and GIS approach. *Sustainable Water Resources Management* 6:38 https://doi.org/10.1007/s40899-020-00402-x

Asode AN, A Sreenivasa and TK Lakkundi (2016). Quantitative morphometric analysis in the hard rock Hirehalla sub-basin, Bellary and Davanagere Districts, Karnataka, India using RS and GIS. *Arab J Geosci* 9:381. https://doi.org/10.1007/s12517-016-2414-x

Ansari ZR, LAK Rao and S Yusuf (2012). GIS based morphometric analysis of Yamuna drainage network in parts of Fatehabad area of Agra district, Uttar Pradesh. *Jour. Geol. Soc. India*, 79(5), pp. 505-514.

Berhanu B, AM Melesse and Y Seleshi (2013). GIS-based hydrological zones and soil geodata base of Ethipia. *CATENA*, 104:21-31 https://doi.org/10.1016/j.catena.2012.12.007

Bogale A (2021). Morphometric analysis of a drainage basin using geographical information system in Gilgel Abay watershed, Lake Tana Basin, upper Blue Nile Basin, Ethiopia. *Appl Water Sci*, 11:122 https://doi.org/10.1007/s13201-021-01447-9

Biswas S, S Sudhakar and VR Desai (1999). Prioritization of sub watersheds based on morphometric analysis of drainage basin: A remote sensing and GIS approach. *J Indian Soc Remote Sens*, 27 (3), pp. 155-166

CGWB (2011). Report on Groundwater of Bagalkote District, Karnataka. *Central Ground Water Board, Bangalore*.

Chandrashekar H, KV Lokesh, M Sameena, J Roopa and G Ranganna (2015). GIS-Based Morphometric Analysis of Two Reservoir Catchments of Arkavati River, Ramanagaram District, Karnataka. *Aquatic Procedia*, 4, 1345-1353. doi:10.1016/j.aqpro.2015.02.175

Chopra R, RD Dhiman and PK Sharma (2005). Morphometric analysis of sub-watersheds in Gurdaspur district, Punjab using remote sensing and GIS techniques. *J Indian Soc Remote Sens*, 33:531–539.

Clarke JI (1996). Morphometry from Maps. *Essays in Geomorphology*. Elsevier publication. Co., New York, pp 235–274

Das S and SD Pardeshi (2018). Morphometric analysis of Vaitarna and Ullas River Basins, Maharashtra India: Using Geospatial Technologies. *Appl Water Sci*, 8:158. https://doi.org/10.1007/s13201-018-0801-z

Dornkamp JC and CAM King (1979). Numerical analyses in geomorphology, an introduction. *St. Martins Press*, New York, p 372.

Dubey SK, D Sharma and N Mundetia (2015). Morphometric analysis of the Banas River Basin using the geographical information system, Rajasthan, India. *Hydrology*, 3 (5), pp. 47-54. 10.11648/j.hyd.20150305.11

Fenta AA, H Yasuda, K Shimizu, N Haregeweyn and K Woldearegay (2017). Quantitative analysis and implications of drainage morphometry of the Agula watershed in the semi-arid northern Ethiopia. *Appl Water Sci*, **7**, 3825–3840. https://doi.org/10.1007/s13201-017-0534-4

Gayen S, GS Bhunia and PK Shit (2013). Morphometric analysis of Kangshabati–Darkeswar interfluves area in West Bengal, India using ASTER DEM and GIS techniques. *J Geol. Geosci*. 2(4):1–10. https://doi.org/10.4172/2329-6755.10001 33

Gundekar HG, DS Arya and NK Goel (2011). Morphometric study of the Dudhana river basin (Maharashtra). *Hydrology Journal*, Vol. 34, Issue 1-2, pp 33-41.

Hadley RF and SA Schumm (1961). Sediment sources and drainage basin characteristics in upper Cheyenne River basin. *USGS Water Supply Paper*, 1531-B, US Geological Survey.

Hajam RA, A Hamid and S Bhat (2013). Application of morphometric analysis for geo-hydrological studies using geo-spatial technology: a case study of Vishav drainage basin. *Hydrol Curr Res*, 4:12

Harsha J, AS Ravikumar and BL Shivakumar (2019). Evaluation of morphometric parameters and hypsometric curve of Arkavathy river basin using RS and GIS techniques. *Appl. Water Sci*, 10:86 https://doi.org/10.1007/s13201-020-1164-9

Horton RE (1932). Drainage-basin characteristics. EOS *Trans Am Geophys Union* 13(1):350–361

Horton RE (1945). Erosional development of streams and their drainage basins; hydrophysical approach to quantitative morphology. *Geol Soc Am Bull* 56(3):275–370

Khan I, R Bali, KK Agarwal, D Kumar and SK Singh (2021). Morphometric Analysis of Parvati Basin, NW Himalaya: A Remote Sensing and GIS Based Approach. *Jour. Geol. Soc. India*, Vol.97, pp. 165-172. https://doi.org/10.1007/s12594-021-1648-8

Krishnamurthy J, G Srinivas, V Jayaram and MG Chandrasekhar (1996). Influence of rock type and structure in the development of drainage networks in typical hard rock terrain. *ITC J*, 4(3):252–259

Kudnar N and M Rajasekhar (2019). A study of the morphometric analysis and cycle of erosion in Waingangā Basin, India. *Model. Earth Syst. Environ.* 6, 311-327 https://doi.org/10.1007/s40808-019-00680-1

Langbein WB (1947). Topographic characteristics of drainage basins. *US Geol Surv Water Supply* 986:157–159. https ://doi.org/10.3133/wsp96 8C

Magesh NS, KV Jitheshlal, N Chandrasekar and KV Jini (2011). GIS based morphometric evaluation of Chimmini and Mupily watersheds, parts of Western Ghats, Thrissur District, Kerala. India. *Earth Sci Inform* 5(2):111–121. https://doi.org/10.1007/s1214 5-012-0101-3

Magesh NS, KV Jitheshal, N Chandrasekar and KV Jini (2013). Geographical information system based morphometric analysis of Bharathapuzha River Basin, Kerla, India. *Appl. Water Sci,* 1–11. https://doi.org/10.1007/s13201-013-0095-0

Mahala A (2019). The significance of morphometric analysis to understand the hydrological and morphological characteristics in two different morpho- climatic settings. *Appl. Water Sci,*10:33 https://doi.org/10.1007/s13201-019-1118-2

Mesa LM (2006). Morphometric analysis of a subtropical Andean basin (Tucuman, Argentina). *Environ Geo,l* 50(8):1235–1242. https://doi.org/10.1007/s0025 4-006-0297-y

Miller VC (1953). Quantitative geomorphic study of drainage basin characteristics in the Clinch Mountain area, Virginia and Tennessee. *Technical Report* (Columbia University Department of Geology); No. 3

Morisawa ME (1985). Relation of Quantitative Geomorphology to Stream Flow in Representative Watersheds of the Appalachian Plateau Province. *Project NR 389-042*, *Technical Report 20*, Department of Geology, ONR, Columbia University, Geography Branch, New York.

Nag S (1998). Morphometric analysis using remote sensing techniques in the Chaka sub-basin, Purulia district, West Bengal. *J Indian Soc Remote Sens,* 26(1–2):69–76

Nag SK and S Chakraborty (2003). Influence of rock types and structures in the development of drainage network in hard rock area. *J Indian Soc Remote Sens,* 31, 25–35. https://doi.org/10.1007/BF03030749

Nautiyal MD (1994). Morphometric analysis of drainage basin, Dehradun district, Uttar Pradesh. *J Indian Soc Remote Sens,* 22 (4), 252–262.

Odiji CA, OM Aderoju, JB Eta, I Shehu, A Mai- Bukar and H Onuoha (2021). Morphometric analysis and prioritization of upper Benue River watershed, Northern Nigeria. *Appl Water Sci,* 11:41 https://doi.org/10.1007/s13201-021-01364-x

PakhmodeV, K Himanshu and SB Deolankar (2003). Hydrological drainage analysis in watershed-programme planning: a case from the Deccan basalt, India. *Hydrogeol. J*. 11:595–604

Panda B, M Venkatesh and B Anshumali (2019). A GIS-based approach in drainage and morphometric analysis of ken river basin and sub-basins, Central India. *J Geol Soc India,* **93**, 75–84. https://doi.org/10.1007/s12594-019-1125-9

Pande PK and SS Das (2016). Morphometric analysis of Usri river basin, Chhota Nagpur Plateau, India, using remote ssensing and GIS. *Arab. J. Geosci*. 9(240). https://doi.org/ 10.1007/s12517-015-2287-4

Rai PK, RS Chandel, VN Mishra and P Singh (2017). Hydrological inferences through morphometric analysis of lower Kosi river basin of India for water resource management based on remote sensing data. *Appl Water Sci*, 8:15. https ://doi.org/10.1007/s13201-018 0660-7

Ramachandra M, KR Babu, M Rajasekhar and BK Pradeep (2020). Identification of Groundwater Potential Zones using AHP and Geospatial Techniques in Western Part of Cuddapah Basin, Andhra Pradesh, India. *Hydrospatial Analysis*, 3(2) pp, 60-71 https://doi.org/10.21523/gcj3.19030202

Reddy GPO, AK Maji and KS Gajbhiye (2004). Drainage morphometry and its influence on landform characteristics in basaltic terrain, Central India – a remote sensing & GIS approach. *Int. J. Appl. Earth Obs. Geoinf.*, 6, 1–16. https://doi.org/10.1016/j.jag.2004.06.003

Risal A, PB Parajuli, P Dash, Y Ouyang and A Linhoss (2020). Sensitivity of hydrology and water quality to variation in land use and land cover data. *Agric. Water Manag.*, Vol. 241, 106366

Rudraiah M, S Govindaiah and SS Vittala (2008). Morphometry using remote sensing and GIS techniques in the sub-basins of Kagna river basin, Gulburga district, Karnataka, India. *J Indian Soc Remote Sens* 36, 351–360. https://doi.org/10.1007/s12524-008-0035-x

Sameena M, J Krishnamurthy, V Jayaraman and G Ranganna (2009). Evaluation of drainage networks developed in hard rock terrain: *Geocarto Int* 24(5): 1-24

Setyorini A, D Khare and SM Pingale (2017). Simulating the impact of land use/land cover change and climate variability on watershed hydrology in the Upper Brantas basin, Indonesia. *Appl Geomat*, 9:191-204 10.1007/s12518-017-0193-z

Schumm SA (1956). Evolution of drainage basins and slopes in bund land of Peth Amboy, New Jersey. *Bull Geol Soc Am*, 67:597–646

Schumm SA (1963). Sinuosity of alluvial rivers on the Great Plains. *Geol. Soc. Am. Bull.,* 74, 1089–1100.

Shrivatra JR, BS Manjare and SK Paunikar (2021). A GIS-based assessment in drainage morphometry of WRJ-1 watershed in hard rock terrain of Narkhed Taluka, Maharashtra, Central India. *Remote Sens. Appl. Soc. Environ*, 22 100467 https://doi.org/10.1016/j.rsase.2021.100467

SiddhiRaju R, GS Raju and M Rajashekhar (2020). Morphometric analysis of Mandavi River in Rayalaseema region of Andhra Pradesh (South India), using remote sensing and GIS. *Ind. Geophys. Union*, 24(1), 54-67.

Singh S and MC Singh (1997). Morphometric analysis of Kanhar river basin. *Natl. Geogr. J. India*, 43 (1), 31–43.

Singh P, JK Thakur and UC Singh (2013). Morphometric analysis of Morar river basin, Madhya Pradesh, India, using remote sensing and GIS techniques. *Environ. Earth Sci*, 68:1967–1977. http://dx.doi.org/10.1007/s12665-012-1884-8

Singh AP, AK Arya and DS Singh (2020). Morphometric Analysis of Ghaghara River Basin, India, Using SRTM Data and GIS. *Jour Geol Soc India*, 95(2):169–178.

Soni S (2017). Assessment of morphometric characteristics of Chakrar watershed in Madhya Pradesh India using geospatial technique. *Appl Water Sci*. 7:2089–2102 DOI 10.1007/s13201-016-0395-2

Sreedevi PD, K Subrahmanyam and A Shakeel (2005). The significance of morphometric analysis for obtaining groundwater potential zones in a structurally controlled terrain. Envi. Geol, 47(3):412–420. https://doi.org/10.1007/s0025 4-004-1166-1

Sreedevi PD, PD Sreekanth, HH Khan and S Ahmed (2013). Drainage morphometry and its influence on hydrology in a semi-arid region: using SRTM data and GIS. Environ. Earth Sci, 70(2), 839-848. doi:10.1007/s12665-012-2172-3

Strahler AN (1958). Dimensional analysis applied to fluvial eroded landform. *Geol Soc Am Bull* 69(9):279–300

Strahler AN (1957). Quantitative analysis of watershed geomorphology. *Transactions of American Geophysics Union*, 38, 913_920.

Strahler AN (1964). Quantitative geomorphology of drainage basins and channel networks. *Handbook of Applied Hydrology*. McGraw-Hill, New York, pp 4–39

Smith KG (1950). Standards for grading texture of erosional topography. *American Journal of Science*, 248, 655-668.

Subba Rao N (2008). A numerical scheme for groundwater development in a watershed basin of basement terrain: a case study from India. *Hydrogeology Jour.*, 17, pp.379–396. http://dx.doi.org/10.1007/s10040-008-0402-2

Vandana M (2013). Morphometric analysis and watershed prioritization: a case study of Kabani river basin, Wayanad district, Kerala, India. *Indian J Geo-Mar Sci* 42:211–222

Venkatesh M and B Anshumali (2019). A GIS based assessment of recent changes in drainage and morphometry of Betwa river basin and sub-basins, Central India. *Appl. Water Sci*. https://doi.org/10.1007/s13201-019-1033-6

Vittala SS, S Govindaiah and HH Gowda (2004). Morphometric analysis of the sub-watersheds in the Pavagada area of Tumkur district, South India using remote sensing and GIS techniques. *J Indian Soc Remote Sens*, 32 (4), 351-361.

Withanage SN, KDN Dayawansa and PR De Silva (2014). Morphometric analysis of the Gal Oya River Basin using spatial data derived from GIS. *Tropical Agricultural Research*, 26 (1) (2014), pp. 175-188

INDIAN SOCIETY OF GEOMATICS: AWARDS

National Geomatics Award for Excellence

This award has been instituted to recognize outstanding and conspicuously important contribution in promoting geomatics technology and applications at the country level. The contributions should have made major impact on the use of this technology for national development.
Areas of contribution considered for the award are:

1. Geographical Information System
2. Global Positioning System
3. Photogrammetry
4. Digital Cartography
5. Applications of Geomatics

The award shall consist of Rs. 50,000/- in cash, a medal and citation.

Eligibility

Any citizen of India, engaged in activities related to geomatics technology and its applications is eligible for this award. The prize is awarded on the basis of work primarily done in India.

The age limit for awardees is 45 years or above as on June 30 of the year of award.

Selection

A duly constituted Award Committee will evaluate all nominations received. The committee shall consist of eminent experts in the field of geo-spatial technology, to be identified by the Executive Council, ISG. The committee shall forward selected name/s to ISG – EC for approval and announcement. Apart from those persons, whose nominations have been received, the Committee may consider any person or persons who, in their opinion, have made outstanding contributions to development of geo-spatial technology and applications.

The award can be withheld in any year if, in the opinion of the committee, no candidate is found suitable in that particular year.

Presentation of the Award

The award shall be presented during the Annual Convention of ISG. Local Hospitality shall be taken care by ISG & Air fare (low cost) may be reimbursed if awardees request for it.

How to make Nomination

The nominations can be proposed by Head of a major research institute/ centre; Vice-Chancellor of a university; Secretary of Government Scientific Departments; President of a National Academy, President, Indian Society of Geomatics / Indian Society of Remote Sensing / Indian National Cartographic Association / ISG fellow or two life members of the society with more than 10 year old membership.

A candidate once nominated would be considered for a total period of two years. Nomination should be sent in the prescribed format to Secretary, ISG.

The last date for receiving nominations shall be September 30 or otherwise extended.

Format for nomination of Geomatics Award for Excellence

1. Name of the Nominee
2. Postal Address
3. Academic Background (Bachelor degree onwards)
4. Field of Specialisation
5. Important positions held (in chronological order)
6. Professional Experience including foreign assignments.
7. Important Awards / Honours
8. Important Publications/Patents: (A set of ten most important publications to be enclosed with this form)
9. Contributions of Nominee based on which the nomination is sent (in 1000 words, also provide a statement in 50 words which may be used for citation.):
10. Other Relevant Information:

Proposer:

Signature
Name
Address
Phone/ Fax
E-mail
Life Membership No. (in case of ISG Member):

Place & Date

Endorsed by (in case nomination is by 2 ISG Life members)

Signature
Name
Address
Phone/ Fax
E-mail
Life Membership No. (in case of ISG Member):

Place & Date
(The proposer should give a brief citation of the nominee's work)

National Geomatics Award

National Geomatics Award to be given each year: a) for original and significant contribution in Geomatics technology, b) for innovative applications in the field of Geomatics. Each award comprises a medal, a citation and a sum of Rs 25,000/- The guidelines for these awards are available on ISG website.

ISG Chapter Award for Best Performance

The best chapter award will be given to an active chapter of Indian Society of Geomatics, which has made significant contribution to further the mandate and goal of the society. The award consists of a citation and medal

President's Appreciation Medal for Contribution to the ISG

This award will be given to a member of the society, who has made noteworthy contribution to the growth of the ISG (its main body or any chapter). The Award consists of a Medal and a Citation.

Prof. Kakani Nageswara Rao Endowment Young Achiever Award

Indian Society of Geomatics instituted a new award from year 2013 named "Prof. Kakani Nageswara Rao Endowment Young Achiever Award", to encourage young researchers/scientists/academicians pursuing research in the field of geospatial technology/applications. The award carries a cash prize of Rs. 10,000/- along with a citation.

NATIONAL GEOMATICS AWARD

Indian Society of Geomatics has instituted two National Geomatics Awards to be given each year for (a) Original and significant contribution in Geomatics technology, (b) Innovative application(s) in the field of Geomatics. Each award comprises a medal, a citation and a sum of Rs. 25,000/-.

The guidelines for the award are as under

Areas of contribution considered for the award (both technology and applications)

1. Geographical Information System
2. Global Positioning System
3. Photogrammetry
4. Digital Cartography
5. Remote Sensing

Eligibility

Any citizen of India engaged in scientific work in any of the above-mentioned areas of research is eligible for the award.

The awards are to be given for the work largely carried out in India.

- First award will be given for original contribution in the field of Geomatics technology supported by publications in a refereed journal of repute.
- Second award will be given for carrying out innovative application(s). Supported by publications in rear reviewed Journals of repute.
- The contribution for the first award should have been accepted by peers through citation of the work.
- Work based on the applications of existing technologies will not be considered for the first award.
- The work should have made impact on the overall development of Geomatics.

How to Send Nomination

Nominations should be sent in the prescribed format, completed in all aspects to the Secretary, Indian Society of Geomatics, Space Applications Centre Campus, Ahmedabad 380 015 by August 31 of the year of award.

Selection Process

An expert committee, consisting of at least three members, constituted by the Executive Council of the Indian Society of Geomatics, will scrutinize the nominations and recommend the awardees' names to the Executive Council. The Council will decide on the award based on the recommendations.

FORMAT FOR AWARD NOMINATION

1. Name of the Candidate:
2. Present Position:
3. Positions held earlier (chronological order):
4. Academic qualifications (Bachelor’s degree onwards):
5. Names of at least three Indian Scientists/Technologist in the area as possible referees *:
6. Brief write up on the work (500 words) for which award is claimed:
7. Publication(s) on the above work (reprint(s) to be enclosed):
8. List of other publications of the candidate:
9. Citation of the work for which award is claimed:
10. Impact of the work (for which award is claimed) on the development in the field of Geomatics (500 words):
11. Whether the work has already won any award? If so, give details:

The Applications in the above format (five copies) should be submitted (by Registered Post or Speed Post) to

The Secretary, Indian Society of Geomatics,
Space Applications Centre Campus,
Ahmedabad-380015

so as to reach by September 30 of the year of award

*ISG is, however, not bound to accept these names and can refer the nomination to other experts/peers

INDIAN SOCIETY OF GEOMATICS: FELLOWS

Shri Pramod P. Kale, Pune
Dr George Joseph, Ahmedabad
Dr A.K.S. Gopalan, Hyderabad
Dr Prithvish Nag, Varanasi
Dr Baldev Sahai, Ahmedabad
Shri A.R. Dasgupta, Ahmedabad
Dr R.R. Navalgund, Bengaluru
Shri Rajesh Mathur, New Delhi
Dr Ajai, Ahmedabad
Prof P. Venkatachalam, Mumbai
Dr Shailesh Nayak
Prof I.V. Murli Krishna
Prof SM Ramasamy, Tiruchirapalli
Dr Ashok Kaushal, Pune
Shri A.S. Kiran Kumar, Bengaluru
Prof. P.K. Verma, Bhopal
Maj. Gen. Siva Kumar, Hyderabad
Dr A S Rajawat, Ahmedabad
Dr Shakil Romshoo, Srinagar

INDIAN SOCIETY OF GEOMATICS: PATRON MEMBERS

P-1 Director, Space Applications Centre (ISRO), Jodhpur Tekra Satellite Road, Ahmedabad - 380 015
P-2 Settlement Commissioner, The Settlement Commissioner & Director of Land Records-Gujarat, Block No. 13, Floor 2, Old Sachivalay, Sector-10, Gandhinagar – 382 010
P-3 Commissioner, Mumbai Metropolitan Region Development Authority, Bandra-Kurla Complex, Bandra East, Mumbai - 400 051
P-4 Commissioner, land Records & Settlements Office, MP, Gwalior - 474 007
P-5 Director General, Centre for Development of Advanced Computing (C-DAC), Pune University Campus, Ganesh Khind, Pune - 411 007
P-6 Chairman, Indian Space Research Organization (ISRO), ISRO H.Q., Antariksha Bhavan, New BEL Road,Bengaluru 560 231
P-7 Director General, Forest Survey of India, Kaulagarh Road, P.O. I.P.E., Dehra Dun – 248 195
P-8 Commissioner, Vadodara Municipal Corporation, M.S. University, Vadodara - 390 002
P-9 Director, Centre for Environmental Planning and Technology (CEPT), Navarangpura, Ahmedabad - 380 009
P-10 Managing Director, ESRI INDIA, NIIT GIS Ltd., 8, Balaji Estate, Sudarshan Munjal Marg, Kalkaji, New Delhi - 110 019
P-11 Director, Gujarat Water Supply and Sewerage Board (GWSSB), Jalseva Bhavan, Sector – 10A, Gandhinagar - 382 010
P-12 Director, National Atlas & Thematic Mapping Organization (NATMO), Salt Lake, Kolkata - 700 064
P-13 Director of Operations, GIS Services, Genesys International Corporation Ltd., 73-A, SDF-III, SEEPZ, Andheri (E), Mumbai - 400 096
P-14 Managing Director, Speck Systems Limited, B-49, Electronics Complex, Kushiaguda, Hyderabad - 500 062
P-15 Director, Institute of Remote Sensing (IRS), Anna University, Sardar Patel Road, Chennai - 600 025
P-16 Managing Director, Tri-Geo Image Systems Ltd., 813 Nagarjuna Hills, PunjaGutta, Hyderabad - 500 082
P-17 Managing Director, Scanpoint Graphics Ltd., B/h Town Hall, Ashram Road, Ahmedabad - 380 006
P-18 Secretary General, Institute for Sustainable Development Research Studies (ISDRS), 7, Manav Ashram Colony, Goplapura Mod, Tonk Road, Jaipur - 302 018
P-19 Commandant, Defense institute for GeoSpatial Information & Training (DIGIT), Nr. Army HQs Camp, Rao Tula Ram Marg, Cantt., New Delhi - 110 010
P-20 Vice President, New Rolta India Ltd., Rolta Bhavan, 22nd Street, MIDC-Marol, Andheri East, Mumbai - 400 093
P-21 Director, National Remote Sensing Centre (NRSC), Deptt. of Space, Govt. of India, Balanagar, Hyderabad - 500 037
P-22 Managing Director, ERDAS India Ltd., Plot No. 7, Type-I, IE Kukatpalli, Hyderabad - 500 072
P-23 Senior Manager, Larsen & Toubro Limited, Library and Documentation Centre ECC Constr. Gp., P.B. No. 979, Mount Poonamallee Road, Manapakkam, Chennai - 600 089.
P-24 Director, North Eastern Space Applications Centre (NE-SAC), Department of Space, Umiam, Meghalaya 793 103
P-25 Progamme Coordinator, GSDG, Centre for Development of Advanced Computing (C-DAC), Pune University Campus, Pune – 411 007
P-26 Chief Executive, Jishnu Ocean Technologies, PL-6A, Bldg. No. 6/15, Sector – 1, Khanda Colony, New Panvel (W), Navi Mumbai – 410 206
P-27 Director General, A.P. State Remote Sensing Applications Centre (APSRAC), 8th Floor, "B" Block, Swarnajayanthi Complex, Ameerpet, Hyderabad- 500 038
P-28 Director, Advanced Data Processing Res. Institute (ADRIN), 203, Akbar Road, Tarbund, Manovikas Nagar P.O., Secunderabad –500 009
P-29 Managing Director, LEICA Geosystems Geospatial Imaging Pvt. (I) Ltd., 3, Enkay Square, 448a Udyog Vihar, Phase-5, Gurgoan- 122 016
P-30 Director, Defense Terrain Research Limited (DTRL), Ministry of Defense, Govt. of India, Defense Research & Development Organisation, Metacafe House, New Delhi – 110 054
P-31 Chairman, OGC India Forum, E/701, Gokul Residency, Thakur Village, Kandivali (E), Mumbai – 400 101
P-32 Managing Director, ML Infomap Pvt. Ltd., 124-A, Katwaria Sarai, New Delhi – 110 016
P-33 Director, Rolta India Limited, Rolta Tower, "A", Rolta Technology Park, MIDC, Andheri (E), Mumbai – 400 093
P-34 Director, State Remote Sensing Applications Centre, Aizawl – 796 012, Mizoram

Instructions for Authors

The journal covers all aspects of Geomatics – geodata acquisition, pre-processing, processing, analysis and publishing. Broadly this implies inclusion of areas like GIS, GPS, Photogrammetry, Cartography, Remote Sensing, Surveying, Spatial Data Infrastructure and Technology including hardware, software, algorithm, model and applications. It endeavors to provide an international forum for rapid publication of developments in the field – both in technology and applications.

A manuscript for publication must be based on original research work done by the author(s). It should not have been published in part or full in any type of publication nor should it be under consideration for publication in any periodical. Unsolicited review papers will not be published.

The Editorial Board or the Indian Society of Geomatics is not responsible for the opinions expressed by the authors.

Language

The language of the Journal will be English (Indian). However, manuscripts in English (US) and English (British) are also acceptable from authors from countries located outside India.

Manuscript Format

Each paper should have a title, name(s) of author(s), and affiliation of each of the authors with complete mailing address, e-mail address, an abstract, four to six keywords, and the text. The text should include introduction/background, research method, results, discussion, followed by acknowledgements and references. The main text should be divided in sections. Section headings should be concise and numbered in sequence, using a decimal system for subsections. Figures, images and their captions should be inserted at appropriate points of the text. Figures, images and tables should fit in two column format of the journal. If absolutely necessary, figures, images and tables can spread across the two columns. Figures and images, however, should not exceed half a page in height. A title should be provided for each Table, Image and Figure. All figures and images should be in 600 dpi resolution and sized as per column/margin width. Authors must ensure that diagrams/figures should not lose easy readability upon reduction to column size. The SI (metric) units and international quantities should be used throughout the paper. In case measurements are given in any other system, equivalent measurements in SI (metric) units should be indicated in brackets.

Use MS Word with English (UK/US) or English (Indian) dictionary. The page size should be A4 paper, with 2 cm margin on all sides. Title, authors and affiliation should be centred. Abstract should be justified across margins. The manuscript text should be in two columns of 8.2 cm each with a gutter of 6mm between them. Use only Times New Roman fonts. Title should be 12 points bold. Authors and affiliation should be 9 points. All other text including headings should be 10 points. Heading numbering scheme should be decimal e.g. 1, 1.1, 1.2.3, etc. Headings should be in bold.

Normally length of a published paper should be about 6-10 pages in A4 size including figures. Use of illustrations in colour should be restricted and resorted to only where it is absolutely necessary and not for enhancing the look of the paper. If the number of colour illustrations exceeds five, authors' institution may be asked to reimburse the extra cost involved, which at current rates is about Rs. 2500 per coloured figure/diagram/plate/illustration.

Submission of Manuscript

Submissions should be in electronic form via email. The manuscript may be sent by email to editorjogisg@gmail.com. In exceptional cases hard copy submission in camera ready form may be allowed with the prior permission of the Chief Editor. Submission in any other form will be returned to the author. To speed up the review process, authors are advised to provide a list of three probable reviewers with their institutional address and e-mail IDs.

Guidelines for Citing References

Names of all cited publications should be given in full. No abbreviations should be used. Following procedure is to be adopted.

Journal Publications

Bahuguna, I.M. and A.V. Kulkarni (2005). Application of digital elevation model and orthoimages derived from IRS-1C Pan stereo data in monitoring variations in glacial dimensions, Journal of the Indian Society of Remote Sensing, 33(1), 107- 112. (to be referred to in the text as Bahuguna and Kulkarni (2005) or if more than two sets of authors are to be referred to, as (Bahuguna and Kulkarni, 2005; Jain et al., 1994)) When more than two authors are to be referred to, use Jain et al. (1994). However, in References, all authors are to be mentioned.

Publication in a Book

Misra, V.N. (1984). Climate, a factor in the rise and fall of the Indus Civilization – Evidence from Rajasthan and Beyond in Frontiers of the Indus Civilization (B.B. Lal and S.P. Gupta: Chief Editors) Books and Books, New Delhi, pp. 461-489

Papers Published in Seminar/ Symposium Proceedings

Jain, A., A.R. Shirish, M. Das, K. Das, M.C. Porwal, and P.S. Roy (1994). Remote Sensing and Geographic Information System – An approach for the assessment of biotic interference in the forest ecosystem. Proceedings. 15th Asian Conference on Remote Sensing, Bangalore, November 17-23, 1994, pp. 65-72.

Books

Possehl, Gregory L. (1999). Indus Age: The beginnings. Oxford and IBH Publishing Corporation, New Delhi.

Reviewing

Each paper will be reviewed by three peers. Papers forwarded by members of the Editorial or Advisory Boards along with their comments would get processed faster and may be reviewed by two referees only.

Sample format for Authors is available in downloadable form at ISG website: www.isgindia.org/JOG/Sample_format.doc

Copyright

The copyright of the paper selected for publication will rest with the Indian Society of Geomatics. Corresponding author shall be required to sign a copyright assignment form, on behalf of all authors, once the paper is selected for publication. Authors are, however, at liberty to use this material elsewhere after obtaining permission from the Indian Society of Geomatics.

If the authors have used any copyright material in their manuscript, it is understood that they have obtained permission from the owner of the copyright material and they should convey the same along with the manuscript to the Chief Editor.

Certificate of Original Work

The authors will also provide a certificate that the paper is an original work, not published or being considered for publication elsewhere.

In the event the certificate turns out to be false, the Journal shall ban the author(s) from publishing in the Journal for a period of five years and inform the same to all other related publications.

Reprints

Authors will be allowed to download the (PDF) of their paper from ISG Website www.isgindia.org, No hard copy reprints will be provided.

Journal of Geomatics

Advertisement Rates

	1 Issue	4 Issues
Back Cover Page in colour	**Rs. 25,000**	**Rs. 80,000**
Inside Cover Page in colour	**Rs. 20,000**	**Rs. 64,000**
Full Page inside in colour	**Rs. 15,000**	**Rs. 48,000**
Full Page inside in B/W	**Rs. 10,000**	**Rs. 32,000**

Advertisement Details

Mechanical Details
Double Spread/Center Spread (42 x 29.7) cm
Full page bleed (21 x 29.7) cm
Full page non-bleed (19 x 27.7) cm

Art Requirements

Negatives: Art must be right reading, emulsion, down. Film must be supplied in one piece per color, each identified by color. Camera-ready art is accepted for black & White adds; however, film is preferred. Electronic Files are also accepted.

Electronic File Requirements: All material must be received before ad close dates.

Software: Adobe illustrator 9.0 (saved as EPS). Adobe Photoshop CS (saved as EPS or TIFF). Please convert higher versions down. If you can only supply an IBM format, the file must be in viewable EPS or TIFF format with fonts embedded as that format.

Colour Ads: Colour separations must be provided, right reading, emulsion down. Please note that files using RGB or Pantone colours (PMS) must be converted to CMYK before we receive files.

To,
The Secretary, Indian Society of Geomatics
6202, Space Applications Centre (ISRO)
AHMEDABAD – 380 015. INDIA

Sir,

I want to become a Member/ Life Member/ Sustaining Member/ Patron Member/ Foreign Member/ Student Member of the Indian Society of Geomatics, Ahmedabad for the year _____. Membership fee of Rs. _____ /- is being sent to you by Cash/ DD/ Cheque. (In case of DD/ Cheque No._________dated________drawn on Bank ____________________________ . I **agree to abide by the Constitution of the Society.**

Date:

Place: **Signature**

- Name: Mr/Ms/Mrs/Dr____
- Address: ____

____PIN: ____________

Phone: _____________ Fax: _______________Email:

___________________________________ • Date of Birth

____

•Qualifications____

- Specialisation: ____
- Designation: _______________________ Organisation. __________________________
- Membership in other Societies: _____________________________________
- Mailing Address: ____

____PIN: __________________

Proposed by:
(Member's Name and No)
Signature of Proposer

For Office Use: A/P/L Member No.		Receipt No.		Date:	

Indian Society of Geomatics (ISG), Room No. 6202 Space Applications Centre (ISRO), Ahmedabad-380015, Gujarat. Url: www.isgindia.org Phone: +91-79 26916202
Email: secretary@isgindia.org or sasharma@sac.isro.gov.in Fax +91-79-26916287

MEMBERSHIP FEES

Sr. No.	Membership	Life/Patron Membership fees		Annual Subscription
	Category	**₹** Indian	**US $** Foreign	**₹** Indian
1.	Annual Member	10	---	300
2.	Life Member a) Admitted below 45 years of age	2500	250	
	b) Admitted after 45 years of age	2000	200	
3.	Sustaining Member	---	---	2000
4.	Patron Member	50000	3000	---
5.	Student Member	10	---	100

MEMBERSHIP GUIDELINES

- Subscription for Life Membership is also accepted in two equal instalments payable within duration of three months, if so desired by the applicant. In such a case, please specify that payment will be in instalments and also the probable date for the second instalment (within three months of the first instalment).
- A Member of the Society should countersign application of membership as proposer.
- Subscription in DD or Cheque should be made out in the name of **'Indian Society of Geomatics'** and payable at Ahmedabad.
- Direct deposit in ISG A/Cs must include bank fee RS. 25/- for cash payment.
- Financial year of the Society is from April 1 to March 31.
- For further details, contact Secretary, Indian Society of Geomatics at the address given above.
- ISG has chapters already established at the following places. Ahmedabad, Ajmer, Bhagalpur, Bhopal, Chennai, Dehradun, Delhi, Hissar, Hyderabad, Jaipur, Ludhiana, Mangalore, Mumbai, Mysore, Pune, Shillong, Trichi, Srinagar, Vadodara, Vallabh Vidya Nagar, Visakhapatnam and Trivandrum. Applicants for membership have the option to contact Secretary/Chairman of the local chapter for enrolment. Details can be found at the website of the Society: www.isgindia.org.
- Journal of the Society will be sent to Life Members by softcopy only.

Indian Society of Geomatics (ISG), Room No. 6202 Space Applications Centre (ISRO),
Ahmedabad-380015, Gujarat. Url: www.isgindia.org Phone: +91-79 26916202
Email: secretary@isgindia.org or sasharma@sac.isro.gov.in Fax +91-79-26916287

Geomatics Revealed

IGiS

Integrated GIS & IP Software

VERSION 2.0

MAKE IN INDIA

National Awards on Technology
By The Former President of India,
Dr. A. P. J. Abdul Kalam

Launch of IGiS Version 2.0
By Padam Shri AS Kiran Kumar, Chairman, ISRO and
Shri Tapan Mishra, DIRECTOR, SAC, ISRO.

What's new in IGiS

IGiS Version 2.0 is full of enhancements which you'll appreciate every day. New advanced GIS/IP and SAR modules are vital now a days. New COM Based Architecture makes you even more productive. The more you do with IGiS Version 2.0, the more you'll wonder how you ever did without it.

Enhancements in IGiS Version 2.0

- Advanced GIS / Image Processing
- Microwave SAR Analysis
- Meteorological Analysis
- COM Based Scalable Architecture
- New Ribbon Bar GUI
- Python Customization
- OGC Standards

Product Development Partner

इसरो isro
Government of India | Department of Space
Indian Space Research Organisation - (ISRO)

SGL Scanpoint Geomatics Ltd.
www.scanpointgeomatics.com

Scanpoint Geomatics Ltd.
Corporate Office : 12, Abhishree Corporate Park, Iskcon - Ambli Road, Ahmedabad - 380 058. Gujrat (India)
[P] +91 2717 297096-98 [F] +91 2717 297039 [E] info@scanpointgeomatics.com [W] www.scanpointgeomatics.com

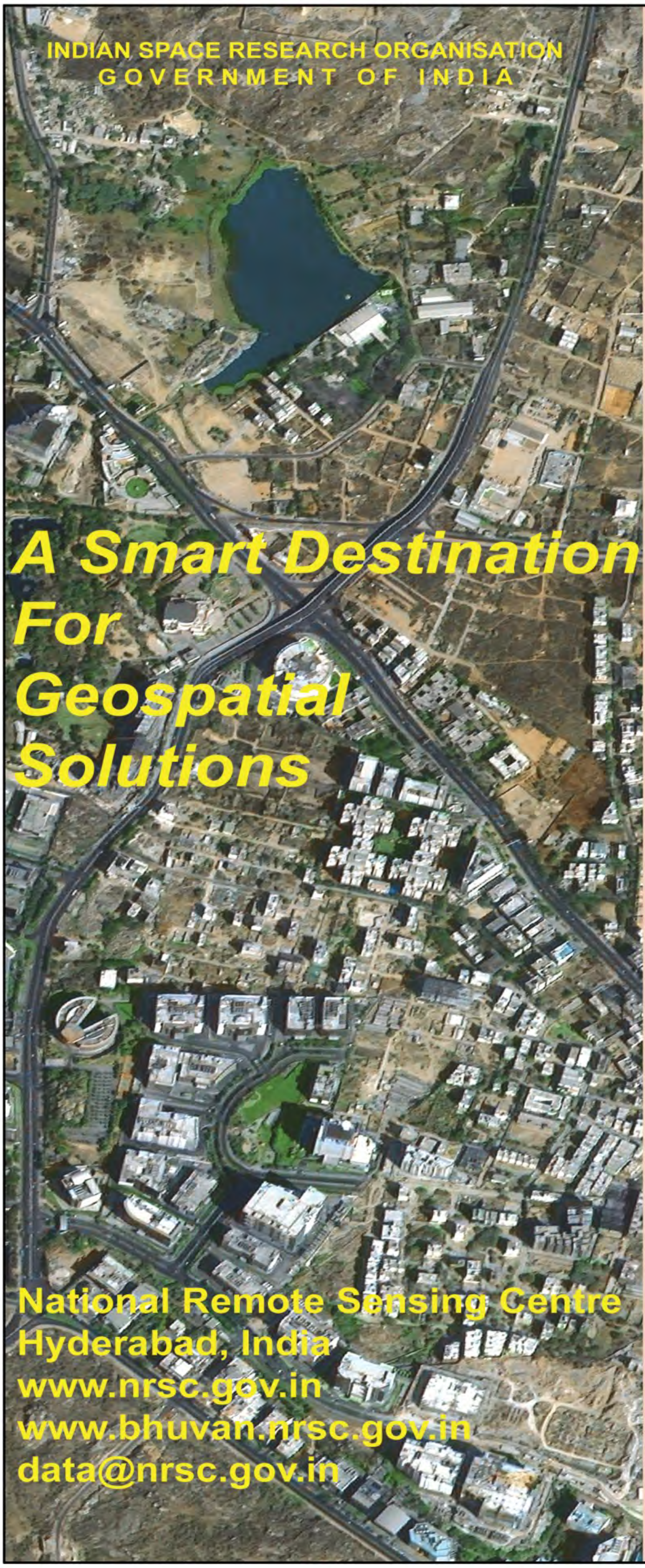

INDIAN SPACE RESEARCH ORGANISATION
GOVERNMENT OF INDIA

A Smart Destination For Geospatial Solutions

National Remote Sensing Centre
Hyderabad, India
www.nrsc.gov.in
www.bhuvan.nrsc.gov.in
data@nrsc.gov.in

nrsc

इसरो isro

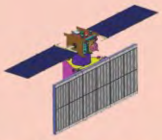

Only Organization in the Country to Acquire & Supply Satellite Data to Users

Aerial Acquisition for Specific User Demands & Disaster Management Support

Open Data & Value Added Products Dissemination Through Bhuvan

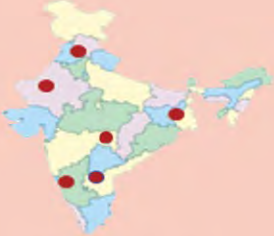

Region Specific Solutions

Capacity Building in Remote Sensing Applications